TECHNISCHE
UNIVERSITÄT
DARMSTADT

Physik

Phase Structure of Strongly Correlated Fermi Gases

Vom Fachbereich Physik
der Technischen Universiät Darmstadt

zur Erlangung des Grades
eines Doktors der Naturwissenschaften (Dr. rer. nat)

genehmigte Dissertation von

Dipl. Phys., M. Sc. Dietrich Roscher
aus Schlema

Referent: Prof. Dr. Jens Braun
Korreferent: Prof. Dr. Hans-Werner Hammer

Tag der Einreichung: 14.07.2015
Tag der Prüfung: 19.10.2015

Darmstadt 2015
D17

Zusammenfassung

Stark korrelierte fermionische Vielteilchensysteme sind in der Natur weit verbreitet. Ihre theoretische Beschreibung stellt ein kompliziertes Problem dar, welches noch weiter durch die Einführung von Ungleichgewichte wie z.B. in den Teilchenzahlen oder -massen der auftretenden Fermionsorten erschwert wird. In dieser Arbeit wird eine Anzahl unterschiedlicher Zugänge zu diesem Problem entwickelt und angewendet, um sich gegenseitig unterstützende und bestätigende Vorhersagen für physikalische Observablen zu erhalten.

In einem ersten Schritt werden analytisch wohlfundierte „mean-field"-Studien durchgeführt. Ein- und dreidimensionale ultrakalte Fermigase im Spin- und Massenungleichgewicht sowie Gross-Neveu und NJL-artige relativistische Modelle mit endlichem Baryon-chemischem Potential werden auf ihre analytischen Eigenschaften im Allgemeinen und das Auftreten von spontaner Brechung der Translationsinvarianz im Besonderen hin untersucht.

Basierend auf diesen Studien werden weitere Methoden entwickelt oder adaptiert um diese Untersuchungen auch jenseits der „mean-field"-Näherung fortführen zu können. Gitter-Monte-Carlo-Simulationen mit imaginären Ungleichgewichtsparametern werden angewandt um das berüchtigte Vorzeichenproblem zu umgehen und die Zustandsgleichung ensprechender unitärer Fermigase zu berechnen. Darüberhinaus werden Zweiteilchenanalysen im Medium genutzt, um die Eigenschaften inhomogener suprafluider Phasen zu bestätigen und zu erklären. Schließlich kommen Methoden der funktionalen Renormierungsgruppe zur Untersuchung unitärer Fermigase im Spin- und Massenungleichgewicht zum Einsatz. Neben quantitativ konkurrenzfähigen Vorhersagen für kritischen Temperaturen des suprafluiden Zustands werden starke Hinweise auf die Stabilität von inhomogenen Phasen bezüglich Ordnungsparameterfluktuationen bei großen Massenungleichgewichten gewonnen. Eine Kombination der mit den unterschiedlichen Methoden gewonnenen Erkenntnisse legt die Möglichkeit nahe, dass solche Phasen in derzeit vorbereiteten Experimenten tatsächlich gefunden werden könnten.

Abstract

Strongly correlated fermionic many-body systems are ubiquitous in nature. Their theoretical description poses challenging problems which are further complicated when imbalances in, e.g., the particle numbers of the involved species or their masses are introduced. In this thesis, a number of different approaches is developed and applied in order to obtain predictions for physical observables of such systems that mutually support and confirm each other.

In a first step, analytically well-founded mean-field analyses are carried through. One- and three-dimensional ultracold Fermi gases with spin and mass imbalance as well as Gross-Neveu and NJL-type relativistic models at finite baryon chemical potential are investigated with respect to their analytic properties in general and the occurrence of spontaneous breaking of translational invariance in particular.

Based on these studies, further methods are devised or adapted allowing for investigations also beyond the mean-field approximation. Lattice Monte Carlo simulations with imaginary imbalance parameters are employed to surmount the infamous sign problem and compute the equation of state of the respective unitary Fermi gases. Moreover, in-medium two-body analyses are used to confirm and explain the characteristics of inhomogeneously ordered phases. Finally, functional RG methods are applied to the unitary Fermi gas with spin and mass imbalance. Besides quantitatively competitive predictions for critical temperatures for the superfluid state, strong hints on the stability of inhomogeneous phases with respect to order parameter fluctuations in the regime of large mass imbalance are obtained. Combining the findings from these different theoretical studies suggests the possibility to find such phases in experiments presently in preparation.

Des Menschen Herz erdenkt sich seinen Weg;
aber der HERR allein lenkt seinen Schritt.

Sprüche 16,9

A man's heart plans his way,
but the LORD directs his steps.

Proverbs 16,9

Contents

Chapter 1

Introduction

Quantum theory as a framework to describe physics on microscopic and mesoscopic length scales has undoubtedly contributed major parts to our current understanding of such diverse branches as atomic, nuclear and particle physics, but also condensed matter and even biological physics. However, it seems to be a natural law by itself, that newly established knowledge, theoretically or experimentally, brings up a number of unresolved, ever more complex questions. In order to be able to address and understand specific properties of a quantum system, it is therefore necessary to "isolate" the respective aspects - once again, theoretically as well as experimentally. On the one hand, this usually implies the need for an idealized theoretical model that is sufficiently simple to be solvable and understandable, yet at the same time adequately captures and explains the essential effects. On the other hand an experimental setup is needed, which is least susceptible to any influences not contained in the theoretical description. The very fact of its unprecedented success, e.g., in elementary particle physics justifies this approach. To name just two, the high level of agreement between predictions for and measured values of $(g-2)$, the electron's anomalous magnetic dipole moment [1, 2], or the recent discovery of the long predicted [3–6] Higgs boson [7, 8] constitute prime examples for the achievements of quantum field theory in describing nature.

Until its experimental discovery and subsequent characterization, many properties of the Higgs boson like e.g. its mass were not known or could only be estimated with large uncertainty. Although the Higgs sector of the Standard Model of Particle Physics is coupled to Quantum Electrodynamics (QED), these uncertainties did not spoil theoretical predictions for the electron's $(g-2)$ for over 10 significant digits, since a pure QED calculation turned out to be sufficient to reproduce the experimentally found value [1]. In this sense, QED can be considered as an *effective theory* [9] describing the properties of the electron up to a certain precision, where the influence of other components of the standard Model or even beyond might set in. In fact, the anomalous magnetic moments of the electron or, in particular, the muon, constitute an active area of search for physics beyond the Standard Model [1]. However, there are situations when the use of effective field theories becomes mandatory in order to keep the computational effort manageable in the first place. These situations are common or even the normal case in nuclear or condensed matter physics. The underlying interactions, Quantum Chromodynamics (QCD) and QED are known, respectively. But since one is often mainly interested in collective properties of the many particles constituting the system, the peculiarities of these fundamental interactions are of minor importance - similarly as the Higgs boson was for the electron's $(g-2)$. Therefore, the analysis of a properly constructed effective theory is most often the method of choice.

As stated above, the goal of understanding particular properties of (collective) quantum systems induces the need for a proper isolation of these aspects in an experiment. Unfortunately, it is often a nontrivial problem to satisfy this demand. For example, the properties of particles which can be derived from elementary particle collisions are often determined with high precision. In contrast, phenomena of the high density regime of the QCD phase diagram such as the quark-gluon-plasma [10] are much harder to characterize, since they require the collision of heavy ions, creating an enormous amount of new particles and entangling physical effects from energy scales over many orders of magnitude. Speaking of solid state systems, metallic low temperature superconductors are understood since the advent of BCS theory [11]. In contrast, even the basic ingredients of high temperature superconductivity [12], such as the origin of the constitutive pairing force [13] or the nature of the so-called "pseudogap" [14] are not unambiguously described yet. Once again, it is the complicated structure of high-T_c materials and the wealth of competing phenomena that inhibits a thorough understanding.

Both high density QCD and high-T_c superconductivity are still under direct and intense investigation in theory as well as in experiment, see, e.g., [15,16] for reviews. A different approach, which is becoming more and more amenable, is the "emulation" of (aspects of) complicated and strongly interacting systems by means of ultracold atomic gases. Since the first experimental realization of Bose-Einstein-condensation in a cloud of bosonic alkali-metal atoms [17–19] and later on also molecules of fermionic constituents [20,21], experimental control as well as theoretical understanding have advanced rapidly. A proper choice of chemical elements, electronic configurations and external distortions, the tunability of the interaction strength and specifically tailored confining geometries allow for a plethora of experimental scenarios. Spectacular effects have been demonstrated and longstanding theoretical challenges were solved, such as atomic lasing [22], vortex lattices indicating the presence of the superfluid state also in a Fermi gas [23] or the occurrence of "second sound" [24] to name but a few very prominent ones. Visionary medium- and long-term goals include analog and digital quantum computing or the efficient simulation of gauge theories, see, e.g., [25, 26].

This thesis addresses the conditions for and certain properties of superfluidity in strongly interacting gases of ultracold fermionic atoms. It is found that pairing and condensation behavior is profoundly changed when deformations like spin polarization, mass imbalance and/or dimensional reduction are admitted. Although a comparatively simple effective field theory description is employed, these deformations as well as the strong correlations inhibit a complete characterization by means of one single theoretical method. This is not uncommon for strongly coupled quantum systems, whose investigation may vastly benefit from complementary analyses. A detailed description of few- and many-body phenomena, in particular of the phase structure and universal properties by combining the strengths of different theoretical approaches is therefore the main goal of this work.

Before giving a more comprehensive overview of the contents of this thesis in sec. 1.3, some basics concepts have to be established. In sec. 1.1, unitary Fermi gases are introduced alongside the field theoretical framework that will be used throughout this work to describe the various physical phenomena occurring in this and related systems. Sec. 1.2 subsequently provides a survey of the deformations explored here and their impact on physical systems that have been investigated in previous studies as well as prospective experimental findings that may be expected on general grounds.

1.1 Unitary Fermi gases in three dimensions

Consider an ensemble of identical fermionic atoms in three spatial dimensions. The spins $\mathbf{S}$ and orbital angular momenta $\mathbf{L}$ of the electrons as well as the nuclear spin $\mathbf{I}$ are coupled. If now an external magnetic field $\mathbf{B}$ is applied, the energy levels of the atoms will exhibit hyperfine splitting. Atoms in different hyperfine states become distinguishable. These states can thus be used to define different *species* or effective "spin" states. For the following considerations, alkali metal atoms with $\mathbf{L} = 0$ will be considered for simplicity.

1.1.1 Feshbach Resonances and universality

For most of the condensed matter or nuclear systems of interest, the type and strength of the interactions are inherent properties and cannot be altered easily. In contrast, one of the most prominent features of cold atomic gases in general and those of fermionic nature in particular is the tunability of the interaction strength. It is achieved by means of *magnetic Feshbach resonances* [27,28], which will be explained briefly in the following. For a more detailed discussion see, e.g., [29–32].

The general situation for a Feshbach resonance to occur is sketched in fig. 1.1a. If the electron spins of two colliding atoms are aligned, the whole configuration will be a triplet, otherwise it constitutes a singlet scattering channel. Since the electron spin can be flipped via its hyperfine coupling to the nuclear spin, $\sim \mathbf{S} \cdot \mathbf{I}$, these *open* (aligned) and *closed* (anti-aligned) channels are coupled. Depending on the energy difference, this coupling leads to tunneling between the two channels, changing the internal states of one of the atoms in the process. This turns out to be particularly dramatic if a bound state is present in the closed channel.

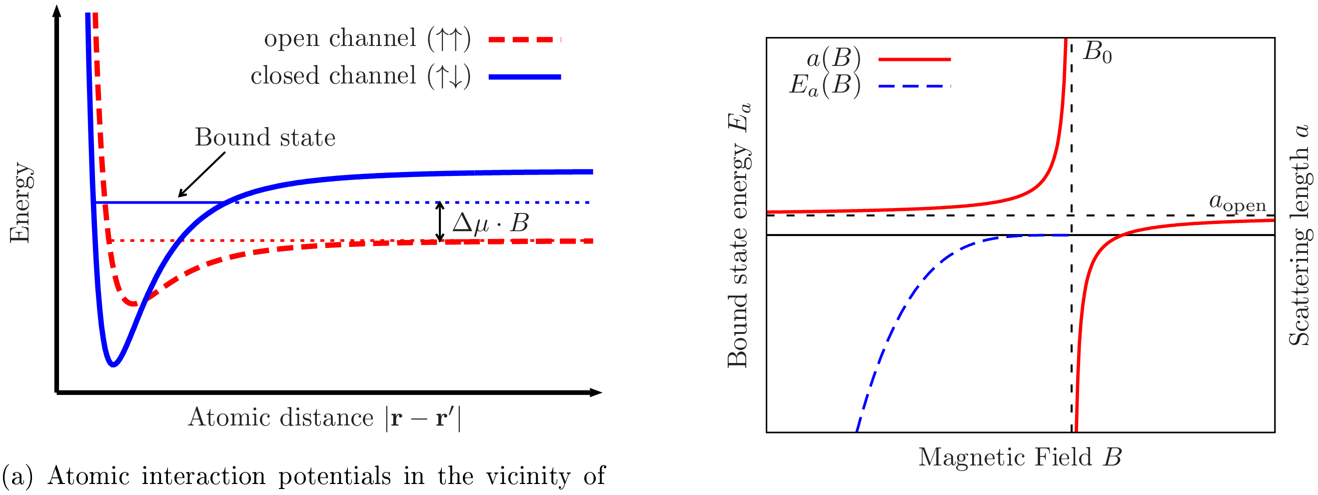

(a) Atomic interaction potentials in the vicinity of a Feshbach resonance. Open and closed scattering channels are coupled via the hyperfine interaction and can be shifted energetically with respect to each other by means of a magnetic field B. Adapted from [31].

(b) Schematic behavior of the scattering length in the vicinity of the resonance at B_0. For positive $a(B)$, a bound state with energy E_a exists in the closed channel.

Figure 1.1: Physics of Feshbach resonances

For differing spin configurations of the atom's internal states, there will be an overall difference $\Delta\mu$ in the magnetic moments of the two states. Consequently, in an external magnetic field B, these states will be shifted with respect to each other by an amount $\Delta\mu B$. In this way, the existence and depth of the closed channel bound state can be tuned which has profound consequences for the scattering properties. The overall *scattering length* of the process becomes B dependent,

$$a(B) = a_{\text{open}} \left(1 - \frac{\Delta B}{B - B_0}\right), \tag{1.1}$$

where a_{open} is the (unaffected) scattering length of the open channel, see also fig. 1.1b. B_0 is the "resonance" magnetic field where the closed channel bound state of energy $E_a = \frac{1}{ma^2}$ [33] exhibits vanishing energy and ΔB parametrizes the width of the resonance[1].

For low energy elastic scattering events as they can be expected in an ultracold environment, the scattering length a directly characterizes the interaction strength. The amplitude $f(k)$ of a scattering event can be decomposed into *partial waves*, i.e. with respect to the relative angular momentum of the collision partners. In this work, only the lowest (*s-wave*) order of this expansion will be considered. The scattering amplitude is then given by (see, e.g., [33, 34])

$$f(k) = \frac{1}{k \cot\delta - ik}, \qquad k \cot\delta = \frac{1}{a} + \frac{r_{\text{eff}}}{2} k^2 + \mathcal{O}(k^3), \tag{1.2}$$

where δ is the *scattering phase shift* and r_{eff} is the effective range of the potential. In order to achieve a most complete characterization of the interaction by the scattering length only, higher order contributions to $k \cot\delta$ like the effective range term must be small. Since the characteristic momentum scale of the gas is given by its Fermi momentum $k_{\text{F}} = (3\pi^2 n)^{\frac{1}{3}}$, this can be achieved by choosing a sufficiently low density $n \simeq 10^{12}...10^{15}\text{cm}^{-3}$ [32]. In the medium, the width ΔB of the Feshbach resonance is also related to the ratio of effective range and Fermi momentum. In this work, only the *broad* resonance limit will be considered, which is characterized by $k_{\text{F}} r_{\text{eff}} \ll 1$ [31]. Furthermore, the temperature T of the "ultracold" gas is chosen such that the thermal *deBroglie wavelength* $\lambda_B = \sqrt{2\pi/(mT)}$, m being the particle mass, is much larger than the average interparticle spacing, $\lambda_B \gg n^{-\frac{1}{3}}$. In an experiment, this corresponds to temperatures of the order $T \simeq 10^{-9} ... 10^{-6} K$ [32].

Under these circumstances, the only scales left in the systems are the scattering length a and the density n. Obviously, the momentum independent part of the scattering amplitude is now completely determined

---

[1] Note that *natural units* will be utilized throughout this work, i.e. $c = \hbar = k_B = 1$.

by the value of a, reaching its maximal value at resonance B_0, where $a \to \pm\infty$, see eq. (1.1). This most strongly interacting case is usually called the *unitary* limit, since it brings about the largest possible total scattering cross section while keeping the scattering matrix $\hat{S}$ unitary as it should be [33]. Furthermore, since a is not a scale of the system anymore, the density is effectively the only scale left. Since physical properties thus cannot depend on details of the interaction anymore, they will exhibit *universal* behavior, see, e.g., [35] for a detailed description of this term and its consequences.

Although the unitary limit is a priori a two-body feature, its intimate relation to the advent of a bound state in the closed channel has also consequences for the many body phase diagram of an ultracold Fermi gas. In the medium, fermionic bound states may exist even at negative scattering lengths. However, those *Cooper pairs* are localized in momentum space rather than in position space, as it is usually understood for *molecules*. Consequently, a condensate of these pairs (see sec. 1.1.3 below) is called a *BCS* (Bardeen-Cooper-Schrieffer) superfluid in analogy to the interaction properties that pairs electrons in a superconductor. For $a > 0$ instead, actual molecules can be formed that become more and more deeply bound and thus localized in position space as $a \to 0$ away from unitarity. Therefore, a condensate of these molecules is termed a *Bose-Einstein-condensate* (BEC). Although the scattering length becomes singular at the unitary point, the transition between BCS and BEC region is actually a smooth crossover [36, 37], which has received much attention in recent years due to the advent of its experimental realizability [21, 38–41], see, e.g., [42–45] for reviews on the subject. Whenever the three-dimensional Fermi gas is discussed in this thesis, only the unitary case will be considered, to which certain deformations are applied, see sec. 1.2 below. It should be mentioned, however, that the findings of this work can most often be straightforwardly generalized to finite a as well.

Microscopically, the atomic interactions can best be described by a power law van-der-Waals potential as sketched in fig. 1.1a. However, in the universal - ultracold and dilute - regime specified above, the details of this potential have negligible impact on physical observables. It is therefore possible to model the realistic potential by a much simpler one, say a hard sphere or even a *contact potential*

$$V_\delta(\mathbf{r}, \mathbf{r}') = g_\delta \delta^{(3)}(\mathbf{r} - \mathbf{r}')\,, \tag{1.3}$$

as long as its coupling g_δ is tuned to reproduce the desired scattering length. This can be achieved by considering the two-body scattering problem, for instance by solving the corresponding Schrödinger or Lippmann-Schwinger equation (see, e.g., [46] for a review), yielding

$$g_\delta = \frac{4\pi}{a^{-1} - c_{\text{reg}}\Lambda}\,. \tag{1.4}$$

Here, Λ is an overall three-momentum cutoff parameter restricting the range of admissible momenta to $|\mathbf{p}| \leq \Lambda$. It had to be introduced as a regularization and c_{reg} is a constant depending on the details of this regularization procedure [47].

1.1.2 Field theoretical description

Since the temperature as a characteristic energy scale of the system is very low compared to the atomic masses involved,[2] a *non-relativistic* treatment is well justified. For any finite number of particles, it is therefore in principle possible to write down a many-body Schrödinger operator and extract any physical observables from its eigenfunctions. However, due to the large number of degrees of freedom, such an approach is usually far from practical, even numerically, if actual thermodynamic quantities are of interest. Still in the spirit of a wave function or density representation of the ground state, but significantly reducing the number of variables to be computed, are methods like Density Renormalization Group [48], Density Functional Theory [49] or the thermodynamic Bethe ansatz [50].

In this work, concepts of thermal effective quantum field theory will provide the basis for mean-field calculations, Monte Carlo studies and renormalization group considerations. In order to establish this framework, the basic field theoretical description of ultracold Fermi gases will briefly be discussed in the following (see, e.g., [51, 52] for introductory textbooks).

The partition function Z is the generating function of all thermodynamic observables. Its field theoretical

---

[2] For instance, $T/m \sim 10^{-19}$ for a gas of ^{6}Li atoms at $T \approx 10^{-6}K$.

version

$$\mathcal{Z} = \mathrm{Tr} e^{-\beta(\hat{H}-\mu\hat{N})} = \int \mathcal{D}\psi^\dagger \mathcal{D}\psi e^{-S_\mathrm{F}[\psi^\dagger,\psi]} \tag{1.5}$$

fulfills an analogous task in the path integral framework. It is obtained from the usual Feynman-type functional field integral by setting time to imaginary values. The Grassmann-valued field vector $\psi^T = (\psi_\uparrow, \psi_\downarrow)$ represents two fermion species whose microscopic properties are encoded in the euclidean action S_F:

$$S_\mathrm{F}[\psi^\dagger,\psi] = \int_0^\beta \mathrm{d}\tau \int \mathrm{d}^3x \left[\psi^\dagger\left(\partial_\tau - \frac{\nabla^2}{2m} - \mu\right)\psi + g_\delta \psi_\uparrow^* \psi_\uparrow \psi_\downarrow^* \psi_\downarrow\right]. \tag{1.6}$$

The non-relativistic character of the theory is most obviously implemented by the kinetic operator $\partial_\tau - \nabla^2/(2m)$, where the spatial coordinates are distinguished from the temporal ones by second order or first order derivatives, respectively. The imaginary "Euclidean" time axis has been compactified such that the fermionic fields are anti-periodic along this direction: $\psi(0,\mathbf{x}) = -\psi(\beta,\mathbf{x})$ and thus obey the Pauli exclusion principle. This procedure guarantees the interpretation of $\beta \equiv 1/T$ as the inverse thermodynamic temperature. The chemical potential μ as the coefficient of the number density operator $\psi^\dagger\psi$ is a Lagrange multiplier that can be used to fix the overall density. Finally, the four-fermion interaction term realizes the s-wave contact potential (1.3) and its coupling g_δ is chosen as in eq. (1.4) to implement the physics of a Feshbach resonance.

Bosonization It is in general not possible to calculate the interacting path integral (1.5) exactly. Approximations have to be employed in one or the other way. Of course, it is possible to do so on the level of the fermionic action (1.6). For the purposes of this work, however, it is more convenient to introduce a complex auxiliary bosonic field φ by means of a *Hubbard-Stratonovich transformation* first [53, 54]. Let $\mathcal{N}$ be a properly chosen normalization constant such that

$$\mathcal{Z} = \int \mathcal{D}\psi^\dagger \mathcal{D}\psi e^{-S_\mathrm{F}[\psi^\dagger,\psi]} = \mathcal{N} \int \mathcal{D}\psi^\dagger \mathcal{D}\psi \mathcal{D}\varphi e^{-S_\mathrm{F}[\psi^\dagger,\psi] - \bar{m}_\varphi^2 \varphi^*\varphi} \equiv \mathcal{N} \int \mathcal{D}\psi^\dagger \mathcal{D}\psi \mathcal{D}\varphi e^{-S_\mathrm{B}[\psi^\dagger,\psi,\varphi]}. \tag{1.7}$$

By linearly shifting $\varphi \to \varphi + \frac{\bar{h}_\varphi}{\bar{m}_\varphi^2}\psi_\uparrow\psi_\downarrow$ and choosing $\bar{h}_\varphi^2 = g_\delta \bar{m}_\varphi^2$, the four fermion interaction can be traded for Yukawa-like terms and an additional path integration over φ. There resulting *partially bosonized* action S_B is given by

$$S_\mathrm{B}[\psi^\dagger,\psi,\varphi] = \int_0^\beta \mathrm{d}\tau \int \mathrm{d}^3x \left[\psi^\dagger\left(\partial_\tau - \frac{\nabla^2}{2m} - \mu\right)\psi + \bar{m}_\varphi^2 \varphi^*\varphi - \bar{h}_\varphi\left(\varphi^*\psi_\uparrow\psi_\downarrow - \varphi\psi_\uparrow^*\psi_\downarrow^*\right)\right]. \tag{1.8}$$

The mathematical trick of introducing this auxiliary field will turn out to be of invaluable use for the considerations presented in this thesis. Besides that, a physical interpretation of $\varphi \sim \psi_\uparrow\psi_\downarrow$ as the Cooper pair or Feshbach molecule can be established in certain situations. This will grant more direct access to the behavior and properties of these composite particles.

Symmetries The fermionic action (1.6) exhibits a number of symmetries (see, e.g., [55] for an extensive discussion) that are of crucial influence on the behavior of the system. By construction, they are preserved by the Hubbard-Stratonovich transformation. Major parts of this work deal with the characterization of phases where some of these symmetries are spontaneously broken. It is therefore worthwhile to introduce these symmetries such that formal analyses can be carried out later on.
Due to the non-relativistic approximation, Lorentz invariance is explicitly broken. However, spatial rotations and translations as well as reflections in space and euclidean time are preserved separately. For vanishing temperature, this implies an invariance under Galilean transformations. The latter can be formulated explicitly in real time $t = -i\tau$:

$$\psi(t,\mathbf{x}) \to \psi'(t,\mathbf{x}) = e^{-i\left(\frac{\mathbf{q}^2}{2m}t - \mathbf{q}\cdot\mathbf{x}\right)}\psi\left(t, \mathbf{x} - \frac{\mathbf{q}}{m}t\right), \tag{1.9a}$$

$$\varphi(t,\mathbf{x}) \to \varphi'(t,\mathbf{x}) = e^{-2i\left(\frac{\mathbf{q}^2}{2m}t - \mathbf{q}\cdot\mathbf{x}\right)}\varphi\left(t, \mathbf{x} - \frac{2\mathbf{q}}{m}t\right). \tag{1.9b}$$

Since there are no derivatives acting on the boson field in (1.8), invariance under (1.9b) is obvious. For the fermions, the energy operator is given by $-i\partial_t - \nabla^2/(2m)$ in real time. It is invariant as well:

$$\psi^\dagger \frac{\nabla^2}{2m}\psi \to \psi^\dagger \frac{\nabla^2}{2m}\psi + 2i\frac{\mathbf{q}}{2m}\psi^\dagger \nabla\psi - \frac{\mathbf{q}^2}{2m}\psi^\dagger\psi, \tag{1.10a}$$

$$\psi^\dagger i\partial_t\psi \to \psi^\dagger i\partial_t\psi - i\frac{\mathbf{q}}{m}\psi^\dagger\nabla\psi + \frac{\mathbf{q}^2}{2m}\psi^\dagger\psi\,. \tag{1.10b}$$

At finite temperature, the euclidean time domain is of finite extent. Thus, an analytical continuation to real time is no more possible and galilean invariance is broken explicitly. Equivalently, the fixed reference frame of the heat bath ensuring the finite T can be seen as the physical cause for the broken galilean invariance [56].

Since the two fermionic species are treated on equal footing, there is an SU(2) rotational symmetry with respect to the $\psi^T = (\psi_\uparrow, \psi_\downarrow)$ "spin" structure. Finally, S_F and S_B are invariant under global U(1) rotations,

$$\psi \to e^{i\alpha}\psi\,, \tag{1.11a}$$

$$\varphi \to e^{2i\alpha}\varphi\,, \tag{1.11b}$$

ensuring particle number conservation.

1.1.3 Spontaneous symmetry breaking and superfluidity

The invariance of the action under the above mentioned symmetries does not necessarily imply, that they are respected by the actual *ground state* $|0\rangle$ of the system as well. This phenomenon is called *spontaneous symmetry breaking* (SSB) and the investigation of the conditions for it to occur in the unitary Fermi gas are a major objective of this work. In mathematical language, a symmetry with generator T is spontaneously broken if

$$\langle 0|[Q_T, \Phi(x)]|0\rangle \equiv \langle [Q_T, \Phi(x)]\rangle \neq 0\,, \tag{1.12}$$

where Q_T is the associated Noether charge, $\Phi(x)$ is some (possibly composite) field operator in the Heisenberg picture with compact support and $|0\rangle$ is the groundstate of the theory [57]. Since $Q_T|0\rangle = 0$ if the symmetry is unbroken, the expectation value in (1.12) constitutes an *order parameter*.

For ultracold atomic gases, the most prominent example of a symmetry that is spontaneously broken under certain circumstances is the group of global U(1) phase rotations. It can be shown (see, e.g., [51]), that its occurrence, signaled for this theory by a non-vanishing *energy gap*,

$$\Delta_0 \equiv \bar{h}_\varphi\,|\langle\psi_\uparrow\psi_\downarrow\rangle|\,, \tag{1.13}$$

is connected to a frictionlessly flowing *supercurrent*. Furthermore, since U(1) is a continuous symmetry, the *Goldstone theorem* [58] applies, resulting in the advent of massless *Goldstone bosons*. These so-called *phonons*, along with a number of other peculiar excitations like quantized vortices but also the very nature of the supercurrent itself make the *superfluid* a fascinating subject of research in theory and experiment. While the properties of the energy gap as well as universal and critical aspects are investigated in depth, a discussion of the hydrodynamics of the superfluid state is not a subject of the present work. For more details on the latter see, e.g., the introductory texts [51, 59].

To substantiate the terminology of *condensation* for the occurrence of spontaneous U(1) symmetry breaking that will be used throughout this thesis, some comments are in order. For interacting Bose gases, a ground state expectation value $\langle\varphi\rangle \neq 0$ of the bosonic field can be identified with a macroscopic occupation of said ground state [51,60]. This is the defining criterion for *Bose-Einstein condensation.* The constituent particles of the Fermi gas can of course not form such a condensate directly. However, the Cooper pairs, being bosonic bound states of two fermions, can. Therefore, a non-vanishing $\langle\psi_\uparrow\psi_\downarrow\rangle \sim \langle\varphi\rangle$ signals the formation of a superfluid BEC of Cooper pairs. Note that in this context, φ is not an elementary Bose field anymore, but the auxiliary variable that was introduced by the Hubbard-Stratonovich transformation in eq. (1.7). The occurrence of superfluidity in fermionic atomic gases therefore justifies a physical interpretation of the initially artificial field φ.

Last but not least, it should be mentioned that the equivalence of Bose-Einstein condensation, superfluidity and spontaneous $U(1)$ symmetry breaking holds true only in three-dimensional interacting systems. BEC exists in low-temperature ideal Bose gases but no SSB, as the ground state of a free theory makes expectation values like the one in eq. (1.13) vanish by definition. In lower dimensional systems on the other hand, superfluidity is not connected to BEC anymore. This will be discussed in more detail in chap. 3 of this thesis.

1.2 Deformations

Even under the assumption that the requirements for a simplification of the interaction as discussed in sec. 1.1.1 are perfectly fulfilled, the action (1.6) represents a highly idealized situation that is conveniently treated in theory but can, as a matter of principle, not be realized in any experiment. In reality, the spatial extent and particle number of the Fermi gas are finite, limited by the size of some trapping potential. The presence of this potential may spoil the predictive power of theoretical consideration based on the infinite space action S_F and has to be accounted for. But it also enables the introduction of certain deformations that open up new regimes to be explored. After a brief discussion of the experimental realization and theoretical implementation of trapping potentials, the following two sections will give an overview over the deformations considered in this thesis.

1.2.1 Trapping and dimensional reduction

Some of the most basic prerequisites for experiments with ultracold atoms are a known position of the atomic cloud as well as control over its density and temperature. All three require the presence of a confining potential whose characteristics can (at least to a certain extent) be tailored to fit the experimental needs. Since electrically neutral atoms are considered here and magnetic fields are required to control the interaction properties (see sec 1.1.1), trapping principles that rely on electric or magnetic interactions are not applicable. Instead, radiation pressure or the interplay of induced dipole moments with incident laser light is used [61] to form a potential that is approximately harmonic, see, e.g., [42, 43, 61]:

$$V_\mathrm{opt} = \frac{m}{2}\left(\omega_x^2 x^2 + \omega_y^2 y^2 + \omega_z^2 z^2\right), \tag{1.14}$$

see fig. 1.2a for a sketch. Since the potential is thus effectively realized by the intensity distribution and interference patterns of laser beams, its depth is finite. The total number of particles that can be kept in the trap is therefore limited and the density can be controlled via the characteristic frequencies $\omega_{x,y,z}$. Finally, besides a number of other mechanisms, cooling of the cloud can be achieved for example by evaporative cooling or adiabatic expansion [61]. The former method works by removing the most highly energetic atoms from the trap. The latter approach achieves an overall decrease of temperature by adiabatically widening the trap and thus increasing the volume available for expansion. In both cases, a controlled change of the trapping potential's shape is the key to precise control over the ensemble's temperature.

It seems clear that the presence of a trap has profound consequences for the behavior of the atomic gas. However, for large enough systems ($N_\mathrm{atom} \approx 10^5 \ldots 10^7$) and sufficiently flat confining potentials, the latter may be dealt with by means of the *Local Density* (LDA) or *Thomas Fermi approximation* of *Density functional theory* (see, e.g., [62, 63] for introductory textbooks). Within this framework, the trap is treated as a space-dependent chemical potential,

$$\mu(\mathbf{r}) = \mu_0 + V_\mathrm{opt}(\mathbf{r}), \tag{1.15}$$

with some basic μ_0 that is determined by the density in the center of the trap [43]. At each point $\mathbf{r}$ of the trap, the effective chemical potential $\mu(\mathbf{r})$ can then be used in an infinite volume calculation to determine the local properties of the gas. By means of the LDA, predictions based on actions like the one in eq. (1.6) can thus be reliably compared to experimental data obtained from trapped fermions and are therefore valuable [64, 65].

By changing the intensity distributions and by generating suitable interference patterns of the laser beams forming the trap, various confining geometries beyond the three-dimensional harmonic oscillator

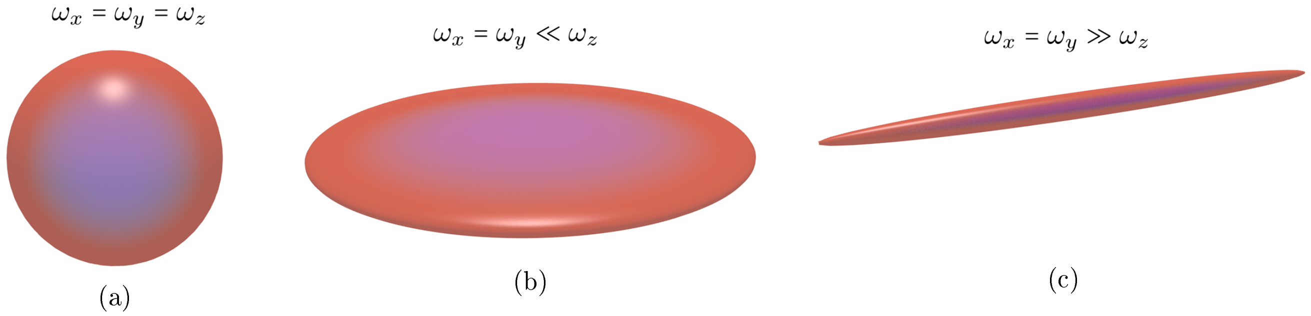

Figure 1.2: Dimensional reduction of optical trapping potentials by means of the aspect ratio: spherical (a), oblate (b) and prolate (c) configurations.

potential (1.14) can be built. In particular, it is possible to modify the *aspect ratio* of the trap, i.e. the ratio of the characteristic frequencies for the spatial directions. If, for example, $\omega_x = \omega_y \ll \omega_z$, it costs much more energy to populate the higher harmonic oscillator levels in z than in the x or y directions. Therefore, the trapped gas becomes effectively two-dimensional if the overall density is sufficiently low, see fig. 1.2b. If, instead, $\omega_x = \omega_y \gg \omega_z$, the now highly elongated trap provides an effectively one-dimensional environment, see fig. 1.2c. By continuously tuning the spatial frequencies between these extremes or, more practicable, populating higher levels even in the confined geometry an actual dimensional crossover can be observed [66].

In contrast to the precise geometry of the trapping potential, dimensional reduction can be incorporated into the theoretical treatment in a comparatively easy way. The first and most obvious change is the reduced dimensionality of the action functional itself, e.g.

$$S_{\mathrm{F}}^{1\mathrm{D}}[\psi^\dagger,\psi] = \int_0^\beta \mathrm{d}\tau \int \mathrm{d}x \left[\psi^\dagger\left(\partial_\tau - \frac{\nabla^2}{2m} - \mu\right)\psi + g_\delta^{1\mathrm{D}}\psi_\uparrow^*\psi_\uparrow\psi_\downarrow^*\psi_\downarrow\right], \tag{1.16}$$

for the one-dimensional case that will be discussed in chap. 3 of this thesis. Since the two-body scattering properties that relate the four-fermion coupling $g_\delta^{1\mathrm{D}}$ with the scattering length are modified with respect to the 3D case, eq. (1.4) does not hold anymore. It can be shown, that

$$g_\delta^{1\mathrm{D}} = -a_{1\mathrm{D}}^{-1} \tag{1.17}$$

instead (see, e.g., [67]). Here, $a_{1\mathrm{D}}$ is the one-dimensional scattering length, which is related to its three-dimensional analog a by

$$a_{1\mathrm{D}} = -\frac{1}{am\omega_{x,y}}\left(1 - a\sqrt{m\omega_{x,y}}C\right), \tag{1.18}$$

with a constant $C \sim \mathcal{O}(1)$ [68]. From eq. (1.17), it is obvious that the "unitary" regime with $a_{1\mathrm{D}} \to \pm\infty$ in one dimension is trivial as it corresponds to the free gas. Instead, strong coupling is achieved for small $a_{1\mathrm{D}}$.

1.2.2 Imbalances

Spontaneous breaking of the global U(1) phase rotation symmetry and the occurrence of superfluidity as discussed in sec. 1.1.3 is certainly a very prominent case of SSB - but it is not necessarily the only one that can occur even in ultracold atomic gases. In fact, a major subject of this thesis will be the (additional) breaking of translational invariance that eventually leads to the formation of space-dependent condensates. As it is probably the best understood instance for such an *inhomogeneous phase* to occur, the following discussion will initially consider the (1+1)-dimensional *Gross-Neveu model* [69] before returning to ultracold Fermi gases.

The Gross-Neveu (GN) model was invented as a toy model for quantum chromodynamics. While there appears to be a huge conceptual as well as phenomenological gap between this theory as part of the standard model of particle physics and ultracold Fermi gases as considered so far, there are in fact close connections and even direct applications of the GN model also to condensed matter systems. This will

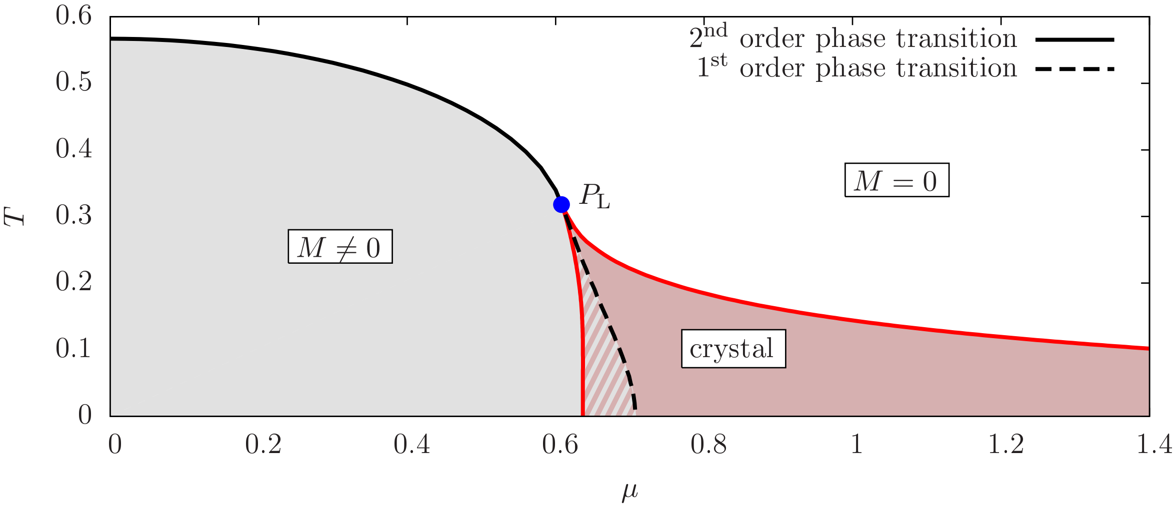

Figure 1.3: Phase diagram of the (1+1)-dimensional Gross-Neveu model. The inhomogeneous "crystal" phase (red shading) supersedes the homogeneous solution (gray shading) close to the former first order transition (striped region). In the fully inhomogeneous solution, all phase boundaries are of second order.

be revisited in more detail below after characterizing the model itself.
The Gross-Neveu model by construction shares important features with QCD, the fundamental theory of the strong interaction: it is *asymptotically free* and its action

$$S_{\mathrm{GN}} = \int_0^\beta \mathrm{d}\tau \int \mathrm{d}x \left[\bar{\psi} \left(i\partial\!\!\!/ + i\mu\gamma_0 \right) \psi + \frac{\lambda^2}{2} \left(\bar{\psi}\psi \right)^2 \right] \quad \text{with} \quad \gamma_0 = \begin{pmatrix} 0 & 1 \\ 1 & 0 \end{pmatrix}, \; \gamma_1 = \begin{pmatrix} 0 & -i \\ i & 0 \end{pmatrix}, \; \gamma_5 = i\gamma_0\gamma_1 \, , \tag{1.19}$$

is invariant under an, albeit discrete, chiral symmetry

$$\bar{\psi} \to -\bar{\psi}\gamma_5, \qquad \psi \to \gamma_5\psi \, . \tag{1.20}$$

The latter can be spontaneously broken for sufficiently low temperatures $T = 1/\beta$ and appropriately chosen chemical potentials μ. In the action (1.19), the fermion field $\psi^T = (\psi_1, ..., \psi_{N_{\mathrm{f}}})$ now exhibits an N_{f}-component vector structure to account for multiple fermion flavors. In the limit of large N_{f}, higher order fluctuation contributions are suppressed and the *mean-field* approximation becomes exact, see sec. 2.2.1 below for a more detailed discussion. Calculating the order parameter for chiral symmetry breaking $\langle \bar{\psi}\psi \rangle \sim \bar{\sigma}(x) = M \cdot f(x)$ as a function of T and μ, the phase diagram of the theory can be mapped out. In early studies [70], the possible x dependence of $\bar{\sigma}$ was not taken into account, resulting in the gray (striped) region in fig. 1.3 for chiral symmetry breaking only. Below the critical *Lifshitz* point P_{L}, the symmetry broken phase was found to be delimited by a first order transition to the normal phase. If now $\bar{\sigma}(x)$ is allowed to vary in space, an inhomogeneous "crystal" phase can be found for arbitrarily large μ (red shaded region in fig. 1.3). Furthermore, parts of the formerly homogeneous phase are now superseded by the inhomogeneous one which turns out to be the true ground state (striped region in fig. 1.3). Last but not least, all phase transitions are found to be of second order in this generalized case. These results could be obtained analytically and were presented in a series of seminal articles [71–74].
The generalization of the phase diagram by the inhomogeneous phase has rather profound consequences. Phenomenologically, the Gross-Neveu model was initially constructed as a toy model for QCD, but it turns out that it may serve as a suitable description for certain solid state systems such as polymer chains [75,76] or quasi-one-dimensional superconducting wires [74] as well. The occurrence of an inhomogeneous phase in the model can be associated with dimerization in the former and e.g. incommensurate charge density wave ordering in the latter realization. From this point of view, it seems obvious that crucial physical effects may be missed if the possible space dependence of the order parameter is neglected.
For the purposes of this thesis, it is particularly interesting to consider more closely the case of quasi-one-dimensional superconductors. These systems are intrinsically non-relativistic and can be related to the relativistic Gross-Neveu model only by a linearization of their dispersion relation [77]. This approximation

is expected to be reasonable, if excitations of the systems are small, such that only the immediate vicinity of the Fermi surface is of importance, see, e.g., [78]. Assuming this to be the case, the inhomogeneous phase is not an artifact of the linearization and should therefore be present in the non-relativistic model as well. In fact, the phenomenon of spontaneous breaking of translational invariance was discussed much earlier than in the high energy context presented so far. In [79] and independently [80], magnetized superconductors were considered and an inhomogeneous ground state was found. Since then, a plethora of very different physical systems has been identified which are expected to exhibit inhomogeneous ordering - last but not least also ultracold atomic gases. A number of selected examples will be touched upon below.

For non-relativistic systems such as ultracold atomic gases, it is not the chemical potential shifting a Dirac sea that induces the possibility of inhomogeneous condensates to occur, but some deformation of the component's Fermi surfaces. In the present work, two types of such *imbalances* will be considered:

Spin imbalance Admitting separate chemical potentials $\mu_\uparrow$ and $\mu_\downarrow$ for the two fermionic species, the respective densities can be detuned with respect to each other. Defining an average chemical potential μ, the spin imbalance can be parametrized as

$$\mu = \frac{\mu_\uparrow + \mu_\downarrow}{2}, \quad h = \frac{\mu_\uparrow - \mu_\downarrow}{2}, \quad \bar{h} = \frac{h}{\mu}. \tag{1.21}$$

The parameter $\bar{h}$ is sometimes called “Zeeman field”, as the relative shift of the chemical potentials may be induced by an external magnetic field coupled to the spin degree of freedom.

Mass imbalance A further generalization can be achieved by permitting different masses $m_\uparrow$ and $m_\downarrow$ for the two species. The conventions adopted in this work for the representation of *mass imbalance* are

$$m_+ = \frac{4m_\uparrow m_\downarrow}{m_\uparrow + m_\downarrow}, \quad m_- = \frac{4m_\uparrow m_\downarrow}{m_\downarrow - m_\uparrow}, \quad \bar{m} = \frac{m_+}{m_-}. \tag{1.22}$$

For convenience and without loss of generality, $m_+ = 1$ will be used throughout this work.

Atomic gases with imbalance In the case of ultracold atomic gases, it seems relatively straightforward (at least from a theorist's point of view) how to implement $\bar{h}$ and $\bar{m}$ in reality. Spin polarizations may be achieved by loading a trap with different amounts of particles of the two respective species. If these species are represented by different hyperfine states of the same chemical element/atomic isotope, a finite spin polarization can also be reached by inducing a transition of one state into the other for a certain amount of atoms. These ideas do of course translate into nontrivial experimental problems, but they can be and have been put into reality indeed. This has famously been accomplished for the first time independently by groups from MIT [81,82] and Rice University [83,84].

A mass-imbalanced system on the other hand can be realized by representing the species by different atomic isotopes. Besides identifying suitable elements in terms of experimental controllability, the interaction properties have to match the conditions detailed in sec. 1.1.1 above. This implies in particular the identification and experimental exploration of *heteronuclear* Feshbach resonances [32]. Some species which are currently under investigation are ^{6}Li, ^{40}K, ^{161}Dy, ^{163}Dy and ^{167}Er, see, e.g., [85–88].

More detailed discussions on experimental results for the phase structure of ultracold Fermi gases follow below in the main part of this work. Chaps. 2 to 4 provide specific theoretical predictions which will be compared to available experimental data where appropriate.

Imbalances and inhomogeneous phases in other physical systems For sure, ultracold Fermi gases are by themselves interesting enough to justify studies of such imbalanced systems. However, connections to other solid state systems or even nuclear and high energy physics can not only be a major motivation but also a useful methodical resource as exemplified above by the Gross-Neveu model. Therefore, some instances of spin and mass imbalances or equivalent deformations that may or do occur in nature, shall now be addressed.

The initial studies [79, 80] were dealing with inhomogeneous phases in the context of superconductors. External magnetic fields are repelled from superconducting materials due to the *Meissner-Ochsenfeld* *effect* [89] or incorporated via *flux tubes* in a *Shubnikov phase* [90, 91]. Thus, a spin polarization of the relevant conduction electrons usually cannot be achieved in this way at least in bulk three-dimensional samples. Instead, the presence of ferromagnetic impurities inside the (metallic) superconductor itself was suggested as a source for polarization and thus the occurrence of inhomogeneous phases. Unfortunately, it is not an easy and not yet thoroughly resolved task, to identify a material that exhibits the corresponding properties.

Although not very intuitive, there might also be realizations of mass imbalance in superconductivity. For certain rare earth or actinide based compounds, termed *heavy-fermion* superconductors, the actual conduction electrons are not the proper degrees of freedom by means of which the occurring phenomena may be described, see, e.g., [92] for an overwiew. Instead, fermionic *quasi-particles* have to be introduced, whose effective mass becomes large due to dressing by strong interaction effects. Since these dressing effects may in principle be spin-dependent [92], a description in terms of an effective mass imbalance seems conceivable as well. In any case, heavy-fermion compounds such as $\mathrm{CeCoIn_5}$ are considered prime candidates for low-dimensional inhomogeneous superconductors, exhibiting certain signs of an FFLO phase in experiment [93].

Layered structures such as in $\mathrm{CeCoIn_5}$, which result in an effectively two-dimensional behavior of the material, are considered to have a large discovery potential for inhomogeneous superconductivity. Besides the above-named Cerium compound, there are also quasi-two-dimensional organic materials, that exhibit signs of an FFLO phase in experiment, see, e.g., [93, 94]. In fact, aside from more favorable magnetic properties [94], lowering the dimensionality appears to increase the parameter space extent of inhomogeneous phases in theory and thus the likelihood of an experimental observation. This constitutes an additional motivation to study low-dimensional atomic gases as introduced in sec. 1.2.1 as well. An extensive discussion of the one-dimensional case will be provided in chap. 3 of this thesis.

Coming back to the domain of high energy and nuclear physics this section started with, the experimental situation becomes even more intricate than for condensed matter systems. This is in part due to the higher energies involved, but mainly due to the complicated nature of the strong interaction dominating this regime. However, there are still cases, where a simple non-relativistic description along the lines of e.g. the action (1.6) can be used as an effective theory. One such an example is the inner crust of a neutron star (see, e.g., [95] for a review), where the constitutive protons and neutrons are believed to be interacting by an almost contact-like potential with large scattering length. The vast neutron excess present in such an environment guarantees a sizable *isospin imbalance*. Furthermore, the explicit breaking of isospin symmetry in nature by the different masses of up and down quarks and consequently also protons and neutrons introduces a small mass imbalance as well. Other imbalanced systems from nuclear and particle physics such as actual finite nuclei or the high-density regime of the QCD phase diagram are way too complicated for a description in terms of non-relativistic actions of the type eq. (1.6) to be in any way complete. Nevertheless it seems reasonable to expect a better general understanding of inhomogeneous and other exotic phases as well in this context from an advancement in the control over corresponding phenomena in ultracold atomic gases.

1.3 Outline

While the solution for the large-N_f phase diagram of the (1+1)-dimensional Gross-Neveu model has indeed been established analytically, exact solutions are rarely achievable in higher dimensional and/or non-relativistic theories. On the one hand, this is due to the tremendous mathematical effort that a serious attempt of this kind requires. On the other hand, it is the *integrability* of these low-dimensional systems and a highly developed theory of partial differential equations of the second order *Sturm-Liouville* type (see [96] and references therein) that renders the corresponding theories accessible to analytic studies in the first place. For ultracold Fermi gases in higher dimensions and with a non-relativistic dispersion relation, nothing comparable is known. Consequently, the scope of this work is not a fully analytic understanding along the lines of Thies' work as summarized in [97]. Instead, this thesis is concerned with the identification, characterization, development, application and evaluation of a range of methods that provide access to the phase structure of strongly correlated fermionic systems in a semi-analytic or numeric way.

Even fully numerical approaches like *lattice Monte Carlo simulations* cannot be pursued without proper analytical preparation. This is particularly true for the imbalanced unitary Fermi gas: the seemingly "straightforward" direct evaluation of the partition function (1.5) by sampling a large number of field configurations is severely hampered by a *sign problem.* In chap. 2, the mechanisms behind the occurrence of this obstacle are worked out and a solution in terms of the *imaginary imbalance approach* is suggested. Before applying this idea to an actual Monte Carlo simulation, its characteristics, benefits and limitations are exposed using the analytically tractable mean-field approximation. Finally, the extraction of the zero-temperature equation of state of the unitary Fermi gas as a function of mass imbalance is demonstrated. This is significant insofar as mass-imbalanced Fermi gases have largely been inaccessible to Monte Carlo methods except for some rare examples. The central goals of chap. 2 are therefore to show the enormous potential of the presented method alongside its limitations the user must be aware of and last but not least to use its power to make nontrivial physical predictions.

Not attempting to find a fully analytical solution of the models considered in this thesis does not preclude the possibility of using knowledge about existing ones. Chap. 3 is mainly devoted to a detailed study of one-dimensional fermionic models within the mean-field approximation. While a direct comparison of such low-dimensional mean-field results to existing experimental data is somewhat problematic, they are well suited to establish methods that may be used in more realistic settings as well. In the first part of chap. 3, a *vertex expansion* technique is introduced and used to study inhomogeneous phases in the spin- and mass-imbalanced one-dimensional Fermi gas. Besides a thorough characterization of systematic errors and comparisons to exact results, the phase structure itself turns out to be interesting enough to justify further investigations on its origin. The second part is therefore concerned with the conditions for and properties of *in-medium bound state formation.* These generalized "Cooper pairs" are capable of explaining many qualitative and even quantitative features of the many-body phase diagram, motivating an exploration of the connections between few-and many-body physics.

As a side effect of the detailed analysis of the vertex expansion results, the quality of simple plane-wave inhomogeneity ansätze becomes apparent. This is not only true for ultracold gases, but also for truly relativistic systems. In order to exploit this finding in the relativistic setting as well, the *fermion doubling trick* is developed in the third part of chap. 3. After proving its capability of exactly reproducing second order transitions between condensate and normal phases using the example of the Gross-Neveu model, it is applied to the *Polyakov loop Nambu-Jona-Lasinio (PNJL) model* which is in fact considered an expedient effective theory for low-energy quantum chromodynamics. In this way, a fairly low-cost method for identifying inhomogeneous phases in relativistic fermion models is established.

With the application of the doubling trick to the PNJL model, one of the methods developed in chap. 3 has already been adapted to the three-dimensional setting there. In the first part of chap. 4, the simple plane wave ansatz as well as the in-medium bound state examination will be used to achieve a first characterization of the phase diagram of spin- and mass-imbalanced unitary Fermi gases in three spatial dimensions. To complement the studies beyond the mean-field approximation from chap. 2, *functional renormalization group (fRG) techniques* are adapted to the imbalanced setting in the further parts of chap. 4. Indeed, complementary information is gained from this approach such as, e.g., the precise location of phase transition manifolds upon inclusion of order parameter fluctuation effects. Furthermore, *pseudogap physics* is explored and strong hints on the stability and location of inhomogeneous phases beyond mean-field are found. Once again, the insight obtained from different approaches is shown to be crucial to a deep understanding of the system's physical properties. The chapter closes with an overview of possible extensions of the fRG formalism for a more direct access to inhomogeneous phases.

In the last chapter 5 of this thesis, all results are finally summarized. Conclusions are drawn along with connections between the individual chapters and some perspectives for possible future research in this field are presented.

Chapter 2

Lattice Monte Carlo studies

For a three-dimensional ultracold Fermi gas with contact interaction (1.3), the unitary limit constitutes the most strongly coupled case. This can readily be seen from eq. (1.4): the coupling g_δ is maximal for $a \to \pm\infty$. The unitary regime is therefore intrinsically *non-perturbative*, as neither the coupling nor any other quantity identified so far may serve as a "small" parameter for a systematic expansion of the partition function or physical observables. No fully analytical solution comparable to the case of the (1+1)-dimensional Gross-Neveu model (see sec. 1.2.2) is known. But even if that was different, it would be of limited practical use, as it relies on the large N_f or mean-field approximation. As will be shown below, this approximation provides qualitative insight into the phase structure of the system, but its quantitative predictions usually cannot stand up to a comparison with experimental data.

Lattice Monte Carlo simulations open up a way of numerically computing quantities like the partition function (1.5) or specific physical observables more or less directly from their path integral representation. They do, by construction, include fluctuation effects that are missed out by the mean-field approximation. Artifacts from, e.g., the finite simulation volume or the discretization may put limits on their predictive power. But as long as these are taken care of properly, Monte Carlo methods are able to achieve impressive agreement with experimental results.

To give an example of the latter statement, consider the *Bertsch* parameter [98], a universal quantity that characterizes the unitary Fermi gas. Due to the vanishing effective range r_eff and the diverging scattering length a, there is only one length scale left in the (balanced) unitary Fermi gas, being the mean inter-particle distance r_mean. Consequently, all thermodynamic quantities can be expressed in terms of the latter or, equivalently the system's particle number density $2n_{\uparrow,\downarrow} = n = r_\mathrm{mean}^{-\frac{1}{3}}$ or Fermi energy $\epsilon_\mathrm{F}^{\uparrow,\downarrow} = (3\pi^2 n_{\uparrow,\downarrow})^{\frac{2}{3}}$ of the free gas for each species times some *universal* constant. In particular, the energy per particle and species $\epsilon_{\uparrow,\downarrow}$ in the unitary Fermi gas is given by

$$\epsilon_{\uparrow,\downarrow} = \frac{3}{5}\epsilon_\mathrm{F}^{\uparrow,\downarrow} \cdot \xi\,, \tag{2.1}$$

with the constant ξ being the universal Bertsch parameter. Figure 2.1 compares various results from Monte Carlo simulations with experimental extrapolations and the mean-field prediction at zero temperature. For a more complete listing and comparison also with analytical approaches other than mean-field, see ref. [99]. In recent years, the predicted and measured values seem to be converging towards $\xi = 0.37 \pm 0.01$. While the mean-field value $\xi_\mathrm{mf} = 0.59$ (e.g. [46, 111]) is off by over 50%, the accuracy of the Monte Carlo results let this class of methods appear as the tool of choice for quantitative predictions.

So far, only the balanced case with perfect symmetry between the ↑ and ↓ fermion species has been considered. It turns out, that an investigation of imbalanced systems as suggested in sec. 1.2.2 is not straightforward: Monte Carlo simulations are hampered and even inhibited by a severe *sign problem* for finite $\bar{h}$ and/or $\bar{m}$. While it is not the aim of this chapter to provide a general introduction into Monte Carlo methods (see, e.g., [112,113] for introductory textbooks or [114–116] for comprehensive presentations of the subject), some basic ideas of Monte Carlo simulations for fermionic field theories are discussed in sec. 2.1. This is necessary in order to clarify the origin of the sign problem and suggest a way out. An examination of the analytic prerequisites and limitations of the latter approach in sec. 2.2 sets the stage for actual simulations of imbalanced unitary Fermi gases. Based on the conceptual ideas from sec. 2.1, some notes on the practical implementation of such an algorithm and finally numerical results are given

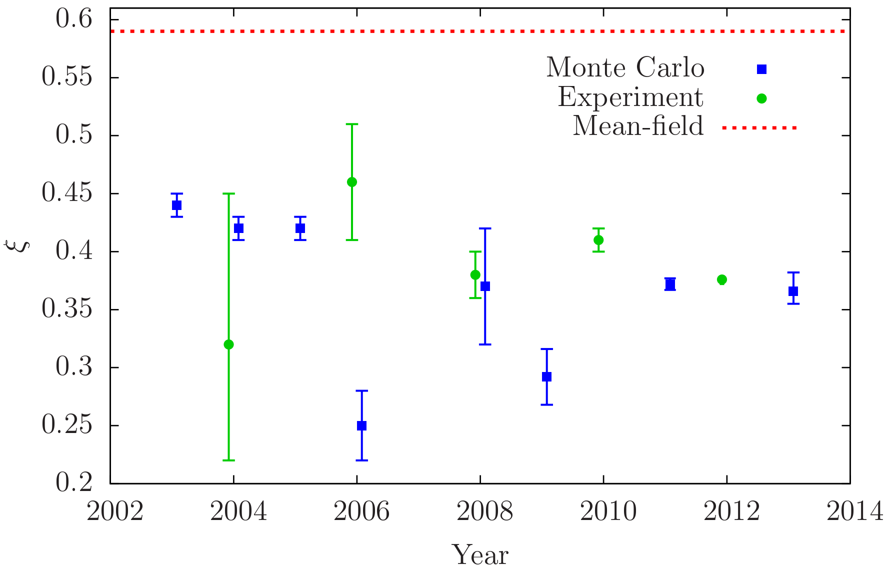

Year	ξ	Ref.
Monte Carlo		
2003	0.44 ± 0.01	[100]
2004	0.42 ± 0.01	[101]
2005	0.42 ± 0.01	[102]
2006	0.25 ± 0.03	[103]
2008	0.37 ± 0.05	[104]
2009	0.292 ± 0.024	[105]
2011	0.372 ± 0.005	[106]
2013	$0.366^{+0.016}_{-0.011}$	[99]
Experiment		
2004	$0.32^{+0.13}_{-0.10}$	[107]
2006	0.46 ± 0.05	[83]
2008	0.38 ± 0.02	[108]
2010	0.41 ± 0.01	[109]
2012	0.376 ± 0.004	[110]

Figure 2.1: Comparison of Monte Carlo and experimental results for the zero-temperature Bertsch parameter ξ with the mean field prediction (see, e.g., [46,111] for reviews). The precision of simulations and measurements has increased enormously within the last years.

in sec. 2.3.
The contents of this chapter, as far as they constitute original work of the author, are mainly based on references [117] and [118].

2.1 Basics of Monte Carlo simulations for non-relativistic fermions

The ultimate goal of Monte Carlo simulations is the numerical computation of physical observables, i.e. thermal expectation values of field operators in the present context. Since all these observables can in principle be deduced from a properly parametrized partition function,

$$\mathcal{Z} = \mathrm{Tr} e^{-\beta(\hat{H}-\mu\hat{N})} = \int \mathcal{D}\psi^\dagger \mathcal{D}\psi e^{-S_\mathrm{F}[\psi^\dagger,\psi]} \qquad \text{(1.5 revisited)}$$

will be used here to demonstrate some of the principle ideas and challenges of Quantum Monte Carlo (QMC) methods. Note, however, that in a practical implementation, it may be more appropriate to compute the observable of interest $\mathcal{O}$ directly

$$\langle\hat{\mathcal{O}}\rangle = \int \mathcal{D}\psi^\dagger \mathcal{D}\psi\, \mathcal{O} e^{-S_\mathrm{F}[\psi^\dagger,\psi]}\,. \tag{2.2}$$

Lattice Monte Carlo approaches strive to calculate $\mathcal{Z}$ by a direct evaluation of the path integral. This is achieved by discretizing space x and (imaginary) time τ on a lattice of, say $N_x^d \times N_\tau$ sites with spacings l_x and l_τ, respectively. Here d is the spatial dimensionality of the problem. The field variables, here given by $\psi^\dagger$ and ψ so far, are then assigned a value at each lattice point. The integrand, i.e. the action S_F, has to be discretized as well. Most obviously, this concerns spatial and temporal derivative operators as they appear in the kinetic term, but it may also apply to interaction terms, see sec. 2.3.1 below. When summing the integrand over all lattice sites and for sufficiently many different field configurations, the exact expression for $\mathcal{Z}$ can be approached.
The action $S_\mathrm{F}[\psi^\dagger,\psi]$ is quartic in the fermion fields, see eq. (1.6). This quartic term can be traded for Yukawa-type interactions by a Hubbard-Stratonovich transformation, see sec. 1.1.2. The resulting bosonic action $S_\mathrm{B}[\psi^\dagger,\psi,\varphi]$ in eq. (1.8) is then only bilinear in the fermion fields. The introduction of the auxiliary field φ is also useful in setting up Monte Carlo simulations, as the proper implementation of quartic interactions turns out to be challenging [116]. Going one step further, the fermionic path integral can now be evaluated at least on a formal level: the bilinear nature of S_B allows for a gaussian integration

with respect to $\psi^\dagger$ and ψ. The partition function is then given by

$$\mathcal{Z} = \int \mathcal{D}\psi^\dagger \mathcal{D}\psi \mathcal{D}\varphi e^{-S_{\mathrm{B}}[\psi^\dagger,\psi,\varphi]} = \int \mathcal{D}\varphi\, e^{-\bar{m}_\varphi^2 \varphi^* \varphi} \det\left[S_{\mathrm{B}}^{(2)}[\psi^\dagger,\psi,\varphi]\right] \equiv \int \mathcal{D}\varphi\, \rho[\varphi] \mathrm{det} K[\varphi]\,, \tag{2.3}$$

where $S_{\mathrm{B}}^{(2)}$ is the second functional derivative of S_{B} with respect to $\psi^\dagger$ and ψ. Besides having got rid of the Grassmann-valued fermion fields, this formulation of $\mathcal{Z}$ will turn out to be a particularly good starting point for the construction of cost-efficient and reliable MC implementations.

The approximations made in order to be able to calculate $\mathcal{Z}$ with finite computational effort have different consequences. There may, for example be artifacts from the discretization. The finite number of lattice sites entails a finite simulation volume, which inhibits simulations in the actual thermodynamic limit. Furthermore, the distance between the lattice points constitutes the smallest possible length scale in the system, which entails a *cutoff* Λ in momentum space. In order to extract observables in the thermodynamic and/or continuum limit, it has to be ensured, that the discretized version of the action indeed corresponds to the initial S_{F} when formally the limits $l_x, l_\tau \to 0$ and $N_x, N_\tau \to \infty$ are taken. The choice of the discretized action is usually not unique, hence there is also room for optimization [115, 116]. Numerically, l_x, l_τ, N_x and N_τ will always be finite, so the simulation has to be carried out for several of their values which then offers the basis for an extrapolation to the desired limit.

The path integral (1.5) in its analytic formulation involves an uncountably infinite number of field configurations which can also not be realized numerically. Just randomly picking a number of configurations can be expected to result in a very bad *signal-to noise ratio* [116]: the simulation may converge arbitrarily slow. The reason is, that not all field configurations are equally important since they are *weighted* with the integrand in eq. (1.5). On the one hand, this explains why approximation schemes like the *saddle point method* (see sec. 2.2 below) that single out one particular path may already give reasonable estimates of the full path integral. On the other hand, it means, that a lattice MC algorithm should be able to choose field configurations according to their weight in the integral for fast convergence. This process is called *importance sampling* [119, 120] and lies at the heart of a large number of MC implementations.

A central prerequisite for the application of importance sampling is the existence and applicability of a *probability measure* $\mathcal{P}$ that represents the weight of any particular field configuration. For the auxiliary field formulation (2.3), $\mathcal{P}[\varphi] \equiv \mathrm{det}K[\varphi]$ appears to be the natural choice. But this is meaningful *if and only if* $\mathcal{P}[\varphi]$ is positive semidefinite, i.e. $\mathrm{det}K[\varphi] \geq 0\ \forall \varphi$. Otherwise, a sign problem is present.

There are different instances, from where such a sign problem may originate. It can, for example, be introduced by particular interactions such as a repulsive (contact) interaction (see p. 26 below). But even for the free gas, finite spin or mass imbalance render $\mathrm{det}K[\varphi]$ indefinite as will be shown in the following[1]. Consider the non-interacting limit $g_\delta, \bar{h}_\varphi \to 0$ of the action (1.6) including spin and mass imbalance:

$$\begin{aligned} S_{\mathrm{F}}^{\mathrm{free}}[\psi^\dagger,\psi] &= \int_{\tau,\mathbf{x}} \sum_{\sigma=\uparrow,\downarrow} \left\{ \psi^*_{\sigma,\tau,\mathbf{x}} \left[\partial_\tau - (1+\bar{m}\sigma_3)\nabla^2 - \mu - h\sigma_3\right] \psi_{\sigma,\tau,\mathbf{x}} \right\} \\ &= \sum_n \int_{\mathbf{p}} \left(\psi^*_{\uparrow,n,\mathbf{p}}, \psi^*_{\downarrow,-n,-\mathbf{p}}\right) S_{\mathrm{F}}^{\mathrm{free}(2)} \begin{pmatrix} \psi_{\uparrow,n,\mathbf{p}} \\ \psi_{\downarrow,-n,-\mathbf{p}} \end{pmatrix}, \end{aligned} \tag{2.4}$$

where

$$S_{\mathrm{F}}^{\mathrm{free}(2)} = \begin{pmatrix} -i\omega_n + (1+\bar{m})\mathbf{p}^2 - \mu - h & 0 \\ 0 & i\omega_n + (1-\bar{m})\mathbf{p}^2 - \mu + h \end{pmatrix}, \tag{2.5}$$

see appendix A for the Fourier and Matsubara conventions employed in this work. For vanishing imbalance, $\bar{m} = \bar{h} = 0$, the eigenvalues of $S_{\mathrm{F}}^{\mathrm{free}(2)}$ are pairwise complex conjugate. Consequently, $\det\left[S_{\mathrm{F}}^{\mathrm{free}(2)}\right] \geq 0$ can be used as a probability measure. For finite $\bar{m}$ and/or $\bar{h}$, this is no longer true and a sign problem occurs[2]. Of course, so far this is only the free theory and the eigenvalue spectrum of its interacting counterpart is not known analytically. However, as the contact interaction is symmetric under an exchange of species, it cannot cure the asymmetry between ↑ and ↓ fermions which is the fundamental cause for the

---

[1] Technically, the fermion determinant for the free gas does not depend on the auxiliary field. Thus, the sign problem does not matter in practice. However, it will be shown that the general argument applies to the problematic interacting case as well.

[2] The partition function $\mathcal{Z}$ itself is of course still real valued. It is just the fermion determinant that becomes oscillatory.

sign problem. The latter is therefore present in the full theory as well.

Consider now a slightly modified theory with complex masses and chemical potentials, leading to imaginary imbalance parameters:

$$\bar{h} \to i \cdot \bar{h} \equiv \bar{h}_{\mathrm{I}}\,, \tag{2.6a}$$

$$\bar{m} \to i \cdot \bar{m} \equiv \bar{m}_{\mathrm{I}}\,. \tag{2.6b}$$

The idea of imaginary "imbalances" came up and has been employed for the first time in the context of the two-dimensional Hubbard model [121] and subsequently also in QCD, see, e.g., [122–124]. There, a finite baryon chemical potential plays an analogous role as it introduces a sign problem by destroying the symmetry between the quark flavors even in the isospin-symmetric case. Recently, the method has been adapted to the case of spin-imbalanced ultracold Fermi gases [125]. The extension to finite mass imbalance will be discussed in depth in the following.

With the imbalance parameters replaced according to eq. (2.6), the second functional derivative of the action in momentum space is given by

$$S_{\mathrm{F,I}}^{\mathrm{free}\,(2)} = \begin{pmatrix} -i\omega_n + (1 + i\bar{m})\mathbf{p}^2 - \mu - ih & 0 \\ 0 & i\omega_n + (1 - i\bar{m})\mathbf{p}^2 - \mu + ih \end{pmatrix}. \tag{2.7}$$

The imaginary imbalance parameters reinstate the pairwise complex conjugate nature of the eigenvalues and thus "remove" the sign problem. Monte Carlo simulations can now in principle be performed for interacting theories based on $S_{\mathrm{F,I}}^{\mathrm{free}}$. However, the latter describes a different theory than $S_{\mathrm{F}}^{\mathrm{free}}$ and is, moreover, of at least questionable physical meaning. It is therefore necessary to "connect" both theories: once Monte Carlo simulations have been performed for a theory with imaginary imbalances, the results have to be subjected to the reverse process as in eqns. (2.6), whereupon physical observables can be extracted.

However, these "reversions" $\bar{m}_{\mathrm{I}} \to \bar{m}$ and $\bar{h}_{\mathrm{I}} \to \bar{h}$ correspond to a mathematically nontrivial *analytical continuation*. A careful investigation of the prerequisites for this technique to yield reliable results is thus in order, before actual Monte Carlo data can be interpreted. This will be the subject of the subsequent section.

2.2 Analytic background of the imaginary imbalance approach

Suppose, one is interested in the physical observable $\mathcal{O}$ as a function of general or for some particular finite mass imbalance[3]. Employing the ideas presented above, the observable can be computed for arbitrary (imaginary) $\bar{m}_{\mathrm{I}}$ by Monte Carlo simulations. An analytic expression for $\mathcal{O}(\bar{m}_{\mathrm{I}})$ cannot be obtained this way, but an approximate representation is achievable by fitting the MC data points. There is considerable freedom of choice with respect to the fitting function(s), depending on the size and structure of the available data set and prior knowledge about the behavior of $\mathcal{O}(\bar{m}_{(\mathrm{I})})$ from other approaches. For the analytic investigation of a purely mass-imbalanced unitary Fermi gas, a polynomial series

$$\mathcal{O}(\bar{m}_{\mathrm{I}}) = \sum_{n=0}^{N_{\mathrm{max}}} C_{\mathcal{O}}^{(n)} \bar{m}_{\mathrm{I}}^{2n} \tag{2.8}$$

truncated at order $2N_{\mathrm{max}}$ will mostly be employed in this work. The action (2.4) for $\bar{h} = 0$ is symmetric under $\bar{m}_{(\mathrm{I})} \to -\bar{m}_{(\mathrm{I})}$ apart from a relabeling of the fermion species, $\uparrow \leftrightarrow \downarrow$. Since the contact interaction does not by itself break the symmetry between the species, only even powers of $\bar{m}_{\mathrm{I}}$ contribute in eq. (2.8). Other possible choices for the fitting functions include Padé approximants that have been used in the QCD context [126] or for the spin-imbalanced unitary Fermi gas [125].

The polynomial (Taylor) expansion (2.8) is particularly convenient for a discussion of the mathematical prerequisites for a successful extraction of the physical observable $\mathcal{O}(\bar{m})$ from $\mathcal{O}(\bar{m}_{\mathrm{I}})$. Consider a situation as it is schematically depicted in fig. 2.2a: Monte Carlo data has been produced and fitted. Superficially,

---

[3] The general argument carries over to $\bar{h}$ and combinations of both imbalances as well. However, specific convergence properties may depend on the type of the imbalance involved, see p. 23 below.

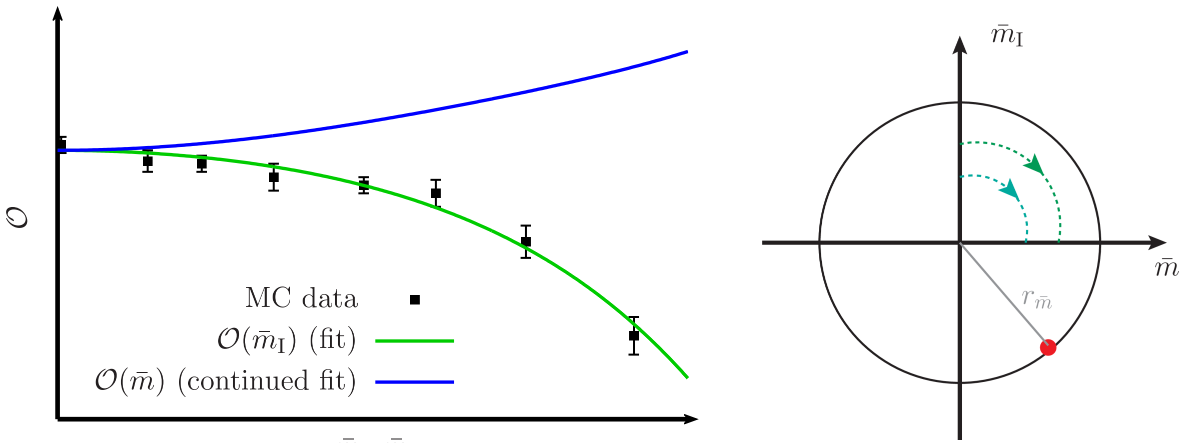

(b)

(a)

Figure 2.2: The physical observable $\mathcal{O}(\bar{m})$ (blue line) is extracted from Monte Carlo data (black dots) obtained at imaginary mass imbalance (schematically): the data points are fitted and the resulting function $\mathcal{O}(\bar{m}_\mathrm{I})$ (green line) is continued to real $\bar{m}$ (a). This is admissible for mass imbalances inside of the radius of convergence $r_{\bar{m}}$ of the expansion. The latter is given by the distance (gray line) between the expansion point and the closest singularity in the complex $\bar{m}$ plane (red dot) (b).

the physical observable is then just given by

$$\mathcal{O}(\bar{m}) = \mathcal{O}(-i\bar{m}_\mathrm{I}) = \sum_{n=0}^{N_\mathrm{max}} (-1)^n C_\mathcal{O}^{(n)} \bar{m}^{2n}. \tag{2.9}$$

The crucial limitation for the validity of eq. (2.9) is the radius of convergence of the Taylor series (2.8). From complex analysis it is known (see, e.g., [127]), that a function is analytic in some point $x \in \mathbb{C}$ *if and only if* it is holomorphic. The domain of convergence of the series is therefore determined by the domain where the function to be represented is holomorphic. In other words, the distance between the point about which the expansion is performed and the closest singularity *anywhere* in the complex plane determines the radius of convergence which will be denoted by $r_{\bar{m}}$ for the concrete case of the mass-imbalanced unitary Fermi gas. The situation for an expansion about[4] $\bar{m}_{(\mathrm{I})} = 0$ is schematically depicted in fig. 2.2b. Although obtained completely on the imaginary axis, the series (2.8) is a convergent representation of the underlying function on the whole disk $B_{r_{\bar{m}}}(0) \subset \mathbb{C}$ of the complex $\bar{m}$ plane (theorem of Cauchy-Taylor [127]). Therefore an “analytic continuation”[5] to real $\bar{m}$ is admissible, as $\mathcal{O}(\bar{m})$ constitutes just another special case of the function $\mathcal{O}$ which is established globally on $B_{r_{\bar{m}}}(0)$.

2.2.1 Mean-field theory for the imbalanced unitary Fermi gas

The prospects of extracting the radius of convergence directly from Monte Carlo data are very limited. It is in principle possible to extract $r_{\bar{m}}$ from the series coefficients themselves, but criteria like, e.g., the one from *Cauchy-Hadamard* [127]

$$r_{\bar{m}} = \left[\limsup_{n\to\infty} \sqrt[n]{\left|C_\mathcal{O}^{(n)}\right|}\right]^{-1}, \tag{2.10}$$

formally require an infinite number of coefficients to be known. In reality, the number of accessible coefficients is directly linked to the number of data points available. Therefore, even an estimate of $r_{\bar{m}}$ may be computationally expensive. On the other hand, an analytically exact computation of $r_{\bar{m}}$ is usually even less feasible, as it would require knowledge about the solution of the problem that would render the whole idea of Monte Carlo simulations obsolete.

---

[4] An expansion about $\bar{m}_{(\mathrm{I})} = 0$ is not mandatory. In fact, there are situations where higher real imbalances/chemical potentials may be reached by subsequent expansions about finite values of these quantities, see, e.g., [128]

[5] Note that the term “analytic continuation” may be somewhat misleading here from a mathematical point of view as it does not necessarily correspond to a continuation of an analytic function beyond its initially known domain of convergence.

As a compromise, this section will consider the convergence properties of observables at the level of a mean-field calculation. This can of course not yield results that are directly applicable to Monte Carlo data. Still, since the mean-field case is contained in the latter and it can be expected to dominate at least the qualitative features of the theory, it is useful in order to obtain first impressions of the characteristic behavior of the theory. Furthermore, possible issues that show up at this level but might not be visible in MC data sets, can be investigated (semi-)analytically.

Basic concepts of mean-field theory Mathematically, the *stationary phase* approximation and its extension to the Euclidean case, the *saddle point method* provide a framework for an approximate evaluation of the path integral (2.3). When representing the integrand,

$$\rho[\varphi]\det K[\varphi] = e^{-\bar{m}_\varphi^2 \varphi^* \varphi + \mathrm{Tr}\ln \mathrm{K}[\varphi]} \equiv e^{-S_{\mathrm{eff}}[\varphi]}, \tag{2.11}$$

in terms of a series expansion about some constant *background field* $\bar{\varphi}$,

$$S_{\mathrm{eff}}[\varphi] \equiv S_{\mathrm{eff}}[\bar{\varphi} + \delta\varphi] = S_{\mathrm{eff}}[\bar{\varphi}] + S^{(1)}_{\mathrm{eff}}[\bar{\varphi}]\delta\varphi + S^{(2)}_{\mathrm{eff}}[\bar{\varphi}]\delta\varphi^2 + \mathcal{O}(\delta\varphi^3)\,, \tag{2.12}$$

it can be shown (see, e.g., [129] for the zero-dimensional case) that the path integral with respect to φ receives its largest contribution from *stationary points* $\bar{\varphi}_0$ which are characterized by

$$S^{(1)}_{\mathrm{eff}}[\bar{\varphi}]\Big|_{\bar{\varphi}_0} = 0\,. \tag{2.13}$$

Since the background field $\bar{\varphi}$ is constant with respect to the path integral measure, eq. (2.3) at the stationary point can be rewritten as

$$\mathcal{Z} = e^{-S_{\mathrm{eff}}[\bar{\varphi}_0]} \int \mathcal{D}(\delta\varphi) e^{S^{(2)}_{\mathrm{eff}}[\bar{\varphi}_0]\delta\varphi^2 + \mathcal{O}(\delta\varphi^3)} \overset{\mathrm{mf}}{\approx} e^{-S_{\mathrm{eff}}[\bar{\varphi}_0]} \cdot \mathcal{N}. \tag{2.14}$$

The final identification corresponds to the *mean-field* approximation of the hitherto exact path integral. The crucial simplification is the neglect of the $\bar{\varphi}_0$-dependence in the remaining path integral over $\delta\varphi$, which renders $\mathcal{N}$ an unimportant global normalization constant that will be omitted in the following.
By construction, $S_{\mathrm{eff}}[\bar{\varphi}_0]$ has no kinetic term as the Hubbard-Stratonovich transformation does not introduce derivative terms. Therefore, it can formally be identified with an effective order parameter potential

$$U(\bar{\varphi}) = \frac{1}{\beta V} S_{\mathrm{eff}}[\bar{\varphi}]\,, \tag{2.15}$$

where V denotes the spatial volume of the system. This identification is formal in the sense that only the points $\bar{\varphi} = 0$ (free gas) and $\bar{\varphi} = \bar{\varphi}_0$ admit a direct physical interpretation. Furthermore, by analogy to the definition of the thermodynamic grand canonical potential

$$\Omega = -\frac{1}{\beta} \ln \mathcal{Z}\Big|_{\varphi_0} = V U(\bar{\varphi}_0)\,, \tag{2.16}$$

it is justified to identify $S_{\mathrm{eff}}[\bar{\varphi}]$ with the mean-field *quantum effective action* $\Gamma_{\mathrm{mf}}[\bar{\varphi}]$.
The latter identification deserves some further comments. The defining relation for the exact effective action of a scalar quantum field theory in terms of the "classical" field ϕ

$$\Gamma[\phi] = \sup_J \left(\int_{\tau,\mathbf{x}} J \cdot \phi - W[J] \right), \tag{2.17}$$

where

$$W[J] = \ln Z[J], \quad Z[J] = \int \mathcal{D}\varphi e^{-S[\varphi] + \int J \cdot \varphi}, \quad \phi = \frac{\delta W[J]}{\delta J}\,. \tag{2.18}$$

Instead, condition (2.13) corresponds to a classical equation of motion for the $\bar{\varphi}$ field. Omitting higher order corrections in eq. (2.14) seems to indicate a completely classical treatment of the problem. However, this is not the case, since the fermion fields were integrated out exactly, see eq. (2.3). In fact, the standard textbook loop expansion of the corresponding fermionic effective action is given by

$$\Gamma[\psi_{\mathrm{c}}^{\dagger},\psi_{\mathrm{c}}] = \Gamma^{\mathrm{tree}}[\psi_{\mathrm{c}}^{\dagger},\psi_{\mathrm{c}}] + \Gamma^{1\text{-loop}}[\psi_{\mathrm{c}}^{\dagger},\psi_{\mathrm{c}}] + \ldots = S[\psi_{\mathrm{c}}^{\dagger},\psi_{\mathrm{c}}] - \frac{1}{2}\ln\det S^{(2)}[\psi_{\mathrm{c}}^{\dagger},\psi_{\mathrm{c}}] + \ldots \tag{2.19}$$

in terms of the "classical" fields $\psi_{\mathrm{c}}^{(\dagger)}$, defined analogously to eq. (2.18). Truncated at first nontrivial order and parametrized by $\bar{\varphi}$ instead of $\psi_{\mathrm{c}}^{(\dagger)}$, Γ matches the shape of $\ln\mathcal{Z}$ as it would be given by eq. (2.3) for constant φ. This is exactly what the mean-field approximation provides. $\Gamma_{\mathrm{mf}}[\bar{\varphi}]$ can therefore be interpreted as the 1-loop effective action of the fermionic theory, parametrized by the auxiliary variable $\bar{\varphi}$. This "diagrammatic" interpretation of the mean-field approximation will be of importance in chap. 4 of this work.

Last but not least, it should be noted that the mean-field approximation becomes better, if larger numbers N_{f} of fermion flavors are considered. This is of particular relevance for relativistic models as presented in the beginning of sec. 1.2.2. It can even be shown (see, e.g., [57]) that the mean-field approximation becomes exact in the limit of $N_{\mathrm{f}} \to \infty$ due to the suppression of the higher order (loop) contributions that have been omitted in eq. (2.14).

Effective potential of the unitary Fermi gas The mean-field formalism can now be applied to the unitary imbalanced Fermi gas [46, 130, 131]. The bosonized action in Fourier space (see app. A) can conveniently be written as

$$S_{\mathrm{B}} = \bar{m}_{\varphi}^2\varphi^*\varphi + \sum_n \int_{\mathbf{p}} \left(\psi_{\uparrow,n,\mathbf{p}}^*, \psi_{\downarrow,-n,-\mathbf{p}}\right) \mathcal{G}_{\psi}^{-1} \begin{pmatrix} \psi_{\uparrow,n,\mathbf{p}} \\ \psi_{\downarrow,-n,-\mathbf{p}}^* \end{pmatrix}, \tag{2.20}$$

where

$$\mathcal{G}_{\psi}^{-1} = \begin{pmatrix} -i\omega_n + (1+\bar{m})\mathbf{p}^2 - \mu - h & \bar{h}_{\varphi}\varphi \\ \bar{h}_{\varphi}\varphi^* & -i\omega_n - (1-\bar{m})\mathbf{p}^2 + \mu - h \end{pmatrix}. \tag{2.21}$$

As the determinant or, alternatively, the trace of $\mathcal{G}_{\psi}^{-1}$ is needed for the computation of Γ_{mf} (see eq. (2.11)), its eigenvalues have to be computed. Since $\varphi \to \bar{\varphi}$ is constant, $\mathcal{G}_{\psi}^{-1}$ has to be diagonalized in the space of fermion species but not in frequency and momentum space. The former diagonalization procedure is often referred to as a *Bogoliubov transformation* [132] and yields the following set of pairwise eigenvalues:

$$E_{\pm} = \pm\left(i\omega_n - \bar{m}p^2 + h\right) + \sqrt{\left(p^2-\mu\right)^2 + \bar{h}_{\varphi}^2\bar{\varphi}^*\bar{\varphi}} \equiv \pm\left(i\omega_n - \bar{m}p^2 + h\right) + E_{\bar{\Delta}}. \tag{2.22}$$

The abbreviation $E_{\bar{\Delta}}$ for the square root term is motivated by the identification $|\bar{\Delta}|^2 \equiv \bar{h}_{\varphi}^2\bar{\varphi}^*\bar{\varphi}$ and the interpretation of $E_{\bar{\Delta}}$ as the energy of *Bogoliubov quasiparticles* that have effectively been introduced by the diagonalization procedure. For finite $\bar{\varphi}$ or rather $\bar{\Delta}$, the energy spectrum of these particles is *gapped*, as $E_{\bar{\Delta}} \geq |\bar{\Delta}|$. This corresponds to an energy region of width $2|\bar{\Delta}|$ around the fictive "average Fermi surface" μ that does not provide admissible states for quasi-particle excitations. The finite energy gap is intimately connected to the occurrence of superfluidity on the one hand and SSB on the other hand. A supercurrent may occur due to the absence of energy-consuming excitations and $\bar{\Delta} \sim \langle\psi_{\uparrow}\psi_{\downarrow}\rangle$ is the order parameter of U(1) symmetry breaking, see sec. 1.1.3.

The Matsubara sum from eq. (2.20) can now be performed analytically. This is a standard procedure that will not be detailed here (see, e.g., [51] for an extensive introduction into the subject). It results in a first expression for the mean-field effective action or the effective order parameter potential, respectively,

$$\frac{1}{\beta V}\Gamma_{\mathrm{mf}}^{\mathrm{bare}}[\bar{\varphi}] = U(\bar{\varphi}) = \frac{\bar{h}_{\varphi}^2}{g_{\delta}}\bar{\varphi}^*\bar{\varphi} - \frac{1}{\beta}\int_{\mathbf{p}} \left\{ \ln\left[1 + e^{-\beta\left(\bar{m}p^2 - h + E_{\bar{\Delta}}\right)}\right] + \ln\left[1 + e^{-\beta\left(\bar{m}p^2 - h - E_{\bar{\Delta}}\right)}\right] \right\}. \tag{2.23}$$

The momentum integration in eq. (2.23) is divergent. Besides the subtraction of unimportant ($\bar{\Delta}$-independent) "vacuum" contributions $\Gamma_{\mathrm{mf}}[0]_{T=\mu=0}$, it is the contact coupling g_{δ} that must be fixed to regularize the integral. Starting from the general two-body result (1.4) and choosing a sharp-cutoff regularization procedure ($c_{\mathrm{reg}} = \pi^{-1}$ in eq. (1.4)), g_{δ}^{-1} assumes the following form in the unitary limit:

$$\frac{1}{g_{\delta}} = \lim_{a\to\infty} \frac{a^{-1}\pi - \Lambda}{4\pi^2} = -\frac{\Lambda}{4\pi^2} = \int_{\Lambda} \frac{\mathrm{d}^3 p}{(2\pi)^3} \frac{1}{2p^2} \,. \tag{2.24}$$

Having applied these steps to $\Gamma_{\mathrm{mf}}^{\mathrm{bare}}$, the cutoff Λ can safely be sent to infinity, yielding the renormalized mean-field effective action

$$\frac{1}{\beta V}\Gamma_{\mathrm{mf}}[\bar{\Delta}] = \int_{\mathbf{p}} \left\{ E_{\bar{\Delta}=0} - E_{\bar{\Delta}} + \frac{|\bar{\Delta}|^2}{2p^2} - \frac{1}{\beta} \sum_{\sigma=\pm1} \ln\left[1 + e^{-\beta\left[\sigma\left(\bar{m}p^2 - h\right) + E_{\bar{\Delta}}\right]}\right] \right\} . \tag{2.25}$$

Since it is necessary for Γ_{mf} to be meaningful, the mean-field condition or *gap equation* (2.13) is provided as well:

$$0 = \int_{\mathbf{p}} \left\{ \frac{1}{p^2} - \frac{1}{E_{\bar{\Delta}_0}} + \frac{1}{E_{\bar{\Delta}_0}} \sum_{\sigma=\pm1} \left[1 + e^{\beta\left[\sigma\left(\bar{m}p^2 - h\right) + E_{\bar{\Delta}_0}\right]}\right] \right\} . \tag{2.26}$$

These analytic expressions can now be used to extract observables $\mathcal{O}$ for real and imaginary imbalances as well as their convergence properties with respect to analytic continuation.

2.2.2 Observables and convergence criteria

The following discussion will mostly be limited to the $\bar{h} = 0$ case for the sake of clarity. Only in the end, some peculiarities of the finite $\bar{h}$ situation will be touched upon. Finally, a brief explanation of the special configuration $\bar{h} = \bar{m}$, which will be relevant for the MC data analyzed in sec. 2.3, is provided.

Effective potential In an actual Monte Carlo simulation, it might not be particularly convenient to calculate the partition function or the effective action. However, since these quantities constitute the formal basis from which all thermodynamic observables can be derived in principle, limitations for an analytic continuation with respect to $\bar{m}$ which show up there will be of relevance for said observables as well. It is therefore a good starting point to examine more closely the properties of eq. (2.25) at $\bar{h} = 0$.
An analytical expression for Γ_{mf} in terms of elementary functions is not known in three spatial dimensions and for finite $|\bar{\Delta}|^2$. In order to find possible singularities in the complex $\bar{m}$ plane, one is therefore limited to an examination of the analytic structure of the integrand. Such an analysis can only provide a lower bound on the actual radius of convergence, as analytic properties might actually be improved by integration (theorem on the analyticity of integrals [127]).
Admitting general complex values for $\bar{m}$ in eq. (2.25), the singularity that is closest to the origin about which the expansion is supposed to be performed is determined by one of the exponential function's arguments becoming equal to $i\pi$. By means of this criterion, a radius of convergence

$$r_{\bar{m}} = \sqrt{\frac{\beta^2|\bar{\Delta}|^2 + \pi^2}{\beta^2|\bar{\Delta}|^2 + \pi^2 + \beta^2\mu^2}} \,, \tag{2.27}$$

is straightforwardly derived. Note that even in the limit of vanishing temperature, $\beta \to \infty$, $r_{\bar{m}}$ remains finite, as long as the U(1) symmetry is spontaneously broken:

$$r_{\bar{m}}\Big|_{T=0} = \sqrt{\frac{|\bar{\Delta}|^2}{|\bar{\Delta}|^2 + \mu^2}} \,. \tag{2.28}$$

By solving eq. (2.26), it can be shown that the (normalized mean-field) fermion gap[6] is given by $|\Delta_0|^2/\mu^2 = 1.351$ for $|\bar{m}| \leq \bar{m}_{\mathrm{c}} = 0.597$. The latter is the value for the mass imbalance where a first order transition to the normal phase occurs for real $\bar{m}$, see fig. 2.4b below. The zero-temperature radius of convergence is therefore given by at least $r_{\bar{m}}\big|_{T=0} = 0.758$ which is well beyond the phase transition. While the effective potential is perfectly analytic across such a transition, this is not necessarily the case for physical observables as will be discussed in the following.

---

[6] The term "fermion gap" is used for $\bar{\Delta}$ and its square simultaneously in this thesis for convenience.

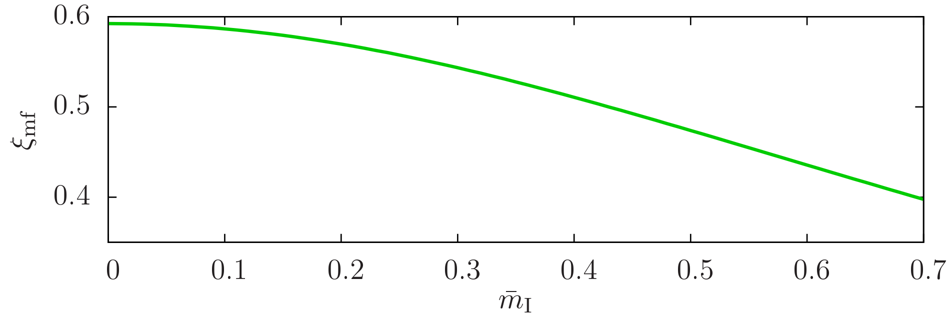

(a) Mean-field zero-temperature Bertsch parameter $\xi_{\rm mf}$ for a range of imaginary mass imbalances $\bar{m}_{\rm I}$.

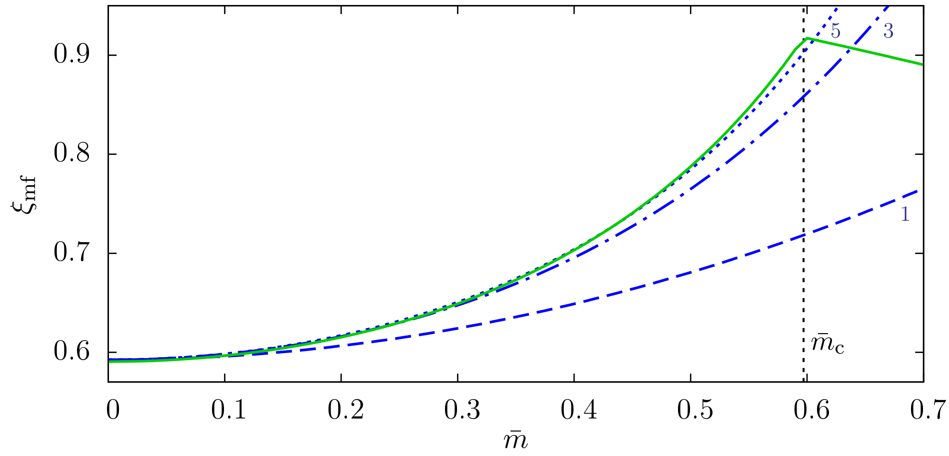

(b) Mean-field zero-temperature Bertsch parameter $\xi_{\rm mf}$ for the same range of real mass imbalances $\bar{m}$ (green, solid line). Continued polynomial fits (blue, dashed/dot-dashed/dotted lines) of order $n = 1, 3, 5$ in the sense of eq. (2.8) converge to the exact result up to the critical $\bar{m}_{\rm c}$.

Figure 2.3

Bertsch parameter The above result motivates to revisit a zero-temperature observable introduced earlier (see the introductory part of this chapter on p. 13), the Bertsch parameter ξ. So far, it has only been defined for the two fermion species separately or the balanced system, respectively. An average Bertsch parameter for imbalanced systems must be defined as well, since it does not follow unambiguously from the balanced one. In the following, the convention of [118] will be adopted:[7]

$$\xi(\bar{m}) \equiv \frac{\xi(\bar{m}=0)}{1-\bar{m}^2} \quad \text{with} \quad \xi(\bar{m}=0) = \left(\frac{4}{3n}\right)^{\frac{2}{3}}, \tag{2.29}$$

where it is understood that n is the overall density of the (possibly imbalanced) system. At mean-field level, this density can be obtained from the effective action,

$$n_{\rm mf} = -\frac{\partial \Omega}{\partial \mu} = -\frac{1}{\beta}\frac{\partial \Gamma_{\rm mf}[\bar{\Delta}]}{\partial \mu}\bigg|_{\bar{\Delta}_0}. \tag{2.30}$$

These definitions imply that the radius of convergence for ξ obtained from complex singularities of the respective integrand is given by eq. (2.27) as well.
The Bertsch parameter $\xi_{\rm mf}$ as a function of imaginary mass imbalance is shown in fig. 2.3a for a range of $\bar{m}_{\rm I}$ that lies well inside the radius of convergence given by eq. (2.28). The 101 data points that this plot is based upon are fitted with polynomials up to order $n = 5$ in the sense of eq. (2.8). Continuing the

---

[7] Note that the conventions in [118] are slightly different from those employed in [117]. This is due to a variation in the definition of the average Fermi energy.

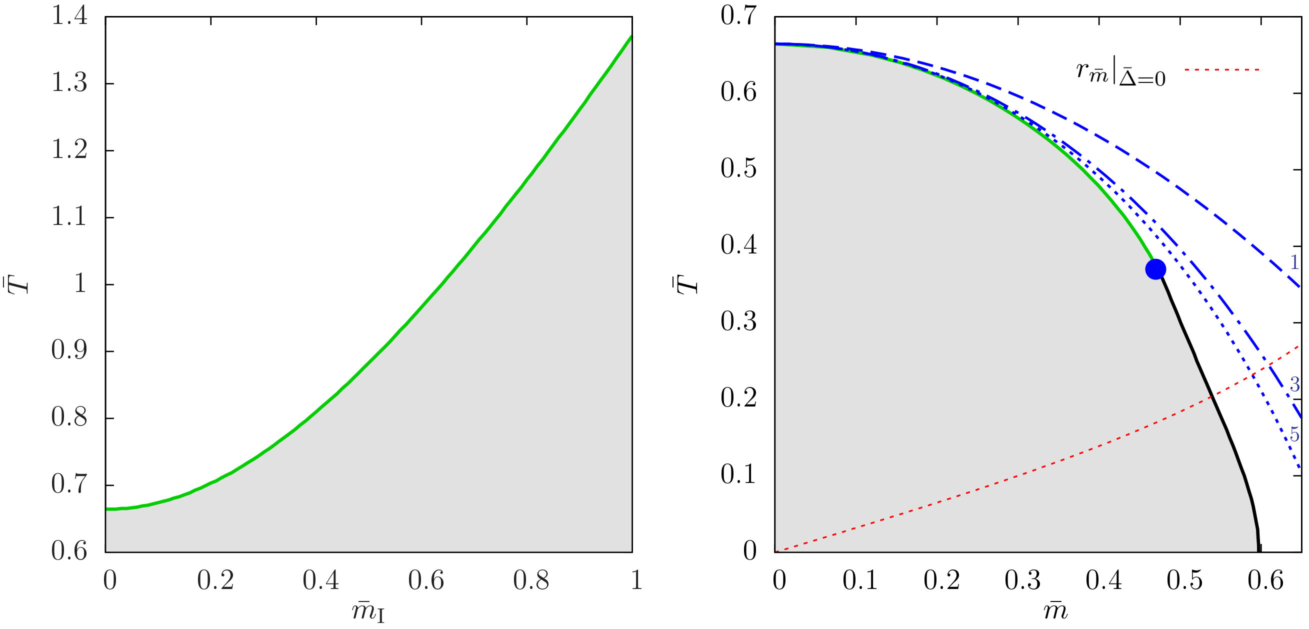

(a) (b)

Figure 2.4: Mean-field phase diagram of the unitary Fermi gas in the plane spanned by (normalized) temperature $\bar{T}$ and imaginary (a) or real (b) mass imbalance. The symmetry broken phase is indicated by gray shading. Second order phase transition lines are depicted by thick green (solid) lines, while the first order transition in (b) is marked with a black (solid) line. Continued polynomial fits of order n=1,3,5 (blue, dashed/dot-dashed/dotted lines) approximate the second order transition line but fail beyond the critical point (blue).

latter to real $\bar{m}$, convergence to the exact result can be observed in fig. 2.3b for $\bar{m} \leq \bar{m}_{\mathrm{c}}$. Contrary to the effective action itself, ξ is only defined on the physical manifold $|\bar{\Delta}| = |\bar{\Delta}_0|(\bar{m})$, which is, by construction, non-analytic at the phase transition occurring at $\bar{m}_{\mathrm{c}}$. Consequently, the validity of the continuation from imaginary $\bar{m}_{\mathrm{I}}$ is not limited by $r_{\bar{m}}$ from eq. (2.28) but by the location of the phase transition: $r_{\bar{m}} = \bar{m}_{\mathrm{c}}$. This is clearly seen in fig. 2.3b, as the kink-like structure at $\bar{m}_{\mathrm{c}}$ is not even rudimentary visible in the continued polynomial fits.

Phase transition line The location of phase transitions is obviously crucial information for the direct continuation of observables as their defining non-analyticities put a fundamental limit to the validity of this procedure. In fig. 2.4a, the finite $\bar{T} = T/\mu$ phase diagram for imaginary mass imbalance is provided. The question, whether a direct continuation of the phase transition manifold to real $\bar{m}$ is admissible and if so, how far it can be trusted requires another piece of (complex) analysis: the implicit function theorem [123].
Consider the gap parameter $|\Delta_0|(\bar{m}, \bar{T})$. By definition, it is analytic in the whole space spanned by $\bar{m}$ and positive $\bar{T}$ *except* for the manifold of phase transitions. For second order phase transitions, an implicit equation for this manifold is given by the special case $|\bar{\Delta}_0| = 0$ of eq. (2.13):

$$\left.\frac{\partial \Gamma_{\mathrm{mf}}}{\partial \bar{\Delta}}\right|_{|\Delta_0|=0} = 0\,. \tag{2.31}$$

Since $\Gamma_{\mathrm{mf}}[\bar{\Delta} = 0]$ itself is analytic at least for mass imbalances $\bar{m}$ smaller than

$$r_{\bar{m}}\big|_{\bar{\Delta}=0} = \sqrt{\frac{\pi^2}{\pi^2 + \beta^2\mu^2}}\,, \tag{2.32}$$

the implicit function theorem guarantees the existence and analyticity of a function $f(\bar{m}, \bar{T})$ describing the phase transition line. The latter therefore has a convergent expansion and can be continued from imaginary to real mass imbalances *as long as* neither $r_{\bar{m}}\big|_{\bar{\Delta}=0}$ is surpassed nor a critical endpoint of any type occurs which would correspond to a change of the analyticity properties the above argument relies upon.

In fact, it can be seen from fig 2.4b that the continued fits to the phase transition line in the imaginary case converge nicely to the low-$\bar{m}$ part of the transition line in the real case. However, the subsequent first order line, which cannot be described by a closed implicit formula similar to eq. (2.31), is not captured.

It can therefore be concluded that second-order phase transitions can be obtained from imaginary imbalance data in a relatively straightforward fashion. Furthermore, there is hope that information on critical points and transition lines of first order can be obtained as well.

Concerning critical points of the type as depicted in fig. 2.4b, it has been found that Padé approximants appear to indicate its presence with their divergence structure [125, 133]. Although there is until now no rigorous mathematical foundation for these findings, they certainly deserve further investigation.

The thin red (dotted) line in fig. 2.4b represents the temperature-dependent estimate of the radius of convergence from eq. (2.32). It crosses the phase transition line well below the critical point. In principle, it should therefore be possible to obtain at least part of the first order transition line by continuing Γ_{mf} directly and only then searching for phase transitions. An analogous procedure has been suggested and successfully applied to the homogeneous mean-field phase diagram of the (1+1)-dimensional Gross-Neveu model [128] whose structure is very similar to the one in fig. 2.4b (conf. the homogeneous part of fig. 1.3).

Finite spin imbalance Estimates of the radius of convergence for spin-imbalanced Fermi gases are constructed largely along the lines presented so far except for a crucial structural difference. In close analogy to the situation that occurs for imaginary chemical potential in relativistic theories [134], an imaginary spin-imbalance h_{I} can be "gauged away" by applying a local U(1) transformation

$$\psi_\uparrow \to e^{ih\tau}\psi_\uparrow, \quad \psi_\downarrow \to e^{-ih\tau}\psi_\downarrow, \tag{2.33}$$

to the fermion fields in the partition function (2.3). Reinforcing anti-periodic boundary conditions on the τ domain, only $h = 2\pi n/\beta$ with $n \in \mathbb{Z}$ may be removed by the transformation (2.33) while leaving the partition function invariant.

This periodicity of $\mathcal{Z}$ with respect to imaginary spin imbalance can more easily be seen on the level of the action in the Matsubara formulation eq. (2.20) or (2.21), respectively: The operator structures of the ω_n and h terms are equivalent. Imaginary h_{I} can thus be absorbed partially into ω_n, increasing the respective index by $m = h \mod 2\pi/\beta$. The resulting ω_{n+m} does not hamper Gaussian integration of the fermion fields in any way as it represents nothing but a linear shift of the frequency component of the eigenvalues (2.22). The latter is of no relevance for the actual Matsubara summation leaving the resulting quantities like the effective potential invariant.

The periodic nature of the partition function is problematic insofar as it limits the amount of nontrivial information that may be obtained by analytic continuation to real spin imbalance. In particular, the zero-temperature limit becomes completely inaccessible: The period length is zero and the value of the partition function becomes equal for all h_{I}. As finite h_{I} does not generate nontrivial information, the range of applicability *besides* radii of convergence is effectively zero.

The imaginary imbalance approach thus appears to be incapable of dealing with spin imbalance at least at zero temperature. By a combination with mass imbalance, however, this obstacle may be overcome as will be explained in the following.

Consider the *canonical* partition function of a system with fixed particle numbers $N_\uparrow$ and $N_\downarrow$,

$$\mathcal{Z}_{N_\uparrow,N_\downarrow} = \mathrm{Tr} e^{-\beta\hat{H}}. \tag{2.34}$$

Introducing mass imbalance $\bar{m} > 0$ and keeping $N_\uparrow = N_\downarrow$ fixed, the chemical potentials of the fermion species are adjusted leading to a finite spin imbalance $\bar{h} = \bar{m}$. This can be seen when considering the Fermi momenta of the species which have to be kept equal,

$$k_{\mathrm{F}}^{\uparrow,\downarrow} = \left(6\pi^2 n_{\uparrow,\downarrow}\right)^{\frac{1}{3}} = \sqrt{\mu}\sqrt{\frac{1 \pm \bar{h}}{1 \pm \bar{m}}}. \tag{2.35}$$

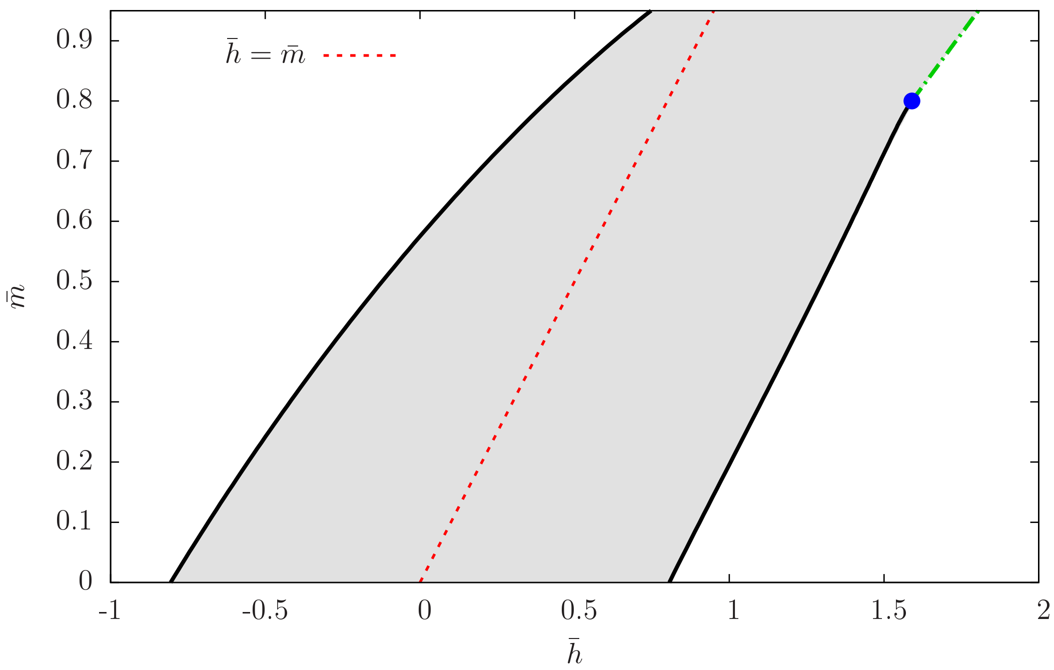

Figure 2.5: Mean-field phase diagram in the plane spanned by $\bar{h}$ and $\bar{m}$ at zero temperature. The superfluid phase is indicated by gray shading. It is limited by first (black, solid lines) or second order (green, dot-dashed line) transitions to the normal phase.

Of course, the imbalances introduce a sign problem in Monte Carlo simulations, but in the canonical formalism it is sufficient to render $\bar{m}$ imaginary. As $\bar{m}_{\mathrm{I}}$ has no physical interpretation, it does for sure not entail (imaginary) spin imbalance as its real counterpart does. A simulation with imaginary mass imbalance may therefore be performed without a sign problem or limiting periodicity of $\mathcal{Z}$.
Continuing $\bar{m}_{\mathrm{I}} \to \bar{m}$ in the way described above but in the canonical formulation, reintroduces real spin imbalance. In this way, $\bar{h} > 0$ may be accessed by Monte Carlo simulations as long as the canonical formalism is used and the line of $\bar{h} = \bar{m}$ is not left.
An estimate of the radius of convergence for the above described method is not straightforward as the mean-field approach used so far relies on the thermodynamic limit in terms of particle number and volume. It can thus not be mapped directly to the canonical picture as required for the specific MC implementation employed below. Nevertheless, some hints may still be obtained. The most central one can be read off fig. 2.5 representing the mean-field phase diagram for the spin- and mass-imbalanced unitary Fermi gas a zero temperature[8]. As the line of $\bar{h} = \bar{m}$ lies completely within the superfluid phase, nonanalyticities associated with phase boundaries are not expected to limit the radius of convergence. There are hints from, e.g., DFT studies [65], that this statement may hold also beyond the mean-field approximation. It is further substantiated by results from the functional RG analysis presented in sec. 4.4.2, where the homogeneous superfluid phase is found to be stable at low temperatures at least up to $\bar{h} = \bar{m} \approx 0.8$.
Quantitative predictions for $r_{\bar{h}=\bar{m}}$ from mean field are as problematic as before concerning the omission of fluctuation effects and become even less trustworthy as the exact scenario cannot easily be reproduced within the grand-canonical formalism. The most closely related case should be the one with finite $\bar{m}$ and zero $\bar{h}$ described on p. 20 above, that resulted in a minimum value of $r_{\bar{m}}\big|_{T=0} = 0.758$ for the radius of convergence.

2.3 Application to MC studies of 3D unitary Fermi gases

In this section, results of Monte Carlo simulations with the method explained above are presented. In contrast to the analytical data processing, the actual implementation of the MC algorithms has not been performed by the author of this work, but by the group of Joaquín E. Drut at the University of North

---

[8] Note that the theory is symmetric under simultaneously transforming $\bar{h} \to -\bar{h}$ and $\bar{m} \to -\bar{m}$ which effectively corresponds to a relabeling of the species. The phase diagram in fig. 2.5 is therefore limited to positive $\bar{m}$ without loss of generality.

Carolina, Chapel Hill. A complete characterization of the numerical methods is therefore not the goal of this chapter. Nevertheless, in order to provide a basis upon which the results may be appreciated, a brief description of the implementation is given in sec. 2.3.1, before proceeding to the analytical continuation of the obtained data and discussions of the physical conclusions in sec. 2.3.2.

2.3.1 Monte Carlo implementation

In sec. 2.1 above, the idea of importance sampling for path integral evaluation by means of an associated probability measure has been introduced in a formal way. For the practical implementation, a number of major tasks has to be performed, which will be sketched in the following along the lines of [116,118].

Projection quantum Monte Carlo In the non-relativistic limit considered here, the number of fundamental fermions is not subject to change. Therefore and due to the peculiarities of finite spin imbalance, it is convenient to manifestly fix the system's density in a (discretized) canonical formulation of the problem,

$$\mathcal{Z}_{N_\uparrow,N_\downarrow} = \int \prod_{\mathbf{n}} \frac{\mathrm{d}\varphi_{\mathbf{n}}}{2\pi} \rho[\varphi_{\mathbf{n}}] \mathrm{det} K_{N_\uparrow,N_\downarrow}[\varphi_{\mathbf{n}}] = \langle \psi_0 | e^{-\beta \hat{H}} | \psi_0 \rangle \,, \tag{2.36}$$

where $\mathbf{n}$ enumerates the lattice sites. Here,

$$\hat{H} = \sum_{\mathbf{n}} \left[\sum_{\sigma=\uparrow,\downarrow} \psi^*_{\sigma,\mathbf{n}} \left(\frac{-\nabla^2_{\mathbf{n}}}{2m_\sigma} \right) \psi_{\sigma,\mathbf{n}} + \bar{g} \psi^*_{\uparrow,\mathbf{n}} \psi_{\uparrow,\mathbf{n}} \psi^*_{\downarrow,\mathbf{n}} \psi_{\downarrow,\mathbf{n}} \right] \equiv \hat{T}_\uparrow + \hat{T}_\downarrow + \hat{V} \tag{2.37}$$

is the formally discretized imbalanced Hamilton operator of the model specified by the action (1.6). Furthermore, $|\psi_0\rangle$ is a $N_\uparrow, N_\downarrow$-particle basis. Here, the particle numbers $N_\uparrow$ and $N_\downarrow$ will always be kept equal, ensuring $\bar{h} = \bar{m}$ when introducing mass imbalance.

The functional form of the "boson mass" function $\rho[\varphi]$ (see eq. (2.3)) is now released to a more general shape. It encodes the specific properties of the particular Hubbard-Stratonovich transformation employed. In order to accommodate for a bounded $\varphi_{\mathbf{n}} \in [-\pi, \pi]$, it is chosen as [135]

$$\rho[\varphi_{\mathbf{n}}] = \theta(-\pi + \varphi_{\mathbf{n}}) \theta(\pi - \varphi_{\mathbf{n}}) \,. \tag{2.38}$$

For a numerical computation of the determinant in eq. (2.36), a concrete basis or *trial wave function* $|\psi_0\rangle$ has to be chosen. Here, a *Slater determinant* of free single particle wave functions for the involved fermions will be employed. This choice is not unique and may exert great influence on the convergence behavior of the simulation [116]. This can be understood, if the term $e^{-\beta\hat{H}}|\psi_0\rangle$ in eq. (2.36) is interpreted as an evolution of the state $|\psi_0\rangle$ in imaginary time. For very low temperatures, i.e. very large β, the evolved state will be dominated by the ground state wave function $|\Omega\rangle$,

$$e^{-\beta\hat{H}} |\psi_0\rangle \sim e^{-\beta E_0} |\Omega\rangle \,, \tag{2.39}$$

with energy E_0, as all other contributions decay faster due to their larger energies $E_{n>0} > E_0$. On the (temporal) lattice, this evolution can be implemented approximately by an N_τ-fold application of the *transfer matrix* $\mathcal{T} \equiv e^{-\tau\hat{H}}$, where $\beta = \tau N_\tau$ and τ is a measure for the temporal lattice spacing.

Since the exact computation of the exponential of the interacting Hamiltonian (2.37) is in general not possible numerically, an approximate *Trotter-Suzuki* decomposition [136,137] is employed,

$$\mathcal{T} = e^{-\tau\hat{H}} \approx e^{-\frac{\tau}{2}\hat{T}} e^{-\tau\hat{V}} e^{-\frac{\tau}{2}\hat{T}} + \mathcal{O}\left(\tau^2\right) . \tag{2.40}$$

It is now desirable to reach as large β as possible since this improves the dominance of the ground state contribution. This must be achieved by large N_τ rather than coarse τ to keep the error introduced by the truncated decomposition (2.40) small. N_τ-fold application of the transfer matrix to the trial wave function will result in

$$\mathcal{T}^{N_\tau} |\psi_0\rangle \to A_0^{N_\tau} e^{-\beta E_0} |\Omega\rangle \,, \tag{2.41}$$

where $A_0 \leq 1$ is the overlap between the initial $|\psi_0\rangle$ and the ground state $|\Omega\rangle$. A proper choice of $|\psi_0\rangle$ in

terms of a sufficiently large A_0 is therefore mandatory for a fast convergence to the ground state.
In practice, N_τ will always be finite, such that an extrapolation of simulated observables to $N_\tau \to \infty$ has to be performed to extract the true ground state just as for the number of spatial lattice sites N_x^3 to remove finite volume and discretization artifacts.
Given the definition of the auxiliary field $\varphi_\mathbf{n}$ fixed through eq. (2.38), the discretized interaction term can now be transformed:

$$e^{-\tau\hat{V}} = \int \prod_\mathbf{n} \frac{\mathrm{d}\varphi_\mathbf{n}}{2\pi} \left(1 + \sqrt{C}\psi^*_{\uparrow,\mathbf{n}}\psi_{\uparrow,\mathbf{n}} \sin\varphi_\mathbf{n}\right) \cdot \left(1 + \sqrt{C}\psi^*_{\downarrow,\mathbf{n}}\psi_{\downarrow,\mathbf{n}} \sin\varphi_\mathbf{n}\right), \tag{2.42}$$

where $C = 2(e^{\tau\bar{g}} - 1)$ encodes the interaction strength.[9] The coupling $\bar{g}$ for some scattering length a cannot simply be taken from equations (1.2) or (1.4) as the latter are continuum results. It must rather be fitted to Lüscher's finite-box solution [138,139] by diagonalization of the two-body transfer matrix $\mathcal{T}_2$. In the present setup, conventions have been employed that render the fermionic coupling $\bar{m}$-dependent, $\bar{g}(\bar{m}) = \bar{g}(\bar{m} = 0)/(1 - \bar{m}^2)$.
Without going into any detail here, it should be noted that a single coefficient C is not able to reproduce an exact finite volume analog of the unitary Fermi gas. This will effectively result in corrections that can be interpreted as being due to a residual finite range of the interaction. To avoid contamination of the results by such effects, it is therefore mandatory to keep the particle density in the simulation sufficiently small, i.e. $N_\uparrow + N_\downarrow \ll N_x^3$.

Determinantal Hybrid Monte Carlo So far, the auxiliary field $\varphi_\mathbf{n}$ has been treated as a given quantity that can just be disposed of at will. In practice, the generation and selection of suitable *samples* of this field is a computationally intensive task. Moreover, this process is crucially hampered by a sign problem as described in sec. 2.1 above which is why methods like the imaginary imbalance approach are needed after all.
Determinantal Hybrid Monte Carlo (DHMC), that has been employed in the work presented here, is an approach that belongs to the large class of *Markov-chain* methods. The general idea is to avoid the costly generation of complete field configurations and evolve some given $\varphi_\mathbf{n}$ according to a Markovian process instead. This means, that after a certain number of evolution steps, the old and new field configurations become sufficiently decorrelated such that the new configuration $\varphi'_\mathbf{n}$ effectively corresponds to a completely new one. Importance sampling is implemented by a *Metropolis* algorithm [119], i.e. the new field configuration is accepted or rejected depending on its associated probability $\mathcal{P}[\varphi_\mathbf{n}]$.
There are many different ways to implement the evolution and selection of the auxiliary field. DHMC combines two of those concepts. The evolution of $\varphi_\mathbf{n}$ takes place globally on the whole lattice which is more efficient than a local site-per-site updating process. This is achieved by applying a fictitious *molecular dynamics* force $F_{\mathbf{n},\tau}$ on $\varphi_{\mathbf{n},\tau}$ derived from the action of the model (Hybrid Monte Carlo). By randomly sampling an artificial conjugate field $\pi_{\mathbf{n},\tau}$ at the initial time slice and numerically solving the equations of motion, a whole chain of new field configurations is generated that is moreover properly weighted. Choosing the molecular dynamics force as

$$F_{\mathbf{n},\tau} = \mathrm{Tr}\left[\mathcal{U}[\varphi]^{-1} \frac{\delta\mathcal{U}[\varphi]}{\delta\varphi_{\mathbf{n},\tau}}\right], \quad \mathcal{U}[\varphi] = \mathcal{T}[\varphi_{\mathbf{n},1}] \cdot \ldots \cdot \mathcal{T}[\varphi_{\mathbf{n},\mathrm{N}_\tau}], \tag{2.43}$$

the evolution is effectively generated by the determinant in eq. (2.36) which is why the method is called "Determinantal" HMC.
For further details on algorithms and issues of practical implementation see, e.g., [116] and references therein.

2.3.2 Results

With the above explained methods, MC simulations have been performed, yielding estimates for the Bertsch parameter ξ for different parameter sets $(N_x, N_\uparrow + N_\downarrow, \beta, \bar{m}_I)$. For each of those sets, approximately 500 decorrelated field configurations $\varphi_{\mathbf{n},\tau}$ were employed, resulting in a statistical uncertainty of about

---

[9] A repulsive interaction, i.e. $\bar{g} < 0$, entails a complex C and introduces a sign problem even in the absence of imbalances.

5%. However, in order to be physically interpretable, the raw data obtained from the simulations has to be processed further.

Data processing In order to arrive at the desired result of $\xi(\bar{h} = \bar{m})$, three different tasks have to be performed on the MC data: extrapolations to zero temperature $\beta \to \infty$ and infinite volume $N_x \to \infty$ as well as the analytic continuation $\bar{m}_\mathrm{I} \to \bar{m}$. Neither the correct order of these limiting processes nor their specific implementation are a priori obvious. While it is indeed found that an interchange of extrapolations and the analytic continuation does not make much of a difference, the details of the different steps are important and will be discussed in the following.

Any practical Monte Carlo simulation can only be performed for a finite number of temporal steps N_τ, making an extrapolation to $\beta = N_\tau \tau \to \infty$ mandatory. In order to facilitate the latter, simulations have been performed for a range of values $\beta \in [2, 5]$ that may be used as basis for an extrapolating fit. From eqns. (2.39) and (2.41), it seems clear that the desired ground state energy E_0 is approached as

$$E(\beta \to 0) \approx E_0 + A e^{-\beta\delta}, \tag{2.44}$$

see also [140] for details. The parameters A and δ encode remnants of finite β and may serve as additional fit parameters besides E_0 itself on some given dataset.

Besides reaching low temperatures, the application of a large number of temporal steps N_τ serves another purpose in a practical MC simulation: The initial configurations $\psi_{\sigma,\mathbf{n}}$ and thus consequently also $\varphi_{\mathbf{n},0}$ do not necessarily represent thermal equilibrium states. The latter status is mediated by the interaction and must be achieved through imaginary time evolution as well. High fermion densities make for fast convergence to thermal equilibrium but, as discussed above, they are problematic in terms of finite range effects. In order to keep the latter under control, only data for densities $(N_\uparrow + N_\downarrow)/N_x^3 \approx 0.05$ will be taken into account here. It turns out that "non-equilibrium" artifacts are still sizable for the corresponding $\beta \lesssim 3$ data points inhibiting their use in an extrapolation to $\beta \to \infty$. As the number of remaining data points is too small for a sensible exponential extrapolation with eq. (2.44), averaging is performed instead. Thus, this very first estimate of zero temperature/ground state quantities of general mass-imbalanced unitary Fermi gases may be considered an upper limit for the respective quantities.

Given the so obtained data points, a subsequent extrapolation in terms of N_x may then be performed,

$$E(N_x \to \infty) \approx E_0 + A_x e^{-N_x \delta_x}, \tag{2.45}$$

providing an estimate of the results with finite-size artifacts removed. Data points computed with lattice sizes of $N_x = 8, 10, 12, 14$ and fixed density were employed for this procedure. Eq. (2.45) is motivated by an analytic finding for certain relativistic theories in a finite volume: The partition function of such a system is invariant under an interchange of spatial and temporal directions [128, 141]. Although a corresponding relation for the unitary Fermi gas is not proven here, eq. (2.45) indeed appears to suit the available data set best, compared with e.g. power law decay formulas. All physical results discussed below are obtained from data which has been extrapolated in terms of β as well as N_x.

While the so far discussed extrapolation procedures are standard for processing MC data, the analytic continuation is particular for the imaginary imbalance approach and thus deserves special attention. Comparing the results obtained with different fit functions may yield insight beyond the pure numerical values. From the discussions in sec. 2.2, the most obvious approach is a polynomial fit of highest possible order

$$\xi^{\mathrm{Poly}}(\bar{m}_\mathrm{I}) = \xi(\bar{m} = 0) + \sum_{n=1}^{n_\mathrm{max}} (-1)^n \xi^{(n)} \bar{m}_\mathrm{I}^{2n}, \tag{2.46}$$

which can in principle be expected to approximate the true functional shape of $\xi(\bar{m}_{(\mathrm{I})})$ most closely, cf. fig. 2.3. However, the fits displayed in fig. 2.3 are based on analytically obtained mean-field results which, by construction, do not exhibit any spread or statistical uncertainty. For actual Monte Carlo data, this approach does not work as reliably. In fact, the spread of data points induces an effect similar to *Runge's phenomenon* for interpolating functions [142]: higher order polynomial fit functions are increasingly able to interpolate the spread, leading to oscillatory behavior. The latter is most often translated into large errors upon analytic continuation, when the counterbalancing effect of coefficients with alternating signs is revoked.

$\xi(\bar{m}=0)$ $\xi^{(1)}$	$n_{\max}=1$	$n_{\max}=3$	$n_{\max}=5$
$\bar{m}_{\mathrm{I}} \leq 0.2$	0.441 ± 0.002 0.319 ± 0.126	0.443 ± 0.003 1.500 ± 0.971	0.444 ± 0.005 2.960 ± 3.750
$\bar{m}_{\mathrm{I}} \leq 0.4$	0.439 ± 0.002 0.233 ± 0.026	0.441 ± 0.002 0.450 ± 0.191	0.441 ± 0.003 0.463 ± 0.571
$\bar{m}_{\mathrm{I}} \leq 0.6$	0.437 ± 0.002 0.176 ± 0.005	0.440 ± 0.002 0.323 ± 0.061	0.441 ± 0.002 0.419 ± 0.197

Table 2.1: Mass-balanced Bertsch parameter and curvature of $\xi(\bar{m})$ for different polynomial fit functions and ranges $\bar{m}_{\mathrm{I}}$. The qualitatively best results are found in the diagonal entries.

For this reason, polynomial functions will not be used for global fits of $\xi(\bar{m}_{\mathrm{I}})$. Instead, a Padé approximant

$$\xi^{\mathrm{Pade}}(\bar{m}_{\mathrm{I}}) = \frac{\xi(\bar{m}=0)}{1+\xi_{\mathrm{M}}\bar{m}_{\mathrm{I}}^2}\,, \tag{2.47}$$

will be employed.

Evaluation The problematics of global polynomial fits do not imply that they are unsuitable for the extraction of local properties as well. A particularly interesting quantity is the curvature of $\xi(\bar{m})$ in the origin as there is an exact analytic relation for it which may be used to assess the quality of the available dataset. Making use of the *Hellmann-Feynman* theorem and employing the representation (2.37) of the system's Hamiltonian, it is

$$\frac{\partial\langle\hat{H}\rangle}{\partial\bar{m}^2} = \frac{1}{1-\bar{m}^2}\left(\langle\hat{H}\rangle - \langle\hat{T}_{\Sigma}\rangle\right), \quad \langle\hat{T}_{\Sigma}\rangle = \frac{1}{2}\left(\langle\hat{T}_{\uparrow}+\hat{T}_{\downarrow}\rangle - \frac{1}{\bar{m}}\langle\hat{T}_{\uparrow}-\hat{T}_{\downarrow}\rangle\right). \tag{2.48}$$

For vanishing mass imbalance and/or non-interacting Fermi gases, one has $\langle\hat{T}_{\Sigma}\rangle = 0$. It can therefore be concluded that the curvature of $\xi(\bar{m})$ for vanishing mass imbalance is given by $\xi(\bar{m}=0)$ itself:

$$\left.\frac{\partial\langle\hat{H}\rangle}{\partial\bar{m}^2}\right|_{\bar{m}=0} = \langle\hat{H}\rangle\big|_{\bar{m}=0} \quad \Leftrightarrow \quad \xi(\bar{m}=0) \overset{!}{=} \xi^{(1)}, \tag{2.49}$$

since $\xi(\bar{m}) = \langle\hat{H}(\bar{m})\rangle / E_{\mathrm{free}}(\bar{m}=0)$ by definition. Here $E_{\mathrm{free}}(\bar{m}=0)$ is the energy of the free, mass-balanced gas.

When considering the Padé formula (2.47), this constraint cannot be fulfilled for any $\xi_{\mathrm{M}} \neq 1$. This does not mean that its global representation of $\xi(\bar{m})$ is necessarily bad, it is just not suited for a precise reproduction of such local quantities. In order to assess, whether the dataset used does in principle admit eq. (2.49) to be fulfilled, local polynomial fits may be employed. Tab. 2.1 shows results for $\xi(\bar{m}=0)$ and $\xi^{(1)}$ from fitting polynomials with different $n_{\max}$ and different ranges of data in terms of $\bar{m}_{\mathrm{I}}$. If higher $n_{\max}$ is admitted, more data points are needed for a precise determination of the coefficients. On the other hand, low order polynomials cannot be expected to reproduce the correct behavior of $\xi(\bar{m})$ over a large domain. Therefore, the best results may be found in the diagonal entries of tab. 2.1.

Indeed, the constraint (2.49) is fulfilled very well within the fitting error bars for these entries, confirming the quality of the dataset. The mass-balanced Bertsch parameter itself is consistently estimated as $\xi(\bar{m}=0) = 0.44 \pm 0.01$ which is in quantitative accordance with older and only about 20% above the most recent accepted values from theory and experiment, see fig. 2.1. Given the rather small amount of data available that technically permits only an estimate of an upper bound for ξ, this result is already very reasonable.

It should be noted that the error given in tab. 2.1 represents only the estimates from curve fitting. Uncertainties of the extrapolation are only included via their respective fitting errors as well which is for sure not a complete characterization. The latter one is not undertaken here, recalling the above statement that the averaging ansatz for the $\beta \to \infty$ extrapolation does in any case only admit the calculation of an upper bound for $\xi(\bar{m})$. In this sense, the results from tab. 2.1 are well compatible with experiment and

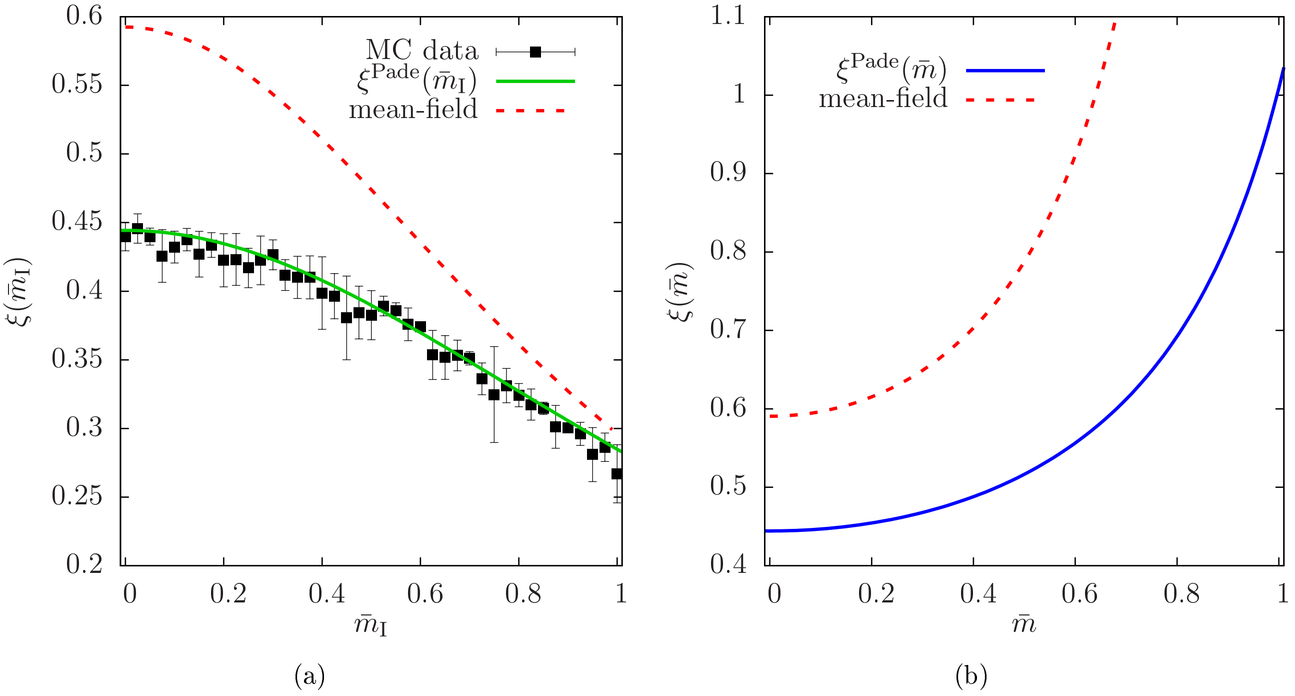

Figure 2.6: Analytic continuation of Monte Carlo data for imaginary mass imbalance (a) to the real domain (b) by means of the Padé ansatz (2.47). Mean-field results are provided alongside for comparison.

other MC approaches. The results presented here constitute the very first MC estimate of the equation of state for general mass imbalance. Once more data should become available, the extrapolation procedures and thus also the results for $\xi(\bar{m})$ may be improved further.

With the data available and the global ansatz (2.47), an overall result for $\xi(\bar{m})$ may be constructed. Employing the full extrapolated dataset for $\bar{m}_{\rm I} \in [0,1]$, the following results are obtained:

$$\xi(\bar{m}=0) = 0.444 \pm 0.002\,, \quad \xi_{\rm M} = 0.560 \pm 0.013\,. \tag{2.50}$$

The corresponding curves along with the extrapolated dataset and mean-field results are shown in figs. 2.6a for $\bar{m}_{\rm I}$ and 2.6b for $\bar{m}$, respectively.

A comparison between the obtained MC prediction for $\xi(\bar{m})$ and mean-field results can readily be drawn from fig. 2.6. The absolute difference for $\bar{m}=0$ has already been discussed in the introduction of this chapter. While the distance between the mean-field and MC curves[10] appears to decrease for $\bar{m}_{\rm I} \to 1$, this does not translate to real $\bar{m}$. According to eq. (2.29), $\xi(\bar{m})$ has to diverge for $\bar{m} \to 1$ at mean field. No signs of such behavior are observed for the MC value which is perfectly finite: $\xi^{\rm Pade}(\bar{m}=1) = 1.01$. Whether this is a physical result or due to the imperfections of the fitting process or even a sign of analytic inaccessibility of the large-$\bar{m}$ regime in the sense of sec. 2.2 cannot be determined from the present data alone. It should, however, be noted that a finite value for ξ is found in ref. [143] as well. There, one of the species' masses is set to infinity which would correspond to $\bar{m}=1$ in the framework employed here. Since it is not entirely clear if the two approaches are in fact completely equivalent, this should also be taken with some caution.

Data to be compared to the present results for finite intermediate $\bar{m}$ are very rare. So far, no condensation experiments with mass-imbalanced mixtures have been performed and most of the other Monte Carlo approaches were hampered by the sign problem. The results of [144] for a ^{6}Li-^{40}K mixture appear to be not completely conclusive, but they are compatible with the ones presented here.

To summarize, it can be stated that the method of imaginary imbalances has proven to be capable of circumventing the Monte Carlo sign problem for mass-imbalanced unitary Fermi gases. An equation of state for all admissible mass imbalances could be extracted that compares well to other approaches and experimental data where available. Systematic improvements may be expected from an increased amount

---

[10] The mean-field curve drawn in fig. 2.6a corresponds to the $\bar{h}=0$ case, see the discussion on p. 23. In contrast, the curve in fig. 2.6b belongs to the $\bar{h}=\bar{m}$ case and does therefore not exhibit signs of a phase transition.

of raw data which should in particular enhance the accuracy of the required extrapolation procedures. Concerning the reliability of these results in the large-$\bar{m}$ regime, no definite answer can be given at this point. Mean-field analyses suggest that there is no phase boundary in the $\bar{T} = 0$ and $\bar{h} = \bar{m}$ regime investigated here, but the overall radius of convergence might be limited. These predictions are, however, not directly applicable to the MC results. At least the issue of possible phase boundaries will be revisited in the conclusions (chap. 5) of this thesis, when results from the functional RG analysis in chap. 4 have been discussed as well.

Chapter 3

Strongly correlated Fermions in 1D

In terms of quantitative accuracy Monte Carlo simulations are often the method of choice when it comes to predicting or reproducing experimental findings. However, they are not without any drawbacks. For the concrete example of the approach presented in chap. 2 above, a most serious roadblock, the sign problem, has been circumvented by means of the imaginary imbalance approach. But the price to be paid comes in the form an additional class of systematic uncertainties on the results - the convergence properties of actual Monte Carlo data can only be estimated and it may happen that important features like phase transitions are not sufficiently discernible. Furthermore, certain qualitative aspects like the spatial variation of the order parameter that most prominently characterizes an inhomogeneous phase can presently be deduced only indirectly by means of modifications in the global equation of state. Therefore, Monte Carlo simulations of ultracold atomic gases have to be complemented by (semi-)analytic studies to fill in these gaps and explore properties that cannot or not easily be addressed by means of MC.

The various analytical approaches one could think of each bring about their own merits and limitations. Aside from rare exceptions, they are usually approximate in one or the other way and it is not always obvious how trustworthy the respective results are. Comparison with MC data if available, but of course also between different analytical approaches is therefore mandatory. In that sense it may even be of use to study models which do not have any direct experimental realization (yet).

In this chapter, the special situation of fermions in one spatial dimension is addressed. In particular for cold atomic gases, there are experimental setups which provide a nearly or "quasi" one-dimensional environment. One advantage of the low dimensionality is the large extent of inhomogeneous phases that can be expected to occur compared to higher-dimensional cases. This has been predicted by a number of different methods as for example mean field [145,146], Bethe ansatz [147,148], density matrix renormalization group [149,150] or Monte Carlo [151–153]. The analogy to solid state systems like superconducting stripe heterostructures and nanowires [154,155] is an additional motivation. Furthermore, exactly solved problems like the (1+1)-dimensional Gross-Neveu model (see sec. 1.2.2) provide excellent benchmarking cases at least at mean-field level. And last but not least, the comparative mathematical simplicity and numerical cost-effectiveness of one-dimensional systems makes them a good starting point for the development of new and advancement of established approaches.

The first section of this chapter is devoted to an investigation of condensation phenomena in general and inhomogeneous phases in particular of the one-dimensional ultracold Fermi gas with spin and mass imbalance. A mean-field vertex expansion technique for the identification and characterization of such FFLO-like structures is presented and thoroughly discussed. Since the findings for the phase diagram are at least partially not intuitive at first glance, sec. 3.2 explores the two-body foundations of inhomogeneous ordering, thereby establishing techniques that turn out to be useful in the three-dimensional system dealt with in chap. 4 as well. Finally, the experience gained in the handling of inhomogeneity is transferred back to the relativistic case in sec. 3.3. There, an approximation scheme specifically tailored for the identification of transitions from the normal to an inhomogeneous phase is developed and applied to one- and, for illustration, three-dimensional models of strongly interacting relativistic fermions.

The work on which this chapter is based has been or will be published in [156], [157] and [158].

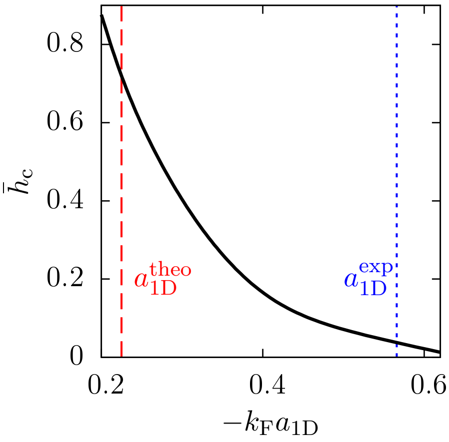

Figure 3.1: Mean-field critical spin imbalance $\bar{h}_c$ as a function of the dimensionless scattering length. The value a_{1D}^{theo} employed in this work (red, dashed line) as well as the experimental a_{1D}^{exp} from [159] (blue, dotted line) are provided for comparison.

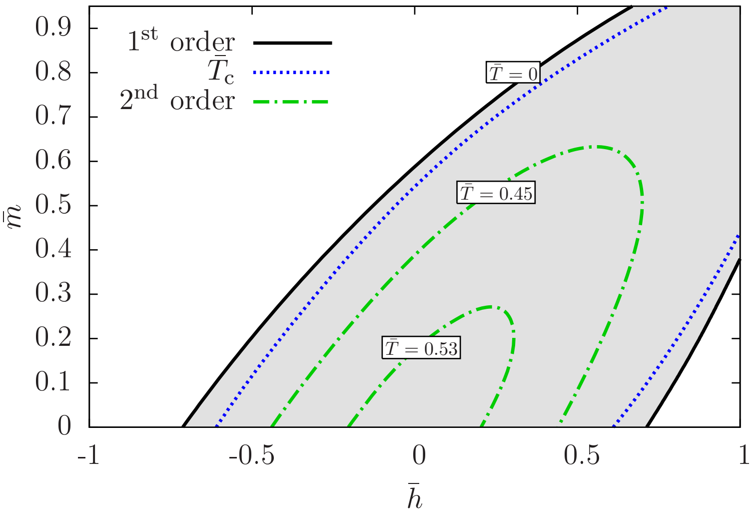

Figure 3.2: Mean-field finite temperature phase diagram in the $\bar{h}$-$\bar{m}$ plane for $g_\delta^{1D} = -1/a_{1D}^{\text{theo}}$. The superfluid region is indicated by gray shading. The first order transition at low $\bar{T}$ (black, solid line) turns into a second order one (green, dot-dashed line) above $\bar{T}_c(\bar{m})$ (blue, dotted line).

3.1 Many-body phase diagram of imbalanced ultracold Fermi gases

In sec. 2.2.1, mean-field theory in general and for the three-dimensional unitary Fermi gas with space independent order parameter in particular has been introduced. An analogous calculation can straightforwardly be performed for the one-dimensional case, yielding

$$\frac{1}{\beta L}\Gamma^{1D}_{\text{mf}} = \frac{|\bar{\Delta}|^2}{g_\delta^{1D}} - \frac{1}{\beta}\int \frac{\mathrm{d}p}{2\pi} \sum_{\sigma=\pm 1} \ln\left[1 + e^{-\beta\left[\sigma\left(\bar{m}p^2 - h\right) + E_{\bar{\Delta}}\right]}\right] \tag{3.1}$$

for the mean-field effective action omitting unimportant vacuum contributions. Here, L is the spatial extent of the system. The contact interaction in 1D does not introduce any divergences, so g_δ^{1D} is not renormalized as in 3D. Recall instead (see sec. 1.2.1), that there is no nontrivial "unitary" limit in 1D, so the scattering length a_{1D} remains to be determined. In fig. 3.1, the critical spin imbalance $\bar{h}_c$ at zero temperature and vanishing mass imbalance as obtained from eq. (3.1) is given for a range of dimensionless scattering lengths. Since $g_\delta^{1D} = -a_{1D}^{-1}$, the system is more strongly coupled for smaller absolute values of the scattering length. Consequently, the critical imbalance above which the condensate vanishes becomes larger for $a_{1D} \to 0$. In the following, a dimensionless scattering length $k_F a_{1D}^{\text{theo}} = 1/(\sqrt{2}\pi)$ will be chosen mainly for numerical reasons: For this value (see red/dashed line in fig. 3.1) $\bar{h}_c$ as well as the other characteristic quantities become $\sim \mathcal{O}(1)$ which is most conveniently dealt with from a computational point of view while still representing a strongly coupled system with $g_\delta^{1D} > 1$.

By minimizing the effective action (3.1), the phase diagram of the model can be computed, see fig. 3.2. A sizable region of finite $\bar{\Delta}_0$, again centered around $\bar{h} = \bar{m}$ is found (gray shading in fig. 3.2), indicating the occurrence of superfluidity for the respective imbalance configurations. The highest critical temperature is achieved for vanishing imbalances at $\bar{T}_{\text{max}} = 0.547$.

However, the *Mermin-Wagner-Hohenberg theorem* [160, 161] clearly states, that spontaneous symmetry breaking cannot occur in finite temperature systems with spatial dimension smaller than three. In one dimension, it is even forbidden at zero temperature. Superfluidity should therefore not occur in the phase diagram of the one-dimensional ultracold Fermi gas, as condensation phenomena are inhibited by long-range fluctuations. Other than in the three-dimensional case, where only quantitative deviations are expected, mean field is evidently not even qualitatively correct anymore in 1D. In chap. 4, it will be demonstrated that the mean-field approximation omits just those *order parameter fluctuations*, which are responsible for the destruction of long range order.

Fortunately, the impossibility of *true* long (infinite) range ordering in low-dimensional systems does not

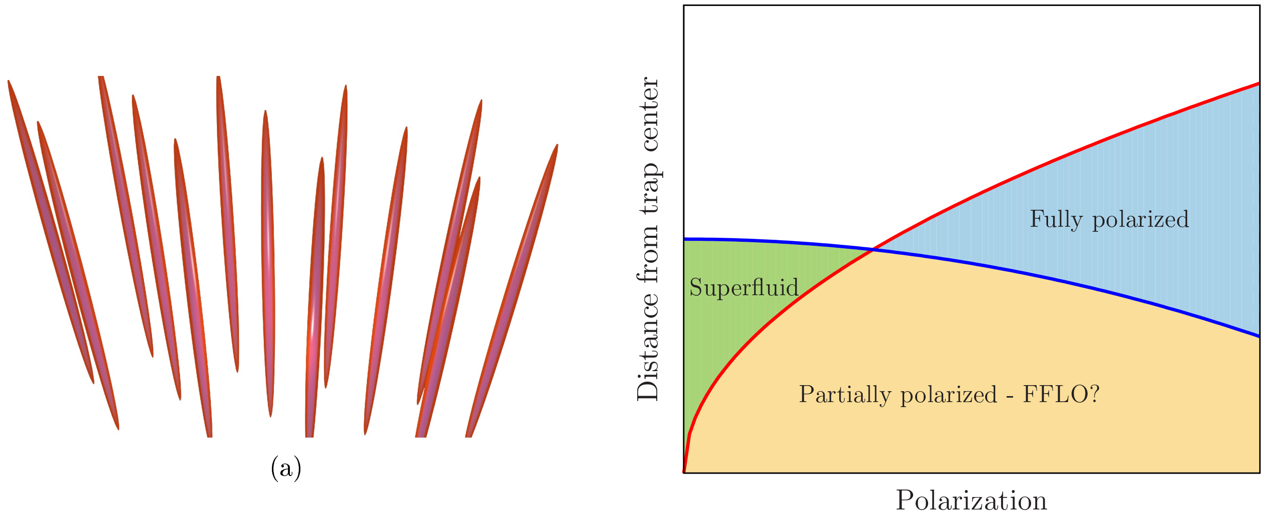

(a)

(b)

Figure 3.3: Experimental realization of one-dimensional (inhomogeneous) superfluidity. An array of longitudinally extended quasi one-dimensional traps is filled with a overall imbalanced mixture of ^{6}Li atoms (a). The distribution of the species in the trap (blue/red solid lines for the maximum range where the respective species can be found) can be interpreted in terms of balanced superfluidity and/or even FFLO phases (b, adapted from [159]), see main text for details.

mean, that no superfluid phenomena can be observed at all. Real world systems are never of infinite extent, which does in fact neither allow for infinite range order, nor infinite range fluctuations. In other words, the physical size of the system effectively provides an *infrared cutoff* for the fluctuations. While low dimensional systems may not exhibit superfluidity in the thermodynamic limit, residual algebraic ordering of finite range can still induce the same phenomenology when the size of the system is of the order of the *coherence length*. The term "algebraic ordering" refers to the fact, that correlations between the system's constituents decrease with a power law in such situations. In two spatial dimensions, this is described by the concept of *Berezinskii-Kosterlitz-Thouless* phase transitions [162–164]. In one dimension, quantum fluctuations exponentially suppress ordering phenomena even at zero temperature. However, real world systems are also never strictly one-dimensional and ordering may quickly be restored by a small, but finite transversal extent, see, e.g., [165] for a review.

It does therefore not come as a surprise, that superfluidity in low-dimensional systems can indeed be observed in experiments. Such a series of measurements with particular relevance to this work has been carried out by the authors of [159] from Rice University. A mixture of ^{6}Li atoms in two different hyperfine states was loaded into an array of quasi one-dimensional traps, see fig. 3.3a for an illustration of the experimental arrangement.

The results from [159] are shown schematically in fig. 3.3b. The polarization on the horizontal axis measures differences in the overall density of the two fermion species and is thus conjugate to the spin imbalance parameter $\bar{h}$. According to eq. (1.15), the (longitudinal) distance from the center of the trap on the vertical axis can be understood as an effective increase in the chemical potential. In agreement with an LDA-extended thermodynamic Bethe-ansatz calculation, the authors of [159] conclude that for low polarization, a fully paired superfluid shell surrounds a partially polarized core.[1] For higher polarization/imbalance, supernumerous atoms of the majority species are repelled from the core and form a fully polarized phase, the balanced superfluid is not present anymore. Though no sign of an actual spatial inhomogeneity beyond the one induced by the trap itself could be detected, the partially polarized phase in the core is identified with FFLO ordering, again due to comparison with predictions from Bethe-ansatz studies.

Overall, it can be concluded that the mean-field prediction of a superfluid phase in the one-dimensional Fermi gas is not that far from reality as it may appear in the first place. Assuming the trapping potential

---

[1] This is a peculiarity of one-dimensional systems. In three spatial dimensions, the superfluid phase is found in the center of the trap.

to be very flat in the longitudinal direction, qualitative insight should again be producible via mean field. Of course, these results should still be handled with care: The occurrence of superfluidity in reality is intimately linked to the finite-volume effects of the trapping potential, residual influence of finite transverse confinement or even coupling between the single tubes. Refs. [145,146] take these considerations into account and, for example, the combined Bethe-ansatz-LDA procedure does so by construction. It can therefore be compared quantitatively to experiments like the one discussed above, but only when approximations like the LDA or truncations of the Bethe-ansatz equations are indeed applicable.

The goal of this section will not be to achieve similar quantitative accuracy. Instead, strictly one-dimensional mean-field theory will be employed. Comparability to experimental studies will remain on a qualitative level. Therefore, the numerically convenient value $a_{1\mathrm{D}}^{\mathrm{theo}}$ for the scattering length will be employed instead of $a_{1\mathrm{D}}^{\mathrm{exp}}$ realized in [159] without loss of explanatory power.

The experimental findings suggest the existence of sizable inhomogeneous phases, but evidence is so far only indirect, as Bethe-ansatz calculations are not able to resolve spatial variations of the order parameter field. The strength of the approach adopted in the following lies in its clean separation of explicit inhomogeneous ordering from any spurious effects that might be induced by trapping. It is therefore expected to improve the understanding of the fundamental mechanisms behind FFLO physics. Furthermore, it will provide useful tools for the analysis of the three-dimensional case in chap. 4, even beyond the mean-field approximation.

3.1.1 Vertex expansion for inhomogeneous order parameters

To accommodate for the possible occurrence of inhomogeneous phases, the order parameter field $\bar{\Delta}$ is now allowed to be spatially varying, $\bar{\Delta} \equiv \bar{\Delta}(x)$. Note that this does not in any way correspond to an extension of the mean-field approximation itself. As before, the path integration is reduced to a single configuration for the order parameter field. The possibility of spatial variation is in fact already included in the general formulation of the mean-field condition in eq. (2.13).

The principal mathematical complication that comes along with the introduction of spatial inhomogeneity is the non-diagonal momentum structure of the Yukawa-type interaction terms in the bosonized action (see app. A for notational conventions):

$$\int_{\mathbf{p}} \psi_{\uparrow,n,\mathbf{p}} \bar{\Delta}^* \psi_{\downarrow,-n,-\mathbf{p}} \xrightarrow{\bar{\Delta}^*(x)} \int_{\mathbf{p},\mathbf{q}} \psi_{\uparrow,n,\mathbf{p}} \bar{\Delta}^*_{\mathbf{p}-\mathbf{q}} \psi_{\downarrow,-n,-\mathbf{q}} \,. \tag{3.2}$$

For general $\bar{\Delta}(x)$, a direct calculation of the trace term (see also eqns. (2.11) and (2.20) for its origin) by diagonalization is thus not possible anymore,

$$\frac{1}{\beta}\Gamma^{1\mathrm{D}}_{\mathrm{mf}}[\bar{\Delta},\bar{\Delta}^*] = -\int \mathrm{d}x \frac{|\bar{\Delta}(x)|^2}{g^{1\mathrm{D}}_{\delta}} + \sum_n \mathrm{Tr}\ln\left[\mathcal{P}_{\psi}^{-1} + \mathcal{F}\right], \tag{3.3}$$

with

$$\mathcal{P}_{\psi}^{-1} = \begin{pmatrix} -i\omega_n - (1+\bar{m})\nabla^2 - \mu - h & 0 \\ 0 & i\omega_n + (1-\bar{m})\nabla^2 + \mu - h \end{pmatrix}, \quad \mathcal{F} = \begin{pmatrix} 0 & \bar{\Delta}(x) \\ \bar{\Delta}^*(x) & 0 \end{pmatrix}. \tag{3.4}$$

Possible ways out of this or analogous situations include the numerical diagonalization of a discretized version of eq. (3.3) [166], spectral methods [96] or Ginzburg-Landau expansions [167]. In this work, a *vertex expansion* of the effective action is employed as will be explained in the following.

Consider the series representation

$$\ln\left[\mathcal{P}_{\psi}^{-1} + \mathcal{F}\right] = \ln\left[\mathcal{P}_{\psi}^{-1}\right] + \ln\left[\mathbb{1} + \mathcal{P}_{\psi}\mathcal{F}\right] = \ln\left[\mathcal{P}_{\psi}^{-1}\right] - \sum_{j=1}^{\infty} \frac{1}{2j}\left[\mathcal{P}_{\psi}\mathcal{F}\right]^{2j} \tag{3.5}$$

of the matrix-valued logarithm in eq. (3.3) about vanishing order parameter $\bar{\Delta} = 0$. This expansion point is particularly convenient as it does not make any assumption on the possible space dependence of $\bar{\Delta}$.

The first term in eq. (3.5) is just the pressure of a free Fermi gas and can be calculated along the lines of sec. 2.2.1. The second term, which comprises the actual series representation, is now diagonal in the space of fermion species and holds only even orders, since $\mathcal{P}_{\psi}\mathcal{F}$ and odd powers thereof are traceless. Applying this representation to eq. (3.3), the summation over powers of the order parameter field can be understood as a vertex expansion,

$$\Gamma = \sum_{j=0}^{\infty} \Gamma^{(2j)} \cdot (\bar{\Delta}\bar{\Delta}^*)^j . \tag{3.6}$$

Every term of this sum comes along with a spatial or, alternatively, $2j$ momentum integrations which are encoded in the "Tr" expression. It is therefore not possible, to explicitly calculate $\Gamma^{1\mathrm{D}}_{\mathrm{mf}}$ at this stage. In fact, the gap equation (2.13) becomes an infinite order integral equation for the determination of $\bar{\Delta}(x)$. Even for some finite truncation of the vertex expansion, $j_{\max} < \infty$, it is far from clear how to solve such an equation.

In order to overcome this obstacle and turn the problem of solving a complicated integral equation into the more manageable one of an algebraic minimization, an explicit representation of the spatially varying order parameter is needed. It is generally assumed that spontaneous breaking of translational invariance leaves a discrete subgroup intact, i.e. the inhomogeneity must be periodic in space. A Fourier expansion of $\bar{\Delta}(x)$ is then possible without loss of generality,

$$\bar{\Delta}(x) = \sum_{l_q=0}^{\infty} \alpha_{l_q} \cos(l_q \omega_{\bar{\Delta}} x) . \tag{3.7}$$

Here, $\omega_{\bar{\Delta}}$ encodes the characteristic frequency of the inhomogeneity for some particular configuration of interaction strength, temperature and imbalances.[2]

The homogeneous case ($\alpha_{l_q \neq 0} = 0$) is contained in this representation as well as the "classical" Larkin-Ovchinnikov (LO) ansatz [80] ($\alpha_{l_q \neq 1} = 0$). In general, the quadratic dispersion relation for spatial momenta ensures that the cosine ansatz (3.7) is indeed sufficient. Using a full Fourier series in terms of plane waves $\sim \alpha_{l_q} e^{i l_q \omega_{\bar{\Delta}} x}$ instead, it is always $\alpha_{l_q} = \alpha_{-l_q}$ due to the non-relativistic structure of the integrands of $\Gamma^{(2j)}$.

For an actual calculation of $\Gamma^{1\mathrm{D}}_{\mathrm{mf}}$, neither the vertex expansion nor the Fourier series can in fact be made use of without a truncation at some finite order $j_{\max}$ or $l_{q,\max}$, respectively. The impact of these approximations as well as the convergence properties/admissibilities of the series expansions themselves have to be evaluated critically which will be done in sec. 3.1.2 below.

Since the zeroth order of the expansion (3.6) is just the pressure of a free gas, the two-point function $\Gamma^{(2)}_{1\mathrm{D,mf}}$ is the first nontrivial result. It is given by

$$\begin{aligned}\frac{1}{\beta L}\Gamma^{(2)}_{1\mathrm{D,mf}} = -\sum_{l_q} \alpha_q^2 \Bigg\{ \frac{1}{g_\delta^{1\mathrm{D}}} + \int_{\mathbf{p}} \frac{1}{[p^2(1+\bar{m}) + (p-\omega_{\bar{\Delta}} l_q)^2(1-\bar{m}) - 2\mu]} \\ \cdot \Bigg[\frac{1}{\big[1+e^{\beta[p^2(1+\bar{m})-\mu-h]}\big]} - \frac{1}{\big[1+e^{-\beta[(p-\omega_{\bar{\Delta}} l_q)^2(1-\bar{m})-\mu+h]}\big]} \Bigg] \Bigg\} .\end{aligned} \tag{3.8}$$

Computational details can be found in app. B. For higher n-point functions, the Matsubara summation becomes increasingly more involved, as the pole structure of the summands depends on the distribution of Fourier indexes. For clarity and convenience, the frequency sum can therefore be left to computer algebra systems like *Wolfram Mathematica*. In order to give an impression of the structure of those higher n-point functions, a corresponding form of $\Gamma^{(4)}_{1\mathrm{D,mf}}$ is provided below,

$$\begin{aligned}\frac{1}{\beta L}\Gamma^{(4)}_{1\mathrm{D,mf}} = \frac{1}{2} \sum_{l_q, l_r, l_s} \int_{\mathbf{p}} \oint \frac{\mathrm{d}z}{2\pi} \frac{1}{1+e^{\beta z}} \frac{\alpha_{l_q}\alpha_{l_r}\alpha_{l_s}\alpha_{l_q+l_s-l_r}}{P^o[z;p] \cdot P^u\left[z; p+\omega_{\bar{\Delta}}(l_r - l_q - l_s)\right]} \\ \cdot \frac{1}{P^u\left[z; p+\omega_{\bar{\Delta}}(l_r - l_q)\right] \cdot P^o\left[z; p-\omega_{\bar{\Delta}} l_q\right]} ,\end{aligned} \tag{3.9}$$

with

$$P^{u/o}[z;p] \equiv [-z \pm p(1 \pm \bar{m}) \mp \mu - h] . \tag{3.10}$$

For a more detailed account on the intricacies of the Matsubara summation procedure as well as expressions for vertex functions up to eighth order see app. B. Furthermore, there are connections to the widely used

---

[2] Fourier cosine transformations of non-periodic square integrable even functions exist as a well-defined limit $\omega_{\bar{\Delta}} \to 0$ of eq. (3.7). Therefore, an occurrence of non-periodic inhomogeneous symmetry breaking should reveal itself even when using the latter periodic ansatz. No signs of such behavior have been detected in the present work.

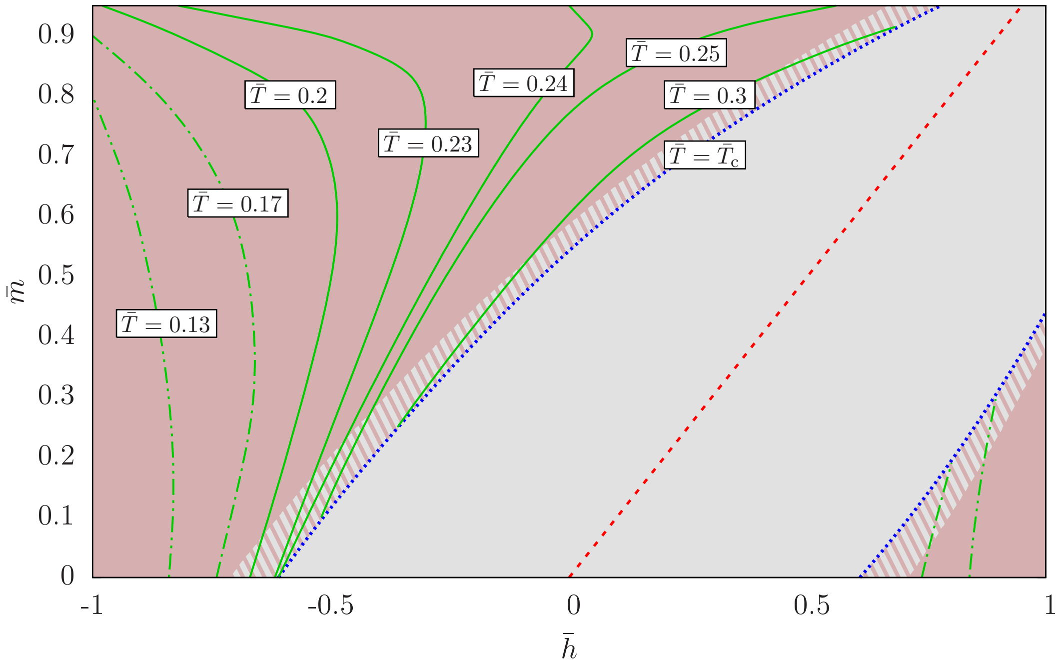

(a) Temperature projected phase diagram of the 1D imbalanced Fermi gas. The light gray area indicates the $\bar{T} = 0$ homogeneous superfluid phase. The inhomogeneous phase is shaded red (dark gray). $\bar{T}$ isolines for the FFLO phase are provided with corresponding labels. The striped areas symbolize regions, where the inhomogeneous solution thermally overlays or supersedes the homogeneous one. A red (dashed) line marks equal spin and mass imbalance.

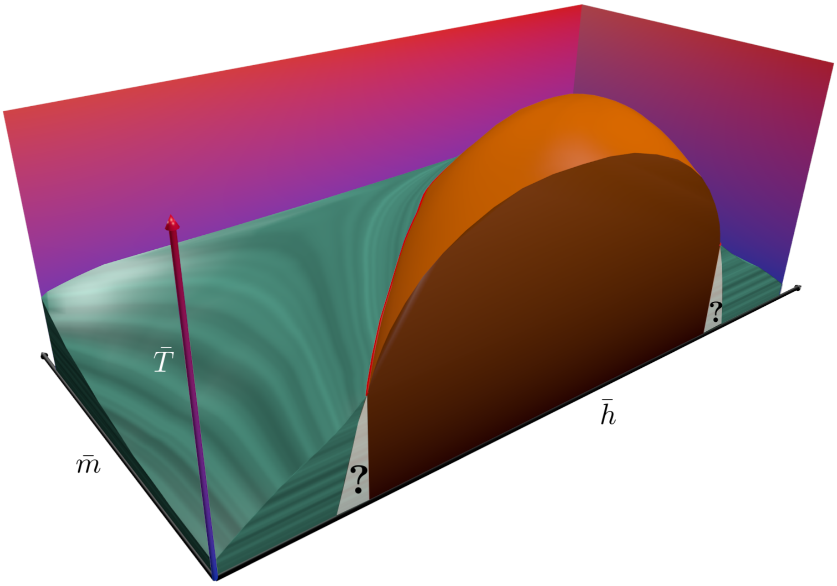

(b) View of the complete parameter space that has been considered for figure (a). The homogeneous phase corresponds to the orange "dome", whereas the inhomogeneous one is represented by the greenish-colored domains. The critical line $\bar{T}_c(\bar{m})$ is drawn in red. The nature and precise location of the homogeneous-inhomogeneous transition in the bulk of the superfluid phase is uncertain (brightened regions with question marks).

Figure 3.4

Ginzburg-Landau expansion technique [168] that will be discussed in more detail on p. 53 below.
Given the above expressions, the gap equation can be derived and solved or, alternatively, the effective action minimized directly. The smallest meaningful truncation for a search of inhomogeneous phases involves $j_{\max} = 2$ and $l_{q,\max} = 1$. The latter represents the above-mentioned LO-type inhomogeneity that cannot be simplified further in the present framework without giving up the option of spatially varying solutions altogether. The former can conceptually be understood along the lines of classical Landau theory of phase transitions [169]: The order parameter potential must be at least quartic (in the absence

of uneven powers) to form a nontrivial symmetry breaking minimum while maintaining positivity.

In fig. 3.4, the phase diagram obtained with this truncation is shown. A temperature projected view is given in fig. 3.4a, while fig. 3.4b attempts to impart an impression of the full $(\bar{h}, \bar{m}, \bar{T})$ parameter space that has been considered.

Moving from high temperatures down, the first condensate to appear is the "ridge"-like structure that indicates homogeneous superfluidity (gray, light shading). Down to the critical line $\bar{T}_{\mathrm{c}}(\bar{m})$, the resulting positions for transitions to the normal phase are identical to those in fig. 3.2. The values $\bar{T}_{\mathrm{c}}(\bar{m})$ do now indicate multicritical behavior: instead of just changing the nature of the transition between normal and homogeneously broken phases, an inhomogeneous phase occurs (red, dark shading). $\bar{T}_{\mathrm{c}}(\bar{m})$ is therefore now a manifold formed by the intersection of three different phase transition surfaces: second order ones between the homogeneous/inhomogeneous superfluid and the normal phase and possibly a first order one between the homogeneous and the FFLO superfluid.

The region, where the newly found inhomogeneous phase overlays the homogeneous condensate is indicated by a striped pattern. Note that this does not necessarily mean that the homogeneous phase is *superseded* by the inhomogeneous one, cf. the Gross-Neveu case depicted in fig. 1.3. Which type of ordering is actually preferred in the bulk cannot be determined reliably at this level of truncation. More detailed discussions on this subject as well as the stability of the so-far presented results with respect to changes of the truncation are discussed in detail in sec. 3.1.2 below.

The inhomogeneous phase itself exhibits quite remarkable properties. First of all, it occupies the whole $\bar{h}$-$\bar{m}$ plane considered here if $\bar{T} < 0.037$. There is no zero temperature normal phase left. In this sense, previous indications (see, e.g., references on p. 31) of a large FFLO phase in low-dimensional Fermi gases are certainly substantiated by the present results. Moreover, the dependence of its stability against thermal effects or the imbalances exhibits a nonintuitive "hook"-like structure. Consider, in particular, the $\bar{T} = 0.23...0.25$ isolines in fig. 3.4a. These features as well as the dependence of the characteristic frequency $\omega_{\bar{\Delta}}$ on imbalance and temperature will be explored in sec. 3.2 in detail.

3.1.2 Reliability and accuracy of the vertex expansion

The above introduced procedure for the approximate calculation of $\Gamma^{\mathrm{1D}}_{\mathrm{mf}}$ involves expansions in terms of the order parameter and of the order parameter itself. A discussion of the convergence properties of these expansions as well as the behavior of their truncated versions that are applied in practice is mandatory for a dependable interpretation of numerical results. The technical details presented in this section are therefore intended to provide a close characterization of the vertex expansion technique and in the same instance establish a firm basis for a more simple approach.

Convergence properties of the vertex expansion An ideal test case for the behavior of the vertex expansion alone is provided by the homogeneously broken phase. No Fourier expansion of $\bar{\Delta}$ is needed and the exact solution (3.1) is known.

For spatially constant $\bar{\Delta}$, the integrand of (3.1) does not exhibit any (complex) singularities, as it depends on the strictly positive $\bar{\Delta}\bar{\Delta}^*$ only. The vertex expansion (3.6) can therefore be expected to exhibit an infinite radius of convergence. However, this does not mean, that the solution $\bar{\Delta}_0$ of the gap equation obtained from any nth order truncation of (3.6) converges in the same way as $n \to \infty$.

In fig. 3.5, the value of the fermion gap (fig. 3.5a) and the corresponding value of $\Gamma^{\mathrm{1D}}_{\mathrm{mf}}$ measured with respect to the free gas (fig 3.5b) are given as functions of temperature for vanishing spin and mass imbalance. Close to the phase boundary at $\bar{T} = 0.55$, convergence indeed seems to improve with growing truncation order. In the bulk of the broken phase, however, the $n = 3$ case yields unnaturally large values for the fermion gap and cannot be used anymore below $\bar{T} \sim 0.4$. This is due to the same behavior that makes a calculation of the gap with $\Gamma^{(2)}$ impossible: for uneven orders n, the truncated vertex expansion is not bounded from below. While $\Gamma^{(2)}$ alone is strictly concave, a truncation of order $n = 3$ may already provide a metastable minimum for small $\bar{\Delta}$, i.e. close to a second order phase transition it may still be used. Even order truncations do not exhibit this kind of problem, albeit naturally convergence is slow for larger $\bar{\Delta}_0$, see fig. 3.5.

Since the coordinates of second order phase transitions are determined solely by a sign change of the two-point function, all truncations displayed in fig. 3.5 reproduce the corresponding exact result correctly. It can therefore be concluded, that the vicinity of such transitions may reliably be explored with finite

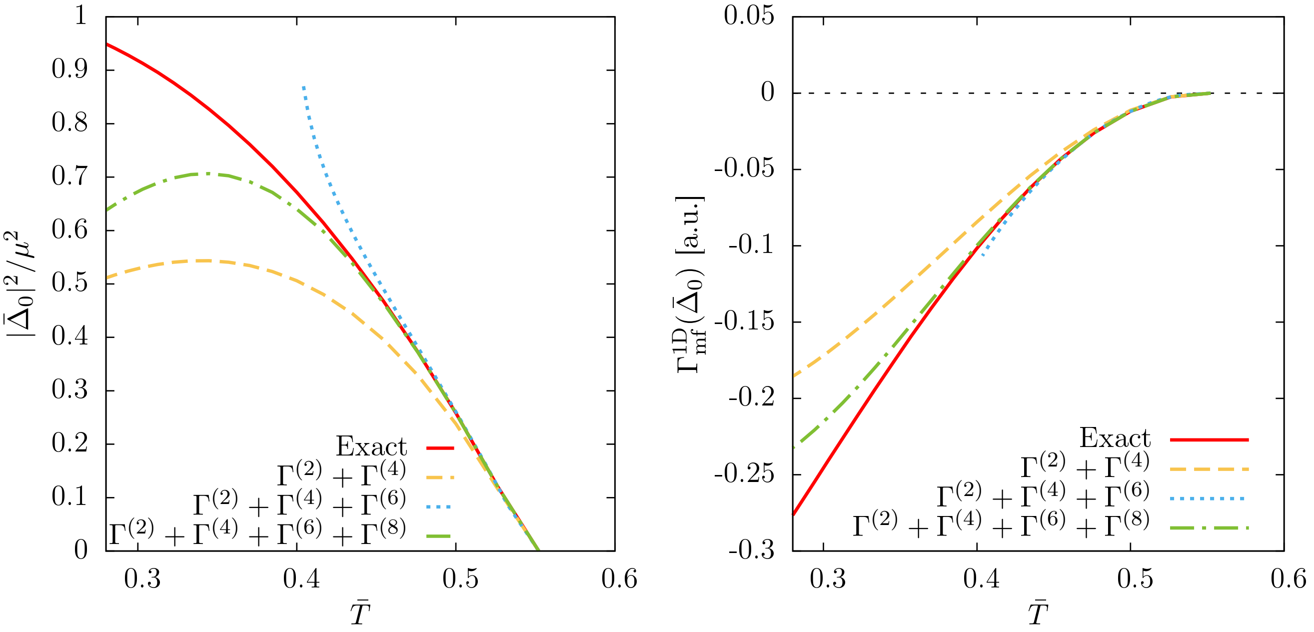

(a) (b)

Figure 3.5: Convergence of homogeneous Fermion gap $|\bar{\Delta}_0|^2/\mu^2$ (a) and the corresponding value of $\Gamma^{\mathrm{1D}}_{\mathrm{mf}}$ measured with respect to the free gas (b) for the $\bar{m} = \bar{h} = 0$ case with $\bar{T}_{\mathrm{c}} = 0.55$. Truncations up to order $n = 4$ are compared to the exact result derived from eq. (3.1).

truncations of the vertex expansion. Numerically, it should be most convenient to prefer the use of even orders, as they do not exhibit the large-$\bar{\Delta}$ instabilities of the odd ones. Finally, if properties deep in the bulk of broken phases are to be investigated, the computation of very high orders n might be necessary.
So far, only the homogeneous case has been discussed. The more interesting, inhomogeneous one is by construction not as easily accessible, since no analytically exact solution is known that can be used for estimates of the convergence properties or even visual comparison. It can be argued, however, that the convergence of the series (3.5) itself can be estimated by the replacement

$$\mathcal{F} = \begin{pmatrix} 0 & \bar{\Delta}(x) \\ \bar{\Delta}^*(x) & 0 \end{pmatrix} \longrightarrow \mathcal{F}_{\max} = \sum_{l_q} \begin{pmatrix} 0 & |\alpha_{l_q}| \\ |\alpha_{l_q}| & 0 \end{pmatrix}. \tag{3.11}$$

The series would then correspond to an expansion of eq. (3.1) for a constant order parameter $\bar{\Delta}_0^{\mathrm{est}} = \sum_{l_q} |\alpha_{l_q}|$ and should be convergent. For any finite truncation of the Fourier series, convergence of the vertex expansion in the inhomogeneous case is therefore ensured. It is, however, not clear, if this doubly truncated series expansion converges to the potentially exact solution or if the latter exists at all, since the existence of a finite $\bar{\Delta}_0^{\mathrm{est}}$ itself is now linked to the (absolute) convergence of the Fourier series (3.7). It is therefore mandatory to study the latter as well.

Convergence properties of the Fourier expansion On the one hand, it appears to be impossible to make any definite statements about the convergence properties of (3.7) since not even the existence of a periodic $\bar{\Delta}(x)$ can be proven beyond the homogeneous regime. On the other hand, the constraints put on the class of possible functional shapes for $\bar{\Delta}(x)$ by the theorems of *Dirichlet* [170] or *Carleson* [171], respectively, are very reasonable from a physical point of view. In particular, the order parameter should be L^2 integrable on a period since a divergence of the fermion gap is simply unphysical. Assuming the existence of a solution, the Fourier expansion (3.7) can therefore be expected to be converging at least *almost everywhere*.
The primary question left to be addressed is thus the rather practical one of how many Fourier coefficients provide a good approximation to the exact result for a particular point of the considered parameter space. This will be discussed in the following, using a generic set of configurations that covers all qualitative phenomena: For $\bar{T} = 0.25$ and $\bar{m} = 0.5$, the range $\bar{h} \in [-0.3, 0]$ encloses transitions from the normal

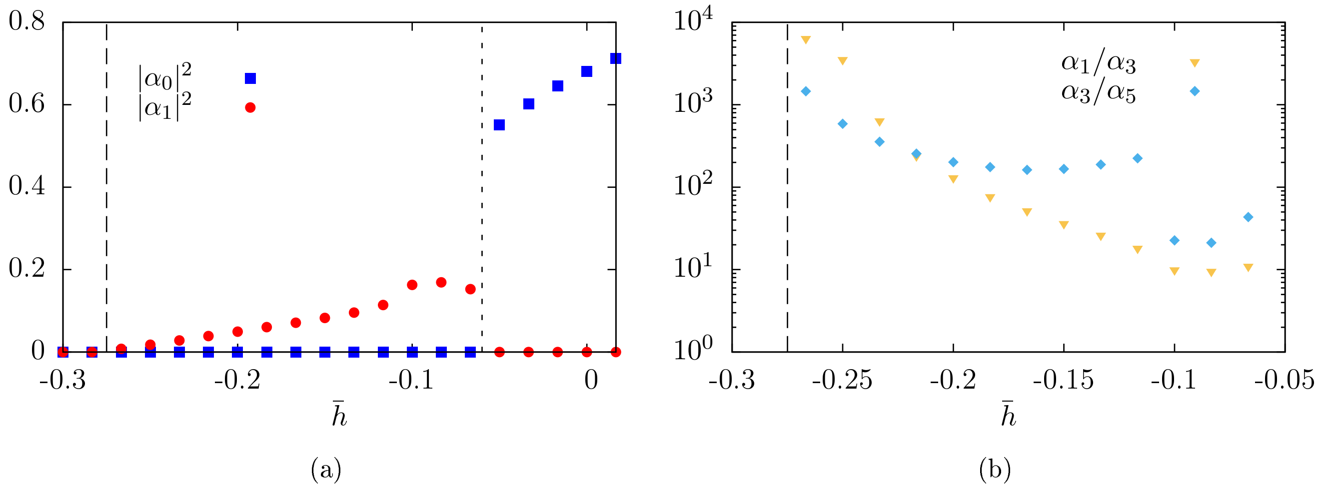

Figure 3.6: Squared values of the first two Fourier coefficients (a) and ratios of higher order ones (b) for different $\bar{h}$ at fixed $\bar{T} = 0.25$ and $\bar{m} = 0.5$. Transitions between the normal and inhomogeneous or homogeneous and inhomogeneous phases are denoted by dashed and dotted lines, respectively. These data have been computed with $j_{\max} = 2$ and $l_{q,\max} = 5$. Note the larger $\bar{h}$ domain in (a) that was chosen to demonstrate the homogeneous-inhomogeneous transition as well.

to the inhomogeneous and from the latter to the homogeneously broken phase. It is here employed to study the behavior of the Fourier coefficients close to the phase boundaries as well as in the bulk of the inhomogeneous phase.

In fig. 3.6a the squared absolute values of the zeroth (homogeneous) and first (LO) order Fourier coefficients are given for the indicated $\bar{h} \in [-0.3, 0]$. As far as the numerical resolution admits such a conclusion, the transition from the normal to the inhomogeneous phase is of second order, while the inhomogeneous-homogeneous one exhibits a significant jump and appears to be of first order. Furthermore, in the FFLO phase, only uneven Fourier coefficients are found to be finite up to numerical noise.

The computations underlying fig. 3.6 have been carried out with $j_{\max} = 2$ for eq. (3.6) and $l_{q,\max} = 5$ for the Fourier series. In fig. 3.6b, the ratios of higher order Fourier coefficients are plotted. Whereas a low order expansion appears to be a reasonable choice close to the normal phase boundary, higher order components become increasingly important inside the bulk of the inhomogeneous phase. This is not too different to the situation for the vertex expansion. The non-smooth behavior of the $\alpha_{l_q \geq 1}$ coefficients[3] close to the FFLO-homogeneous transition may therefore be caused either by to low $j_{\max}$ or $l_{q,\max}$ or a combination of both. Computations up to order $j_{\max} = 4$ in the vertex expansion do not yield conclusive answers either. Even higher order calculations can be expected to eventually become reliable but were deemed too costly. The question for the nature and exact location of the homogeneous-inhomogeneous transition must therefore be left open in this work.

Last but not least, it should be noted that the higher order Fourier coefficients do not grow uniformly even in the vicinity of the second order transition, where the low order expansions should still be reliable. This can be seen from the curved profiles and the crossing of the two ratios in fig. 3.6b. Rebuilding the spatial dependence of the order parameter from this corresponds to change of its functional shape when penetrating into the bulk of the inhomogeneous phase. Such a result is very much in accordance with what has been found for the relativistic Gross-Neveu model presented in sec. 1.2.2 above, see, e.g., [97]. There, a complicated kink-antikink structure becomes more and more cosine-like towards the phase boundary which corresponds to a disproportionate drop of higher order coefficients just as observed in fig. 3.6b.

The exact FF-solution: benchmark for the combined expansions The ultimate benchmark of the quality of a chosen truncation can only be provided by an exact solution. For the Gross-Neveu case, where such a solution is available (see sec. 1.2.2 and references therein), an expansion scheme corresponding to the one applied here does indeed yield the correct inhomogeneous to normal phase transition as well as

---

[3] Note that the α_0 values in the homogeneous phase are not taken from the vertex expansion but from a minimization of the exact eq. 3.1.

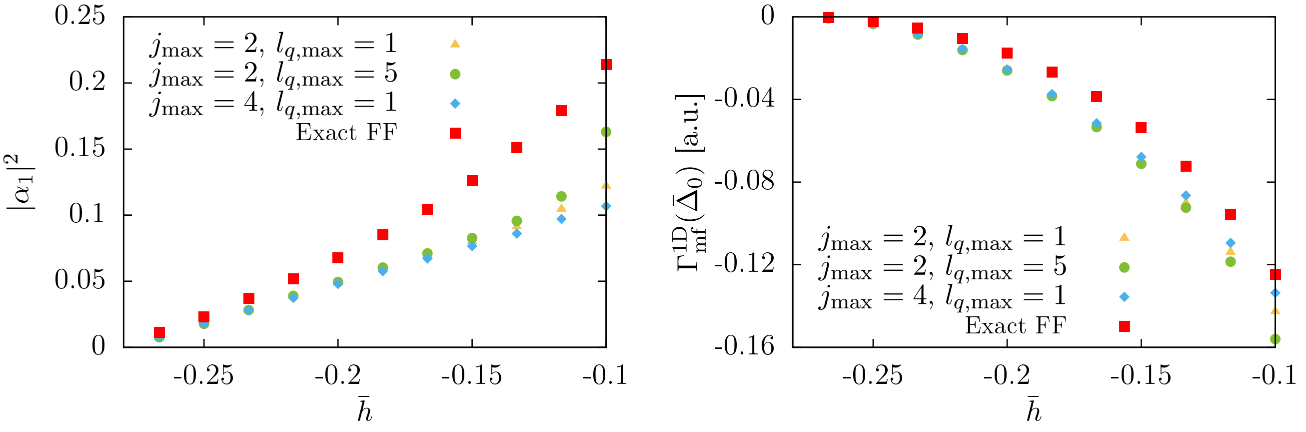

(a) (b)

Figure 3.7: Comparison of $|\alpha_1|^2$ (a) and the value of the mean-field effective action (b) for different truncations with the exact FF solution inside the inhomogeneous phase. $\bar T = 0.25$ and $\bar m = 0.5$ as in fig. 3.6b above.

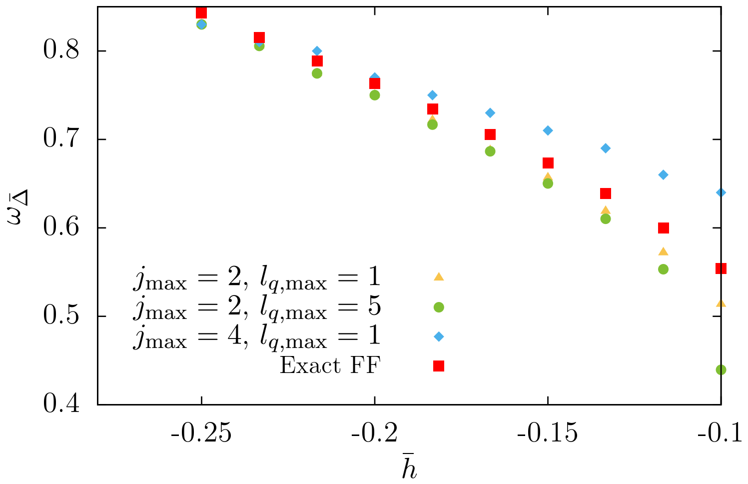

Figure 3.8: Characteristic frequency $\omega_{\bar\Delta}$ for different truncations and the exact FF solution. $\bar T = 0.25$ and $\bar m = 0.5$ as in fig. 3.6b above.

the dependence of the Gross-Neveu analog of the characteristic frequency $\omega_{\bar\Delta}$ on the chemical potential within numerical errors.

As no exact analytic solution is known for the 1D ultracold Fermi gas, such a comparison cannot be made here. There is, however, a way to get at least an impression of the relative errors introduced by the Fourier and Vertex expansions, respectively. For a single-plane-wave Fulde-Ferrell (FF) ansatz $\bar\Delta(x) = \alpha_1 e^{i\omega_{\bar\Delta}x}$ [79], the $\omega_{\bar\Delta}$ dependence of the Yukawa-type terms like in eq. (3.2) may be absorbed completely into the kinetic term of the interaction by a shift of the integration momentum. This allows again for an exact diagonalization, yielding

$$\frac{1}{\beta L}\Gamma^{\mathrm{1D,FF}}_{\mathrm{mf}} = \frac{\alpha_1^2}{g_\delta^{\mathrm{1D}}} - \frac{1}{\beta}\int_{\mathbf{p}}\sum_{\sigma=\pm1}\ln\left[1+e^{-\beta\left[\sigma\left(\bar m(p+\omega_{\bar\Delta}/2)^2-p\omega_{\bar\Delta}-h\right)+\sqrt{(p^2+\omega_{\bar\Delta}^2/4-\bar m p\omega_{\bar\Delta}-\mu)^2+\alpha_1^2}\right]}\right]. \tag{3.12}$$

Eq. (3.12) can be understood to be of infinite order in the vertex expansion but, loosely speaking, even less than first order in terms of Fourier cosine coefficients. It does indeed reproduce the location of the normal to inhomogeneous transition presented in fig. 3.4 above. In the bulk of the phase, however, differences are more subtle.

From fig. 3.7, it is apparent that the interplay of vertex and Fourier expansions is nontrivial. For fixed $j_{\max} = 2$, an increase of $l_{q,\max}$ improves the solution as expected: The ground state energy in the bulk of the inhomogeneous phase is lowered (fig 3.7b). However, comparing to higher orders in the vertex expansion which should be more accurate at fixed $l_{q,\mathrm{max}}$, the absolute ground state energy appears to have been overestimated in the low order $j_{\mathrm{max}} = 2$ case which is now corrected for, cf. the $j_{\mathrm{max}} = 4$ data in fig. 3.7 (blue diamonds). This is substantiated by the even higher values for the exact FF solution. As the latter is of lowest possible order in a general Fourier expansion, even the $l_{q,\mathrm{max}} = 1$ results from the vertex expansion can be expected to be more accurate in this respect.

Considering the inhomogeneous fermion gap in fig. 3.7a, it comes as no surprise that the vertex expansion tends to underestimate its value, cf. also fig. 3.5a

Finally, the characteristic frequency $\omega_{\bar{\Delta}}$ is depicted in fig. 3.8. The results coming from vertex expansion and FF ansatz are compatible, but it is not possible at this stage to decide which one can be considered the best approximation to the true ground state or which type of expansion dominates the overall convergence behavior.

In conclusion it can be said that the interplay of vertex and Fourier expansions is rather involved. Given the mathematical considerations, convergence may be expected. In practice and given a finite amount of computational resources, it is not easy to decide which truncation should be extended how far beyond the absolute minimum number of contributions needed to obtain nontrivial results. The latter is already sufficient to reliably determine the location of transitions from normal to symmetry broken phases. Inside the bulk phases, even orders of the vertex expansion are preferable, as they do not exhibit the instability of uneven orders, cf. fig. 3.5b. However, higher orders of both the vertex as well as the Fourier expansions become increasingly important as the transition to the homogeneous superfluid is approached. Although the treatment of high order contributions quickly becomes involved numerically, the expansion scheme presented in this section constitutes a conceptually straightforward, systematic method to characterize the physics of inhomogeneous phases.

Most importantly, the results from the vertex expansion show that the simple FF ansatz is sufficient to reproduce the inhomogeneous-to-normal phase boundaries for the one-dimensional ultracold Fermi gas. This statement is based not only on the numerical coincidence of phase transition lines from both methods, but in particular on the disproportionate drop of higher order Fourier coefficients depicted in fig. 3.6b. The exploration of convergence properties in this section thus not only serves a closer characterization of the vertex expansion technique but also substantiates the versatility of the far simpler FF ansatz approach.

3.2 Finite momentum Cooper pairs

As the positions of the second order phase boundary manifolds between symmetry broken and unbroken phases have been found to be stable and not influenced by artifacts of the chosen truncation, it is worthwhile to discuss the findings depicted in fig. 3.4 in somewhat more detail.

In sec. 2.2.2 it had already been found for the three-dimensional case, that the occurrence of a homogeneous condensate is centered around the line of equal spin and mass imbalance, see fig. 2.5. This is very similar to what can be observed in fig. 3.4 as well. Considering the definition of the absolute values of the Fermi momenta for the two species,

$$k_{\mathrm{F}}^{\uparrow,\downarrow} = \sqrt{2m_{\uparrow,\downarrow}\mu_{\uparrow,\downarrow}} = \sqrt{\mu}\sqrt{\frac{1 \pm \bar{h}}{1 \pm \bar{m}}}\,, \tag{3.13}$$

which are independent of spatial dimensionality, the following explanation seems intuitive (see, e.g., [111]). At the respective Fermi surfaces or in their close vicinity, there are plenty of unoccupied states available for scattering processes. The energetic cost of occupying such a state is, by definition of “Fermi surface”, minimal. It is therefore natural to expect pair formation to take place predominantly in this region of phase space. For equal imbalances, this situation is symbolically depicted in fig. 3.9a[4]. It is known from BCS theory [11,172] that pair formation is energetically most favorable for fermions with opposite momenta of equal magnitude, which can also be seen from, e.g., equation (2.20) when homogeneous condensation is expected. The newly formed pair can obviously not have a finite center of mass momentum. A condensate of such pairs does therefore not introduce a new momentum scale such as $\omega_{\bar{\Delta}}$ - it is homogeneous.

For general imbalances, the Fermi surfaces do not match anymore as depicted in fig. 3.9b. The requirement of pairing still taking place at the Fermi surfaces now introduces a net center of mass momentum which

---

[4] Note that the Fermi surface in 1D consists of two points only and is a sphere in 3D.

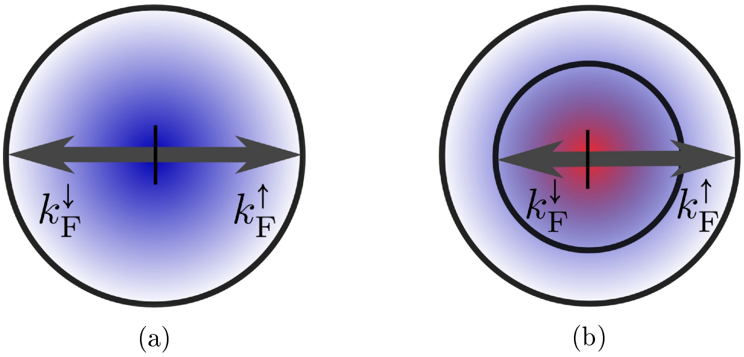

(a) (b)

Figure 3.9: Fermi momenta for balanced or counterbalanced $\left(\bar{h} = \bar{m}\right)$ (a) and imbalanced (b) fermionic mixtures.

can be expected to transfer its characteristics to a condensate that is eventually formed from those pairs. An inhomogeneity then occurs whose characteristic frequency $\omega_{\bar{\Delta}}$ should somehow be related to the center of mass momenta of its constitutive pairs.

However, this simple picture would imply that inhomogeneous phases should occur as soon as the line of equal imbalances is left. This is obviously not the case, see fig. 3.4. An intuitive understanding of the many-body phase structure is further obscured by the back-bending "hook"-like shape of the inhomogeneous phase at high $\bar{m}$ and $\bar{T} < 0.25$, see fig 3.4a. Contrary to the finding at pure spin imbalance (see also [173] and [174]) of a destabilization of the condensate towards large $|\bar{h}|$, mass imbalance appears to have the opposite effect in this region although the mismatch of the Fermi surfaces is still enhanced. The principal goal of this chapter will be to establish a more elaborate connection between pairing and the characteristics of condensates, which is capable of explaining the features presented above at least on a qualitative, partially even quantitative level.

3.2.1 Bound state formation in the presence of Fermi seas

One of the cornerstones of BCS theory is the seminal work of L. N. Cooper [172] in which for the first time the formation of "Cooper" pairs of electrons is identified as the cause of the superconducting energy gap, see, e.g., [78] for a review. Besides the assumption of an attractive force between electrons of opposite spin in the vicinity of the Fermi surface, the presence of the latter turned out to be of crucial importance for the existence and characteristics of these bound states. In particular, it could be shown that pairs with vanishing center of mass momentum are most deeply bound and therefore preferred.

Pairing and Schrödinger equation The general idea of Cooper can be adapted to the case of strongly interacting Fermi gases rather straightforwardly. There are, however, some conceptual differences to the solid state context for which this theory was initially devised:

- The attractive force between the electron species in an actual BCS superconductor is induced by phonon interactions see, e.g., [175] for a review. This energetically limits it to the vicinity of the Fermi surface. For a theory of ultracold Fermi gases, there is in principle no energy dependence of the interaction as long as the model assumptions (see sec. 1.1.1) are not violated. In the following, the few-body analog of the model developed in secs. 1.1.2 and 1.2.1 will be employed. This implies in particular a two-body potential $V_\delta = g_\delta^{1\mathrm{D}}(x_\uparrow - x_\downarrow)$ without finite momentum cutoff and $g_\delta^{1\mathrm{D}} = -a_{1\mathrm{D}}^{-1}$.
- The linearization of the non-relativistic dispersion relation employed in [172] is based on the assumption that the contribution of excitations far away from the Fermi surface is negligible [78]. While such an approximation may be reasonable in the weakly coupled BCS regime and with an energy cutoff for the interaction, it is not necessarily true anymore for the situation of the strongly coupled Fermi gas. The full dispersion relations $|\epsilon_{\uparrow,\downarrow} - \epsilon_F^{\uparrow,\downarrow}|$ will therefore be employed.
- Imbalance has to be accounted for by a modification of these dispersion relations. This can be achieved by making use of eq. (3.13).

Putting these ingredients together, the Schrödinger equation for the modified Cooper problem can be written down,

$$\left[\sum_{\sigma=\uparrow,\downarrow}\frac{\left|-\partial_{x_\sigma}^2 - k_{\mathrm{F}}^{\sigma 2}\right|}{2m_\sigma} - g_\delta^{\mathrm{1D}}\delta(x_\uparrow - x_\downarrow) + E_{\mathrm{B}}\right]\Psi(x_\uparrow, x_\downarrow) = 0\,, \tag{3.14}$$

where $\Psi(x_\uparrow, x_\downarrow)$ is the two-body wave function and $E_{\mathrm{B}} = \epsilon_{\mathrm{F}}^{\uparrow} + \epsilon_{\mathrm{F}}^{\downarrow} - E$ is the energy eigenvalue measured with respect to the species' Fermi energies. As $E = \epsilon_{\mathrm{F}}^{\uparrow} + \epsilon_{\mathrm{F}}^{\downarrow}$ in the non-interacting case, positive E_{B} signals a gain of energy and thus the formation of a bound state.[5]

Before solving equation (3.14), a few comments as to its interpretation and validity are in order. One of the crucial approximations underlying this "artificial" two-body problem is the notion of *inert* or "quiescent" [172] Fermi seas. The concept of a Fermi sea itself originates from the maximum occupation in the free gas at vanishing temperature. "Blurred" by finite temperature and/or interactions, there is no such a thing as a completely (un)occupied region of phase space above or below a well-defined Fermi surface anymore. Furthermore, the two fermions described by eq. (3.14) which could be imagined to be injected into an existing two-component ensemble, are in reality going to interact with the constituents of this ensemble. The existence of even an arbitrarily blurred version of a Fermi sea is therefore a genuine many-body phenomenon and can never be captured in its whole by an equation of type (3.14) which does not allow for these interactions. For example, the *Fermi polaron* problem describes a single spin-down (w.l.o.g.) impurity immersed in a sea of spin-up fermions as having negative chemical potential [177,178]. This results in a spin imbalance $\bar{h} > 1$. It is immediately clear from eq. (3.13), that this can never occur within the present framework as it would lead to imaginary magnitudes for either one of the Fermi momenta.

When comparing results obtained from equations like (3.14) to actual many-body calculations, the following conditions should therefore be kept in mind to retain maximal correspondence: $|\bar{h}|$ must not be greater than one on the many-body side and the Fermi surfaces should be as sharp as possible. The latter can be achieved by focusing on the low-$\bar{T}$ regime. Furthermore, configurations are to be preferred, where the number of pairs that is formed is finite but small. Finally, pairing effects should dominate the physics rather than dressing, which would be the case for the above mentioned polaron.

The two-body "phase diagram" The non-separable structure of the kinetic term in the Schrödinger operator does not allow for an explicit solution of equation (3.14). However, the delta shape of the interaction still makes a direct integration possible. Introducing momentum space with normalized relative $\bar{p} = (k_\uparrow - k_\downarrow)/(2\sqrt{\mu})$ and center-of-mass coordinates $\bar{P} = (k_\uparrow + k_\downarrow)/\sqrt{\mu}$, the wave function Ψ can be canceled out and an implicit equation for the now momentum-dependent normalized binding energy $\bar{E}_{\mathrm{B}}(\bar{P})$ results:

$$\frac{2\pi\sqrt{\mu}}{g_\delta^{\mathrm{1D}}} = \int \frac{\mathrm{d}\bar{p}}{\epsilon_\uparrow\left(\frac{\bar{P}}{2} + \bar{p}\right) + \epsilon_\downarrow\left(\frac{\bar{P}}{2} - \bar{p}\right) + \bar{E}_{\mathrm{B}}(\bar{P})}\,. \tag{3.15}$$

Here,

$$\epsilon_{\uparrow,\downarrow}(k_{\uparrow,\downarrow}) = \left|(1 \pm \bar{m})\left(k_{\uparrow,\downarrow}^2 - k_{\mathrm{F}}^{\uparrow,\downarrow 2}\right)\right| \tag{3.16}$$

represent the respective dispersion relations in momentum space. Fixing the interaction strength to the value introduced on p. 32, $a_{\mathrm{1D}}^{\mathrm{theo}}\sqrt{\mu} = k_{\mathrm{F}} a_{\mathrm{1D}}^{\mathrm{theo}} = 1/(\sqrt{2}\pi)$ and providing trial values for $\bar{E}_{\mathrm{B}}$, eq. (3.15) can be solved numerically for given $\bar{P}$. If bound states are found, the center of mass momentum $\bar{P}$ for which $\bar{E}_{\mathrm{B}}$ becomes maximal can be identified. Following this procedure for any admissible imbalance, the results are mapped to the $\bar{h} - \bar{m}$ plane in fig. 3.10 as for the many-body phase diagrams above.

As expected, the binding energy reaches its overall maximum along the line of $\bar{h} = \bar{m}$ for vanishing center of mass momentum, see fig. 3.10a. However, the region of equal momentum pairing is extended up to a finite distance to both sides of this line as it is analogously found by the many-body calculation. It comes with no surprise, that the shapes of the $\bar{T} = 0$ homogeneous superfluid region in fig. 3.4a and of the $\bar{P} = 0$ pairing domain in fig. 3.10b do not match exactly. Deep inside the superfluid region where the large

---

[5] It should be noted that Cooper pairs are sometimes not referred to as actual bound states in the literature. This is due to their finite lifetime and localization in momentum rather than position space as opposed to the molecules formed on the BEC side of the 3D crossover, see, e.g., [176] for a detailed discussion. In this work, the term "bound state" will be used for any situation where a finite binding energy occurs.

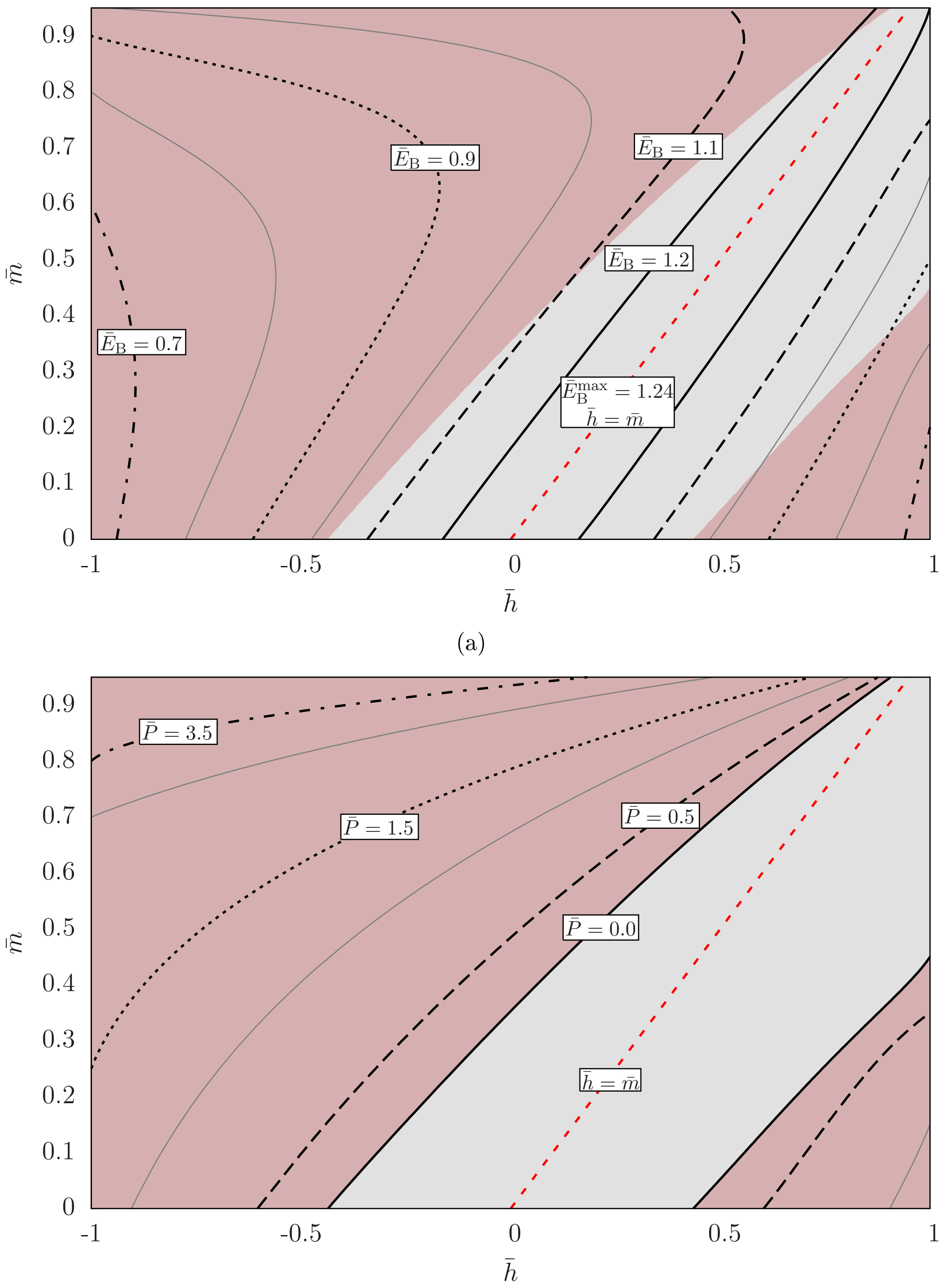

(a)

(b)

Figure 3.10: Results for the maximal binding energy $\bar{E}_{\mathrm{B}}$ (a) and momentum $\bar{P}$ for which this value of $\bar{E}_{\mathrm{B}}$ is reached. The shading distinguishes domains where $\bar{P} = 0$ (light, gray shading) from those with $\bar{P} \neq 0$ (dark, red shading).

fermion gap leads to a sizable modification of the respective dispersion relations, the coincidence cannot be expected to be more than qualitative as discussed above. The central insight here is, that even for mismatched Fermi surfaces, it can still be energetically favorable to form bound states with zero center of mass momentum. Unlike in the BCS case, pairing is obviously not bound to take place in the immediate vicinity of both Fermi surfaces anymore.

For fixed negative $\bar{h}$ and increasing $\bar{m}$, the center of mass momentum of pairs increases monotonously as soon as the region of finite $\bar{P}$ has been entered. This is rather intuitive, as the mismatch $|k_{\mathrm{F}}^{\uparrow} - k_{\mathrm{F}}^{\downarrow}|$ is bound to increase as well. One might expect that the binding energy $\bar{E}_{\mathrm{B}}$ decreases along the same path,

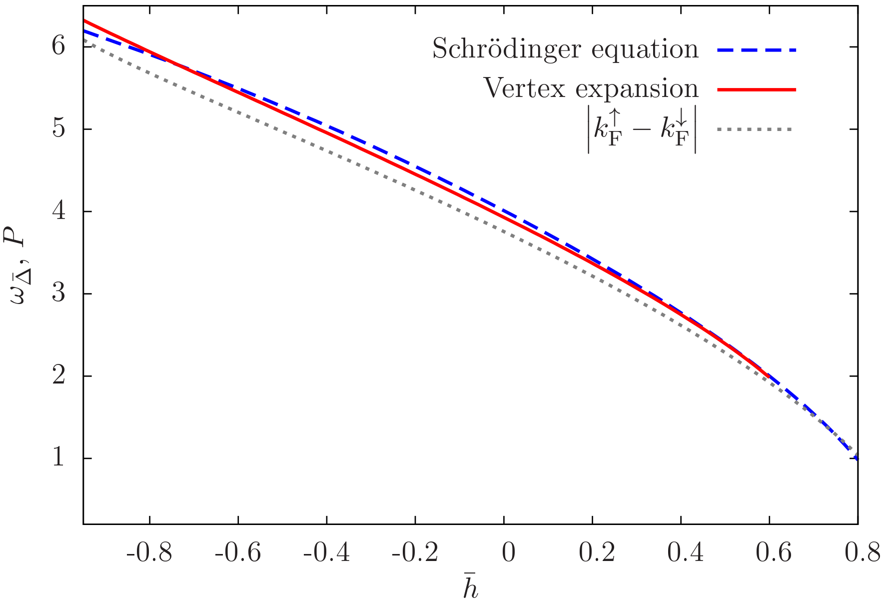

Figure 3.11: Comparing the characteristic frequency $\omega_{\bar\Delta}$ found by the vertex expansion (red, solid line) with predictions from the Schrödinger equation (blue, dashed line) and an estimate from the Fermi momenta (gray, dotted line). The red (solid) line ends close to the transition to the homogeneous superfluid phase, where the expansion becomes unreliable. The physical parameters for the many-body results are $\bar m = 0.95$ and $\bar T = 0.17$.

since the growing mismatch must be compensated for in some way. However, this is only true up to some critical $\bar m_{\text{hook}}(\bar h)$ above which the binding energy increases again. This results in a hook-like structure of the energy isolines very similar to the one for the phase boundaries observed in fig. 3.4. Indeed, the reason for this similarity can be identified rather straightforwardly: Pairs that are more deeply bound are also more stable with respect to, e.g., thermal fluctuations. As more thermal energy may be absorbed into the bound states themselves before their destruction, a condensate should be stabilized as well.

At this point, it can safely be concluded, that specific features of the many-body phase diagram like the finite "transversal" extent of the homogeneous superfluid as well as the seemingly counterintuitive hook-like structure can be traced back to the few-body physics of pairing itself. Moreover, a closer inspection of the energy manifolds given by the sum over the dispersion relations in eq. (3.16) reveals a partial delocalization of the pair wave function. This suggests that the notion of pairs with a single, fixed center of mass momentum may have to be abandoned for an even more accurate treatment. This is particularly intriguing, as the many-body inhomogeneous phase is characterized by a whole spectrum of momentum modes, see sec. 3.1.2 above. The latter rather speculative point is one instance, where explicit connections between the few- and many-body perspective are suggestive. An exploration of related findings will be undertaken in the next section.

3.2.2 From two- to many-body physics

The initial motivation for considering the Schrödinger equation (3.14) came from the seemingly oversimplified picture of FFLO pairing underlying fig. 3.9. While the two-body approach is indeed capable of explaining the finite extent of the homogeneous superfluid phase, it should also be able to yield better predictions for the characteristic frequency inside the FFLO phase than the estimate $\left|k_F^\uparrow - k_F^\downarrow\right|$ does. As discussed above, such a quantitative prediction from eq. (3.14) is expected to hold best in a region where only few pairs can be formed. In the regime of large mass imbalance and negative spin imbalance, this condition should be fulfilled best as the heavy majority species vastly outnumbers the light minority.

Figure 3.11 shows the situation for $\bar m = 0.95$ and $\bar T = 0.17$ for the many-body results. The latter have been obtained by a minimal vertex expansion with $j_{\max} = 2$, $l_{q,\max} = 1$ and are drawn as far as to the vicinity of the transition to the homogeneous superfluid phase. As expected, the Schrödinger equation does indeed yield a quantitatively reliable prediction for the characteristic frequency $\omega_{\bar\Delta}$, whereas $\left|k_F^\uparrow - k_F^\downarrow\right|$ is somewhat off. This not only corroborates the general insight provided by the two-body perspective. It

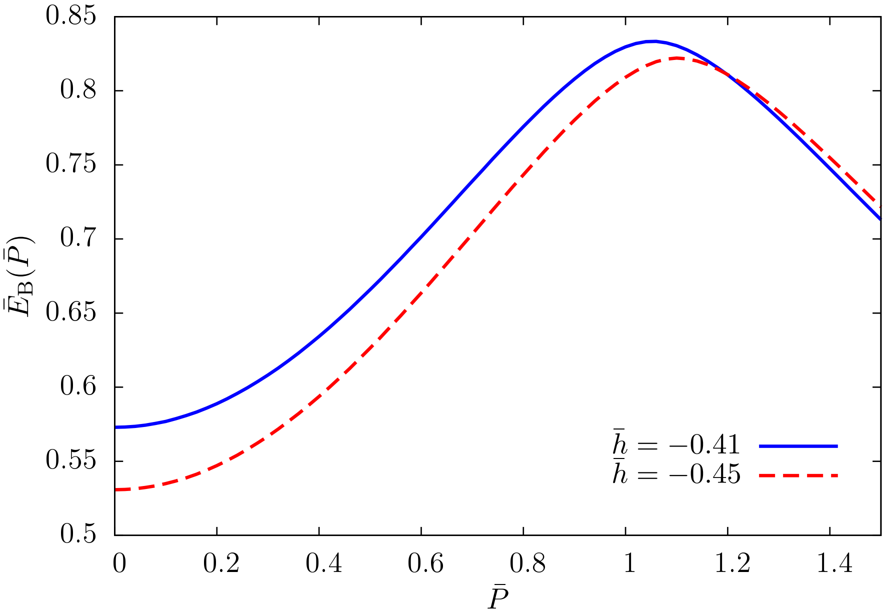

Figure 3.12: Two-body binding energies for different $\bar{h}$ enclosing a many-body phase transition for fixed $\bar{m} = 0.5$ and $\bar{T} = 0.4$. The blue (solid) line belongs to the homogeneous superfluid region, the red (dashed) one to the FFLO phase.

is also very useful for the numerical identification of inhomogeneous phases, since the parameter space to be searched may be diminished substantially by a good initial guess for $\omega_{\bar{\Delta}}$.

The precise location of the transition between homogeneous and inhomogeneous symmetry broken phases is not only difficult to locate within the many-body framework. Also the two-body prediction does not help on a quantitative level in this case. The discrepancy between the extent of the gray (light) shaded regions in figs. 3.4a and 3.10 therefore indicates the importance of many-body effects in this region which cannot be reproduced by eq. (3.14). In the following, the exemplary configuration $\bar{m} = 0.5$, $\bar{T} = 0.4$, $\bar{h} \in [-0.45, -0.41]$ enclosing such a phase transition will be discussed in order to obtain some insight into the nature of these effects.

For the two values of $\bar{h}$ representative for homogeneous superfluid ($\bar{h} = -0.41$) or FFLO ($\bar{h} = -0.45$) phases, respectively, the two-body binding energy can be calculated as shown in fig. 3.12. In both cases, pairing with finite center-of-mass momentum is clearly preferred, with little variation for the optimal momentum: $\bar{P}_{-0.41} = 1.06$ and $\bar{P}_{-0.45} = 1.10$. However, the situation is quite different for the many-body calculation. While a phase transition is found also with the vertex expansion, the exact “FF” solution eq. (3.12) is employed here to avoid artifacts of finite j_max.

Clearly, the mean-field effective action depicted in fig. 3.13a is minimized for vanishing frequency when $\bar{h} = -0.41$, whereas $\omega_{\bar{\Delta}} = 0.62$ for $\bar{h} = -0.45$, indicating a phase transition taking place between those two values for the spin imbalance. Furthermore, even in the FFLO phase the prediction for the frequency is off by almost a factor of two compared to the actual finding. While the value for $\omega_{\bar{\Delta}}$ cannot be determined with high precision close to this type of transition by the many-body methods employed here (see fig. 3.8 and associated discussions), the observation of a deviation this large combined with the failed prediction of a phase transition itself clearly points to the importance of many-body correlations.

Unfortunately, it is far from obvious how to bring the latter into a quantifiable form as required for a deep understanding. At this point, only a qualitative argument can be given. In fig. 3.13b the squared absolute fermion gap parameters determining the respective values of $\Gamma^{1\mathrm{D}}_\mathrm{mf}$ in fig. 3.13a are provided. The gap appears to be a monotonously decreasing function of $\omega_{\bar{\Delta}}$. The values actually assumed in the mean-field solution are therefore quite different for the two representative spin imbalances: $|\bar{\Delta}_0|^2_{-0.41} = 0.34$ and $|\bar{\Delta}_0|^2_{-0.45} = 0.29$.

It can be shown (see, e.g., [179]) that the number of Cooper pairs N_Coop in the condensate is $N_\mathrm{Coop} \sim |\bar{\Delta}_0|^2$. The transition between the regions of homogeneous and inhomogeneous condensation thus appears to be determined by a competition of two mechanisms. Energy may be gained by pair formation, but also by condensation of those pairs or, in other words, opening up a gap in the fermionic density of states.

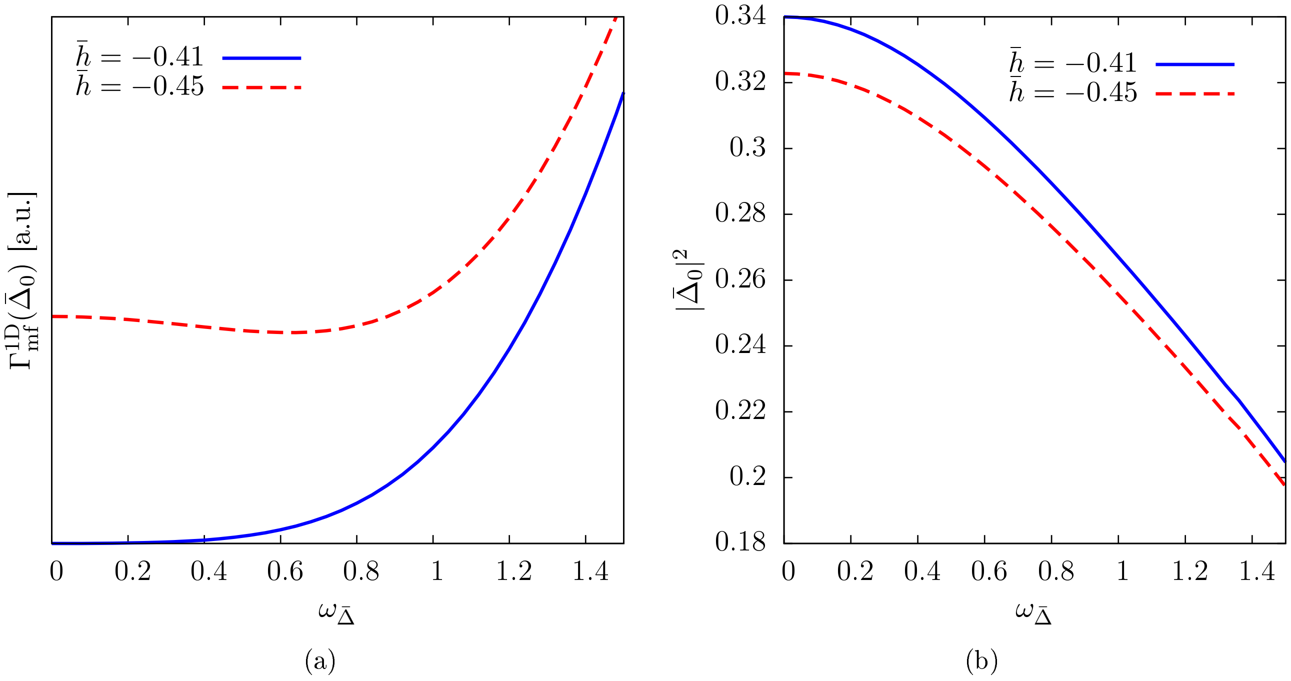

(a) (b)

Figure 3.13: Evidence for a transition between homogeneous (blue, solid line) and inhomogeneous (red, dashed line) superfluidity for $\bar{h} \in [-0.45, -0.41]$ with $\bar{m} = 0.5$ and $\bar{T} = 0.3$. While the mean-field effective action develops a global minimum for non-vanishing $\omega_{\bar{\Delta}}$ (a), the fermion gap remains a monotonously decreasing function (b).

While the binding energy of pairs with vanishing center-of-mass momentum is clearly not preferred for the configurations considered here (see fig. 3.12), the larger gap for $\omega_{\bar{\Delta}} = 0$ indicates a more favorable situation for condensation. The eventually assumed ground state thus appears to be an energetic compromise between optimal pairing and condensation.

A more quantitative description of these mechanisms is beyond the scope of the present work. However, there is still a major conclusion that can be drawn from this section: The underlying two-body physics of pair formation is of great importance for the understanding of the many-body phase diagram. Qualitative and even some quantitative features can be explained. No (truncated) ansatz for an inhomogeneous order parameter is involved in the solution of the Schrödinger equation. In this sense, the two-body argument is rather general and may be used to distinguish between artifacts of such an ansatz in many-body calculations and actual physical phenomena. Most importantly, there is no reason why the application of this method should be limited to the one-dimensional case. This is particularly relevant, since a direct interpretation of the results in this chapter in terms of experimental observables is at the very least not straightforward as discussed in sec. 3.1 above. However, in chap. 4 below, the three-dimensional case also beyond mean field will be discussed and the two-body perspective will be of great use again.

3.3 Inhomogeneous phases and relativistic fermions

It is a generally valid statement that the precise characterization of inhomogeneous ground states is a complex and costly issue. This is not only true for the vertex expansion technique presented above, but for any (semi-)analytic or numeric approach referred to so far. Methods to reliably determine at least some properties of inhomogeneous phases in a more simple manner are therefore highly inviting. In this sense, observations such as the exact reproduction of inhomogeneous phase boundaries by the FF effective action (3.12) and the disproportionate drop of higher order Fourier coefficients in fig. 3.6b may become very useful. These findings support the hope for the suitability of the simple plane-wave calculation also for ultracold gases in higher dimensions, which will be made use of explicitly in chap. 4.

Although the exact solution of the (1+1)-dimensional Gross-Neveu model can be shown to reduce to a cosine function at the transition to the normal phase [97], this does no mean that corresponding mean-field effective actions in relativistic models with spontaneous chiral symmetry breaking (χSB) are as easy to compute as for ultracold gases with the FF ansatz. Even for the most simple plane wave ansatz[6] $\bar{\sigma}(x) = Me^{i2Qx}$, the partially bosonized version of the Gross-Neveu model's action (1.19) in momentum space reads as

$$\begin{aligned} S^{\mathrm{B,FF}}_{\mathrm{GN}} &= \int_0^\beta \mathrm{d}\tau \int \mathrm{d}x \left[\bar{\psi}\left(i\partial\!\!\!/ + i\bar{\sigma} + i\mu\gamma_0\right)\psi + \frac{1}{2\lambda^2}\bar{\sigma}^2 \right] \\ &= \frac{1}{2\lambda^2}\int_{\tau,\mathbf{x}} \bar{\sigma}^2 + \sum_n \int_{\mathbf{p}} \left[\bar{\psi}_n(p)\left(\omega_n\gamma_0 + p\gamma_1 + i\mu\gamma_0\right)\psi_n(p) + iM\bar{\psi}_n(p+2Q)\psi_n(p)\right]. \end{aligned} \tag{3.17}$$

Unlike the corresponding equation for the U(1) symmetric ultracold Fermi gas, it cannot be brought into a diagonal form straightforwardly. The eigenvalues of the second functional derivative of $S^{\mathrm{B,FF}}_{\mathrm{GN}}$ are not accessible analytically. This observation is generic in the sense that it holds true for purely chiral symmetry breaking condensates in any relativistic fermion model, including in particular Nambu-Jona-Lasinio (NJL) type models [180, 181],

$$\mathcal{L}_{\mathrm{NJL}} = \bar{\psi}(i\partial\!\!\!/ + i\mu\gamma_0) + \frac{\lambda^2}{2}\left[(\bar{\psi}\psi)^2 + (\bar{\psi}i\gamma_5\psi)^2\right], \tag{3.18}$$

see also sec. 3.3.2 below. The additional *pseudoscalar* interaction ~ $(\bar{\psi}i\gamma_5\psi)^2$ furnishes this model with a continuous U(1) chiral symmetry,

$$\bar{\psi} \to \bar{\psi}e^{i\gamma_5\theta}, \quad \psi \to e^{i\gamma_5\theta}\psi, \tag{3.19}$$

as opposed to the discrete one (1.20) in the Gross-Neveu case. Possible extensions employed to allow for a more direct phenomenological interpretation include in particular the introduction of isospin degrees of freedom [181] or some dependence on gauge physics [182].

Motivated by the structure of the interaction in the Lagrange density (3.18), another simple inhomogeneous ansatz can be devised [183]. The so-called "chiral spiral",

$$\phi = Me^{i\gamma_5 Qx} \sim \langle\bar{\psi}\psi\rangle\cos(Qx) + i\langle\bar{\psi}\gamma_5\psi\rangle\sin(Qx), \tag{3.20}$$

leads to a simple analytic solution for the mean-field effective action in analogy to the FF ansatz for ultracold fermions.

In the following this ansatz will not be used though. For the Gross-Neveu model, where the chiral symmetry is discrete, a finite pseudoscalar condensate does not correspond to a spontaneously broken symmetry of the microscopic action and does therefore not foster the search for the true ground state. In case of the NJL model, a finite expectation value $\langle\bar{\psi}\gamma_5\psi\rangle$ can be interpreted as a pion condensate. For homogeneous breaking of the chiral symmetry, the order parameter is indeed given by the sum $\langle\bar{\psi}\psi\rangle + i\langle\bar{\psi}\gamma_5\psi\rangle$ that can always be mapped onto a purely scalar (chiral) condensate by means of the transformation (3.19). This is desirable, as the chiral direction is preferred in nature due to the existence of finite quark masses m_q. The corresponding terms ~ $m_q\bar{\psi}\psi$ explicitly break the chiral symmetry and are therefore neglected in the *chiral limit* in the Lagrangian (3.18). However, if the chiral spiral ansatz is used, the scalar and pseudoscalar condensates have to be of the same size and cannot be transformed into each other anymore. As the pseudoscalar condensate breaks parity, which is not observed in nature (see, e.g., [184]), the phenomenology of the chiral spiral and purely scalar inhomogeneous condensates is a priori different.

In order to gain access to inhomogeneous χSB of scalar nature, one is therefore left with the FF ansatz or extensions thereof. As there is no straightforward analytical way to calculate the mean-field effective action in this case, the goal of this section is to develop an approximate procedure that is nevertheless capable of exactly localizing inhomogeneous phase boundaries at fairly low cost. The general idea as well as a proof of its correctness will be given in sec. 3.3.1 on the basis of the Gross-Neveu model. For further illustration, the method will then be applied to the Polyakov-loop extended NJL (PNJL) model [182] in sec. 3.3.2. The inclusion of the Polyakov loop constitutes an extension of the usual NJL model and is believed to capture some important aspects of gluon physics that are relevant for QCD phenomenology.

---

[6] The characteristic frequency/momentum of the inhomogeneity will be named Q in the relativistic setting for greater distinctiveness.

3.3.1 The fermion doubling trick for the Gross-Neveu model

Although the method presented in the following would also work for the FF ansatz,

$$-i\langle\bar{\psi}\psi\rangle = \bar{\sigma}(x) = M\cos(2Qx) = \frac{M}{2}\left(e^{2iQx} + e^{-2iQx}\right) \tag{3.21}$$

is chosen instead. This is motivated by the fact, that the inhomogeneity is indeed known to become cosine-shaped at the transition from the inhomogeneous to the normal phase in the Gross-Neveu model [97]. Furthermore, in the framework employed here, the cosine does not require any additional effort to be made. The Yukawa term in eq. (3.17) then receives a second contribution ~ $\bar{\psi}_n(p-2Q)\psi_n(p)$ and the corresponding microscopic action will be called $S_{\mathrm{B}}^{\mathrm{GN,cos}}$ from now on.

Formal diagonalization The aim is to arrive at a representation for $S_{\mathrm{B}}^{\mathrm{GN,cos}}$ that is diagonal in momentum space and can therefore be used to directly compute the mean-field effective action. Splitting up the kinetic term and conveniently shifting the integration momentum, the microscopic action can be rewritten as

$$\begin{aligned} S_{\mathrm{B}}^{\mathrm{GN,cos}} =& \frac{1}{2\lambda^2}\int_{\tau,\mathbf{x}} \bar{\sigma}^2 + \frac{1}{2}\sum_n \int_{\mathbf{p}} \left\{\bar{\psi}_n(p-Q)\gamma_0\left[\omega_n + \gamma_0\gamma_1(p-Q) + i\mu\right]\psi_n(p-Q) + iM\bar{\psi}_n(p+Q)\psi_n(p-Q)\right. \\ &\left. + \bar{\psi}_n(p+Q)\gamma_0\left[\omega_n + \gamma_0\gamma_1(p+Q) + i\mu\right]\psi_n(p+Q) + iM\bar{\psi}_n(p-Q)\psi_n(p+Q)\right\} && (3.22a) \\ =& \frac{1}{2\lambda^2}\int_{\tau,\mathbf{x}} \bar{\sigma}^2 + \frac{1}{2}\sum_n \int_{\mathbf{p}} \Psi_n^\dagger \Delta S_B^{(2)} \Psi_n\,. && (3.22b) \end{aligned}$$

Here, the artificial double spinor field

$$\Psi_n = \begin{pmatrix} \psi_n(p-Q) \\ \psi_n(p+Q) \end{pmatrix} \tag{3.23}$$

facilitates the formally momentum-diagonal representation of the action with

$$\Delta S_{\mathrm{B}}^{(2)} = \begin{pmatrix} P_+^{-1}(p-Q) & 0 & 0 & iM \\ 0 & P_-^{-1}(p-Q) & iM & 0 \\ 0 & iM & P_+^{-1}(p+Q) & 0 \\ iM & 0 & 0 & P_-^{-1}(p+Q) \end{pmatrix}, \tag{3.24}$$

and $P_\pm^{-1}(p+Q) = \omega_n + i\mu \pm (p+Q)$. The previously non-diagonal action has of course not become diagonal by a simple rewriting. In fact, Gaussian integration of the fermion fields cannot be performed in the space of the Ψ_n spinors directly, as its components are not independent of each other. Considering $\psi_n(p-Q)$ and $\psi_n(p+Q)$ as independent variables effectively comes up to dealing with a different theory with doubled number of fermion fields. For homogeneous order parameters, i.e. $Q = 0$, this does not make any difference, as (3.24) can be recast into a block diagonal form. For $Q \neq 0$, however, it is a priori not clear in which way the resulting effective action $\Gamma_{\mathrm{D}}^{\mathrm{GN,cos}}$ is related to the true $\Gamma_{\mathrm{mf}}^{\mathrm{GN,cos}}$ from which the phase structure of the GN model could be read off.

In the following, it will be shown that knowledge of $\Gamma_{\mathrm{D}}^{\mathrm{GN,cos}}$ is indeed sufficient to reliably determine (second order) transitions from symmetry broken to normal phases. The circumvention of the complicated evaluation of $\Gamma_{\mathrm{mf}}^{\mathrm{GN,cos}}$ by means of the artificial doubling of fields justifies the term *fermion doubling trick* for this procedure. For an explanation of the relation between $\Gamma_{\mathrm{D}}^{\mathrm{GN,cos}}$ and $\Gamma_{\mathrm{mf}}^{\mathrm{GN,cos}}$ on the level of the path integral, see app. C.

Mean-field effective action from fermion doubling The first step towards establishing the method consists in actually computing and properly renormalizing $\Gamma_{\mathrm{D}}^{\mathrm{GN,cos}}$. Along the lines of sec. 2.2.1, it is given by

$$\frac{1}{\beta L}\Gamma_{\mathrm{D}}^{\mathrm{GN,cos}} = \lim_{N_{\mathrm{f}}\to\infty}\left[\frac{1}{2\lambda^2\beta N_{\mathrm{f}} L}\int_{\tau,\mathbf{x}} \bar{\sigma}^2 - \frac{1}{2\beta N_{\mathrm{f}} L}\mathrm{Tr}\ln \Delta S_{\mathrm{B}}^{(2)}\right] \equiv \frac{M^2 \mathcal{I}}{2\lambda_{\mathrm{mf}}^2} - \Delta U\,. \tag{3.25}$$

Here, the number of fermion flavors N_{f} is sent to infinity while keeping the product $N_{\mathrm{f}}\lambda^2 \equiv \lambda_{\mathrm{mf}}^2$ fixed. This is also known as the *'t Hooft limit* [185]. As discussed in sec. 2.2.1 above, mean-field theory becomes

exact in this limit.
The first term of the RHS of eq. (3.25) requires the integration of the squared order parameter over the full spatial extent L of the system. In the limit $L \to \infty$, the oscillations of the order parameter are completely averaged and the integral $\mathcal{I}$ becomes a uniquely defined quantity also for finite Q,

$$\mathcal{I} = \lim_{L\to\infty} \frac{1}{L} \int_{-L/2}^{L/2} \mathrm{d}x \cos^2(2Qx) = \begin{cases} 1 \text{ for } Q = 0 \\ \frac{1}{2} \text{ for } Q \neq 0 \end{cases}. \tag{3.26}$$

Whenever N_f or L occur in the following, their associated limits are tacitly assumed to be considered implicit.
The eigenvalues of the matrix (3.24) can straightforwardly be computed and are given by

$$E_1^\pm = \omega_n + i(\mu \pm E_M - Q) \text{ and } E_2^\pm = \omega_n + i(\mu \pm E_M + Q), \tag{3.27}$$

with $E_M = \sqrt{p^2 + M^2}$. Performing the sum over the Matsubara frequencies ω_n, the second term in eq. (3.25) can be computed as well,

$$\Delta U = \frac{1}{2\beta} \int_\mathbf{p} \left\{ 2\beta(E_M + \mu) + \sum_{\alpha_1,\alpha_2=\pm1} \ln\left(1 + e^{-\beta(E_M + \alpha_1 Q - \alpha_2 \mu)}\right) \right\}. \tag{3.28}$$

While the second (thermal) contribution is finite, the first (vacuum) term $\sim (E_M + \mu)$ diverges. The mean-field effective action must therefore be renormalized which is largely done in analogy to the procedure presented e.g. in ref. [71]. The only modification accounts for the presence of inhomogeneities, i.e. finite Q.
In order to fix the value of the coupling λ_mf^2, the *vacuum limit* $T, \mu \to 0$ of eq. (3.25) is considered:

$$\lim_{T,\mu\to0} \frac{1}{\beta L} \Gamma_\mathrm{D}^\mathrm{GN,cos} = \frac{M^2 \mathcal{I}}{2\lambda_\mathrm{mf}^2} - \frac{M^2}{4\pi} + \frac{M^2}{2\pi} \ln\left(\frac{M}{\Lambda}\right), \tag{3.29}$$

where Λ is an ultraviolet cutoff for the momentum integration. An irrelevant constant that does not depend on M or Q has been dropped here for convenience. Imposing the mean field condition

$$\frac{\partial}{\partial M} \lim_{T,\mu\to0} \frac{1}{\beta L} \Gamma_\mathrm{D}^\mathrm{GN,cos} \bigg|_{M=M_0} = \frac{M_0 \mathcal{I}}{\lambda_\mathrm{mf}^2} + \frac{M_0}{\pi} \ln\left(\frac{M_0}{\Lambda}\right) \overset{!}{=} 0, \tag{3.30}$$

and fixing the value of the fermion gap to some $M = M_0$, the desired relation is obtained:

$$\frac{\pi \mathcal{I}}{\lambda_\mathrm{mf}^2} = -\ln\left(\frac{M_0}{\Lambda}\right). \tag{3.31}$$

Plugging the latter into eq. (3.25) renders the mean-field effective potential finite and cutoff-independent. The phase diagram may then be computed via the usual minimization procedure for $\Gamma_\mathrm{D}^\mathrm{GN,cos}$. It should furthermore be noted that continuity in Q which may have appeared to be violated by the integral (3.26) is reinstated by the renormalization procedure as it should be. This implies in particular that the vacuum gap M_0 remains the only input parameter of the theory even if finite Q is considered. In other words, the vacuum gap is considered to be Q-independent and the values for Q that are found to minimize $\Gamma_\mathrm{D}^\mathrm{GN,cos}$ for configurations away from the vacuum limit are predictions of the theory.

Implications for the phase diagram As expected, the renormalized version of eq. (3.25) coincides with the well-known expression [70] for the $Q = 0$ case. The homogeneous phase diagram can therefore be reproduced exactly. The approximate nature of the fermion doubling trick comes into effect only for $Q \neq 0$, where $\Gamma_\mathrm{D}^\mathrm{GN,cos}$ is, by construction, manifestly different from the exact result.
Revisiting the discussion of a minimal truncation for the vertex expansion in sec. 3.1.1, it was argued that the first two nontrivial terms $\Gamma^{(2)}$ and $\Gamma^{(4)}$ are sufficient to retrace the occurrence of a nontrivial minimum of the effective action in the vicinity of a second order phase transition. This argument can be pursued even further. By analogy to Landau's picture of phase transitions [169], the occurrence of the minimum characterizing the onset of (chiral) symmetry breaking is solely determined by a *sign change* of

the two-point function $\Gamma^{(2)}$. The knowledge of nothing more but the overall sign of the two-point function is therefore sufficient to determine the exact location of second order phase transitions between phases of broken or unbroken chiral symmetry.

In complete analogy to the calculation for the one-dimensional ultracold Fermi gas in sec. 3.1.1 above, a vertex expansion can be constructed for the Gross-Neveu model as well[7]:

$$\Gamma^{\mathrm{GN}}_{\mathrm{mf}} = \sum_{n=1}^{\infty} \frac{1}{(2n)!} \prod_{j=1}^{2n} \int_{\mathbf{x}_j} \Gamma^{(2n)}_{\mathrm{mf}} \bar{\sigma}(x_1) \cdot \ldots \cdot \bar{\sigma}(x_{2n}) = \frac{1}{2} \int_{\mathbf{q}} \Gamma^{(2)}_{\mathrm{mf}}(q) \bar{\sigma}(q) \bar{\sigma}(-q) + \ldots \; . \tag{3.32}$$

For general $\bar{\sigma}(q)$, the kernel $\Gamma^{(2)}_{\mathrm{mf}}$ of the exact (mean-field) two-point function can be computed. It is given by

$$\frac{1}{\beta L} \Gamma^{(2)}_{\mathrm{mf}}(q) = -\frac{1}{\pi} \ln\left(\frac{M_0}{\Lambda}\right) + 2 \int_{\mathbf{p}} \frac{1}{q + 2p} \left[1 - \bar{N}_{\mathrm{F}}(p - \mu) - \bar{N}_{\mathrm{F}}(p + q + \mu)\right], \tag{3.33}$$

where

$$\bar{N}_{\mathrm{F}}(p) = \frac{1}{e^{\beta p} + 1} \tag{3.34}$$

is the Fermi distribution function.

A two-point function can of course also be computed from $\Gamma^{\mathrm{GN,cos}}_{\mathrm{D}}$ as obtained from the doubling trick:

$$\frac{1}{\beta L} \Gamma^{(2)}_{\mathrm{D,cos}} = -\frac{1}{2\pi} \ln\left(\frac{M_0}{\Lambda}\right) + \int_{\mathbf{p}} \frac{1}{2p} \left[2 - \sum_{\alpha_1, \alpha_2 = \pm 1} \bar{N}_{\mathrm{F}}(p + \alpha_1 Q + \alpha_2 \mu)\right]. \tag{3.35}$$

Plugging the cosine ansatz (3.21) and the kernel of the exact two-point function (3.33) into eq. (3.32), properly shifting the integration variable and making use of the invariance of the integrand under $p \to -p$, it is found that $2\Gamma^{(2)}_{\mathrm{D,cos}} = \Gamma^{(2)}_{\mathrm{mf,cos}}$ for $Q \neq 0$ and $\Gamma^{(2)}_{\mathrm{D,cos}} = \Gamma^{(2)}_{\mathrm{mf,cos}}$ for $Q = 0$. This is in agreement with the findings of app. C. There it is shown by means of the path integral representation of the respective partition functions that spurious terms introduced by the fermion doubling procedure enter only past the quadratic order.

As the sign of $\Gamma^{(2)}_{\mathrm{D,cos}}$ is not obscured by a factor of 2 missing with respect to the exact result, a minimization of $\Gamma^{\mathrm{GN,cos}}_{\mathrm{D}}$ indeed yields the correct location not only of the homogeneously broken phase, but also of the boundary between normal and inhomogeneous phases. The full phase diagram of the Gross-Neveu model introduced in fig. 1.3 is now redrawn in fig. 3.14 to compare the exact results from [71–74] to those obtained from the doubling trick. Both the transitions between domains of homogeneous as well as inhomogeneous condensation and the normal phase are perfectly reproduced by the doubling trick. Furthermore, the location of the *Lifshitz point* P_{L} in between the homogeneous and inhomogeneous phase boundaries agrees with the exact result as well. Last but not least, the characteristic momentum $Q(\mu)$ as a function of the chemical potential at the phase boundary resulting from the minimization of $\Gamma^{\mathrm{GN,cos}}_{\mathrm{D}}$ is in agreement with the exact result up to numerical accuracy. This is not only a further verification of the doubling trick's validity but also of the permissibility of the simple cosine ansatz (3.21): $Q(\mu) \to 0$ continuously when approaching P_{L} as it should be. For large chemical potential $\mu \gg M$ on the other hand, $Q(\mu) \sim \mu$. This is in analogy to the rough coincidence $\omega_{\bar{\Delta}} \sim \left|k^{\uparrow}_{\mathrm{F}} - k^{\downarrow}_{\mathrm{F}}\right|$ far away from the line of equal imbalances $\bar{h} = \bar{m}$ in sec. 3.2.2 above. While inhomogeneous condensation is caused by imbalances introducing a mismatch of Fermi surfaces for ultracold gases, it is a shift of the Dirac sea by the chemical potential that is responsible for this phenomenon in the relativistic setting.

The Lifshitz point P_{L} is also the starting point of the boundary between homogeneous and inhomogeneous chirally broken phases. This particular transition line is reproduced only approximately by the fermion doubling procedure in terms of its position. Furthermore, its nature is found to be of (weak) first instead of second order as predicted by the exact solution. The crucial difference to the other transitions is that the magnitude M of the chiral order parameter $\bar{\sigma}(x)$ does not vanish. It is therefore not the sign of the two-point function that determines this transition, as its actual order parameter is the characteristic momentum Q. The simple analogy to Landau's theory of phase transitions detailed above therefore does not hold anymore. As the transition, or in general the properties of the condensate, are more and more

---

[7] In fact, this Vertex expansion has successfully been utilized to benchmark the numerics employed for the one-dimensional ultracold Fermi gas in sec. 3.1 above.

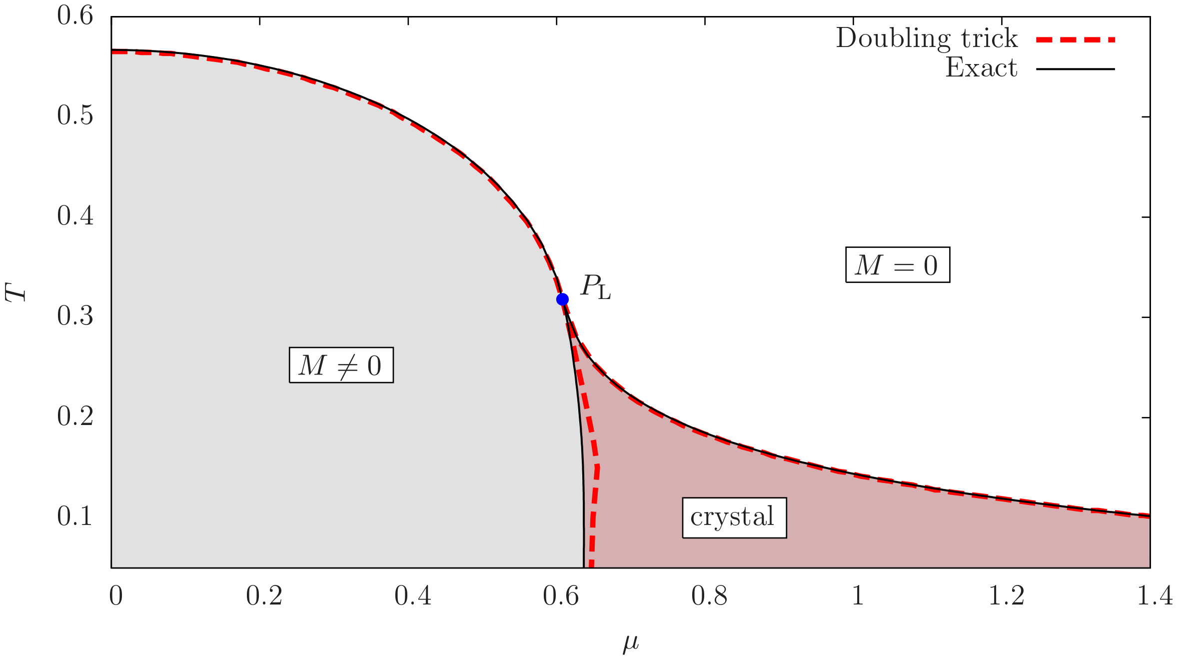

Figure 3.14: Phase diagram of the 1+1-dimensional GN model with T and μ measured in units of the vacuum gap M_0. In contrast to fig. 1.3, the exact general solution from e.g. [97] (black, solid lines) is now compared to the results obtained from the fermion doubling trick (red, dashed lines). While the boundaries between chirally broken and normal phases agree identically, the homogeneous-inhomogeneous transition is not reproduced exactly by the doubling trick.

dominated by higher order n-point functions as the bulk of the chirally broken phases is penetrated, corrections to $\Gamma_{\mathrm{D}}^{\mathrm{GN,cos}}$ become increasingly more important and its predictions deviate from the exact result. While this effect is small for small condensate amplitudes, i.e. in the vicinity of the Lifshitz point, it becomes larger as T is lowered further. Consequently, the two results for the homogeneous-inhomogeneous phase transitions are still in reasonable agreement close to P_{L} (see fig. 3.14), while the discrepancy becomes larger towards $T \to 0$ until the occurrence of multiple non-smooth minima below $T \sim 0.2$ somewhat spoils a further physical interpretation of $\Gamma_{\mathrm{D}}^{\mathrm{GN,cos}}$.

However, it should be noted that corrections to $\Gamma_{\mathrm{D}}^{\mathrm{GN,cos}}$ are not the only source for deviations from the exact result. The cosine ansatz (3.21) can only be expected to yield good results in the vicinity of the normal phase. Deep inside the bulk, the inhomogeneity is known to acquire a complicated kink-antikink shape, see, e.g., [97]. This behavior cannot be captured by a single cosine. An increasing number of higher order Fourier modes would have to be included as $T \to 0$ to keep up the quality of the approximation. Again, this is in close analogy to the non-relativistic case discussed above, see in particular fig. 3.6b and the associated discussions.

Generalization of the method It is in fact possible to extend the fermion doubling trick and include higher order Fourier components and generalize the ansatz for the chiral order parameter to

$$\bar{\sigma}(x) = \sum_{n=0}^{n_{\max}} M^{(n)} \cos(2Qnx)\,, \tag{3.36}$$

which could in principle reproduce any (square integrable on a finite domain) periodic function in the limit $n_{\max} \to \infty$. In order to allow for such an extended ansatz, the number of fermion fields would have to be enhanced by a factor of $2n_{\max}$ instead of only 2 as for the single cosine.

It is, however, at least questionable if such an extension would indeed improve the approximation. It can be shown (see app. C) that a higher number of artificially introduced fermion fields entails larger corrections to higher order n-point functions. This can be traced back to the fact, that the doubling (or rather multiplication) trick misses out nontrivial coupling between the different Fourier modes. As higher order coefficients of both Fourier and the vertex expansions become significant as the bulk of inhomogeneous phases is penetrated, it is not clear if a more complete ansatz like (3.36) should be considered useful within the framework of fermion multiplication.

So far, only relations between exact calculations, vertex expansions and the doubling trick have been discussed. Other methods, in particular numerical searches, can often be compared on quantitative grounds alone, as explicit analytical relations are not easily constructed. The famous and widely-used *Ginzburg-Landau* expansion [96, 168], however, constitutes an exception as it can be viewed as a special case of a vertex expansion. Consider an expansion of the effective action in terms of the order parameter $\bar{\sigma}$ and its spatial derivatives,

$$\Gamma_{\mathrm{GL}}[\bar{\sigma}] = \int_{\mathbf{x}} \sum_{i=1}^{\infty} \sum_{j=0}^{\infty} \frac{1}{(2i)!j!} \Gamma_{2i,j} \cdot \left(\partial_x^j \bar{\sigma}\right)^{2i} . \tag{3.37}$$

For fixed $i = 1$, the remaining series in powers of spatial derivatives corresponds to a polynomial expansion of the exact two-point function in momentum space. For a homogeneous ground state, all coefficients with $j > 0$ are therefore bound to vanish and second order phase boundaries can again be determined by the sign of $\Gamma_{2,0}$ alone. In an inhomogeneous scenario, however, such a polynomial expansion can at best be an asymptotic representation of the exact result. Without even having to rely on the specific cosine ansatz, it can be concluded from eq. (3.33) that the momentum dependence of the full two-point function is at least partially determined by the Fermi distribution function $\bar{N}_{\mathrm{F}}$ being a function of q. The radius of convergence for the latter is proportional to $1/\beta$ and thus vanishes for $T \to 0$. No finite order truncation in j of the Ginzburg-Landau series (3.37) is therefore able to describe second order phase transitions from inhomogeneous to normal phases exactly as the doubling trick does and ever higher orders are needed at low temperatures[8] to arrive at an acceptable level of precision. These considerations are in line with actual Ginzburg-Landau calculations of the phase diagram, see, e.g., [96, 186]. In fact, the doubling trick with cosine ansatz already corresponds to an infinite order series in j albeit with limitations on the possible $\Gamma_{2,j}$. On the downside, vertex as well as Ginzburg-Landau expansions can be improved systematically in practical computations by including higher order contributions. This is of questionable use (Fourier components) or completely impossible (higher n-point functions) for the doubling trick.

If only the 1+1-dimensional Gross-Neveu model could be analyzed by means of the doubling trick, it would not be of much use, as the exact results are known. Fortunately, it can also be generalized to other theories as well. First and foremost, the proof of the exact reproduction of the two-point function's momentum structure does not rely on the specific dimensionality of the problem. Any Gross-Neveu type model in arbitrary dimension can therefore be analyzed by means of the doubling trick and exact solutions are not known beyond 1+1 dimensions. Furthermore, models with related interaction structure such as NJL- or PNJL models (see sec. 3.3.2 below) are admissible as well. This can be concluded along the lines of app. C, which shows that corrections are of higher than second order only for these interaction structures without actually having to calculate two-point functions. Further generalizations to even more classes of fermionic models may be possible. However, such investigations are well beyond the scope of this work.

3.3.2 Inhomogeneous phases in the PNJL model

The 1+1-dimensional Gross-Neveu model is a versatile toy model for the investigation of strong interaction physics, but its quantitative outcomes can of course not be expected to describe actual particle physics experiments. Considering the NJL model defined by the Lagrangian (3.18) in 3+1 dimensions instead comes much closer to reality already. But there are still important features of the accepted theory of the strong interaction (in a particle physics sense), *quantum chromodynamics* (QCD), that are missing and it is a priori not clear if this affects the existence and properties of inhomogeneous phases.

QCD, confinement and the Polyakov loop The quartic fermion interaction terms in Gross-Neveu or NJL-type models are not fundamental. They are effective representations of an interaction that is in

---

[8] This implies large μ in the 1+1-dimensional Gross-Neveu model, cf. fig 3.14.

fact mediated by a *gauge* boson, the gluon field $A^a_\mu(x)$. It is introduced into the microscopic QCD action

$$S_{\mathrm{QCD}} = \int_{\tau,\mathbf{x}} \left[\bar{\psi} \left(i\partial\!\!\!/ + g_{\mathrm{QCD}} A\!\!\!/^a \frac{\lambda_a}{2} \right) \psi - \frac{1}{4} F^a_{\mu\nu} F^{\mu\nu}_a \right], \tag{3.38}$$

by requiring a theory of free relativistic fermions[9] to be invariant under local SU(3) "gauge" transformations. The corresponding charge introduced by this procedure is called "color". For details on the construction and properties of QCD as a non-abelian gauge theory as well as the many intricacies that come along with that status see, e.g., [57, 187] for introductory textbooks. The focus of this work will rather be on phenomenological consequences that eventually lead to the construction of the PNJL model. As described in more detail for an analog situation in sec. 4.2.2, the Yukawa-type interaction $\sim g_{\mathrm{QCD}} \bar{\psi} A\!\!\!/^a \psi$ generates quartic fermion terms that have to be accounted for when considering effective theories. The interaction structures in the (effective) Gross-Neveu or NJL-type models are therefore well motivated. However, they are by construction not suited to capture effects like *confinement* (see, e.g., [188]) which are solely due to the physics of the gauge field.

Consider for a moment the limit of infinitely heavy "static" quarks. In this setting, which effectively corresponds to *pure Yang-Mills theory*, the so-called *Polyakov loop*

$$L(\mathbf{x}) = \mathcal{P}\exp\left[- \int_0^\beta \mathrm{d}\tau A_0(\mathbf{x}, \tau) \right], \tag{3.39}$$

where $\mathcal{P}$ is the path-ordering operator, becomes an order parameter for the confinement phenomenon. More precisely, the particularly convenient *Polyakov gauge* where L becomes diagonal in color space [189], as well as spatially constant (averaged) A_0 will be considered in the following. Then, the traces Tr_c of L in color space

$$\Phi = \frac{1}{3}\mathrm{Tr}_c L, \qquad \bar{\Phi} = \frac{1}{3}\mathrm{Tr}_c L^\dagger, \tag{3.40}$$

are just constants as well. Their interpretation in terms of the free energy $F_{q/\bar{q}}$ of quarks or antiquarks, respectively, demonstrates the interpretation of L as an order parameter for confinement [190, 191]. For example, a vanishing $\Phi \sim e^{-F_q/T}$ indicates the requirement of infinite energy to remove a single quark from a color-neutral object - it is thus perfectly confined. For $\Phi = 1$, no energy is required anymore and the quark is deconfined.

In the static limit, quarks are confined at low temperatures and become deconfined via a first order phase transition when T is increased. Considering the more realistic situation of finite quark masses instead, the picture changes depending on the precise value of these mass parameters [192] and the phase transition becomes a smooth crossover in the situation with two light quark flavors considered in the following.

The Polyakov loop or its color-traced versions may now be used to allow for the inclusion of confinement effects in the purely fermionic low-energy models of QCD. For the NJL model, this is achieved [189] by promoting

$$\partial\!\!\!/ \longrightarrow D\!\!\!\!/ = \partial\!\!\!/ - iA\!\!\!/ = \partial\!\!\!/ - i g_{\mathrm{QCD}} \gamma_0 A^0_a \frac{\lambda_a}{2} \tag{3.41}$$

in the fermion kinetic term of the Lagrange density (3.18). Furthermore, an order parameter potential $\mathcal{U}(\Phi, \bar{\Phi})$ is introduced that is parametrized in such a way as to yield confinement ($\Phi = 0$) at vanishing temperature and deconfinement ($\Phi = 1$) at $T \to \infty$ [190, 191]. Pure Yang-Mills theory can reliably be simulated with lattice Monte Carlo methods, yielding $T_0 = 270\,\mathrm{MeV}$ for the confinement-deconfinement transition temperature (e.g. [193]). These data may furthermore be used to fix the parametrization of $\mathcal{U}$ such that it reproduces the desired behavior.

Overall, the action of the PNJL model[10] is given by

$$S_{\mathrm{PNJL}} = \int_{\tau,\mathbf{x}} \left\{ \bar{\psi} \left[iD\!\!\!\!/ - i\mu\gamma_0 \right] \psi + \frac{\lambda^2}{2} \left[\left(\bar{\psi}\psi \right)^2 + \left(\bar{\psi} i \gamma_5 \psi \right)^2 \right] + \mathcal{U}\left(\Phi, \bar{\Phi}, T \right) \right\}. \tag{3.42}$$

---

[9] In nature, these *quarks* are found to be massive, explicitly breaking chiral symmetry. Since the chiral limit is of particular interest here, the corresponding quark mass matrix has been omitted nevertheless.

[10] The generators $\boldsymbol{\tau}$ of the flavor symmetry group $\mathrm{SU}(N_\mathrm{f})$ in the pseudoscalar interaction term have been omitted for convenience. They do not play a role in the subsequent considerations as only the scalar channel for symmetry breaking will be investigated.

Neither the functional form of $\mathcal{U}$ nor its precise parametrization are uniquely determined by lattice data and the above named criteria. In the following, the model of ref. [194] will be used,

$$\frac{\mathcal{U}\left(\Phi,\bar{\Phi},T\right)}{T^4} = -\frac{b_2(T)}{2}\bar{\Phi}\Phi - \frac{b_3}{6}\left(\Phi^3+\bar{\Phi}^3\right) + \frac{b_4}{4}\left(\bar{\Phi}\Phi\right)^2 , \tag{3.43}$$

where

$$b_2(T) = a_0 + a_1\left(\frac{T_0}{T}\right) + a_2\left(\frac{T_0}{T}\right)^2 + a_3\left(\frac{T_0}{T}\right)^3 . \tag{3.44}$$

The values for the a_i and b_i parameters obtained in [182] by fitting MC data from ref. [193] are given in tab. 3.1 below.

a_0	a_1	a_2	a_3	b_3	b_4
6.75	-1.95	2.625	-7.44	0.75	7.5

Table 3.1: Parameter set for the Polyakov loop potential (3.43).

As it is not pure Yang-Mills theory that will be considered here, the additional scales introduced by a finite number of quark flavors as well as a finite chemical potential μ have to be accounted for. The incorporation of these quantities into the parametrization of $\mathcal{U}$ is not unique and has been realized in different ways in the literature. In this work, the parametrization of ref. [194] will be employed, which was derived from a perturbative analysis. It is given by an explicitly μ-dependent T_0,

$$T_0(\mu) = T_\tau e^{-1/[\alpha_0 b(\mu)]} , \tag{3.45}$$

with

$$b(\mu) = \frac{33-2N_\mathrm{f}}{6\pi} - b_\mu \frac{\mu^2}{T_\tau^2} , \tag{3.46}$$

and

$$\alpha_0 = 0.304 , \quad T_\tau = 1770\,\mathrm{MeV}, \quad b_\mu = \frac{16N_\mathrm{f}}{\pi} . \tag{3.47}$$

The assumption of two massless quark flavors is already implicit here. The physical reason for the choice of $N_\mathrm{f} = 2$ is that the up and down quarks are indeed much lighter than any of the other flavors, justifying the chiral limit employed in the action (3.42).

A deviating parametrization may have consequences for the phenomenological results obtained from the action (3.42). In order to demonstrate this, the alternative μ-independent $T_0 = 208\,\mathrm{MeV}$ from ref. [194] will be considered as well. This deconfinement temperature incorporates the effect of finite flavor number but is otherwise incomplete as it ignores the presence of a chemical potential.

Doubling trick and effective action Along the lines described for the Gross-Neveu model in sec. 3.3.1 above, an approximate effective action allowing for plane-wave-inhomogeneous condensation may now be computed also for the PNJL model. As the calculation proceeds in a largely equivalent manner, only a few steps will be highlighted here.

For the reasons explained on p. 48 above, only scalar condensates ~ $\langle\bar{\psi}\psi\rangle$ with a slightly modified ansatz for the inhomogeneity

$$-i\langle\bar{\psi}\psi\rangle = \bar{\sigma}(\mathbf{x}) = M\cos(2\mathbf{Q}\cdot\mathbf{x}) = \frac{M}{2}\left(e^{2i\mathbf{Q}\cdot\mathbf{x}} + e^{-2i\mathbf{Q}\cdot\mathbf{x}}\right) , \tag{3.48}$$

will be considered. The eigenvalues of the (doubled) quark propagator matrix are then

$$E_{1\ldots4} = \omega_n + i\mu - iA_0 \pm i\sqrt{p^2+Q^2+M^2 \pm 2Q\sqrt{p^2\cos^2\vartheta + M^2}} =: \omega_n + i\mu - iA_0 \pm iE_\pm , \tag{3.49}$$

where $|\mathbf{Q}| = Q$, ϑ is the angle between the integration momentum and $\mathbf{Q}$ and each eigenvalue occurs twice.

Performing the color trace and the Matsubara sum, the doubling trick effective action is given by

$$
\begin{aligned}
\frac{1}{\beta V}\Gamma^{\mathrm{PNJL}}_{\mathrm{D,cos}} =& \,\mathcal{U}(\Phi,\bar{\Phi},T) + \frac{T}{V}\int_{\tau,\mathbf{x}} \frac{\sigma(\mathbf{x})^2}{2\lambda^2} - N_{\mathrm{f}}T\int_{\mathbf{p}}\sum_{\pm}\Big\{\ln\Big[1+3\left(\Phi+\bar{\Phi}e^{(\mu-E_\pm)/T}\right)e^{(\mu-E_\pm)/T}+e^{3(\mu-E_\pm)/T}\Big] \\
&+\ln\Big[1+3\left(\bar{\Phi}+\Phi e^{-(\mu+E_\pm)/T}\right)e^{-(\mu+E_\pm)/T}+e^{-3(\mu+E_\pm)/T}\Big]\Big\} - 3N_{\mathrm{f}}\int_{\mathrm{p}}\left[E_+ + E_-\right],
\end{aligned}
\tag{3.50}
$$

where terms indicating an unimportant constant vacuum shift have been dropped.

In a next step, the fermionic coupling λ^2 must be fixed. Experimentally, the proton mass is know to be $m_{\mathrm{p}} = 938\,\mathrm{MeV}$. As the proton is formed of three constituent quarks, the dynamically generated masses of the latter have to be roughly one third of this value each. Therefore, $M_0 = 325\,\mathrm{MeV}$ is required at $T = \mu = 0$ which serves to fix the value of λ^2.

In contrast to the (1+1)-dimensional Gross-Neveu model considered above, the PNJL model is not renormalizable, i.e. the momentum cutoff parameter Λ as well as details of the cutoff procedure itself remain parameters of the model. This persistence of Λ makes the effective nature of the present model even more apparent. Following in part ref. [182], a sharp cutoff with $\Lambda = 651\,\mathrm{MeV}$ is employed here. Another difference to the Gross-Neveu model is that the vacuum limit of eq. (3.50) depends on the magnitude of the inhomogeneity momentum $\mathbf{Q}$. To render the physical vacuum independent of this quantity, the condition for fixing λ^2 becomes $\mathbf{Q}$-dependent. The regularized approximate effective action is then given by

$$
\begin{aligned}
\frac{1}{\beta V}\Gamma^{\mathrm{PNJL}}_{\mathrm{D,cos}} =& \,\mathcal{U}(\Phi,\bar{\Phi},T) + \frac{3N_{\mathrm{f}}}{8\pi^2}\sum_{\pm}\int_{-1}^{1}\mathrm{d}x\int_0^{\Lambda}\mathrm{d}p\frac{p^2}{E_\pm}\left.\left(1\pm\frac{Q}{\sqrt{p^2x^2+M^2}}\right)\right|_{M_0}\cdot M^2 \\
&-\frac{3N_{\mathrm{f}}}{4\pi^2}\int_{-1}^{1}\mathrm{d}x\int_0^{\Lambda}\mathrm{d}p p^2\left(E_+ + E_-\right) \\
&-\frac{N_{\mathrm{f}}T}{4\pi^2}\sum_{\pm}\int_{-1}^{1}\mathrm{d}x\int_0^{\Lambda}\mathrm{d}p p^2\Big\{\ln\Big[1+3\left(\Phi+\bar{\Phi}e^{(\mu-E_\pm)/T}\right)e^{(\mu-E_\pm)/T}+e^{3(\mu-E_\pm)/T}\Big] \\
&\qquad+\ln\Big[1+3\left(\bar{\Phi}+\Phi e^{-(\mu+E_\pm)/T}\right)e^{-(\mu+E_\pm)/T}+e^{-3(\mu+E_\pm)/T}\Big]\Big\}.
\end{aligned}
\tag{3.51}
$$

Phase diagram of the PNJL model By minimizing the effective action (3.51) with respect to M,Φ, $\bar{\Phi}$ and Q for different (T,μ), the phase diagram of the PNJL model can be mapped out. The result for the chiral order parameter M is shown in fig. 3.15.

For vanishing and small chemical potential, the transition between homogeneously ordered and normal phases is of second order with a critical temperature of $T_{\mathrm{c}} = 228\,\mathrm{MeV}$ at $\mu = 0$. For larger μ, the Lifshitz point at $(T_{P_{\mathrm{L}}},\mu_{P_{\mathrm{L}}}) = (103.6, 279)\,\mathrm{MeV}$ indicates the onset of inhomogeneous ordering. A quantitative comparison to the literature is difficult due to the strong parameter dependence of these values.

Inhomogeneous phases such as the red (dark) shaded one in fig. 3.15 have been identified previously for the NJL and PNJL models (e.g. [166,195]) with qualitatively similar shape. However, to the best of the author's knowledge, no survey for inhomogeneous phases for the PNJL model with μ-dependent T_0 has been performed before, making a more detailed comparison difficult. A doubling trick calculation with fixed T_0 instead yields results which appear to be in agreement with ref. [195] up to differences in the employed regularization schemes.

As anticipated from the non-renormalizability property of the (P)NJL model in (3+1) dimensions, the dependence of quantitative results on the value of Λ and details of the regularization scheme is quite strong indeed. This becomes particularly apparent in the large-μ region of the phase diagram 3.15. For increasing μ, the inhomogeneity momentum generally grows. At some chemical potential μ that depends on the precise values of Λ and M_0 in the sharp-cutoff framework, the "fixing term" in the first line of eq. (3.51) changes sign, rendering the effective action unstable in Q direction. This is due to the presence of a cutoff Λ for the high-momentum modes and thus it is in the end an artifact of the non-renormalizability property. In fig. 3.15, this is indicated by an end of the homogeneous-to normal phase boundary at $\mu \sim 345\,\mathrm{MeV}$. Beyond this point, the Q-instability dominates and makes a unique determination of the ground state impossible. This artifact does not necessarily appear, if other regularization schemes are used, such as, e.g., a Pauli-Villars-type exponential cutoff [195] which incorporates weighted high-momentum modes beyond

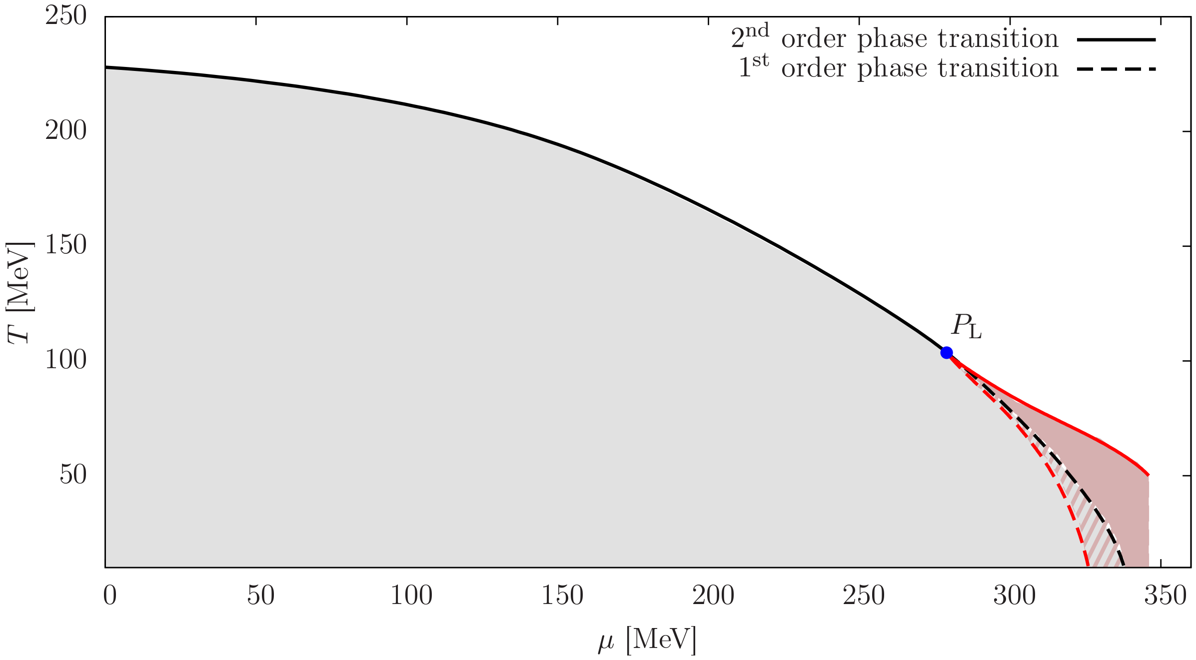

Figure 3.15: Mean-field chiral phase diagram of the PNJL model. Black lines correspond to the homogeneous solution, red lines to the one obtained with the doubling trick. While gray (light) shading indicates homogeneous condensation, the red (dark) region is predicted to exhibit inhomogeneous ordering. In the striped domain, the inhomogeneous phase supersedes a previously found homogeneous one.

the sharp-cutoff scale Λ. Independently of the employed scheme, however, regions of the phase diagram that are dominated by physical scales of the same order of magnitude as the cutoff should generally be treated with care as the effective description underlying such models becomes increasingly worse.

Concerning the chiral order parameter, there is an interesting observation to be discussed. It concerns the Lifshitz point P_L and goes beyond the general statement of the existence of a sizable inhomogeneous phase also upon inclusion of (some) gauge degrees of freedom. In the Gross-Neveu model, the inhomogeneous phase emerged exactly from the same point as the previously found first-order transition in the homogeneous calculation. It has been found that this does not necessarily have to be the case for actual effective fermionic models for QCD [196]. For the present PNJL model with μ-dependent T_0, this coincidence appears to be lifted as well. In fact, while the inhomogeneous-to-normal transition crosses the homogeneous phase boundary at P_L within limits of numerical accuracy, it does not appear to end there anymore. It does rather extend *into* the homogeneous phase, forming a small inhomogeneous “sliver” that is fully enclosed by the homogeneous phase. Due to the tenuity of this “sliver” of at most $\mathcal{O}(1\,\text{MeV})$ in T direction making it invisible on the scale of fig. 3.15, it is numerically challenging to determine its exact extent in terms of μ. Furthermore, since the fermion doubling trick is, strictly speaking, not suited for a reliable characterization of such a “bulk” property of the symmetry broken phase, quantitatively more concrete predictions on the characteristics of this phenomenon are not appropriate. However, the fact that the inhomogeneity momentum Q does not converge to $Q = 0$ as in the Gross-Neveu model but rather remains as large as $Q \approx 50\,\text{MeV}$ in the immediate vicinity of P_L gives confidence that this finding may be more than just a numerical artifact.

Last but not least, some comments are in order on the effective gauge degrees of freedom $\bar{\Phi}$ and Φ. When considering quarks away from the chiral limit, i.e. with finite bare mass, the second order homogeneous chiral phase transition in fig. 3.15 is washed out into a crossover. The deconfinement temperature is then usually assigned to the maximum of the susceptibilities $\frac{\partial \Phi}{\partial T}$ or $\frac{\partial \bar{\Phi}}{\partial T}$, respectively. For finite μ and in the chiral limit, this criterion is not unique anymore. Firstly, it is $\bar{\Phi} > \Phi$ for given T and μ due to the shift of the Dirac sea introduced by μ. This results in general in different deconfinement temperatures for quarks and antiquarks. Secondly, the presence of actual chiral phase transitions instead of a smooth crossover induces nonanalyticities in the functional shape of $\bar{\Phi}(T)$ and $\Phi(T)$ as well. It is therefore tempting to interpret these features associated with *chiral* transitions also with a simultaneous *deconfinement* transition.

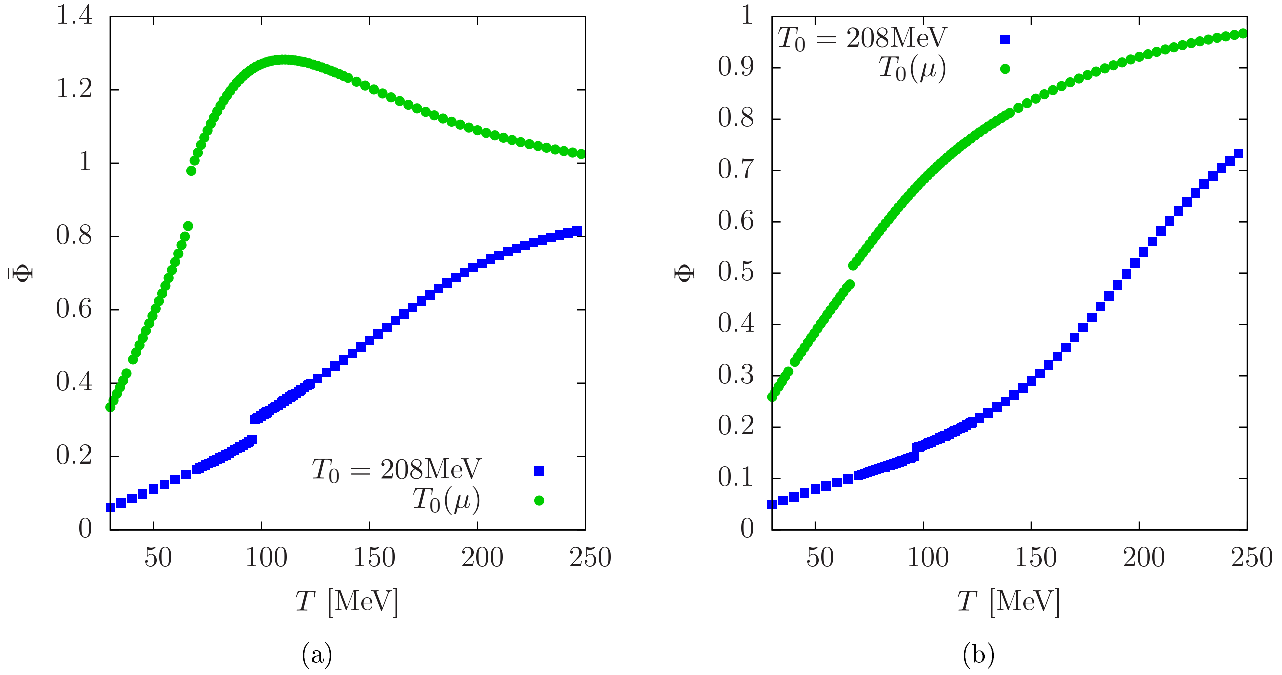

Figure 3.16: Temperature dependence of $\bar{\Phi}$ (a) and Φ (b) for fixed $\mu = 330\,\text{MeV}$ and two different parametrizations of $\mathcal{U}$. The results for μ-dependent T_0 make a simultaneous chiral and deconfinement transition much more plausible.

In fact, nonperturbative studies indicate a locking of the chiral and deconfinement transitions [197]. It is a priori not clear, whether this behavior is indeed consistently reproduced within the present inhomogeneous setting. In fig. 3.16, the temperature dependence of $\bar{\Phi}$ and Φ is plotted at fixed $\mu = 330\,\text{MeV}$ for the two different parametrizations of the Polyakov loop potential $\mathcal{U}$ introduced on p. 55 above. In both cases, the chiral inhomogeneous-to-normal transition leaves a distinctive feature in the functional shapes[11]. It is of course located at the same temperature for both $\bar{\Phi}$ and Φ ($T_c^{208} = 97\,\text{MeV}$ and $T_c^{\mu} = 67\,\text{MeV}$).

Comparing the two displayed parametrizations of fixed $T_0 = 208\,\text{MeV}$ (blue squares) and μ-dependent T_0 (green circles), the discrepancy indicated upon their introduction becomes apparent. The values of $\bar{\Phi}$ and Φ for fixed, μ-independent T_0 are much too low at the chiral transition in order to go together well with an interpretation as deconfinement transition. Thus, an exotic so-called *quarkyonic phase* appears [198]. It is characterized by confinement for the quarks but restored chiral symmetry.

The situation is much different for $T_0(\mu)$, where even $\Phi = 0.5$ at the chiral transition. In this case, the findings are compatible with a simultaneous chiral and deconfinement transition. This is a nontrivial result for the inhomogeneous phase, as the parametrization of $\mathcal{U}$ taken from [194] was constructed with only homogeneous chiral ordering in mind.

Of course, much more could be said about the PNJL model and the validity of approximations coming along with its construction and characterization independently of the doubling trick. This is, however, beyond the scope of this thesis whose main goal for this section was a further illustration of the fermion doubling procedure "at work". In conclusion, it may be stated that the fermion doubling trick is capable of revealing interesting features of inhomogeneous chiral condensates also beyond the (1+1)-dimensional Gross-Neveu model for which it was initially devised.

---

[11] The range of temperatures covered fig. 3.16 includes only inhomogeneous and normal phases, cf. also fig. 3.15. The apparent jump of $\bar{\Phi}$ and Φ appears to indicate a first order chiral transition. However, this is not the case. In fact, an extremely sharp but continuous drop of the chiral condensate is found in this domain. It is due to a rather sharp localization of the global minimum of $\Gamma^{\text{PNJL}}_{\text{D,cos}}$ in Q-direction.

Chapter 4

Unitary imbalanced Fermi gases in 3D

Neither in theory nor in experiment, a *dimensional crossover* for ultracold gases is in general a matter of triviality. In reality, laser frequencies and arrangements have to be changed [42] which, if feasible at all, requires a fair amount of construction and readjustment. From a mathematical point of view, characteristics such as the renormalizability properties may change. While, for example, the one-dimensional interacting Fermi gas was described by a convergent theory up to vacuum energy contributions, its three-dimensional analog has to be renormalized in order to keep diverging terms under control (see sec. 3.1 and sec. 2.2.1, respectively). Features of qualitative phenomenological importance are subject to change as well: While no true long-range order may occur in one spatial dimension, three-dimensional Fermi gases exhibit actual superfluidity [20, 21] which is directly linked to spontaneous symmetry breaking, see sec. 1.1.3.

On the other hand, crucial components of what determines the physical content of a theory are not changed by an altered dimensionality. The field content,[1] i.e. the type of particles involved in an experiment as well as the symmetries of the action remain largely the same. In particular, both one- and three-dimensional Fermi gases described by the actions (1.16) or (1.6), respectively, exhibit a global U(1) particle number conservation symmetry.

It is therefore not unreasonable to assume that there might also be qualitative similarities concerning the phenomenology described by these theories. And in fact, the homogeneous zero temperature mean-field phase diagrams in figs. 3.2 and 2.5 appear to be rather similar. While such “similarities” should not be relied upon without actual calculations of the respective quantities, they may be very useful in guiding studies of unexplored terrain.

The three-dimensional unitary Fermi gas has already been discussed from a Monte Carlo perspective in chap. 2. In terms of accuracy for quantities like the Bertsch parameter ξ, Monte Carlo methods can hardly be beaten by approximate analytic approaches even for imbalanced systems. The detection of critical values for the imbalances at transitions from normal to symmetry broken phases is, however, difficult, in particular in the framework of the imaginary imbalance approach presented here. Furthermore, access to and identification of inhomogeneous phases remains a challenging problem. In this respect, studies based on but not limited to the mean-field approximation combined with the insight obtained from one-dimensional systems may be expected to constitute fruitful complements. The main goal of the present chapter is thus to characterize the phase structure of unitary imbalanced Fermi gases as comprehensively as possible. It will in particular be necessary to go beyond the mean-field approximation as, e.g., it turns out that the very existence of an inhomogeneous phase cannot conclusively be predicted from mean-field results.

In the first section below, approaches like the FF-ansatz-aided mean-field calculations and bound state considerations that have successfully been applied in chap. 3 will be adapted to the three-dimensional case. In order to go beyond the mean-field approximation, a functional renormalization group (fRG) framework for ultracold gases will be introduced in sec. 4.2. Its application to imbalanced systems will yield a considerable amount of results that will be discussed in the last two sections: 4.3 deals with vanishing and 4.4 with nonzero mass imbalance.

Methodical developments and results presented in this chapter have been published in [200] and [201].

---

[1] Note that the dimensionality of available representations of *relativistic* fermion fields generally depends on the dimension of spacetime, see, e.g., [199]. This is not of much concern in the present *non-relativistic* setting.

4.1 Adaptation of 1D approaches

Before proceeding to the discussion of actual calculations and results, a remark on the choice of parameters is in order. For neither of the approaches presented in this chapter, it is in principle a problem to deal with finite scattering lengths a, i.e. to consider the situation away from the unitary limit. Systems with finite a are certainly not uninteresting and there is of course a vast bulk of literature on the behavior of physical observables along the BCS-BEC crossover (see, e.g., [42–45] and references therein). In this work, however, *only* the unitary case will be considered just as for the lattice MC simulations of chap. 2. This is done for reasons of clarity but also because of the plethora of phenomena that is found and has to be understood already at infinite scattering length. Along the lines and using the methods summarized here, further explorations of the vast parameter space of ultracold Fermi gases may readily be undertaken. However, this is beyond the scope of this work.

4.1.1 Mean-field phase diagram

As a primary result of the preceding chapter it was found that even the most simple cosine or plane-wave ansätze were sufficient to exactly reproduce boundaries of the inhomogeneous phase. This was proven rigorously for the Gross-Neveu model [74] and could be confirmed for its non-relativistic analog as well. While this assumption is not necessarily true in three spatial dimensions, it constitutes at least a good starting point for the search for inhomogeneous phases in the unitary Fermi gas. This assumption was confirmed when considering the (3+1)-dimensional PNJL model where an inhomogeneous phase could be identified and characterized as well. Employing the slightly adapted ansatz

$$\bar{\Delta}^{\mathrm{3D}}_{\mathrm{FF}}(\mathbf{x}) = \bar{\Delta} e^{i\mathbf{Q}\cdot\mathbf{x}}, \tag{4.1}$$

and following the usual mean-field procedure as in sec 2.2.1, the (renormalized) effective order parameter potential

$$\frac{1}{\beta V}\Gamma^{\mathrm{3D,FF}}_{\mathrm{mf}} = U^{\mathrm{3D,FF}}_{\mathrm{mf}}(\bar{\Delta}, Q) = \int_{\mathbf{q}} \left\{ E_{\bar{\Delta}=0} - E_{\bar{\Delta}} + \frac{|\bar{\Delta}|^2}{2q^2} - \sum_{\sigma=\pm1} T \ln\left(1 + e^{-\frac{1}{T}E_{\bar{\Delta}} - \frac{\sigma}{T}\left[(q^2+Q^2/4)\bar{m} - \mathbf{q}\cdot\mathbf{Q} - h\right]}\right)\right\} \tag{4.2}$$

is found. The absolute values of momentum vectors are denoted as $|\mathbf{q}| = q$ and $|\mathbf{Q}| = Q$, respectively, while $E_{\bar{\Delta}}$ is again the energy of the Bogoliubov quasiparticles,

$$E_{\bar{\Delta}} = \sqrt{(q^2 + Q^2/4 - \bar{m}\mathbf{q}\cdot\mathbf{Q} - \mu)^2 + |\bar{\Delta}|^2}\,. \tag{4.3}$$

Eq. (4.2) is the analog of eq. (3.12) but with a more complicated momentum structure due to the higher dimensionality. The occurrence of terms $\sim \mathbf{q}\cdot\mathbf{Q}$ introduces an angular dependence into the integrand of eq. (4.2) that was naturally not present in one dimension. This slightly complicates the numerical integration but a global minimization of the order parameter potential is still feasible. The resulting phase diagram is shown in fig. 4.1.

For temperatures $\bar{T} \lesssim 0.3$, mass imbalances $\bar{m} \gtrsim 0.6$ and a finite range $\bar{h}(\bar{m})$ of spin imbalances, an inhomogeneous (Fulde-Ferrell) phase is found, delimited by a second order transition to the normal phase. In contrast to the region of homogeneous condensation, it is considerably smaller than in the one-dimensional case, cf. fig. 3.4. Remarkably, a mixture of ^{6}Li and ^{40}K atoms that is currently under investigation [85,86], corresponding to $\bar{m} = 0.74$, lies within the region where inhomogeneous superfluidity is predicted to occur. Given the qualitative reliability of mean-field theory in three spatial dimensions, it may be tempting to conclude that such an inhomogeneous phase should be found roughly at the given values for $\bar{T}$ and $\bar{h}$ in an experiment. However, such a prediction should be considered somewhat premature for at least two reasons.

Firstly, it is in fact not true, that *all* symmetries of the one- and three-dimensional Fermi gases are identical. Naturally, the group of spatial translation and rotation symmetries is larger for the three dimensional case. In particular, this implies that there are more possibilities for the system to spontaneously break said symmetries. While one-dimensional modulations are the only way for an inhomogeneous phase to be formed in 1D, one-, two- or even three-dimensional patterns may form in 3D, depending on the specific configuration. The Fulde-Ferell ansatz (4.1) provides a better estimate of the true ground state than

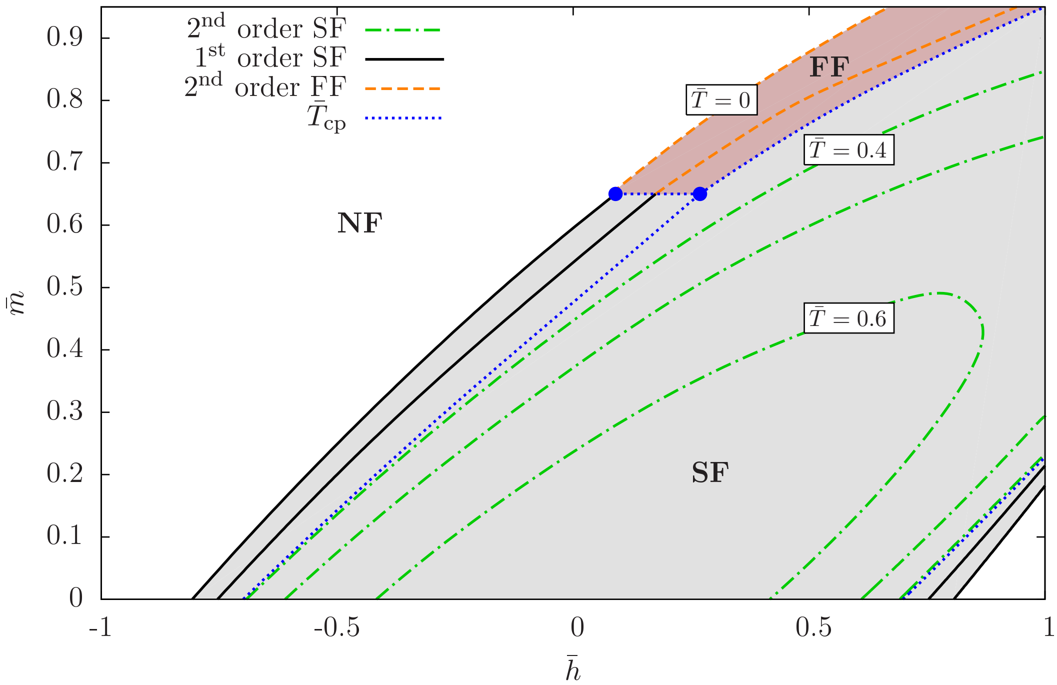

Figure 4.1: Mean-field phase diagram of the three-dimensional unitary ($a^{-1} \to 0$) Fermi gas in the $\bar{h} - \bar{m}$ plane with $\bar{T}$ isolines. The gray (light) shading symbolizes homogeneous superfluidity (SF) while the red (dark) coloring depicts an inhomogeneous Fulde-Ferrell (FF) phase. Black (solid) lines symbolize first order transitions, while green (dot-dashed) and orange (dashed) lines denote second order boundaries between the normal phase (NF) and SF or FF domains, respectively. Intersections of these phase transition manifolds are depicted by blue (dotted) multi-critical lines ($\bar{T}_{\mathrm{cp}}$).

the purely homogeneous solution, but higher dimensional modulations might extend the inhomogeneous phase even more. In the literature, such patterns have indeed been found to be of significance in diverse contexts, see, e.g., [166, 202]. In any case, the prediction of the existence of an inhomogeneous phase by the Fulde-Ferrell ansatz is not affected by this argument. It is rather the range of admissible temperatures and imbalance parameters that might be changed.

The second reason is more severe in that it might altogether inhibit experimental detection of the inhomogeneous phase displayed in fig. 4.1. While the mean-field approximation is believed to be qualitatively reliable in three spatial dimensions, sizable quantitative corrections to observables like condensate magnitudes or critical temperatures are still expected by comparison with existing experimental or MC data, see, e.g., [203] for an overview. Consider now some fixed generic mass imbalance $\bar{m} = 0.725$ within the region where the FF phase occurs. Fig. 4.2 shows the $\bar{h}$-$\bar{T}$ phase diagram for this situation. The inhomogeneous phase turns out to be a rather thin "slice" capping a large region of homogeneous condensation. From a computational point of view, this makes an accurate determination of critical lines challenging, as the inhomogeneous phase is not easily resolved anymore in their vicinity. The location of the critical line (blue, dotted) in fig. 4.1 delimiting the FF phase as the boundary to the homogeneous superfluid should therefore be considered a numerical estimate rather than an exact result. In particular, the error on the lower $\bar{m}_{\mathrm{crit}}(\bar{h}, \bar{T})$ may be as large as $\delta\bar{m} \sim 0.1$.

Assuming for a moment that this tenuity is not an artifact of the simple ansatz (4.1), the mean-field prediction itself becomes somewhat problematic. Fluctuation corrections to the critical temperature do not even need to be large for the inhomogeneous phase to possibly vanish completely. For example, the discrepancy $\bar{T}_{\mathrm{c}}^{\mathrm{mf}} - \bar{T}_{\mathrm{c}}^{\mathrm{exp}} \approx 0.27$ between the mean-field and experimental [110] values for the critical temperature of balanced systems is already more than twice as big as the largest thermal extent of the FF phase in fig. 4.1. The qualitative results of mean-field theory may therefore be sufficient to predict a superfluid phase but, from fig. 4.2, it is rather unclear if this holds true for the existence of inhomogeneity as well.

These numerical and conceptual questions are also reflected in the literature on the subject. For example, the so-called *T-matrix calculation* in [204] includes certain fluctuation effects and finds an inhomogeneous

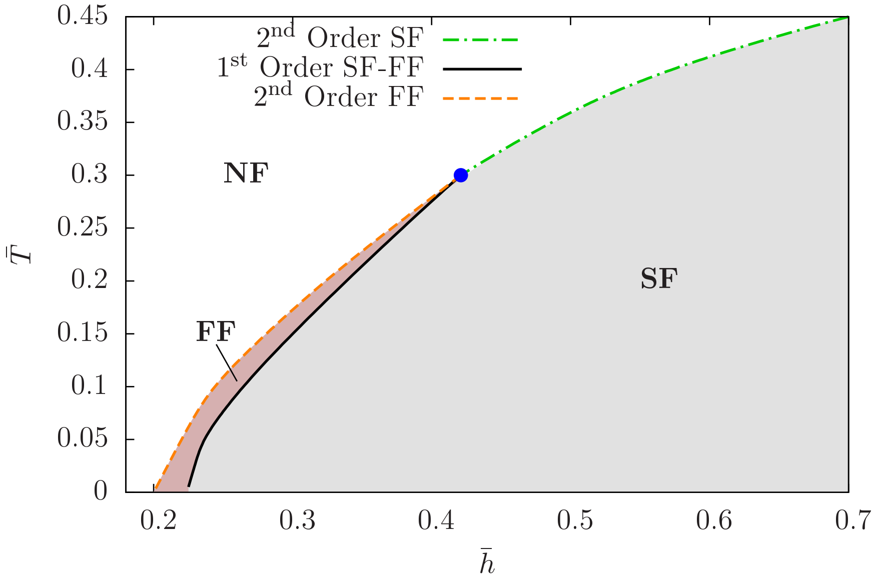

Figure 4.2: Temperature versus spin imbalance phase diagram for fixed $\bar{m} = 0.725$. Line types and color coding are as in fig. 4.1. While the extent of the FF phase projected onto the $\bar{h}$-axis is sizable, it is in fact only a very thin layer "on top of" the homogeneous phase.

phase that extends down to vanishing mass-imbalance in the unitary limit. It may not be too surprising that such a different approach yields deviating results for a delicate structure like the FFLO phase. On the other hand, there are also T-matrix calculations which do not find an FFLO phase at $\bar{m} = 0$ [205] and mean-field ones that do [206]. Again, the findings of [202] agree very well with the ones presented here although a more complicated three-dimensional inhomogeneity has been admitted there.

So far, it can only be said that the sensitivity of the phase structure on details of the approximation as well as numerical inaccuracies inhibits the emergence of a clear picture. One of the main goals of the subsequent sections is to provide further evidence that the scenario presented in fig. 4.1 is at least qualitatively correct also beyond mean-field and for generic inhomogeneity structures.

4.1.2 In-medium bound states in 3D

The problem of more complicated inhomogeneity patterns that are not captured by the simple FF ansatz could in principle be resolved by applying an adapted version of the vertex expansion technique presented in sec. 3.1. An extension of the ansatz (3.7) to a three-dimensional Fourier series is straightforward and the higher-dimensional analogs of n-point functions as in eqns. (3.8) and (3.9) are formally written down without much additional effort. The actual integration of these vertex functions for generic three-dimensional inhomogeneity patterns is, however, very challenging. While the complicated structure of the integrands required considerable numerical effort even in one dimension, additional angular integrals in the 3D case quickly drive the cost to unattractive magnitudes. This approach is therefore not pursued further in the present work.

Another technique that has been introduced in sec. 3.2 is more suitable for an adaptation to the 3D Fermi gas: the investigation of bound state properties in the presence of Fermi seas for the respective species. Generalizing the Schrödinger equation (3.14) is a rather formal task,

$$\left[\sum_{\sigma=\uparrow,\downarrow} \frac{\left|-\partial_{\mathbf{x}_\sigma}^2 - \mathbf{k}_\mathrm{F}^{\sigma\,2}\right|}{2m_\sigma} - g_\delta \delta(\mathbf{x}_\uparrow - \mathbf{x}_\downarrow) + E_\mathrm{B}\right] \Psi(\mathbf{x}_\uparrow, \mathbf{x}_\downarrow) = 0\,. \tag{4.4}$$

Besides the dimensionality of coordinate and momentum variables, it is in particular the coupling that is now set to its value according to the scattering solution (1.4). Choosing the same sharp-cutoff regularization procedure as in sec. 2.2.1, eq. (4.4) may again be recast into an integral equation for the normalized

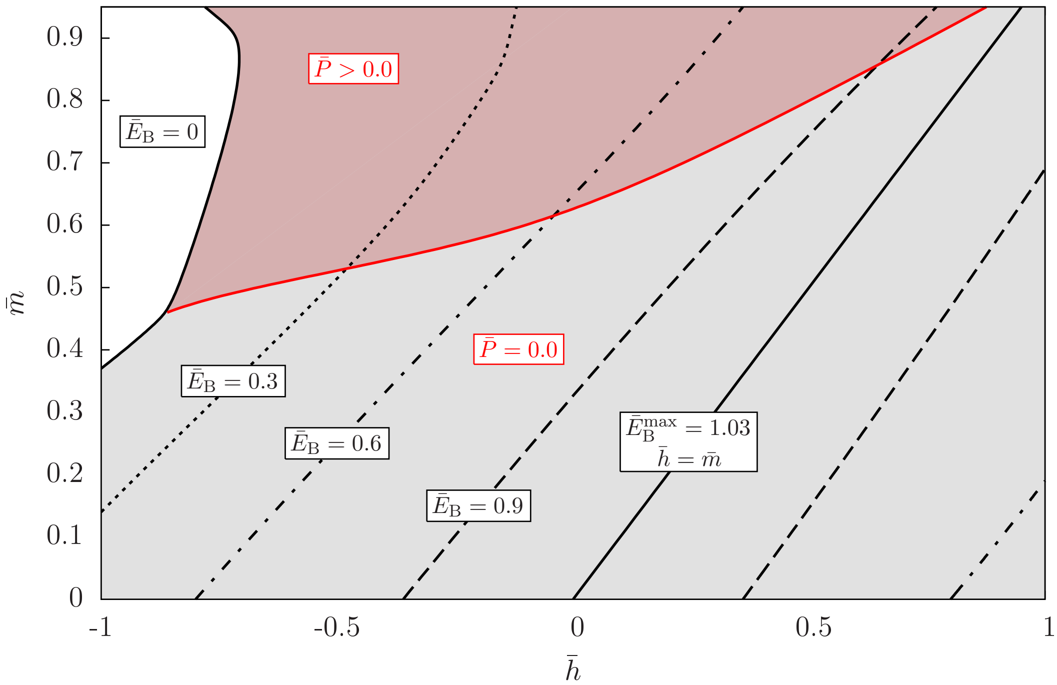

Figure 4.3: Maximal (normalized) binding energies $\bar{E}_\mathrm{B}$. Gray (light) shading symbolizes a preference for zero-center-of-mass-momentum bound states and red (dark) shading indicates finite $\bar{P}$. While the most deeply bound states are again found along the line of equal Fermi momenta ($\bar{h} = \bar{m}$), a domain without bound state formation (white) is now present as well.

momentum-dependent binding energy $\bar{E}_\mathrm{B}(\bar{P})$,

$$\int_{\bar{\mathbf{p}}} \left[\frac{1}{\epsilon_\uparrow\left(\frac{\bar{\mathbf{P}}}{2} + \bar{\mathbf{p}}\right) + \epsilon_\downarrow\left(\frac{\bar{\mathbf{P}}}{2} - \bar{\mathbf{p}}\right) + \bar{E}_\mathrm{B}\left(\bar{P}\right)} - \frac{1}{2\bar{p}^2} \right] = 0\,. \tag{4.5}$$

As the integral is invariant under rotations of the relative momentum $\mathbf{p}$, its value and consequently also $\bar{E}_\mathrm{B}$ may only depend on the absolute value of the center-of-mass momentum $|\bar{\mathbf{P}}| \equiv \bar{P}$. Numerically solving eq. (4.5) for the admissible range of imbalances, the behavior of the binding energy can again be mapped to the $\bar{h} - \bar{m}$ plane which is shown in fig. 4.3.

Similarly to the one-dimensional case depicted in fig. 3.10, in the vicinity of equal Fermi momenta, i.e. $\bar{h} = \bar{m}$, pairs with $\bar{P} = 0$ are energetically favored. Furthermore, the domain of large mass imbalance is dominated by pair formation with finite center-of-mass momentum. Besides that, however, there are notable discrepancies between the different dimensionalities.

First of all, the domain of finite $\bar{P}$ pairing is much smaller in 3D and it is limited to mass imbalances $\bar{m} > 0.45$. Secondly, for large $\bar{m}$ and negative $\bar{h}$, no bound states are found at all (white region in fig. 4.3). And last but not least, a back-bending of energy isolines as in fig. 3.10a is present for very high $\bar{m}$, but it is much less pronounced.

Each of these observations may be used for the interpretation of the many-body phase diagram in fig. 4.1. Starting with the most obvious finding, there should be no condensate of pairs in a region of parameter space where those pairs may not even be formed for energetic reasons. In fact, the author is not aware of any work that predicts the existence of a superfluid phase for the domain in the $\bar{h} - \bar{m}$ plane where $\bar{E}_\mathrm{B} = 0$.

Passing from the physics of a single bound state to the description of condensation processes is nontrivial. It has been found in sec. 3.2.2 that the location of homogeneous versus inhomogeneous phase transitions does not agree quantitatively with the boundaries of preferred finite-momentum pairing. However, it would be hard to explain how in a region where the formation of finite-momentum bound states does not even occur anywhere close, an inhomogeneous condensate that would consist of said pairs could be formed. Such a situation is present for $\bar{m} \ll 0.5$ in fig. 4.3. This result can therefore be considered as a support for the above finding of an FFLO phase that does not extend to $\bar{m} = 0$.

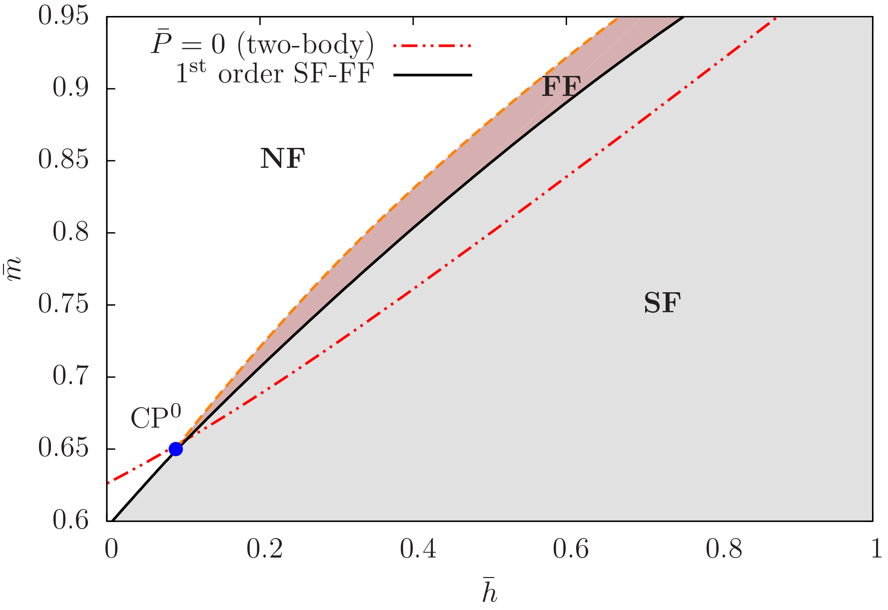

Figure 4.4: Comparison of the mean-field phase structure at $\bar{T} = 0$ with the lower bound for finite center-of-mass pair formation (red, dot-dot-dashed line). The critical endpoint CP^0 of the FF phase is found to agree with the intersection of the two-body bound with the limit of the condensate region.

In fact, quantitatively comparing the mean-field phase structure at $\bar{T} = 0$ with the boundary of finite momentum pairing obtained from eq. (4.5) in fig. 4.4 yields astonishingly good coincidence between the intersection of the latter with the boundary of the superfluid region and the endpoint CP^0 of the FFLO phase. The difference between the two-body boundary and the transition from homogeneous to inhomogeneous supefluidity, on the other hand, does not come unexpected. As in the one-dimensional case, an overall greater amount of more weakly bound $\bar{P} = 0$ pairs may enlarge the homogeneous superfluid region. Furthermore, the FF ansatz (4.1) that has been used to locate the inhomogeneous phase is expected to work best in the vicinity of the transition to the normal phase and cannot be expected to reproduce the boundary towards the homogeneous superfluid as well, cf. also sec. 3.1.2 for the analog finding in 1D. Given the above mentioned numerical problems with an accurate determination of the location of CP^0, even the precision of its coincidence with the two-body boundary should not be overrated. However, recalling the fact that no specific ansatz for an inhomogeneity pattern had to be made in order to solve equation (4.4), the qualitative support for the general conjecture of the FFLO phase being limited to the regime of high mass imbalance is not affected.

Last but not least, it is found (see fig. 4.4) that the width of the FF phase in terms of $\bar{h}$ increases with $\bar{m}$. While this effect is by far not as obvious as the hook-like shape of the inhomogeneous phase in 1D (see fig. 3.4a), it is still in accordance with the stabilization of finite $\bar{P}$ bound states at high $\bar{m}$ indicated by the slight back-bending of the energy isolines in fig. 4.3.

As the influence of approximations appears to be of particular importance for an accurate localization of the inhomogeneous phase in the present setting, a somewhat more detailed analysis of the Schrödinger equation (4.4) is in order. While including certain medium effects through the presence of the Fermi seas, it is by construction not a true many-body equation. Therefore, the approximations involved are not easily compared to the "mean-field" procedure discussed in sec. 2.2.1. However, an analogous treatment of few-particle problems in the presence of a medium is well established within the framework of *Dyson equations* for Green's functions and the *Hartree-Fock* approximation, see, e.g., [34, 207] for introductory texts. It is found to be conceptually equivalent to mean-field approaches as the collective action of the medium on a single particle is considered instead of the full problem.

However, there is a crucial difference to the formulation employed in eq. (4.4): The Fermi seas are usually considered to be *completely* inert, as no propagation of any kind is allowed in their regime. This would correspond to replacing the absolute values of the kinetic energy operators in eq. (4.4) with Heaviside step functions. It is shown in [208], that eq. (4.5) with a correspondingly modified dispersion relation reproduces the results of Dyson-type equations. In other words, the treatment of the in-medium two-body problem in the framework presented here already goes beyond "mean-field" in some sense. Propagation of "particles" or "holes" inside of the Fermi sea are allowed at the energetic cost that is needed to free up the respective phase space.

Neither does the Schrödinger equation describe condensation physics nor is the correspondence between these types of approximation particularly accurate. Still, this comparison makes the coincidences displayed in fig. 4.4 even more astonishing. An investigation also of condensate physics beyond the mean-field approximation appears to be more than worthwhile. In the subsequent section, the functional renormalization group will be introduced as a candidate to fill this gap.

4.2 Functional renormalization group for ultracold Fermi gases

The quantum effective action Γ is the central object of interest in the analytic many-body studies presented in this work. Knowing this quantity does in principle solve the underlying quantum field theory as it contains all thermal and quantum fluctuations by construction (see eq. (2.17)) and physical observables may be read of rather directly. Aside from numerical MC results that do in fact incorporate the full set of fluctuations, it has so far only been computed in the 1-loop mean-field approximation in this work. The focus of chap. 3 was rather conceptual, in particular as the inclusion of fluctuation effects in 1D would have destroyed any sign of spontaneous symmetry breaking. For the three-dimensional unitary Fermi gas, the preceding section delivered a number of reasons to strive for an effective action beyond mean-field in a (semi-)analytical manner in order to complement MC studies.

Probably the most straightforward way one could think of extending the mean-field results would be by taking higher order terms of the loop expansion (2.19) into account. Unfortunately, this cannot be expected to work well for the strongly coupled unitary gas: the expansion (2.19) is essentially a *perturbative* series in powers of the fermionic coupling g_δ. The latter is known to be large in the unitary limit. Thus, eq. (2.19) is at best an asymptotic series. Any finite order truncation which would have to be made for practical calculations may be an arbitrarily bad representation of the true result for Γ.

Non-perturbative methods are therefore needed for the system at hand. This includes techniques such as ϵ- [209, 210] and $1/N$-expansions [211], Dyson-Schwinger equations [212], two-particle-irreducible methods [213], ladder resummations [214], universal relations [215–218] and, last but not least, renormalization group flow equations as used in this work.

Many of the above-named methods are not geared towards an investigation of Γ itself. In this work, the *functional renormalization group* (fRG) in the form of the *Wetterich equation* [219] for the effective action will be employed. Its basic concept is to interpolate between a given *microscopic* action S and the full quantum effective action Γ by means of an *effective average action* Γ_k,

$$\lim_{k\to\Lambda}\Gamma_k = S, \qquad \lim_{k\to 0}\Gamma_k = \Gamma. \tag{4.6}$$

The term "microscopic" or *ultraviolet* action for the initial S results from the large momentum or, equivalently, short distance scale Λ to which it is associated in the RG picture. As it is a *bare*, unrenormalized quantity, no fluctuations have been incorporated or "integrated out" yet. The latter may therefore be of arbitrarily large momentum Λ.

The central concept dating back to Wilson [220] and implemented for example by the Wetterich equation is the successive "integration" of those fluctuations, i.e. incorporation of their influence into the structure of Γ_k as k is lowered. When the *infrared* limit $k \to 0$ is reached, all fluctuations have been integrated out and the full Γ is obtained.

Filling the rather formal term of "integrating fluctuations" with mathematical meaning, i.e. devising a concrete and viable way to implement this general idea will be the main content of sec. 4.2.1, where the Wetterich equation is discussed.

Subsequently, the general functional RG equation will be specialized to the case of unitary imbalanced Fermi gases in sec. 4.2.2. Approximation schemes are discussed as well as conceptual details of the implementation. Finally, the actual RG flow equations to be analyzed in secs. 4.3 and 4.4 are derived.

4.2.1 The Wetterich equation

The functional RG equation that is the subject of this section has for the first time been derived in [219]. By the time this thesis is written, it has become a standard tool in field theory. Extensive reviews on its derivation and application in different contexts are available, see, e.g., [47, 221, 222] for a selection of which this work has particularly profited. Any computational details that are omitted here for brevity can be found in these works.

Functional RG derives its name from the fact that it is based on the "functional" or path integral formalism introduced in sec. 2.2.1. To define the interpolating action Γ_k, the definitions for the generating functionals $Z[\mathbf{J}]$, $W[\mathbf{J}]$ and naturally also $\Gamma[\boldsymbol{\phi}]$ are modified by the introduction of a *regulator term* ΔS_k,

$$W_k[\mathbf{J}] = \ln Z_k[\mathbf{J}], \quad Z_k[\mathbf{J}] = \int_\Lambda \mathcal{D}\boldsymbol{\varphi} e^{-S[\boldsymbol{\varphi}]-\Delta S_k[\boldsymbol{\varphi}]+\int \mathbf{J}^T\cdot\boldsymbol{\varphi}}, \tag{4.7}$$

where

$$\Delta S_k[\boldsymbol{\varphi}] = \frac{1}{2}\int_{\hat{q}} \boldsymbol{\varphi}^T(-\hat{q}) R_{\boldsymbol{\varphi},k}(\hat{q}) \boldsymbol{\varphi}(\hat{q}) = \frac{1}{2}\int_{\hat{q}} \varphi(-\hat{q}) R_{\varphi,k}(\hat{q}) \varphi(\hat{q}) + \int_{\hat{q}} \bar{\psi}(\hat{q}) R_{\psi,k}(\hat{q}) \psi(\hat{q}) \,. \tag{4.8}$$

Here, generalized field and source functions

$$\boldsymbol{\varphi}(\hat{q}) = \begin{pmatrix} \varphi(\hat{q}) \\ \psi(\hat{q}) \\ \bar{\psi}^T(-\hat{q}) \end{pmatrix}, \qquad \mathbf{J}(-\hat{q}) = \begin{pmatrix} J(-\hat{q}) \\ \bar{\eta}^T(-\hat{q}) \\ \eta(\hat{q}) \end{pmatrix}, \tag{4.9}$$

have been introduced to allow for a unified treatment of bosonic and fermionic degrees of freedom as needed for ultracold Fermi gases. Note that the fields are defined on Euclidean spacetime. Since the derivation is valid for general temperatures, the Matsubara notation is not introduced yet. Instead, generalized momentum variables $\hat{q} = (q_0, \mathbf{q})$ are used here. Finally, the effective average action may be defined,

$$\Gamma_k[\boldsymbol{\phi}] = \sup_{\mathbf{J}} \Big(\int \mathbf{J}^T \boldsymbol{\phi} - W_k[\mathbf{J}] \Big) - \Delta S_k[\boldsymbol{\phi}] \text{ where } \boldsymbol{\phi} = \langle \boldsymbol{\varphi} \rangle_{\mathbf{J}} = \frac{\vec{\delta} W_k[\mathbf{J}]}{\delta \mathbf{J}} \,. \tag{4.10}$$

Exhibiting the general structure of a mass term, the behavior of ΔS_k is controlled by the bosonic and fermionic *regulator* functions $R_{\varphi,k}(\hat{q})$ and $R_{\psi,k}(\hat{q})$. While being in general adapted to the properties of the type of field it is supposed to regularize, any such function is bound to obey the following three constraints:

$$\lim_{k^2/q^2 \to 0} R_{\boldsymbol{\varphi},k}(\hat{q}) = 0 \,, \tag{4.11a}$$

$$\lim_{k^2 \to \Lambda \to \infty} R_{\boldsymbol{\varphi},k}(\hat{q}) \to \infty \,, \tag{4.11b}$$

$$\lim_{q^2/k^2 \to 0} R_{\boldsymbol{\varphi},k}(\hat{q}) > 0 \,. \tag{4.11c}$$

The first two conditions implement the endpoints of the interpolation given in eq. (4.6). Prescription (4.11a) simply reduces the definition (4.10) of Γ_k to the usual one (2.17) for Γ in the deep infrared. The condition (4.11b) makes a saddle point approximation of the path integral for $Z[\mathbf{J}]$ exact, which results in Γ_k becoming the microscopic action again. The last constraint finally implements the Wilsonian principle of successive integration of fluctuations. This can be understood along the following lines. For momenta $q = |\hat{q}|$ smaller than the regulator scale k, the propagator of the respective field type is dominated by the regulator contribution which acts as an artificial mass gap. The respective contributions thus cannot contribute to Γ_k which therefore incorporates only fluctuations with momenta $q \gtrsim k$. Lowering k, more and more momentum modes are included until finally the full Γ is reached and the regulator vanishes by (4.11a).

Besides the conditions (4.11), there are no further constraints on the shape of $R_{\boldsymbol{\varphi},k}$. On the one hand, this means that the correspondence to the Wilsonian picture of sharp momentum shells is not necessarily exact anymore. Smoothing the onset of the behavior associated with condition (4.11c) distributes the integration of a particular momentum mode over a range of RG scales k. An accurate interpretation of k as a physical momentum or length scale is therefore not possible due to the strong dependence on the shape of $R_{\boldsymbol{\varphi},k}$. On the other hand, freedom in the choice of regulator shapes opens up the possibility for optimization with respect to particular physical systems or even verification of approximation schemes. This point is of great practical relevance and will be revisited below.

As the Legendre transform (4.10) defining Γ_k is not a particularly convenient prescription for actual calculations, the scale evolution or *flow* described above is cast into the form of the integro-differential Wetterich equation

$$\partial_t \Gamma_k = \frac{1}{2}\int_{\hat{q}} \mathrm{Tr}\left[\partial_t R_{\varphi,k}\cdot \mathcal{G}_{\varphi,k}\right] = \frac{1}{2}\mathrm{STr}\left[\frac{\partial_t R_{\varphi,k}}{\Gamma_k^{(2)} + R_{\varphi,k}}\right], \tag{4.12}$$

see, e.g., [222] for further details. Here, the derivative with respect to the "RG time" $\partial_t = k\partial_k$ with $t = \ln(k/\Lambda)$ has been introduced for reasons of consensus with notation found in the literature. The "supertrace" operation STr symbolizes a summation over all discrete and continuous indexes. Note that fermionic sectors of the theory acquire an extra minus sign which is also meant to be included in the STr notation.

The central object of the RHS of eq. (4.12) is the full regularized propagator (matrix) $\mathcal{G}_{\varphi,k}$ which is defined by the second functional derivative $\Gamma_k^{(2)}$ of the effective average action itself. This gives the Wetterich equation a formal 1-loop structure which should, however, not be confused with the usual notion of a 1-loop approximation: $\mathcal{G}_{\varphi,k}$ is, at least on a formal level, the *exact* propagator. Its dressing does contain loop corrections of all orders, the formal 1-loop structure of eq. (4.12) simply reflects the particular ordering of diagrams that comes along with the derivation of $\partial_t\Gamma_k$.

In particular, this means that (perturbative) loop diagrams of arbitrarily high order contribute to the Wetterich equation [223]. As it is of particular relevance for the present work, consider for example the 1-loop approximation of the effective action [47]. For this most simple approximation, the dependence of the RHS of eq. (4.12) on $\Gamma_k^{(2)}$ is replaced by the k-independent bare $S^{(2)}$. The flow equation may then be integrated analytically,

$$\Gamma^{1\text{-loop}} = S - \int_{k=0}^{\Lambda} \mathrm{d}k \left(\partial_k \Gamma_k\big|_{\Gamma_k^{(2)}=S^{(2)}}\right) = S - \frac{1}{2}\mathrm{STr}\ln S^{(2)} + \frac{1}{2}\mathrm{STr}\ln\left(S^{(2)} + R_{\varphi,\Lambda}\right). \tag{4.13}$$

These are precisely the first terms of the loop expansion (2.19), supplemented by a renormalization counter term that renders $\Gamma^{1\text{-loop}}$ finite. Recall that this corresponds to the mean-field approximation as detailed in sec. 2.2.1.

For interacting theories it is in general not possible to solve the Wetterich equation exactly. An approximate ansatz has to be chosen for Γ_k which may be used on the right hand side. As the simplest possible choice $\Gamma_k \equiv S$ already reproduces the 1-loop effective action, truly k-dependent ansätze for Γ_k lead to results for Γ that go beyond mean field. A proper choice of Γ_k is a pivotal point for the fRG analysis of field theoretical models. The next section will therefore be concerned with the construction of such an ansatz for the unitary Fermi gas and its formal evaluation with the Wetterich equation, leading to a system of flow equations that encodes the evolution of physical observables.

4.2.2 Flow equations for the unitary Fermi gas

The microscopic action,

$$S_{\mathrm{F}}[\psi^\dagger,\psi] = \int_0^\beta \mathrm{d}\tau \int \mathrm{d}^3x \left[\sum_{\sigma=\uparrow,\downarrow} \psi_\sigma^* \left(\partial_\tau - \frac{\nabla^2}{2m_\sigma} - \mu_\sigma\right)\psi_\sigma + g_\delta \psi_\uparrow^*\psi_\uparrow\psi_\downarrow^*\psi_\downarrow\right], \tag{1.6 with imbalance}$$

should be the starting point of the RG evolution. For the Wetterich equation, it does in principle not make a difference, if the fermionic or bosonized version (1.8) is used as both are equivalent by construction. However, once approximations come into play, this equivalence may be violated. For example, phases with spontaneously broken U(1) symmetry are not accessible anymore if the fermionic coupling g_δ is kept momentum independent during the flow (point-like limit). Although the onset of SSB may still be detected, the RG evolution can, in general, not be carried through $k \to 0$. Thus, no direct calculation of physical observables connected to condensation is possible. See [47] for a review on the fermionic RG formulation and [224] for recent work on the inclusion of momentum dependent fermion couplings.

Besides these rather technical reasons, the bosonic formulation (1.8) is more apt to the purposes of this work also for phenomenological reasons. As condensate formation is a bosonic effect, it is more convenient to deal with the latter *effective* degrees of freedom directly. An order parameter potential $U(\varphi)$ may again

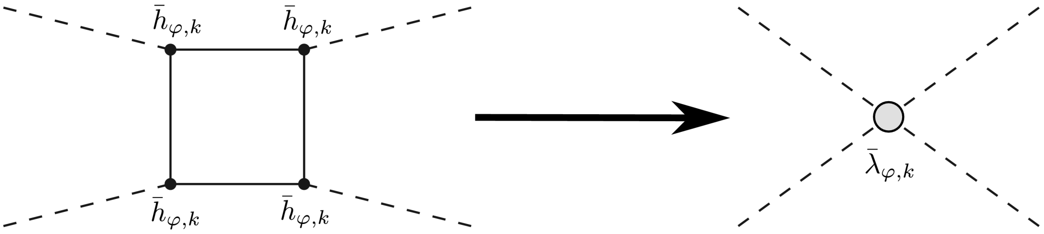

Figure 4.5: Generation of an effective four-boson vertex with coupling $\bar{\lambda}_{\varphi,k}$. A finite initial Yukawa interaction $\sim \bar{h}_{\varphi,k}\bar{\varphi}^*\psi_\uparrow\psi_\downarrow$ is sufficient to generate bosonic operators of arbitrarily high order during the RG flow. Dashed lines symbolize boson propagators while fermion lines are solid.

be obtained from which the condensate properties of interest can be read off directly.

Structure of Γ_k Having thus determined the field content of Γ_k, an appropriate choice of operators[2] to be included has to be made. In principle, any operator that is compatible with the imposed symmetries may be generated during the flow and existing ones receive k-dependent contributions. This can be understood diagrammatically with the help of fig. 4.5. When the scale k is lowered by δk, loop diagrams with high internal momenta $q > k-\delta k$ are integrated out. Since their internal structure cannot be "resolved" anymore, they appear as an effective new vertex function with k-dependent coupling determined by the RG flow. Of course, also existing operators receive contributions due to this "mechanism" and therefore have to be equipped with *running* couplings.

In practice, it is in general not possible to evolve the infinite number of compatible operators that would have to be taken care of for an exact solution of the Wetterich equation. Furthermore, it is not always clear what an appropriate representation for the structure of Γ_k looks like. For example, non-analyticities may be introduced during the flow and thereby invalidate polynomial series expansions, see, e.g., [225] for the occurrence of such a scenario in a derivative expansion. A *truncated* ansatz for Γ_k must therefore be made. As this constitutes an approximation, the choice of operators must be justified and results have to be analyzed with respect to possible artifacts of the truncation.

The ansatz made in this work is based upon experience gained for balanced systems [55, 226–228] for which the framework was initially developed. It is given by

$$\begin{aligned}\Gamma_k = \int_{\tau,\mathbf{x}} \Bigg[&\sum_{\sigma=\uparrow,\downarrow} \psi_\sigma^* \left(\partial_\tau - \frac{\nabla^2}{2m_\sigma} - \mu_\sigma\right)\psi_\sigma + \bar{\varphi}^* \left(Z_{\varphi,k}\partial_\tau - A_{\varphi,k}\frac{1-\bar{m}^2}{2}\nabla^2\right)\bar{\varphi} \\ &+ \bar{U}_k(\bar{\rho}) - \bar{h}_{\varphi,k}\left(\bar{\varphi}^*\psi_\uparrow\psi_\downarrow - \bar{\varphi}\psi_\uparrow^*\psi_\downarrow^*\right)\Bigg],\end{aligned} \tag{4.14}$$

where $\bar{\rho} = \bar{\varphi}^*\bar{\varphi}$.

The fermionic parts of Γ_k are essentially of the same structure as in the microscopic action (1.8). Neither the (inverse) fermion propagator nor the bare Yukawa coupling $\bar{h}_{\varphi,k} \equiv \bar{h}_\varphi$ are renormalized here. It is tempting to assume that fermionic renormalization is unimportant for the aim of this work, as mainly bosonic (condensate) properties are of interest. However, the nontrivial coupling of bosonic and fermionic degrees of freedom beyond mean field as introduced by the Wetterich equation always leaves a trace of doubt in such considerations. On the other hand, it has been explicitly checked for the balanced configuration [203], that renormalizing the fermion propagator and/or the Yukawa coupling does not significantly alter the observables of interest, in particular the critical temperature. The vast increase in the number of running couplings and corresponding flow equations therefore makes such an extension unattractive for the present work.

As exemplified diagrammatically in fig. 4.5, higher order bosonic operators are generated during the flow due to the existence of the Yukawa term. This process is not limited to a quartic coupling $\bar{\lambda}_{\varphi,k}$ but extends to infinite order already at the mean-field level. A full order parameter potential $\bar{U}_k(\bar{\rho})$ as a function of

---

[2] As the path integral framework is used here, the fields φ and ψ and combinations of them are actually not operators. However, the canonical operator formalism is equivalent to the path integral approach. In this sense, the widely used term appears to be justified.

the U(1) invariant $\bar{\rho}$ is therefore taken into account. As in the mean-field calculations in previous chapters of this work, spontaneous symmetry breaking is signaled by a nontrivial minimum $\bar{\rho}_{0,k}$ of this potential. In the RG framework, the latter must furthermore persist down to $k = 0$ in order to constitute an actual physical observable. This will be discussed in more detail in sec. 4.3.1 below.

There are different ways to represent $\bar{U}_k(\bar{\rho})$ in an actual calculation. The probably most widespread one is a polynomial expansion about the minimum,

$$\bar{U}_k(\bar{\rho}) = -p_k + \bar{m}^2_{\varphi,k}(\bar{\rho} - \bar{\rho}_{0,k}) + \frac{\bar{\lambda}_{\varphi,k}}{2}(\bar{\rho} - \bar{\rho}_{0,k})^2 + \dots \ , \tag{4.15}$$

being truncated at some finite order to achieve a finite and closed system of flow equations for the couplings. Besides further expansions schemes one could in principle think of, another possibility is the discretization of the full potential on a grid. The latter will be the primary approach employed in this work. Reasons for this as well as a comparison with results from polynomial truncations will be provided in sec. 4.3.1 below.

The auxiliary bosonic fields $\bar{\varphi}$ are here equipped with their own dynamics, i.e. their inverse propagator,

$$\bar{P}^{-1}_{\varphi}\left(\omega_n, \mathbf{q}^2\right) = -iZ_{\varphi,k}\omega_n + \frac{1 - \bar{m}^2}{2}A_{\varphi,k}\mathbf{q}^2 + \left.\frac{\partial^2 \bar{U}_k}{\partial\bar{\varphi}\partial\bar{\varphi}^*}\right|_{\bar{\varphi}_0} , \tag{4.16}$$

is nontrivial in frequency and momentum space. While at mean-field level only the last term in eq. (4.16) was present (see, e.g., eq. (1.7)), now the momentum and frequency dependence of $\bar{P}^{-1}_{\varphi}$ resolves the corresponding structure the fermionic coupling g_δ - at least partially [47]. This is due to the mediation of fermionic interactions by the now nontrivial boson propagator. In fact, there is a priori no good reason, why the *derivative expansion* of the inverse boson propagator should be truncated at the first nontrivial term, as the momentum structure may in principle be arbitrarily complicated. While the lowest order truncation in case of the frequency may indeed be justified (see p. 71 below), the limitations for spatial momenta will be discussed extensively in sec. 4.4.2.

The precise form of $\bar{P}^{-1}_{\varphi}(\omega_n, \mathbf{q}^2)$, in particular the factor of $(1 - \bar{m}^2)/2$ for the spatial momentum part, is obtained by requiring Γ_k to be Galilean invariant for $T = 0$ at $k = \Lambda$ analogously to eqns. (1.9) and (1.10). In general, each of the couplings discussed so far can in principle depend on momenta or invariant field operators itself, again. In other words, there are many more terms that could (or should) be included in the ansatz (4.14) due to their compatibility with the symmetries of the theory. In particular, the possibilities of letting $Z_{\varphi,k}(\bar{\rho})$, $A_{\varphi,k}(\bar{\rho})$ and/or $\bar{h}_{\varphi,k}(\bar{\rho})$ have not been addressed in the course of the discussion so far. However, it does not seem systematically justifiable to include higher order contributions to the Yukawa coupling while not even renormalizing the field-independent $\bar{h}_{\varphi,k}$ itself. An inclusion of the full field dependence of the bosonic renormalization coefficients is also beyond the scope of this work. However, projecting their evolution equations from the RHS of the Wetterich equation leaves a residual $\bar{\rho}$ dependence to be dealt with, see [203] for a detailed discussion. Here, $\bar{\rho}$ will be set equal to the effective potential's minimum $\bar{\rho}_{0,k}$ in the flow equations for $Z_{\varphi,k}$ and $A_{\varphi,k}$. In other words, the wave function renormalization parameters are evaluated on the flowing ground state, which appears to be a reasonable approach to account for their field dependence at least in parts.

Last but not least, the *partial bosonization* procedure that led to eq. (1.8) has to be revisited once more. The term “partial” refers to the fact, that the Hubbard-Stratonovich transformation has been performed only once, at the scale $k = \Lambda$. By a process with analogous diagrammatic structure as the one depicted in fig. 4.5, the quartic fermion coupling g_δ is, however, regenerated during the flow. For completeness, its flow would therefore have to be taken into account even though the bosonized formulation is employed. Alternatively, *dynamic* or re-bosonization [229] may be applied at each scale k to feed back the contributions of $\partial_t g_\delta$ into the bosonic sector.

Neither approach is followed in the present work. Dynamical bosonization techniques have been applied to the balanced system in [230]. While yielding corrections to observables like the critical temperature, the latter were not of large quantitative or qualitative impact at least at unitarity. Once again, these findings are here assumed to carry over to the imbalanced case as well. The regeneration of g_δ during the flow is therefore ignored in the following.

To complete the discussion of the structural aspects of Γ_k, renormalized fields $\varphi^{(*)} = \sqrt{A_{\varphi,k}}\bar{\varphi}^{(*)}$, $\rho = A_{\varphi,k}\bar{\rho}$

and quantities $S_{\varphi,k} = Z_{\varphi,k}/A_{\varphi,k}$, $h_{\varphi,k} = \bar{h}_\varphi/\sqrt{A_{\varphi,k}}$, $U_k(\rho) = \bar{U}_k(\bar{\rho})$ are introduced. The resulting effective action reads as

$$\begin{aligned}\Gamma_k = \int_{\tau,\mathbf{x}} \Bigg[\sum_{\sigma=\uparrow,\downarrow} \psi_\sigma^* \left(\partial_\tau - \frac{\nabla^2}{2m_\sigma} - \mu_\sigma\right)\psi_\sigma + \varphi^*\left(S_{\varphi,k}\partial_\tau - \frac{1-\bar{m}^2}{2}\nabla^2\right)\varphi \\ + U_k(\rho) - h_{\varphi,k}\left(\varphi^*\psi_\uparrow\psi_\downarrow - \varphi\psi_\uparrow^*\psi_\downarrow^*\right)\Bigg],\end{aligned} \tag{4.17}$$

and will be used throughout the remainder of this thesis.

Regulator choice It has been shown [231, 232] that a regulator function shaped as

$$R_{\varphi,k}(\mathbf{q}) = A_{\varphi,k}k^2 r_{\varphi,k}(y)\,, \quad y = \frac{\mathbf{q}^2}{2k^2}\left(1-\bar{m}^2\right), \quad r_{\varphi,k}(y) = (1-y)\Theta(1-y)\,, \tag{4.18}$$

is optimal with respect to a derivative expansion as employed for the boson propagator (4.16). Ideally, this means that systematic uncertainties introduced by the truncation of higher order derivative terms are kept minimal. This regulator is therefore used for the bosonic fields in accordance with the majority of the literature on the balanced case. Only a small adjustment in the definition of y had to be made to allow for finite mass imbalance. Spin imbalance does not affect the bosonic fields directly.

A comment about consistency and applicability of the optimization criteria for the present case is in order. Originally, regulators of the "Litim" type (4.18) were devised for relativistic systems, where temporal and spatial derivatives are treated on equal footing. The usage of the Heaviside step function Θ, however, does not permit the inclusion of the linear complex frequency components of non-relativistic dispersion relations into the resulting $r_{\varphi,k}$. At first sight, this appears to be advantageous as it allows for an analytical treatment of the frequency sum as usual within the Matsubara formalism. On closer inspection, however, there are two less agreeable consequences. Firstly, the conditions upon which the optimization criteria in [231, 232] were formulated do not hold anymore and it is thus unlikely that the regulator (4.18) is still the optimal choice for the system at hand. Secondly, spatial and thermal modes are effectively regularized by completely different schemes. In particular, the running scale k does not affect thermal fluctuations at all, as they are "integrated" directly. This inconsistency may in principle add to the systematic error of the analysis.

For balanced systems, a Litim-type regularization has been benchmarked against a family of exponential cutoff functions that do incorporate frequency regularization [203]. Indeed, the exponential regulator produced results closer to the experimental values for the corresponding observables. As the deviations were on the percent level, regulators like (4.18) may still be considered suitable for an fRG analysis of the unitary Fermi gas. In particular, the exponential cutoff renders an analytic evaluation of the supertrace operation in eq. (4.12) impossible. The additional numerical effort entailed by this drawback makes (4.18) the most reasonable choice for the present work.

As a matter of course, the fermionic degrees of freedom have to be regularized as well. It is in principle possible to use a completely similar regulator function as for the bosonic case since it would fulfill the conditions (4.11). However, there are two peculiarities of the fermionic sector that should be taken into account when constructing $R_{\psi,k}$.

Firstly, the finite average chemical potential μ introduces a scale into the system that affects the behavior of fluctuations. Phenomenologically, the energy of any (real or virtual) excitation is measured with respect to this μ or, equivalently, the Fermi energy as already discussed in conjunction with the particular form of the kinetic term of the in-medium Schrödinger equation in sec. 3.2.1. Better convergence of the flow towards $k \to 0$ can therefore be expected when applying a corresponding prescription to the regulator function [55, 227]:

$$R_{\psi,k}(\mathbf{q}) = k^2 r_{\psi,k}(z)\,, \quad z = \frac{\mathbf{q}^2-\mu}{k^2}\,, \quad r_{\psi,k}(z) = \left[\mathrm{sign(z)} - \mathrm{z}\right]\Theta\left(1-|z|\right). \tag{4.19}$$

The inclusion of μ into the fermionic regulator effectively introduces somewhat of a disparity of scales for bosonic and fermionic regularization for a given scale k. While this should be of minor importance when

$k \to 0$, it further obscures any interpretation of k as a physical momentum or length scale for intermediate values of observables.

The second possible modification becomes relevant only for imbalanced systems. There are separate ψ_σ fields for the two fermion species and for any finite $\bar{h}$ and/or $\bar{m}$, their (free) propagator structure becomes different. It seems therefore obvious to require separate regularization as well, which can for example be implemented by defining $z_\sigma = \left(\mathbf{q}^2(1 \pm \bar{m}) - \mu \mp h\right)/k^2$. However, such a regularization scheme vastly complicates the calculation of flow equations for the fermionic sector without actually improving the results. In sec. 4.3.1, values for the critical temperature for both approaches are shown to agree within limits of numerical accuracy. Therefore, the balanced regulator (4.19), promoted to an "averaged" one, will be used for the derivation of the actual flow equation on p. 72 below and in app. D.

Initial conditions for the flow In order to comply with the constraints (4.6), the initial conditions $Z_{\varphi,\Lambda}$, $A_{\varphi,\Lambda}$, h_φ and $U_\Lambda(\rho)$ have to be set accordingly.

Introduced by a Hubbard-Stratonovich transformation, the boson fields are not dynamical in the ultraviolet. Therefore,

$$\lim_{k\to\Lambda\to\infty} A_{\varphi,k} = \lim_{k\to\Lambda\to\infty} Z_{\varphi,k} = 0\,. \tag{4.20}$$

Since a numerical integration of the flow equations, as it will be necessary in practice, always starts at some finite $k = \Lambda$, this limit alone is not of much help. Instead, initial conditions at the scale Λ are needed. The actual values of these wave function renormalization coefficients do not carry physical meaning, since observables like the fermion gap $|\Delta_0|^2 = h^2_{\varphi,0}\rho_{0,0}$ do not depend on them explicitly[3]. It is rather a question of numerical convenience to choose proper initial conditions that do not introduce an artificial stiffness into the system. In the present case, the cutoff will be $\Lambda = \mathcal{O}(1000\sqrt{\mu})$ and $A_{\varphi,\Lambda} := 1$.

The case of $Z_{\varphi,k}$ or rather $S_{\varphi,k}$ is somewhat more intricate. When naively calculating and solving the evolution equation $k\partial_k S_{\varphi,k}$, the linear frequency component is found to vanish logarithmically as $k \to 0$, leaving the boson propagator without any frequency dependence in the physical limit. This behavior is not unexpected as it has previously been found for purely bosonic systems [233,234]. It can be considered an artifact of the truncated derivative expansion for the inverse boson propagator (4.16), since the linear frequency dependence is replaced by a quadratic one $\sim V_{\varphi,k}q_0^2$ if such a term is taken into account [234]. Strictly speaking, the truncation (4.16) is therefore inconsistent. Fortunately, it turns out that the vanishing of $S_{\varphi,k}$ and the emergence of $V_{\varphi,k}$ largely counterbalance their respective effects on observables like the fermion gap [203]. Up to corrections of a few percent, it is therefore consistent to set $S_{\varphi,k} := 1$ not only for $k = \Lambda$ but also during the flow.

The order parameter potential is initially given by the Hubbard-Stratonovich boson mass term

$$U_\Lambda(\rho) = m^2_{\varphi,\Lambda}\rho\,. \tag{4.21}$$

For fixing the two parameters $m^2_{\varphi,\Lambda}$ and $h_{\varphi,\Lambda}$, only one constraint is available, the value of the fermion coupling eq. (1.4). Additionally, however, properties of the Feshbach resonance may be taken into account that have not been considered so far. It can be shown [228] that large $h_{\varphi,\Lambda} \sim \sqrt{\Lambda}$ corresponds to the universal broad resonance limit that is of interest here. While this does not yet determine the precise values, it has been shown that choosing

$$h_{\varphi,\Lambda} = \sqrt{6\pi^2\Lambda}\,, \qquad m^2_{\varphi,\Lambda} = \nu_\Lambda + \frac{h^2_{\varphi,\Lambda}}{6\pi^2}\Lambda\,, \tag{4.22}$$

leads to optimal convergence properties for the flow. This is due to the existence of an ultraviolet fixed point of the RG flow at the values given by eq. (4.22) which dominates the scaling behavior of $h_{\varphi,k}$ also for $k < \Lambda$ prior to the advent of a condensate [226].

The value for $m^2_{\varphi,\Lambda}$ is then dictated by the scattering solution for g_δ, see eq. (1.4), with $c_{\text{reg}} = 2/(3\pi)$ for the above regulator choice [55]. The parameter $\nu_\Lambda \sim (B - B_0)$ is a measure for the magnetic detuning from the resonance position and thus for the scattering length. Since only the unitary limit at resonance shall be investigated here, $\nu_\Lambda = 0$.

---

[3] The running fermion gap parameter Δ_k will be denoted without a bar if contributions beyond mean-field are included.

Flow equations All ingredients for a derivation of the explicit flow equations can now be brought together and plugged into the Wetterich equation (4.12). In the following, these flow equations along with some conceptual points are discussed. For details of the derivation, see app. D.
To begin with, the structure of the evolution equation for the effective order parameter potential is given by a projection of the Wetterich equation on vanishing fermion and constant boson fields,

$$k\partial_k\Gamma_k\big|_{\bar\psi=\psi=\varphi_2=0,\varphi_1=\sqrt{2\rho}} = k\partial_k U_k = \eta_{A,k}\rho U_k' + [k\partial_k U_k]^\psi + [k\partial_k U_k]^\varphi\,, \tag{4.23}$$

where the cartesian representation of the complex boson field $\varphi = 1/\sqrt{2}(\varphi_1 + i\varphi_2)$ has been employed. Without loss of generality, the condensate has been placed in the φ_1 direction. Here and further on, primes attached to U_k denote derivatives with respect to ρ. The first term on the RHS of eq. (4.23) results from the renormalization of ρ with $A_{\varphi,k}$ and involves the boson anomalous dimension $\eta_{A,k}$ which is defined as

$$\eta_{A,k} = -k\partial_k \ln A_{\varphi,k}\,. \tag{4.24}$$

The other two terms are contributions from the fermionic and the bosonic sector of Γ_k, respectively. Diagrammatically, the fermionic contribution $[k\partial_k U_k]^\psi$ is determined by an inner fermion loop,

$$[k\partial_k U_k]^\psi \sim \sum_{n=0}^{\infty}$$

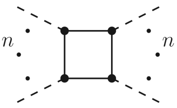

$$\cdot\,(\varphi^*\varphi)^n\,, \tag{4.25}$$

and therefore constitutes the mean-field contribution, cf. also sec 2.2.1.
Explicit expressions for the fermionic and bosonic contributions to $k\partial_k U_k$ are

$$[k\partial_k U_k]^\psi = \frac{k^5}{2\pi^2}\int_{\max[-\tilde\mu,-1]}^{1} \mathrm{d}\tilde z\,\frac{\sqrt{\tilde z+\tilde\mu}}{\sqrt{1+w_3}}\sum_{\sigma=\pm1}\sigma N_{\mathrm F}\left(\bar m(\tilde z+\tilde\mu)-\tilde h+\sigma\sqrt{1+w_3}\right), \tag{4.26a}$$

$$[k\partial_k U_k]^\varphi = \frac{\sqrt{2}k^5}{3\pi^2}\frac{1}{(1-\bar m^2)^{\frac{3}{2}}}\left(1-\frac{\eta_{A,k}}{5}\right)\left[\sqrt{\frac{1+w_1}{1+w_2}}+\sqrt{\frac{1+w_2}{1+w_1}}\right]\left[\frac{1}{2}+N_{\mathrm B}\left(\sqrt{1+w_1}\sqrt{1+w_2}\right)\right], \tag{4.26b}$$

where

$$N_{\mathrm F}(x) = \frac{1}{e^{x/\tilde T}+1}\,, \qquad N_{\mathrm B} = \frac{1}{e^{x/\tilde T}-1}\,, \tag{4.27}$$

and

$$w_1 = \frac{U_k'}{k^2}\,, \qquad w_2 = \frac{U_k' + 2\rho U_k''}{k^2}\,, \quad w_3 = \frac{h_{\varphi,k}^2\rho}{k^4}\,, \tag{4.28}$$

and quantities divided by k^2 are denoted with a tilde sign, e.g. $\tilde T \equiv T/k^2$.
The dependence of eq. (4.26a) on $w_3 \sim h_{\varphi,k}^2\rho$ instead of ρ and/or $h_{\varphi,k}$ separately guarantees the reproduction of the homogeneous mean-field results e.g. in fig. 4.1, if eq. (4.25) is integrated separately. If the unrenormalized potential $\bar U_k$ is considered instead, the flow of $\eta_{A,k}$ is decoupled and $\partial_k\bar h_\varphi = 0$ by construction. A crucial subtlety results from this decoupling: Even if $\eta_{A,k\to0}$ does not converge due to, e.g., singular behavior, the mean-field result for the effective potential can still be reproduced without the problem with $\eta_{A,k}$ even being noticed. This finding will be important in sec. 4.4.2 below.
Contributions renormalizing the bare Yukawa coupling are not taken into account in this work. It is consequently determined by the running of the boson anomalous dimension alone,

$$k\partial_k h_{\varphi,k} = \frac{1}{2}\eta_{A,k}h_{\varphi,k}\,. \tag{4.29}$$

The latter is therefore the only evolution equation that remains to be determined. It can be extracted by applying the following projection rule [55]:

$$\eta_{A,k} = -\frac{k}{A_{\varphi,k}}\frac{2}{1-\bar m^2}\frac{\partial}{\partial\mathbf{q}^2}\partial_k\left[\left(\bar{\mathcal P}_\varphi^{-1}\right)_{12}(0,\mathbf{q})\right]_{\mathbf{q}=0} \equiv \eta_{A,k}^{\psi,1}+\eta_{A,k}^{\psi,2}+\eta_{A,k}^{\varphi}\,. \tag{4.30}$$

Here, it is

$$\left(\bar{\mathcal{P}}_{\varphi}^{-1}\right)_{12}(\omega_n,\mathbf{q})\delta^{(4)}(p-q) = \frac{\overrightarrow{\delta}}{\delta\bar{\varphi}_1(-p)}\Gamma_k\frac{\overleftarrow{\delta}}{\delta\bar{\varphi}_2(q)}\Bigg|_{\bar{\psi}=\psi=\varphi_2=0,\varphi_1=\sqrt{2\rho_{0,k}}}, \tag{4.31}$$

see app. D for further details of the derivation.
Once again discriminating between fermionic and bosonic contributions, the explicit expression for the boson anomalous dimension is composed of

$$\begin{aligned}
\eta_{A,k}^{\psi,1} =& \frac{1}{1-\bar{m}^2}\frac{h_{\varphi,k}^2}{6\pi^2k(1+w_3)^{\frac{3}{2}}}\sum_{\sigma,\kappa=\pm1}(\tilde{\mu}+\kappa)^{\frac{3}{2}}\,\theta\left(\tilde{\mu}+\kappa\right)\\
&\cdot\left[\sigma N_{\mathrm{F}}\left(\bar{m}(\tilde{\mu}+\kappa)-\tilde{h}-\sigma\sqrt{1+w_3}\right)+\sqrt{1+w_3}N_{\mathrm{F}}'\left(\bar{m}(\tilde{\mu}+\kappa)-\tilde{h}-\sigma\sqrt{1+w_3}\right)\right], && (4.32a)\\
\eta_{A,k}^{\psi,2} =& -\frac{h_{\varphi,k}^2\bar{m}^2}{6\pi^2k(1-\bar{m}^2)}\int_{\max[-\tilde{\mu},-1]}^{1}\mathrm{d}\tilde{z}\frac{(\tilde{z}+\tilde{\mu})^{\frac{3}{2}}}{(1+w_3)^{\frac{5}{2}}}\sum_{\sigma=\pm1}\left[3\sigma N_{\mathrm{F}}\left(\bar{m}(\tilde{z}+\tilde{\mu})-\tilde{h}+\sigma\sqrt{1+w_3}\right)\right.\\
&\left.-3\sqrt{1+w_3}N_{\mathrm{F}}'\left(\bar{m}(\tilde{z}+\tilde{\mu})-\tilde{h}-\sigma\sqrt{1+w_3}\right)-\sigma(1+w_3)N_{\mathrm{F}}''\left(\bar{m}(\tilde{z}+\tilde{\mu})-\tilde{h}-\sigma\sqrt{1+w_3}\right)\right], && (4.32b)\\
\eta_{A,k}^{\varphi} =& \frac{\rho_{0,k}U_k''^2}{(1-\bar{m}^2)^{\frac{3}{2}}}\frac{\sqrt{2}}{3\pi^2k}\frac{1}{[(1+w_1)(1+w_2)]^{\frac{3}{2}}}\\
&\cdot\left[1+2N_{\mathrm{B}}\left(\sqrt{1+w_1}\sqrt{1+w_2}\right)-2N_{\mathrm{B}}'\left(\sqrt{1+w_1}\sqrt{1+w_2}\right)\right]. && (4.32c)
\end{aligned}$$

Here, the w_i are all evaluated at $\rho = \rho_{0,k}$ according to the discussion on page 69. Primes attached to the thermal distribution functions N_{F} and N_{B} symbolize derivatives with respect to their full arguments.

4.3 Fluctuation effects for the spin-imbalanced unitary gas

At the truncation level discussed extensively above, eqns. (4.23), (4.29) and (4.30) form a closed set of coupled differential equations that have to be solved in order to obtain predictions for physical observables. If the bosonic contributions are neglected, the right hand sides do not depend on the order parameter potential U_k or its derivatives in any way and direct integration with respect to k is possible, though generally not in a closed analytical form. The full set of equations, on the other hand, is of a highly nonlinear *partial differential* nature and can only be solved numerically. In order to demonstrate the approach adopted in this work, for comparison to different techniques and also to present some findings of phenomenological relevance, mass imbalance is set to $\bar{m} = 0$ for the present section.
From a mathematical point of view, this vastly simplifies the explicit expressions for the evolution equations. In particular, the fermionic contribution to $k\partial_k U_k$ can now be written in closed form, as the explicit momentum dependence is removed from the Fermi distribution functions:

$$\begin{aligned}
\left[k\partial_k U_k\right]_{\bar{m}=0}^{\psi} =& \frac{k^5}{3\pi^2\sqrt{1+w_3}}\left[\Theta(\tilde{\mu}+1)(\tilde{\mu}+1)^{\frac{3}{2}}-\Theta(\tilde{\mu}-1)(\tilde{\mu}-1)^{\frac{3}{2}}\right]\\
&\cdot\left[N_{\mathrm{F}}\left(\tilde{h}+\sqrt{1+w_3}\right)-N_{\mathrm{F}}\left(\tilde{h}-\sqrt{1+w_3}\right)\right].
\end{aligned} \tag{4.33}$$

The contribution $\eta_{A,k}^{\psi,2}$ vanishes completely as it is proportional to $\bar{m}^2$. The resulting reduced system of equations will be used in sec. 4.3.1 to illustrate the concepts and numerical techniques employed here. The goal is to demonstrate the reliability of the method and its advantages that justify the higher numerical cost and conceptual complexity compared to the other approaches that will be presented alongside.
Considering the mass-balanced system first may also be expected to reduce the richness of phenomena observed. In particular, signs of inhomogeneous phases are not necessarily expected to occur, cf. the discussion in sec. 4.1 above. Nevertheless, there are still phenomenologically important findings that are best discussed in the present setting as they are less obscured by the richness of structures found in the fully imbalanced phase diagram. Sec. 4.3.2 is going to deal with these results.

4.3.1 Implementations and reliability analysis

For the present work, three different solution strategies have been applied: a discretization of the order parameter potential on a grid and consistent numerical integration of the flow equations, a simplified version of this approach along the lines of [235, 236] and the widely used polynomial expansion of U_k. It turns out that the consistent grid approach is the most demanding, but also by far most reliable alternative. In fact, both of the other approaches exhibit not only quantitatively deviating results but also serious qualitative drawbacks.

Although, strictly speaking, only the deep infrared limit $k \to 0$ carries physical meaning, the numerical treatment which is mainly about the behavior at finite k teaches a lot about the general behavior of the flow. As some of these lessons are of importance for the phenomenological understanding of the results presented in sec. 4.3.2, the different numerical implementations will be discussed in some detail in the following. Furthermore, a thorough discussion of possible sources for systematic uncertainties is in order for any numerical technique. Last but not least, this section may serve as a guideline for future approaches to related problems.

Grid representation Being partial differential equations in terms of the RG scale and the order parameter, a direct numerical solution of the full set of flow equations requires a discretization of both k and ρ space.

The basic idea is to put the effective potential on a lattice in ρ which may be deformed to concentrate its nodes where phenomenologically relevant behavior like the formation of a nontrivial global minimum is expected to occur. Each point is then k-evolved separately. This latter evolution is also discretized and for each (finite) RG step δk, the numerically nonlocal quantities U_k' and U_k'' are computed. One of the main challenges is a proper determination of those derivatives. Generally, derivative operations tend to "roughen" the shape of a function. The numerical consequence is that any errors which might have been induced by the inexactness of discretized derivative operators in general and at the boundaries of the grid in particular or even the finite precision of floating point number representation are amplified. This is particularly severe in the regime of large $k \sim \mathcal{O}(\Lambda)$. The bosonic contribution to $k\partial_k U_k$ in eq. (4.26b) is highly sensitive to non-smooth behavior especially of U_k'', essentially amplifying any roughness by a factor of $\mathcal{O}(k^4)$.

This inherent instability of the flow equations with respect to numerical inaccuracies may be devastating already at very early stages of the evolution. It becomes less severe only for $k \ll \sqrt{\mu}$. A careful smoothing of U_k'' has therefore proven mandatory at least for $k \gtrsim \sqrt{\mu}$. For large $k \gg \sqrt{\mu}$, a polynomial fit of U_k, whose derivatives can even be determined analytically, is sufficiently precise. Changes to the linear initial potential U_Λ (4.21) are small yet. Lowering k to $\mathcal{O}(\Lambda/10)$ and further down to $k \approx 2\sqrt{\mu}$, U_k' and subsequently also U_k'' have to be computed with higher precision. A higher-oder global polynomial fit is not useful anymore at some point as it tends to introduce artificial oscillatory behavior [142]. Therefore, local *basis splines* are applied, guided by analytic knowledge about the functional shape of U_k. Finally, at $k \lesssim \sqrt{\mu}/2$, a simple five-point discretization of the derivative operators is sufficient, as numerical errors are not amplified anymore.

As a word of caution it may be mentioned that noise filtering in the frequency domain, for example by means of Gaussian or Savitzky-Golay-type filters [237], does not work very well for the problem at hand. The deformations of the spectrum introduced by these methods lead to a relative amplification of low frequency components that do in some cases introduce self-stabilized artificial minimums of U_k. As they are not easily distinguished from the physical minimum, they may spoil the identification of the true ground state of the system.

For the actual RG evolution, i.e. integration in k space, standard numerical techniques have been applied [238]. Starting from some sufficiently large initial values $k = \Lambda$, a step-size-controlled implicit Runge-Kutta solver of fifth order Gauss type is used to lower k down to an acceptably small value k_{IR}.

There are plenty of numerical "screws" in this setup that may and even have to be tuned in order to check for artifacts. This includes the size and resolution of the ρ-grid, its deformation properties, details of the smoothing process and error limits for the Runge-Kutta solver. While it is hard to achieve complete certainty that no artifacts are present, all of these options have been thoroughly tested and deviations were found to be at most at the few percent level. In the following, these deviations will be used to provide estimates for uncertainties of computed observables. Finally, the initial scale Λ is set to $1000\sqrt{\mu}$. While

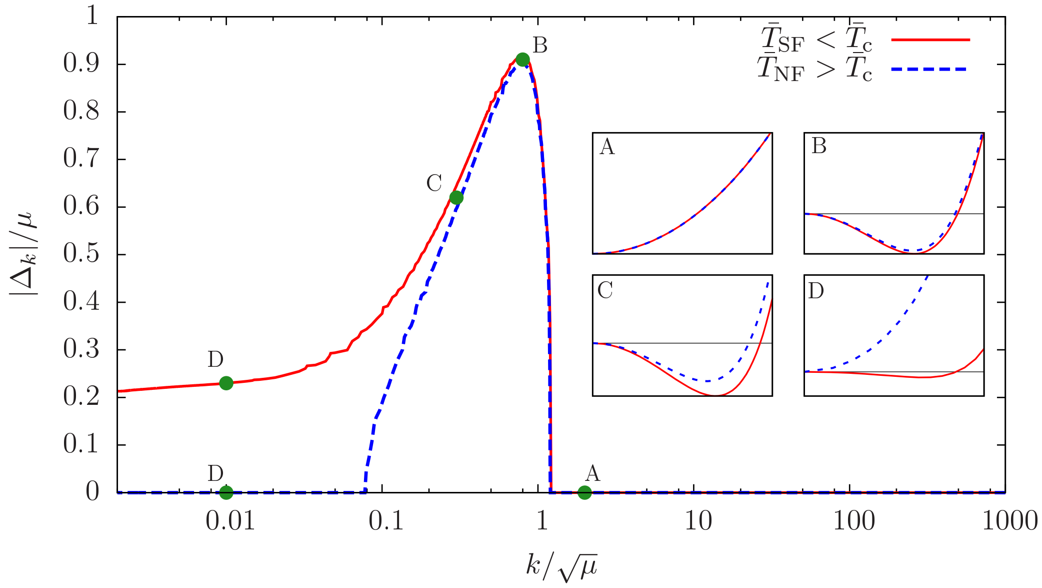

Figure 4.6: RG evolution of the order parameter $|\Delta_k| = h_{\varphi,k}\sqrt{\rho_{0,k}}$ on a ρ grid for $\bar{h} = 0.3$ and $\bar{T}_{\rm SF} = 0.275$ (red, solid lines) or $\bar{T}_{\rm NF} = 0.28$ (blue, dashed line), respectively. The slight "wiggling" is caused by numerical inaccuracies. The insets show the shape of U_k for different values of $k/\sqrt{\mu} = 2.0$ (A), 0.8 (B), 0.3 (C) and 0.01 (D).

higher values vastly increase the effort necessary for the full system to keep amplified noise under control, studies of mean-field flows show that there is very little dependence on Λ left at these scales (sub-percent level for, e.g., $\bar{T}_{\rm c}$).

The determination of $k_{\rm IR}$ merits a somewhat more detailed discussion as it is already connected to the occurrence and interpretation of physical phenomena. In fig. 4.6, the RG evolution of the flowing order parameter $|\Delta_k| = h_{\varphi,k}\sqrt{\rho_{0,k}}$ is depicted for fixed $\bar{h} = 0.3$ and two temperatures $\bar{T}_{\rm SF} < \bar{T}_{\rm c} < \bar{T}_{\rm NF}$ slightly below and above the critical temperature for condensation at this particular value for $\bar{h}$. The respective data is obtained in the most straightforward manner: for each RG step, the global minimum of U_k is read off. Although the blue (dashed) line corresponds to a configuration without symmetry breaking, a "temporally" nontrivial minimum occurs at some scale $k_{\rm sb}$ and vanishes again at $k_{\rm sr}$.

This behavior will be discussed in more detail from a physical point of view in sec. 4.3.2, but it has to be taken into account on purely numerical grounds as well. In order to obtain perfectly reliable information whether a certain $(\bar{T}, \bar{h})$ configuration leads to spontaneous symmetry breaking, the flow has to be integrated to $k = 0$, as $k_{\rm sr}$ may in principle assume any finite value. In fact, $k_{\rm sr} \to 0$ when a second order phase transition is approached. However, the drop of $k_{\rm sr}(\bar{T}, \bar{h})$ is found to be rather steep across the phase transition. It was therefore found sufficient to evolve down to $k \sim 10^{-2}\sqrt{\mu}$ in order to arrive at sub-percent-level precision for the location of the phase boundary. For first-order transitions, the situation is even more comfortable and will be commented on page 79 below.

For observables like the fermion gap $|\Delta_{k\to 0}|$ in the symmetry broken regime or particle densities in general[4], the situation is somewhat more complicated. Their values are physical only in the strict IR limit $k \to 0$. In fact, the red (solid) line in fig. 4.6 describing the evolution of the order parameter, has still a finite slope at $k_{\rm IR} \sim 2\cdot 10^{-3}\sqrt{\mu}$ where the flow was stopped. It is thus not fully converged and the physical value will lie somewhat below the finite-$k_{\rm IR}$ result of $|\Delta_{k_{\rm IR}}|/\mu = 0.21$.

From an extrapolation of evolution curves like the red (solid) one in fig. 4.6 to $k = 0$, uncertainties are estimated to be on the percent level if $k_{\rm IR} \lesssim 10^{-3}\sqrt{\mu}$. However, deep inside the symmetry broken phase, such values are difficult to reach and the corresponding estimates for observables may be afflicted by larger uncertainties.

Mapping the $\bar{h} - \bar{T}$ plane, the phase diagram shown in fig. 4.7 is obtained. The green (thick, dot-dashed)

---

[4] Results for the densities or the Bertsch parameter ξ are not discussed in more detail in this chapter. The values obtained from the system of flow equations presented here are only marginally improved with respect to the mean-field prediction. As these are fermionic observables, the simplistic treatment of the fermion propagator in the ansatz (4.14) does not allow for an of improvement beyond this level.

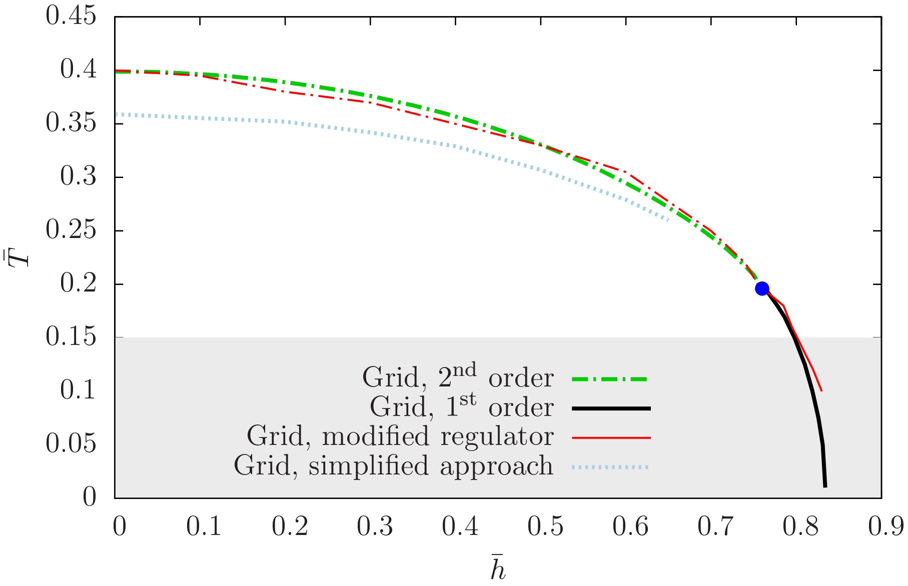

Figure 4.7: Phase boundaries for the spin-imbalanced unitary Fermi gas obtained with different grid methods. The thick green (dot-dashed) and black (solid) lines represent the consistent approach with averaged fermionic regularization. The thin (red) lines were produced with the same method but using separate regulator functions for the fermion species [239]. The light blue (dotted) line is obtained from the simplified grid approach. Gray shading indicates the region of high $k_{\mathrm{IR}} \sim 10^{-1}\sqrt{\mu}$, see main text for details.

and black (thick, solid) lines denote phase boundaries of second or first order, respectively, that have been found with the grid approach described so far. Focusing on questions of the implementation and once again deferring discussions of the phenomenology to sec. 4.3.2, it is in particular the gray shaded region that has to be addressed. It marks the domain of low temperatures $\bar{T} \lesssim 0.15$, where it becomes increasingly difficult to reach the above requested $k_{\mathrm{end}} \sim 10^{-2}\sqrt{\mu}$. Rather, $k_{\mathrm{end}} \sim 10^{-1}\sqrt{\mu}$ has been used for $\bar{T} < 0.1$. On the one hand, this is caused, as indicated above, by the large values for the fermion gap in the symmetry broken region that renders the shape of U_k less favorable. On the other hand and more importantly, this is due to the very structure of the fermionic contribution (4.33) to $k\partial_k U_k$. In the limit $\bar{T} \to 0$, the RHS of the Wetterich equation is rendered non-analytic. This is due to the Fermi distribution functions N_{F} becoming Heaviside step functions. While it might in principle be possible to think of a mathematically clean way to solve the flow equations in a distributional sense, the naïve numerical approach is bound to fail, as the approximate derivative operators do not capture the essential contributions anymore. Traces of this problem occur already at finite, but low $\bar{T}$ where the slopes of the respective Fermi functions are still finite but very large. Overall, this makes an integration of the flow equations more and more difficult as $\bar{T} = 0$ is approached, utterly inhibiting it at $\bar{T} = 0$ and being largely responsible for the behavior associated with the gray shaded region in fig. 4.7.

Fortunately, the transition from the superfluid to the normal phase is found to be of first order in this regime. As will be discussed in more detail on p. 79 below, this alleviates the constraints on k_{IR} somewhat. It turns out that $k_{\mathrm{IR}} \sim 10^{-1}\sqrt{\mu}$ is sufficiently small to locate the phase transition with a precision comparable to the high-temperature regime.

For comparison, red (thin) lines that represent the results when separate regulator functions for the fermionic species are employed (see p. 70f), are shown in fig. 4.7 as well. These data [239] are somewhat sparse and less precise, as the more complicated form of the flow equations entailed by this regularization procedure increases numerical cost. Nevertheless, the results agree well within numerical errors particularly of the additional integration procedures involved in the modified approach. This finding confirms the stability of the method with respect to (modest) changes of the regularization procedure: If the Wetterich equation was solved exactly, there could by definition not be a dependence of physical observables on the choice of the regulator function, cf. eq. (4.11a). Such a dependence may be introduced by the approximate nature of the ansatz for Γ_k. Its absence in the present case therefore confirms the quality of the chosen truncation.

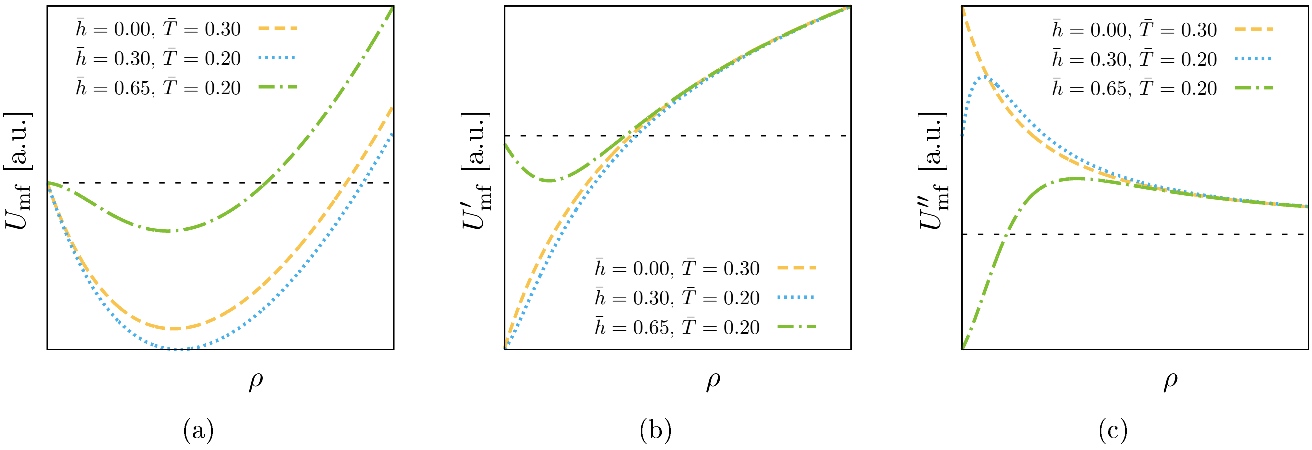

Figure 4.8: Mean-field effective order parameter potential $U_{\rm mf}$ (a) and its first (b) and second (c) derivatives w.r.t ρ for three different configurations. They are used as initial conditions for the simplified grid approach.

Simplified grid approach In [235], a modified approach to the solution of fRG flow equations on a grid was suggested. There, the mean-field effective order parameter potential is used as an initial condition for the flow. Since bosonic fluctuations predominantly occur at low k, the now purely bosonic-driven evolution is started at some $k \sim \mathcal{O}(k_{\rm F})$. In principle, this scheme promises a major simplification of the problem, as the numerically sensitive regime of high $k \sim \mathcal{O}(\Lambda)$ is avoided. For the two-dimensional imbalanced Fermi gas, it has indeed been employed in [236] to investigate the impact of bosonic fluctuations on quantum phase transitions.

Applying this prescription to the theory considered in this work yields the light blue (dotted) prediction for the phase transition in fig. 4.7. Having obtained $U_{\rm mf}$ by integrating eq. (4.33) from $\Lambda = 10^4\sqrt{\mu}$ to $k_{\rm IR} = 10^{-3}\sqrt{\mu}$, a subsequent bosonic flow beginning at $k_{\rm bos} = \sqrt{1.5\mu}$ with $U_{\rm mf}$ as initial condition is evolved.

For small spin imbalance parameter and even improving towards larger $\bar h$, agreement between the simplified and the full grid approaches for the phase transition may be considered reasonable. The critical temperature appears always to be somewhat underestimated. Moving to lower temperatures and/or even larger $\bar h$, however, the simplified flow becomes more and more unstable until it does not converge to any acceptable $k_{\rm IR}$ anymore. While it might in principle be possible to push the limits of this behavior by tuning e.g. $k_{\rm bos}$, there is a fundamental problem with this approach that would only be covered, but not resolved.

By construction, the effective action is a *convex* quantity, i.e. its second derivative is positive or zero everywhere. It can be shown [240] that a truncation of the type of the ansatz employed here (see eq. (4.14)) reproduces this feature, while the mean-field approximation does not. Indeed, the former fact can already be discerned from the insets of fig. 4.6. The latter implies that the initial condition for the simplified grid approach exhibits rather strong variations which are found to become larger as $\bar T$ is decreased or $\bar h$ is increased, see fig. 4.8. In the context of numerical noise problematics, it was already discussed on page 75 above that the bosonic contribution $[k\partial_k U_k]^\varphi$ to the flow of the effective potential is very sensitive to variations in particular of U''_k. Furthermore, its dependence on $\sqrt{1+w_1}$ and $\sqrt{1+w_2}$ (see eq. (4.26b)) renders large negative U'_k, as they appear for low-$\bar T$ mean-field potentials in the vicinity of the origin (see fig. 4.8b), potentially problematic.

When integrating the full set of flow equations consistently, bosonic fluctuations continuously "smear out" variations in U_k which are introduced by the fermionic contributions. In the simplified approach, however, the initial mean-field potential equips the bosonic flow with large values for U'_k and U''_k right at the beginning of the evolution, where k is still fairly large. As $[k\partial_k U_k]^\varphi \sim k^4$, bosonic fluctuations are vastly amplified. For small $\bar h$ and intermediate $\bar T$, this leads to a disproportionate suppression of condensation, effectively lowering the prediction for the critical temperatures. In the low $\bar T$ or large $\bar h$ regimes, the properties of $U'_{\rm mf}$ are such that the flow equations eventually become mathematically invalid. This is where the phase transition line ends in fig. 4.7.

Formulated in different terms, these observations can be traced back to the fact that bosonic and fermionic fluctuations are not treated on equal footing. Their regularization schemes are effectively different and this inconsistency eventually entails limitations of the procedure. Due to this fundamental issue, the simplified grid approach is not used in this work. Although there is a regime where it yields reasonable results, caution is in order at least if it is applied to the present physical system.

Polynomial expansion The numerically most convenient approach to solving the system of flow equations relies upon a polynomial expansion of the order parameter potential U_k as introduced in eq. (4.15). Since the ρ derivatives of U_k can now be expressed with the help of the respective coefficients, the flow is described by a set of *ordinary* differential equations which is in general far easier to integrate.
In chap. 3 of this work, an extensive discussion of polynomial (vertex) expansions of the order parameter potential has been given. In principle, fRG has to struggle with the same problems as the mean-field approach presented there due to the expansion about $\rho = 0$. As soon as the immediate vicinity of second order transitions to the normal phase is left, an expansion about the origin has to include very high order terms to produce reasonable results for the nontrivial minimum. In order to circumvent this costly issue, the expansion in eq. (4.15) is about the k-dependent minimum $\rho_{0,k}$ of U_k.
In the ultraviolet, the global minimum of the effective potential is always zero, as U_Λ is linear in ρ by construction, see eq. (4.21). The flow of the effective potential is then determined by a hierarchy of evolution equations

$$\partial_k p_k = -\partial_k U_k|_{\rho=0}\,, \quad \partial_k m^2_{\varphi,k} = \partial_k U'_k|_{\rho=0}\,, \quad \partial_k \lambda_{\varphi,k} = \partial_k U''_k|_{\rho=0}\,, \quad \dots\,, \tag{4.34}$$

for the expansion coefficients evaluated at $\rho_{0,k} = 0$.
If the system exhibits spontaneous breaking of the U(1) symmetry in the infrared, a nontrivial minimum $\rho_{0,k} \neq 0$ has to occur at some point in the flow. The crucial assumption is now that this new global minimum evolves continuously out of the origin as k is lowered. In this case, the linear coefficient $m^2_{\varphi,k_{\mathrm{sb}}}|_{\rho=0}$ is bound to change sign at the scale k_{sb} where $\rho_{0,k}$ becomes finite for the first time. For $k < k_{\mathrm{sb}}$, the system (4.34) has to be replaced in order to allow for the expansion point to continuously evolve. This requirement can be formulated mathematically. The linear coefficient of the effective potential *at* the nontrivial minimum vanishes by definition and so does its total scale derivative:

$$0 = \frac{\mathrm{d}}{\mathrm{d}k} U'_k|_{\rho=\rho_{0,k}} = \partial_k U'_k|_{\rho=\rho_{0,k}} + \left(\partial_k \rho_{0,k}\right) U''_k|_{\rho=\rho_{0,k}} = \partial_k U'_k|_{\rho=\rho_{0,k}} + \lambda_{\varphi,k} \partial_k \rho_{0,k}\,. \tag{4.35}$$

This gives an evolution equation for the global minimum that replaces the one for the linear coefficient $m^2_{\varphi,k}|_{\rho=\rho_{0,k}} = 0$. Since $\rho_{0,k}$ is supposed to emerge continuously, the flow equations for the other coefficients do not have to be changed structurally. They just have to be evaluated at $\rho = \rho_{0,k}$ now:

$$\partial_k p_k = -\partial_k U_k|_{\rho=\rho_{0,k}}\,, \quad \partial_k \rho_{0,k} = -\partial_k U'_k|_{\rho=\rho_{0,k}} \cdot \lambda^{-1}_{\varphi,k}\,, \quad \partial_k \lambda_{\varphi,k} = \partial_k U''_k|_{\rho=\rho_{0,k}}\,, \quad \dots\,. \tag{4.36}$$

If $\rho_{0,k}$ should be found to vanish continuously at some $0 < k_{\mathrm{sr}} < k_{\mathrm{sb}}$, the set of eqns. (4.34) is employed again. This behavior is the exact equivalent of the one symbolized by the blue (dashed) line in fig. 4.6.
For balanced unitary Fermi gases, this approach gives reasonable estimates for the critical temperature and the fermion gap $|\Delta_0|^2$ already for a leading order (parabolic) truncation [55]. In ref. [203], expansions up to $\mathcal{O}\left(\rho^5\right)$ were investigated and improvement of the numerical values for these observables could be achieved in some cases. At least for low temperatures, however, higher order truncations may introduce numerical artifacts as correspondingly high derivatives of the RHS of eq. (4.33) are required. Since the latter involves Fermi distribution functions N_{F} which become step-like in the zero temperature limit, $\partial_k U^{(n)}_k$ may become very large for higher n which makes the systems (4.34) or (4.36) *numerically stiff*. The low-temperature problematics found for the grid representation above are thus not solved, but rather worsened by the polynomial approach.
Applying the polynomial expansion to spin-imbalanced systems, the results for the phase boundary appear to be reasonable for low to intermediate $\bar{h}$, see fig. 4.9 and ref. [241]. The grid solution is approached for higher order truncations at least as long as the transition is of second order.
In order to understand why the polynomial approach breaks down when advancing towards the domain of first-order transitions for large $\bar{h}$, it is necessary to revisit the assumptions made. For the set of equations (4.34) and (4.36) to be properly applicable, the nontrivial minimum has to emerge and/or

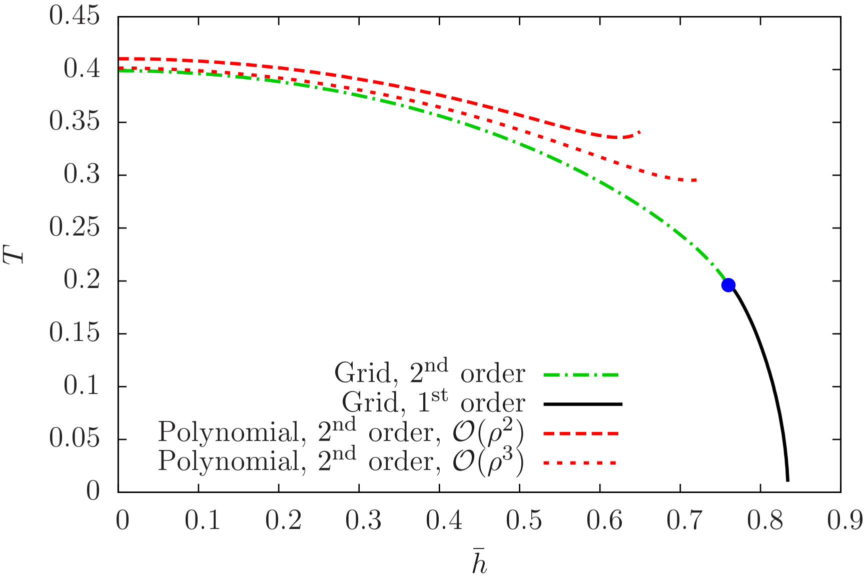

Figure 4.9: Phase boundaries for the spin-imbalanced unitary Fermi gas obtained with the consistent grid (green/black, dot-dashed/solid line) versus polynomial approaches of different order (red, dashed/dotted lines).

vanish continuously. Otherwise, the scales k_{sb} and/or k_{sr} cannot be discerned. Switching between (4.34) and (4.36) then does not take place properly and the expansion is performed around an unsuitable ρ that does not represent the global minimum of U_k anymore.

Fig. 4.10 displays the behavior of the flowing order parameter $|\Delta_k|$ across a first-order phase transition at $\bar{T} = 0.17$ and $\bar{h} \geq 0.78$ as obtained from the grid. The emergence of a finite $|\Delta_k| \sim \sqrt{\rho_{0,k}}$ in the RG flow is steep, yet still continuous - but its vanishing in the normal phase is not. This can be understood from the insets which do again display the evolution of U_k itself. For $k_{\mathrm{C}} = 0.5\sqrt{\mu}$, which is close to k_{sr} for the IR-symmetric configuration (blue, dashed line), the local minimum at finite $|\Delta_k|$ is not moved notably closer to the origin. This is in contrast to the behavior observed in the vicinity of second-order transitions discussed above. Instead, the minimum is raised until it does not represent a global extremum of the potential anymore. This is the reason for the slight up-bending at large $\bar{h}$ of the polynomial phase boundaries in fig. 4.9. As symmetry restoration is not properly identified, spurious condensates "survive" at much higher temperatures.

Thus, one of the conditions for the naïve polynomial approach is violated. This behavior cannot be detected directly in the way described so far. A possibility to circumvent this issue would be to evolve $p_k|_{\rho=0}$ alongside the ground state pressure $p_k|_{\rho=\rho_{0,k}}$, even if $\rho_{0,k}$ becomes finite. Comparing these two values gives insight into the relative "height" of the nontrivial minimum and helps to identify k_{sr}. However, a comparison of these two values basically involves global properties of the potential for the reproduction of which the polynomial approach is not designed. Although first-order phase transitions may in principle be identified again, their location is found to be imprecise and error-prone even at mean-field level. This can be expected to worsen upon inclusion of bosonic fluctuations. The approach to convexity and the emergence of a kink at $\rho_{0,k\to 0} > 0$ of U_k as $k \to 0$ renders global representations by polynomial series more and more involved and finally asymptotic, cf. inset (D) of fig. 4.10.

These problematics arising for the polynomial approach from the domain for large $\bar{h}$ turn out to be a benefit for the grid representation. The different way of "symmetry restoration" compared to the vicinity of second order phase boundaries leads to a substantial raise of the scale $k_{\mathrm{sr}} \sim 0.5\sqrt{\mu}$ which does not go to zero anymore across the transition. Therefore, the phase transition may reliably be detected even in the low $\bar{T}$ regime of the phase diagram, cf. also the gray shaded region in fig. 4.7 where $k_{\mathrm{IR}} \sim 10^{-1}\sqrt{\mu}$.

The overall conclusion is that, for imbalanced unitary Fermi gases in three spatial dimensions, the fRG equations should be solved consistently on an order parameter grid. Neither the polynomial method nor the simplified grid approach are found to be sufficiently reliable in particular in the large $\bar{h}$ regime, not even speaking of the intricacies introduced by mass imbalance. Fortunately, the choice of "averaged" fermion regularization (4.19) vastly reduces numerical cost and provides a manageable way to investigate

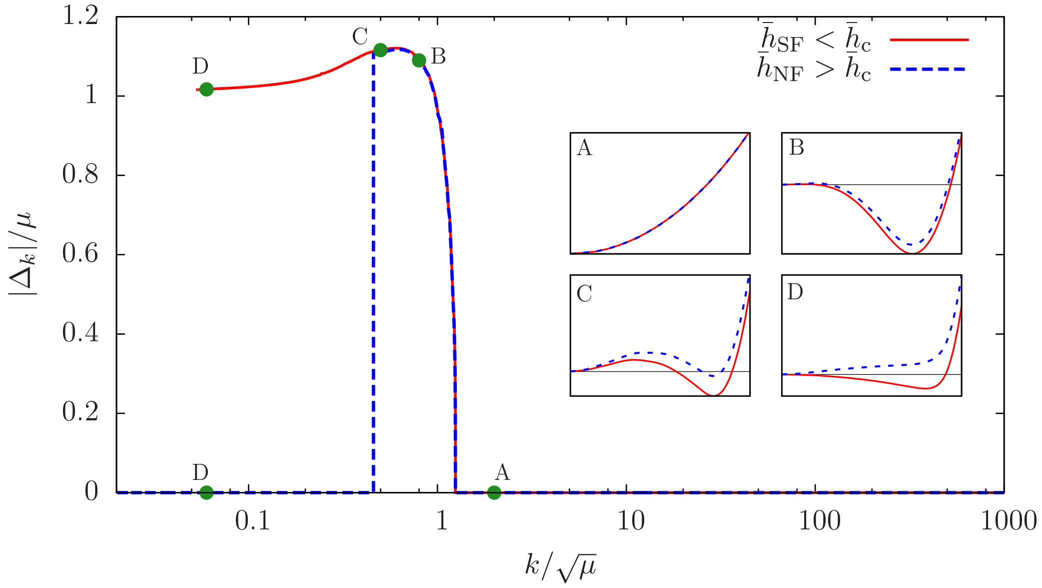

Figure 4.10: RG evolution of the order parameter $|\Delta_k| = h_{\varphi,k}\sqrt{\rho_{0,k}}$ on a ρ grid for $\bar{T} = 0.17$ and $\bar{h}_{\mathrm{SF}} = 0.78$ (red, solid lines) or $\bar{h}_{\mathrm{NF}} = 0.79$ (blue, dashed line) respectively. The insets show the shape of U_k for different values of $k/\sqrt{\mu} = 2.0$ (A), 0.8 (B), 0.5 (C) and 0.06 (D).

the beyond-mean-field phenomenology of imbalanced Fermi gases on solid grounds.

4.3.2 Phenomenology of the spin-imbalanced unitary gas

Phase diagram Having shown the phase diagram obtained with the fRG grid approach already twice in figs. 4.7 and 4.9 above for rather technical purposes, a discussion of the physical findings is now in order. In fig. 4.11, the fRG results are shown once more (thick lines), this time alongside the mean-field data obtained from a minimization of eq. (4.2).

The qualitative phase structure does not change compared to mean field: for small $\bar{h}$, the transition from the superfluid to the normal phase is of second, beyond a critical point of first order. The quantitative predictions are, however, modified quite dramatically. As expected, the critical temperature is lowered for small to intermediate $\bar{h}$. The result in the balanced case, $\bar{T}_{\mathrm{c}} = 0.40$, is in good agreement with recent quantum Monte Carlo studies [242] as well as experimental [110] findings.

Intuitively, it appears to be clear that the effect of the “additional” bosonic fluctuations included by the fRG approach tends to counteract ordering, thus lowering the manifold of critical temperatures $\bar{T}_{\mathrm{c}}(\bar{h})$ also for general $\bar{h}$. However, the actual results as shown in fig. 4.11 indicate a more complex scenario. Firstly, the critical point where the order of the phase transition changes, is not only found at lower temperatures but also slightly larger spin imbalances: $\left(\bar{T}_{\mathrm{cp}}^{\mathrm{MF}}, \bar{h}_{\mathrm{cp}}^{\mathrm{MF}}\right) = (0.37, 0.70)$ versus $\left(\bar{T}_{\mathrm{cp}}^{\mathrm{fRG}}, \bar{h}_{\mathrm{cp}}^{\mathrm{fRG}}\right) = (0.20, 0.76)$. The precise localization in the fRG case should be taken with a grain of salt, being numerically rather challenging. In particular, the apparent coincidence of the fRG critical point with the crossing of transition lines from the two approximation schemes as apparent in fig. 4.11 may be purely accidental.

The existence of such a crossing itself and consequently the larger extent of the superfluid phase found by fRG is, on the contrary, firmly established. Extrapolating the phase boundary down to $\bar{T} = 0$, a critical value for the spin imbalance of $\bar{h}_{\mathrm{c}}^{\mathrm{fRG}} = 0.83$ is found while $\bar{h}_{\mathrm{c}}^{\mathrm{MF}} = 0.807$. It can therefore be concluded that bosonic fluctuations *stabilize* superfluid ordering at large spin imbalances and low temperatures rather than destroying it. Whether the phase boundary is in this way pushed beyond the zero temperature Clogston-Chandrasekhar limit [173,174] of $\bar{h}_{\mathrm{CC}} = |\Delta_0|/\sqrt{2}$, where $|\Delta_0|$ is the fermion gap at $\bar{h} = 0$, cannot be determined reliably within the present framework. While the localization of the phase transition itself does not suffer from convergence issues as discussed in sec. 4.3.1 above, this is not true for estimates of $|\Delta_0|$ at low $\bar{T}$. Within the numerical uncertainties in particular for $|\Delta_0^{\mathrm{fRG}}|$, the respective Clogston-Chandrasekhar limit and $\bar{h}_{\mathrm{c}}^{\mathrm{fRG}}$ do coincide. As the only way to evade the energetic argument given by Clogston and Chandrasekhar would be an increase of the zero-temperature fermion gap with growing spin imbalance, the observed coincidence is physically reasonable despite numerical uncertainties. Furthermore,

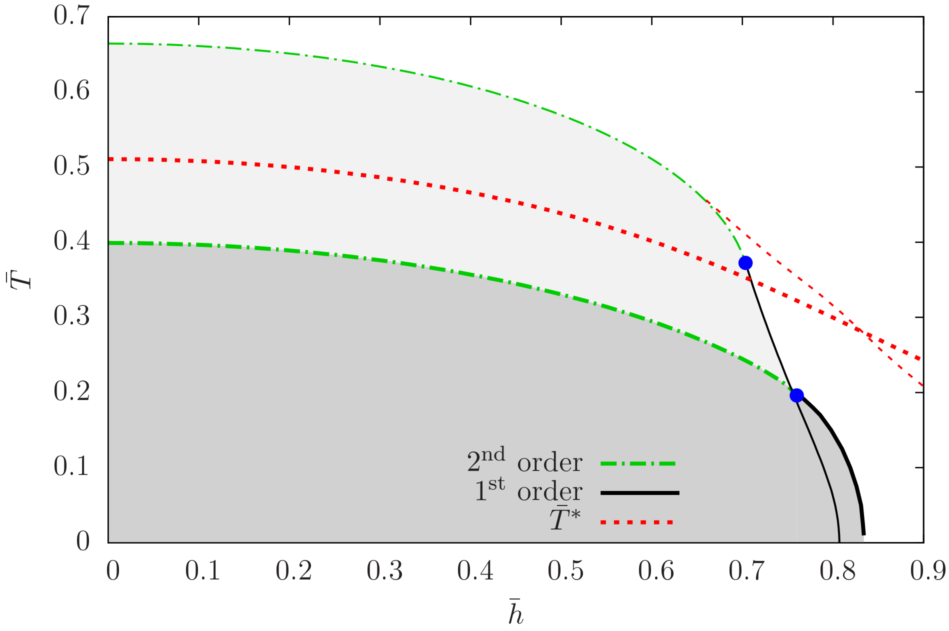

Figure 4.11: Comparison of mean-field (thin lines, light shading) versus fRG grid results (thick lines, dark shading) for the phase diagram of a unitary Fermi gas with spin imbalance. Green (dot-dashed) and black (solid) lines symbolize phase transitions of second or first order, respectively, whereas blue dots denote the corresponding critical points. The red (dotted) lines delimit the regime of "precondensation".

recent experimental results do indeed indicate an enhanced critical imbalance $\bar{h}_c^{\text{exp}} = 0.89$ associated with a first order phase transition [243]. While quantitative agreement is not perfect, the qualitative finding supports the validity of the fRG result and encourages a further investigation of the reasons underlying this behavior.

Understanding the stabilizing effects of bosonic fluctuations from the evolution equations (4.26), (4.29) and (4.32) is far from trivial. First and foremost, this is due to the complicated nonlinear structure of the equations, inhibiting a straightforward interpretation in terms of established many-body terminology. Secondly, the bosonic degrees of freedom are not fundamental and there are thus several equivalent formulations of or perspectives on the issue.[5] From the point of view adopted in this work, the enhanced $\bar{h}_c$ is a consequence of feedback from the bosonic contributions into the fermionic flow in terms of a renormalization of the effective vertices, as symbolically shown in eq. (4.25). A more detailed explanation requires an in-depth analysis of the influence of (spin) imbalance on the fermionic flow equation (4.33). To this end, the role of the "symmetry restoration scale" k_{sr} introduced in sec. 4.3.1 has to be revisited first.

Symmetry restoration and precondensation As discussed above and shown in figs. 4.6 and 4.10, for certain normal fluid configurations in the vicinity of a phase transition, a finite $|\Delta_k|$ may occur during the flow without persisting to $k \to 0$. Instead, it vanishes again at some scale k_{sr} which can be considered to "restore" the global U(1) symmetry. Analogous behavior is known to occur in relativistic systems as well [244]. As this happens by definition at finite $k > 0$, a straightforward interpretation in terms of physical observables, let alone quantitative predictions are, strictly speaking, not admissible.

Nevertheless, the construction principles of the regulator (4.11) establish a rough coincidence of the RG scale k with physical momenta q. It is in general not exact and moreover depends on the specific shape of $R_{\varphi,k}$, inhibiting the extraction of any quantitatively reliable prediction. The coincidence itself, however, may be exploited to obtain insight into the qualitative behavior of the system also beyond global (infrared) properties.

In this sense, the existence of $|\Delta_k| > 0$ for $k_{\text{sb}} > k > k_{\text{sr}}$ in the regime below the red (dotted) lines in fig. 4.11 may be linked to the physics of *precondensation* and/or *pseudogap* states. In [245], it was first found that the mean-field approximation overestimates the critical temperature when leaving the strict

---

[5] The fermionic and partially bosonized formulations are mathematically equivalent, cf. sec. 1.1.2.

BCS limit for stronger coupling. In the BEC regime, it does not describe the onset of condensation at all, but is rather related to the formation of bosonic bound states which do by no means have to condense right away. It was found that it is the omission of bosonic fluctuations by the saddle point approximation that leads to this behavior. It may consequently be corrected by including those fluctuations. This is achieved at least partially by the fRG flow scheme presented here. Since the appearance of a finite $\rho_{0,k}$ at k_{sb} is largely driven by the fermionic "mean-field" contributions, it seems logical to interpret $\rho_{0,k>0}$ in terms of the occurrence of bound states and local ordering rather than actual condensation which is, strictly speaking, only present if $\rho_{0,0} > 0$.

A further, albeit weak confirmation that it may indeed be those *preformed pairs* that render $|\Delta_k| > 0$ above $\bar{T}_{\mathrm{c}}$, is provided by a comparison to the bound state calculation in sec. 4.1.2. For vanishing mass imbalance, pairs are formed for all available $\bar{h}$. Analogously, the fRG "precondensation" line in fig. 4.11 does not drop to $\bar{T} = 0$ for any $\bar{h} \leq 1$.

Later on, the notion of preformed pairs was extended [246] to explain (part of) the pseudogap state observed in high temperature superconductors (HTSC) [247]. It was argued that the occurrence of this state may be caused by local ordering phenomena rather than global ones as for an actual superconducting gap. This fits even better with the fRG picture. The inverse symmetry restoration scale k_{sr}^{-1} provides a qualitative estimate of the maximum correlation length for the pairs. When $k_{\mathrm{sr}} \to 0$, the latter diverges and true long range order occurs. For any finite k_{sr}, ordering is only local. Furthermore, the flowing order parameter $|\Delta_k|$ itself may be considered. Constructing a flowing dispersion relation for the fermionic quasiparticles in analogy to eq. (4.3) for the homogeneous case,

$$E_{\Delta_{k\approx q}} = \sqrt{(q^2 - \mu)^2 + |\Delta_{k\approx q}|^2}\,, \tag{4.37}$$

the now q-dependent gap suppresses excited states above the Fermi surface. This phenomenon can indeed be observed directly in high temperature superconductors in the pseudogap regime with the help of tunneling spectroscopy techniques like STM (scanning tunneling microscopy) or ARPES (angle resolved photoemission spectroscopy), see, e.g., [14] for an extensive review.

It should, however, be noted that the pseudogap phenomenon in HTSC materials is likely to be much more complex to be explained by the single mechanism focused on here. While the scenario of preformed pairs and precondensation may indeed help to understand certain materials under particular conditions, others are expected to be described by, e.g., competing ordering processes involving antiferromagnetism or charge density waves [14].

Once again, ultracold Fermi gases themselves provide a much cleaner environment for an investigation of these phenomena. Indeed, evidence for a pseudogap regime has been found with radio-frequency spectroscopy methods in a number of experiments [248–250]. Although simpler than in the case of HTSC materials, the extraction of critical temperatures $\bar{T}^*$ for pseudogap formation is far from easy also in ultracold Fermi gases. This is in particular due to the fact that the features believed to indicate the presence of such a state are by definition less distinct than for the actual superfluid gap. Nevertheless, a rough estimate from the data presented in [248] appears to be compatible with the fRG finding for the balanced case: $\bar{T}^*_{\mathrm{exp}}/\bar{T}_{\mathrm{c}}^{\mathrm{exp}} \approx 1.5$ and $\bar{T}^*_{\mathrm{fRG}}/\bar{T}_{\mathrm{c}}^{\mathrm{fRG}} = 1.28$.

Comparing to other theoretical approaches, agreement is found with Monte Carlo simulations [104] ($\bar{T}^*_{\mathrm{MC}}/\bar{T}_{\mathrm{c}}^{\mathrm{MC}} \approx 1.5$) as well as T-matrix calculations [251, 252]. Although the latter references unfortunately do not provide results in a way that could be used for quantitative comparison, good qualitative agreement is found in all cases.

So far, the balanced case has been discussed almost exclusively. The good qualitative agreement with experiment as well as other theoretical approaches renders fRG in the present setup trustworthy also for finite $\bar{h}$. This is particularly beneficial, as the identification of $\bar{T}^*$ with fRG requires practically no additional effort beyond the determination of the phase diagram if only superfluid and normal phases are considered. Furthermore, the large $\bar{h}$ regime does indeed comprise further interesting insight to be revealed.

The early findings on pseudogap physics suggested that it is not present at mean-field level approximations due to the omission of bosonic fluctuations [245]. While this finding is confirmed for low to intermediate $\bar{h}$, it is not found to be true anymore beyond $\bar{h}^*_{\mathrm{mf}} = 0.65$. There, symmetry breaking and restoration scales k_{sb} and k_{sr} are found to exist even at mean field level.[6] Consequently, it cannot be the bosonic fluctuations alone that are responsible for precondensation, at least for large spin imbalances.

The basic mechanism underlying this finding can be understood along the lines of the insets in fig. 4.10. The nontrivial minimum $\rho_{0,k}$ of the effective potential does not vanish continuously as in the low $\bar{h}$ regime. Rather, its value is raised above the trivial one as $k \to 0$. From fig. 4.10 alone, it could not be discerned, whether bosonic or fermionic fluctuations were predominantly responsible for this mechanism. The existence of $\bar{h}^*_{\mathrm{mf}}$ deduced from fig. 4.11 now proves that fermionic fluctuations are indeed involved in a significant way.

Consider again the corresponding flow equation:

$$\begin{aligned}[k\partial_k U_k]^{\psi}_{\bar{m}=0} =& \frac{k^5}{3\pi^2\sqrt{1+w_3}}\left[\Theta(\tilde{\mu}+1)(\tilde{\mu}+1)^{\frac{3}{2}} - \Theta(\tilde{\mu}-1)(\tilde{\mu}-1)^{\frac{3}{2}}\right] \\ &\cdot\left[N_{\mathrm{F}}\left(\tilde{h}+\sqrt{1+w_3}\right) - N_{\mathrm{F}}\left(\tilde{h}-\sqrt{1+w_3}\right)\right].\end{aligned} \qquad \text{(4.33 revisited)}$$

While the first Fermi function has a positive definite argument for $\bar{h} \geq 0$, the argument of the second one may change its sign. For large enough $\bar{h}$ as well as sufficiently small k and $h^2_{\varphi,k}\rho$, it becomes positive and this may even change the sign of the whole contribution. If this happens, the nontrivial minimum is not deepened anymore but raised instead, which is exactly what can be observed in the insets of fig. 4.10. Thus, precondensation can occur even at mean-field.

There is yet another consequence of this finding. As the bosonic contributions modify the flow of the Yukawa coupling $h_{\varphi,k}$, they feed back into the fermionic flow. By lowering $h_{\varphi,k}$, they may stabilize the sign of the second Fermi function's argument and thus of the whole fermionic contribution. This ultimately leads to the stabilization of the condensate itself in the large $\bar{h}$ domain of the phase diagram and a crossing of $\bar{T}^*$ lines predicted by mean-field and fRG, respectively, as observed in fig. 4.11.

Unfortunately, it is not obvious if and how these fRG-picture explanation could be recast into the usual many-body language due to the complicated, intertwined nature of the nonlinear evolution equations. At this point, it may safely be stated that functional RG is capable of investigating precondensation physics also for imbalanced systems and that, even for the comparably "simple" unitary Fermi gas, the nature of the pseudogap is more involved than it might appear at first sight. Moreover, the finding of the importance of fermionic fluctuations also beyond the usual mean-field picture will prove to be invaluable in the subsequent section when finite mass imbalance is admitted as well.

4.4 Inhomogeneous phases beyond mean-field: spin and mass imbalance

Having thoroughly discussed the simpler case of the mass balanced unitary Fermi gas in the previous section, it is now time to set $\bar{m}$ to finite values in the full functional RG equations. In the first part of this section, general homogeneous phase structures obtained from integrating the latter are discussed. While the behavior of critical temperatures and spin imbalances for given $\bar{m} > 0$ is qualitatively similar to the mass-balanced case, a special type of homogeneous superfluid, the so-called *Sarma* [253] phase emerges. The introduction of spin imbalance alone did not lead to the occurrence of any signs of inhomogeneous ordering in sec. 4.3. Although this is in accordance with the mean-field and few-body results presented in sec. 4.1, it does not add to the arguments disfavoring the existence of such a phase at $\bar{m} = 0$ yet. In fact, the present fRG formalism does not account for inhomogeneous phases in any obvious way and may therefore be expected to miss the latter just as a purely homogeneous mean-field calculation does, cf. also chap. 3. In fact, this conclusion proves to be premature as will be discussed in sec. 4.4.2 below. Functional RG as it is set up in this work is very well able to detect the presence of inhomogeneous ordering. It does, however, not provide direct access to infrared properties of such phases. Possible extensions and modifications of the formalism to allow for this as well are presented in sec. 4.4.3.

4.4.1 Homogeneous phase structure

Mass imbalance adds not only a phenomenologically interesting deformation to the system, it also complicates its numerical treatment substantially. Most prominently, the fermionic part of the boson anomalous

---

[6] This finding is a benefit of the application of fRG. It may easily be missed by "conventional" mean-field approaches.

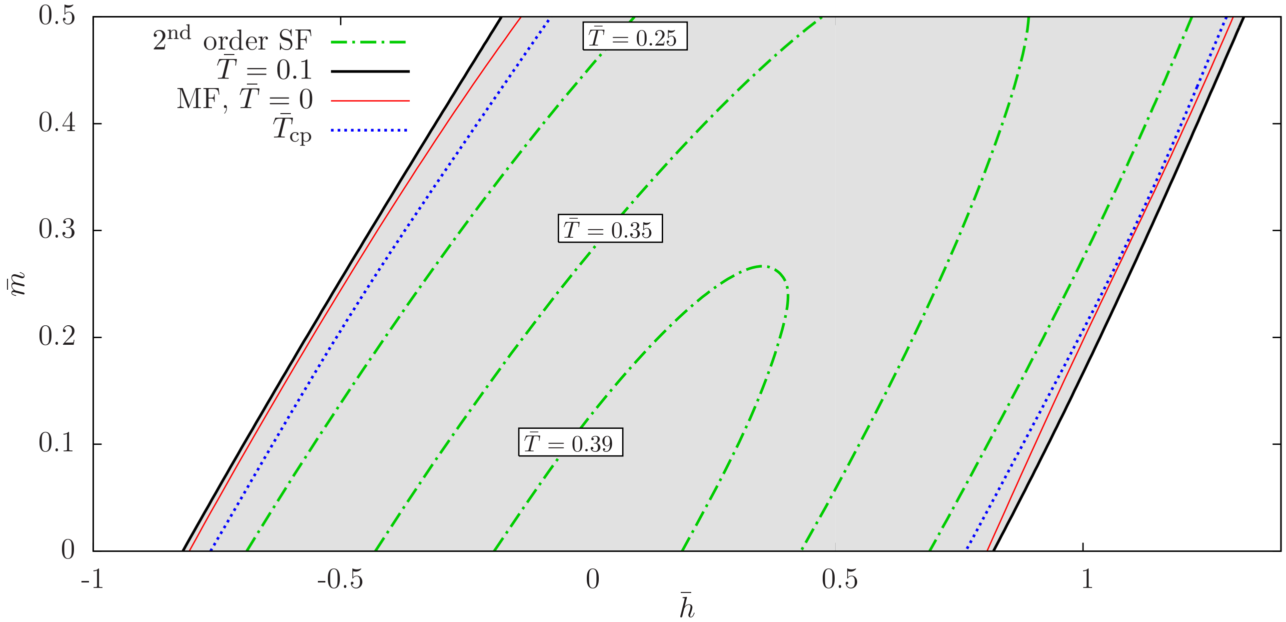

Figure 4.12: Phase diagram of the spin- and mass-imbalanced unitary Fermi gas for $\bar{m} \leq 0.5$ obtained from the full fRG flow equations. Green (dot-dashed) lines symbolizing second order and black (solid) lines for first order transitions enclose the (shaded) superfluid region. The manifold of critical points between the surfaces of second and first order phase transitions is given by the blue (dotted) line. For comparison, the zero temperature mean-field boundary (red, thin solid line) is provided as well.

dimension receives an extra contribution $\eta_{A,k}^{\psi,2}$ that is simply not present at $\bar{m} = 0$, see eq. (4.32b). Secondly, as mass imbalance is associated to the kinetic term of the fermion propagators, it introduces a momentum dependence into the arguments of the Fermi functions inhibiting analytic integration for any $\bar{T} > 0$. The numerical treatment of the corresponding integral not only slows down the evaluation of the fermionic flow equations substantially, its unavoidable error adds to the systematic inaccuracy of the results. Although analytic integrability is not sustained anymore, the regulator choice (4.19) is still advantageous as it renders the domain of integration finite. The integration itself is carried out by a *Gauss-Legendre* type algorithm [238]. Its precision is benchmarked against the analytically known result at $\bar{m} = 0$. Furthermore at $\bar{m} \neq 0$, convergence of the results for increasing numbers of sampling points can be ensured. The uncertainty for critical temperatures and imbalances is thus reliably kept on the sub-percent level.

Last but not least, a more subtle effect has to be accounted for. Eqns. (4.26b) and (4.32), responsible for the implementation of bosonic fluctuation effects, come along with coefficients $\sim \left(1 - \bar{m}^2\right)^{-r}$ where $r \geq 1$. The contributions from bosonic fluctuations are therefore amplified as $\bar{m}$ increases. Besides this being an interesting finding with potential physical meaning by itself, it substantially complicates the numerical evolution of U_k for large $\bar{m} \gtrsim 0.7$. As discussed in detail in sec. 4.3.1, eq. (4.26b) is particularly sensitive to any inaccuracy in the computation of the derivatives of the effective potential with respect to the order parameter. The additional amplification by $\bar{m}$ further increases this sensitivity and severely affects the stability of the numerical evolution. Special care is therefore needed in the regime of large $\bar{m}$ also in terms of internal precision of the grid solver.

Phase diagram for low mass imbalances For the latter reason, but mainly since an inhomogeneous phase is expected to occur at large mass imbalance, the phase diagram in fig. 4.12 is limited to the regime of $0 \leq \bar{m} \leq 0.5$. In general it can be said that its qualitative features are similar to the mass balanced case. Critical temperatures for the superfluid to normal transition are lowered for most parts of the available parameter space. As expected from the mean-field result in fig. 4.1, mass imbalance tends to lower $\bar{T}_{\mathrm{c}}$ as well, with the respective maximal values located roughly along the line of equal imbalances $\bar{h} = \bar{m}$. A line of critical points $\bar{T}_{\mathrm{cp}}(\bar{h}, \bar{m}) \approx 0.19...0.20$ is found to separate the manifolds of second and first order transitions to the normal phase.

For comparison, the $\bar{T} = 0$ mean-field phase boundary is also shown in fig. 4.12 (red, thin/solid lines). Again, an integration of the full flow at exactly $\bar{T} = 0$ is not possible. But even the first order transition at $\bar{T} = 0.1$ takes place at larger values $|\bar{h}|$ for all $\bar{m}$ compared to the zero temperature mean-field result. The stabilization mechanism at large spin imbalance discussed in sec. 4.3.2 obviously works for finite $\bar{m}$ as well. Only the notion of "large $\bar{h}$" has to be adapted to the respective value of $\bar{m}$.

Furthermore, the amplification of bosonic fluctuations discussed above exhibits its impact on observables in fig. 4.12. The stabilizing effect is not only present at finite mass imbalance, it apparently grows with increasing $\bar{m}$. This can be concluded from the growing distance between the solid lines as $\bar{m}$ is enhanced. Quantitatively, this distance has increased by a factor of ~ 1.6 between the $\bar{m} = 0$ and the $\bar{m} = 0.5$ configurations. For even larger $\bar{m}$, this issue will be revisited on p. 86 below.

Sarma phase Inhomogeneous condensates are not the only "exotic" type of ordering. Before moving on to the discussion of such phenomena, it is worthwhile to consider another example of unusual behavior in fermionic systems, the so-called *Sarma phase* [253]. In the Bogoliubov quasiparticle picture introduced in sec. 2.2.1, the energy of excitations for the respective fermionic species is given by

$$E^{\pm} = \pm h \mp \bar{m} p^2 + \sqrt{(p^2 - \mu)^2 + |\Delta_0|^2}\,. \tag{4.38}$$

A finite order parameter $|\Delta_0|$ for balanced and slightly imbalanced systems renders both dispersion relations positive definite, i.e. it costs energy to excite a single particle in the presence of a condensate of Cooper pairs. For suitably chosen $\bar{h}$ and $\bar{m}$, however, the lower branch may become negative for a certain range of momenta p, favoring the existence of those single particle excitations. As they do now exist alongside with the condensate even at zero temperature, the latter is also called "polarized", "gapless", "interior-gap" or "breached-pair" superfluid [131, 254]. The possible occurrence of such a phase has recently drawn some attention (see, e.g., [131, 255] and references therein), as it is supposed to be distinctively visible in experiments by measuring momentum distributions of the fermionic constituents. At zero temperature, the transition between the usual BCS-like superfluid and the Sarma phase is in fact a true quantum phase transition. A product of the fermion gap and the occupation number of gapless fermionic excitations provides an order parameter in this case. At finite temperature, this transition turns into a smooth crossover [46].

For purely spin-imbalanced systems, the so-called Sarma criterion $h_{\text{sa}} \geq |\Delta_0|$ is never fulfilled in the zero-temperature superfluid phase at unitarity. This has been confirmed with functional RG also beyond the mean-field approximation [255]. For spin- and mass-imbalanced configurations instead, a Sarma phase is found within the mean-field approximation, see, e.g., [131] and references therein. This is already apparent from fig. 2.5: for large $\bar{m}$ and $\bar{h}$, the transition from the superfluid to the normal phase is of second order even at vanishing temperature. As $|\Delta_0| \to 0$ continuously in this regime and $\bar{h} > \bar{m}$, the more complicated Sarma criterion

$$h_{\text{sa}} \geq \begin{cases} \mu\bar{m} + |\Delta_0|\sqrt{1 - \bar{m}^2}, & \bar{m} < \mu\left(\mu^2 + |\Delta_0|^2\right)^{-\frac{1}{2}} \\ \sqrt{\mu^2 + |\Delta_0|^2}, & \bar{m} \geq \mu\left(\mu^2 + |\Delta_0|^2\right)^{-\frac{1}{2}} \end{cases} \tag{4.39}$$

is fulfilled.

So far, no qualitative changes could be discerned between the phase structures found at mean field and by fRG. The Sarma phase can therefore be expected to occur also upon inclusion of bosonic fluctuations. This conclusion is, however, nontrivial as the stabilizing effects discussed above might shift the onset of the $\bar{T} = 0$ second-order phase transition to higher $\bar{m}$ or even inhibit it completely. It is therefore desirable to obtain direct evidence of the fate of this phase from fRG. On the other hand, a numerical evolution at strictly zero temperature is not possible as discussed above and the fermion gap $|\Delta_0|$ inside the bulk of the symmetry broken phase is not an observable that can be extracted with particularly high precision, see sec. 4.3.1.

While the position of a possible onset of the zero-temperature Sarma phase can thus not be determined with satisfactory precision, a reliable estimate on its existence can nevertheless be made. In fig. 4.13a the evolution of $|\Delta_k|$ for different temperatures in the balanced case is shown. Obviously, it is not converged to the observable $|\Delta_{k=0}|$ for the smallest $k = 0.1\sqrt{\mu}$ shown, in particular for high temperatures. On the other hand, the destructive influence of bosonic fluctuations which is responsible for the decrease of $|\Delta_k|$ in this regime becomes less severe for decreasing $\bar{T}$.

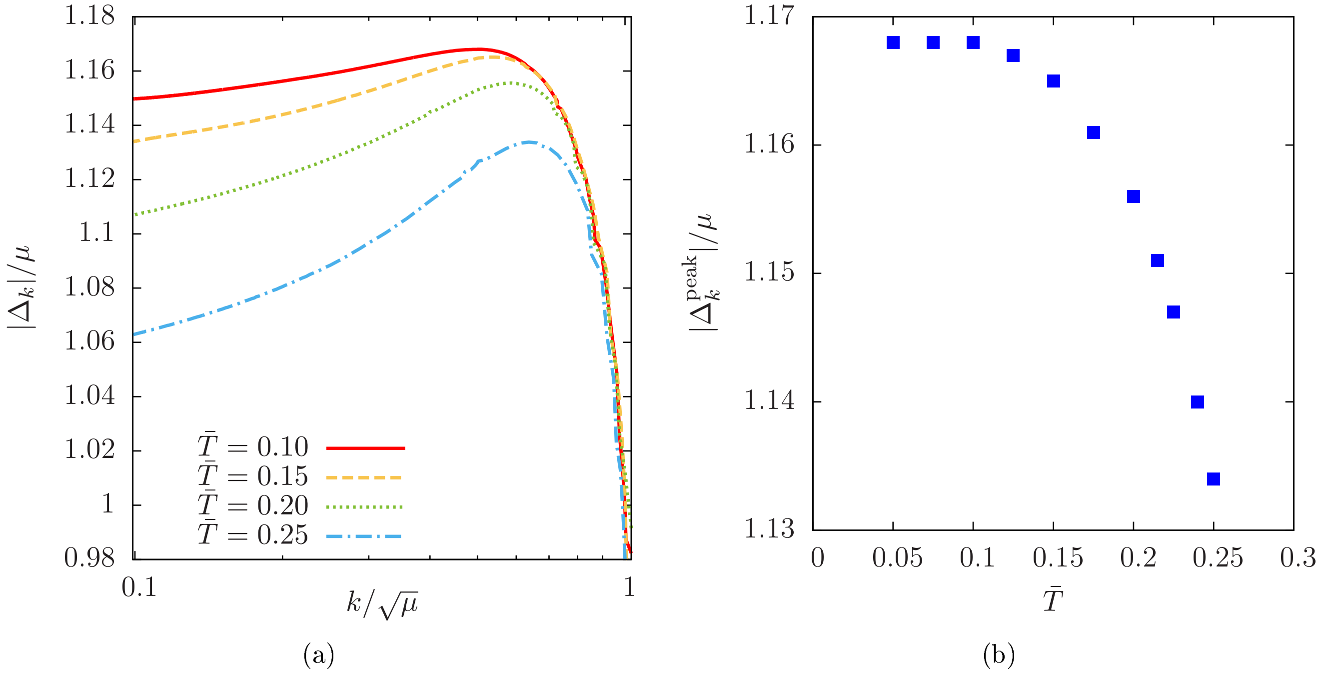

Figure 4.13: Estimating the magnitude of the zero-temperature fermion gap $|\Delta_0^{\max}|$ in the balanced case. Since the $k \ll \sqrt{\mu}$ regime of $|\Delta_k|$ becomes difficult to access as $\bar{T} \to 0$ (a), the k-global peak values $|\Delta_k^{\mathrm{peak}}|$ are considered instead (b).

Without further caring about the difficulty to access regime of $k \ll \sqrt{\mu}$, the maximum values $|\Delta_k^{\mathrm{peak}}|$ assumed during the flow thus become an increasingly better estimate. The latter are plotted over temperature in fig. 4.13b. Below $\bar{T} = 0.1$ they appear to be essentially converged within numerical accuracy. An estimate of $|\Delta_0^{\max}| \approx 1.17\mu$ may therefore be slightly overestimating the true balanced zero temperature gap, but this is not problematic in the following. As the zero temperature balanced case is the most favorable situation for pairing in the whole parameter space, it is reasonable to assume that the magnitude of the fermion gap is nowhere larger than at this point. This is further substantiated by the finding that the critical temperature is also maximal in the balanced case.

Using this estimate for $|\Delta_0^{\max}|$, a "worst-case" scenario for the Sarma phase to exist may be constructed by inserting it into the criterion (4.39). The resulting boundary together with the $\bar{T} = 0.1$ phase transition from fRG and the $\bar{T} = 0$ mean-field result are depicted in fig. 4.14. Evidently, there is a Sarma phase beyond mean field even if the fermion gap would retain its maximal size. Since the phase transition turns into a second order one again, this is clearly not the case and the true extent of the gapless superfluid phase may be considerably larger than indicated in fig. 4.14. In any case, since the true zero temperature phase boundary will be shifted to even larger $\bar{h}$ compared to the $\bar{T} = 0.1$ one shown, the existence of a Sarma phase also beyond mean field can safely be assumed.

Besides these considerations, fig. 4.14 provides another interesting detail on the respective roles of bosonic and fermionic fluctuations in the presence of a condensate. Unlike expectable from the low-$\bar{m}$ regime in fig. 4.12, the distance between the fRG and mean-field low temperature phase boundaries does not increase anymore for $\bar{m} \gtrsim 0.5$. The reason for this can be understood when reconsidering the stabilization mechanism discussed in sec. 4.3.2 above. The latter was primarily induced by the bosonic feedback into the fermionic flow equation at large $\rho_{0,k}$ as it occurs in the vicinity of (strong) first order phase transitions. For the regime of large mass imbalances depicted in fig. 4.14, however, the gap at the phase boundary diminishes with increasing $\bar{m}$ and vanishes altogether when the transition becomes second order. Although bosonic fluctuations are further enhanced, the effect of continuously vanishing gap inevitably "prevails" at some point, as second order phase transitions are naturally much less affected.

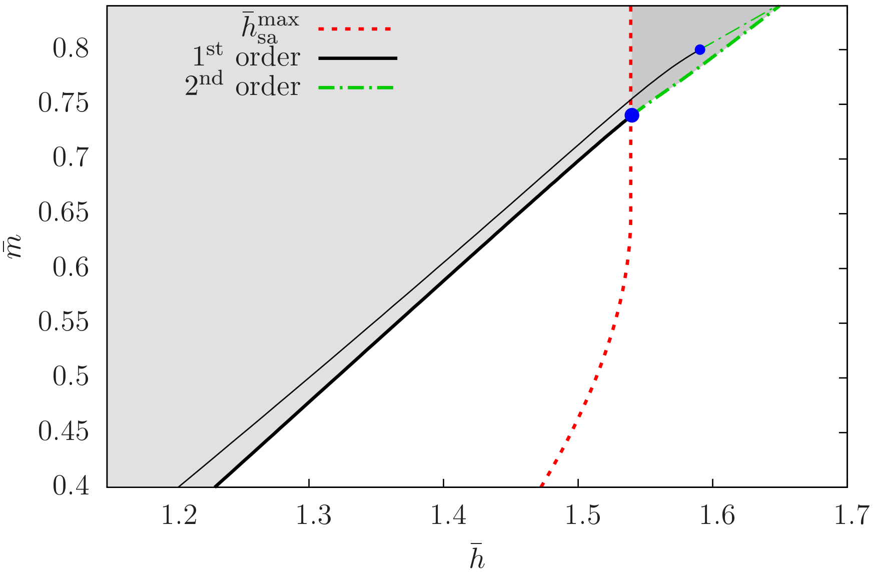

Figure 4.14: Large $\bar{m}$-regime of the unitary Fermi gas in the domain of $\bar{h}$ where a Sarma phase is expected from mean-field studies inside the superfluid phase (light shading). As the "worst-case" estimate $\bar{h}_{\mathrm{sa}}^{\mathrm{max}}(\bar{m})$ crosses the fRG phase boundary ($\bar{T} = 0.1$, thick lines), a Sarma phase is indeed found (dark shading). For comparison, the mean-field result ($\bar{T} = 0$, thin lines) is given as well.

4.4.2 Prospects of inhomogeneity: the boson propagator

Searching for inhomogeneous phases, the inability to solve the full flow equations for $\bar{T} = 0$ becomes particularly obstructive. The strongest hint for the existence of inhomogeneously ordered phases also beyond mean field came from the coincidence of mean-field and bound state calculations displayed in fig. 4.4 - at vanishing temperature. In order to get at least partial access to this regime also with fRG, a reduced set of flow equations will be considered in a first step, that can indeed be integrated at $\bar{T} = 0$. Afterwards, the insight gained by this procedure can be used to interpret results from the full flow also at finite temperatures.

Fermionic flow: mean field and beyond When considering only those contributions to the overall flow that originate from fermionic loop diagrams, i.e. $[k\partial_k U_k]^\psi$ and $\eta_{A,k}^{\psi,1/2}$, the infrared effective potential $U_{k\to 0}$ may be obtained, since the flow equations can be rendered independent of U_k itself or its derivatives. While the RHS of eqns. (4.26a), (4.32a) and (4.32b) do not depend on U_k by construction, this is a priori not true for the structural evolution equation (4.23) of U_k itself, even if $[k\partial_k U_k]^\varphi \equiv 0$. The term $\eta_{A,k}\rho U_k'$, spoiling the desired structure, originates from the $A_{\varphi,k}$-dependence of the renormalized ρ. Having been convenient so far, the use of renormalized quantities is not mandatory, as physical observables such as the fermion gap $|\Delta_0|^2 = h_{\varphi,k}^2\rho_{0,0} = \bar{h}_\varphi^2\bar{\rho}_{0,0}$ do not depend on $A_{\varphi,k}$ anyway. Reformulating the flow equations in terms of unrenormalized quantities, the bothersome inner derivative term vanishes and the fermionic flow is reduced to

$$k\partial_k\bar{U}_k(\bar{\rho}) = \left[k\partial_k\bar{U}_k\right]^\psi , \quad -k\partial_k \ln A_{\varphi,k} = \eta_{A,k} = \eta_{A,k}^{\psi,1} + \eta_{A,k}^{\psi,2} . \tag{4.40}$$

The flow equation for $\bar{U}_k$ is now decoupled from $\eta_{A,k}$. The effective potential, described diagrammatically by eq. (4.25), exactly reproduces the well-known mean-field results. A boson anomalous dimension $\eta_{A,k}$ does not arise in the standard (homogeneous) mean-field approach as the boson propagator is not equipped with any spatial momentum dependence. While this is expressed by the decoupling of the equations for $\eta_{A,k}$ and $\bar{U}_k$, it does of course not prohibit an evolution of $A_{\varphi,k}$ alongside $\bar{U}_k$. Although the former does not have direct impact on the phase structure at first glance, it still encodes nontrivial physical information. In fig. 4.15a, three generic cases for the evolution of $A_{\varphi,k}$ are shown. The most usual one is represented by the green (solid) line. The boson anomalous dimension $\eta_{A,k}$ is always positive in this case, leading to monotonous growth of the boson spatial renormalization coefficient. An evolution of both $\bar{U}_k$ and $A_{\varphi,k}$ to arbitrarily low k is possible and reproduces the mean-field results for the phase diagram.

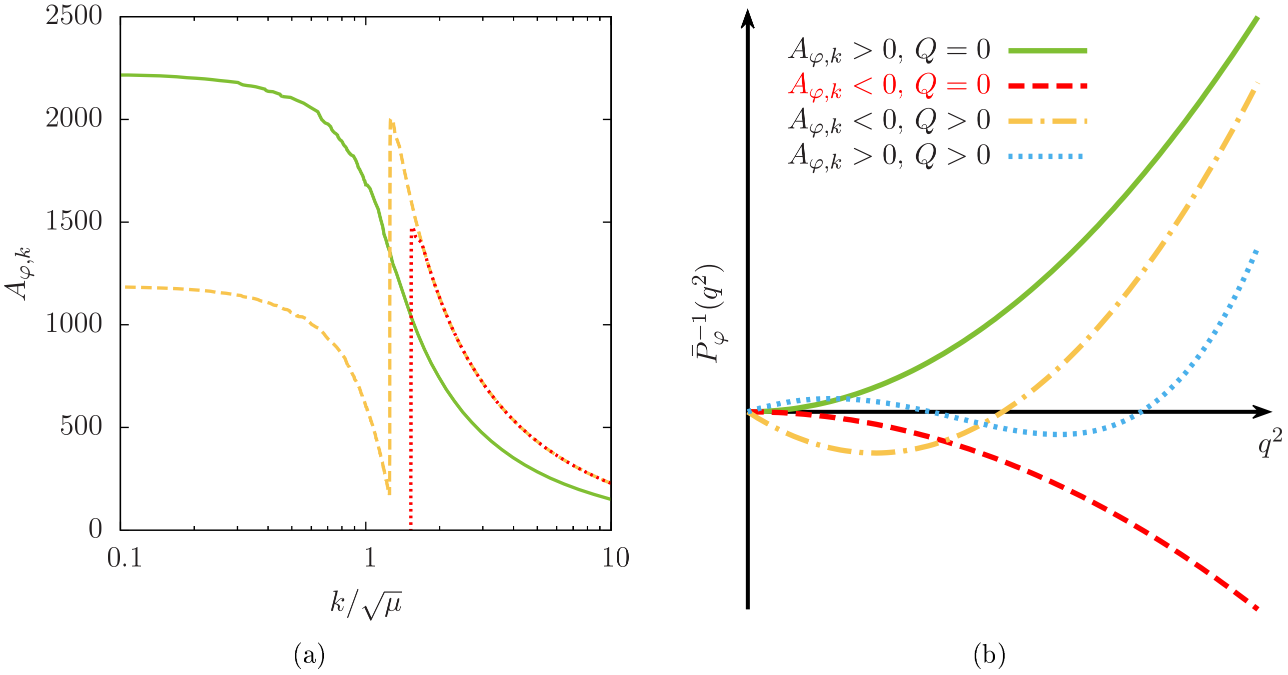

Figure 4.15: Generic types of $A_{\varphi,k}$ evolution at $\bar{T} = 0$ driven only by fermionic contributions (a). The vanishing of $A_{\varphi,k}$ during the flow may give hints on a nontrivial shape of the inverse boson propagator $\bar{P}_{\varphi}^{-1}$ (b), see main text for details.

A more complicated scenario arises, if $\eta_{A,k} = -k\partial_k \ln A_{\varphi,k}$ changes its sign at some point during the flow. If the sign change is reversed "soon" enough, a curve like the yellow (dashed) one in fig. 4.15a arises. This may happen in particular, if a condensate forms: While $\partial_k \bar{U}_k$ is decoupled from $\eta_{A,k}$, the reverse is not true even for the purely fermionic equations. The only consequence here is that the flow of both quantities may again be continued towards $k = 0$. If bosonic fluctuations are included, there are more dramatic implications that will be discussed in detail on p. 90 below.

Either of these two cases leads to an exact reproduction of the well-known mean-field results for the phase diagram, as the actual values of $A_{\varphi,k}$ do not affect $\bar{U}_{k=0}$ in any way. As long as $A_{\varphi,k}$ remains positive, the inverse boson propagator (4.16) is shaped as schematically depicted by the green (solid) line in fig. 4.15b as it should be. The evolution in large parts of the zero-temperature $\bar{h} - \bar{m}$ plane is determined by the above described behavior of one of the two types. In fig. 4.16, this is marked by the usual white or light gray shading associated with superfluid or normal phases, cf. also fig. 2.5.

The third (red, dotted) curve in fig. 4.15a describes a qualitatively different scenario. Here, the drop of $A_{\varphi,k}$ after the sign change of $\eta_{A,k}$ is not intercepted and the boson spatial renormalization coefficient eventually vanishes. At the corresponding scale k_{break}, the evolution stops, since it can no more be physically meaningful. A negative $A_{\varphi,k}$ naïvely plugged into the ansatz (4.16) results into an inverse propagator that is not bounded from below anymore, see the red (dashed) line in fig. 4.15b. Since this would correspond to the possibility of infinite energy gain by the formation of high-momentum bosons, it has to be rejected as being unphysical.

In fact, this behavior must be regarded as an artifact of the lowest order truncation of the derivative expansion for the inverse boson propagator (4.16) that includes only one nontrivial term for the dependence on spatial momenta. If only one more term, say $\sim q^4$ was included, a boson propagator shaped like the yellow (dot-dashed) curve in fig. 4.15b might result. The latter corresponds to a perfectly physical, bounded kinetic term albeit with a nontrivial minimum at some finite momentum $Q > 0$. This assumption is not as speculative as it may appear. In ref. [256], similar behavior was observed for the two-dimensional fermionic Hubbard model [257]. There, the evolution was not stopped at k_{break} but rather continued with a different ansatz for the inverse boson propagator that allowed for a nontrivial minimum in momentum space. In certain cases, such a nontrivial minimum was indeed found and associated to lattice-incommensurate ordering, the discrete analog of an inhomogeneous phase.

When mapping the domain where $A_{\varphi,k_{\mathrm{break}}} = 0$ during the flow to the zero-temperature $\bar{h} - \bar{m}$ plane as

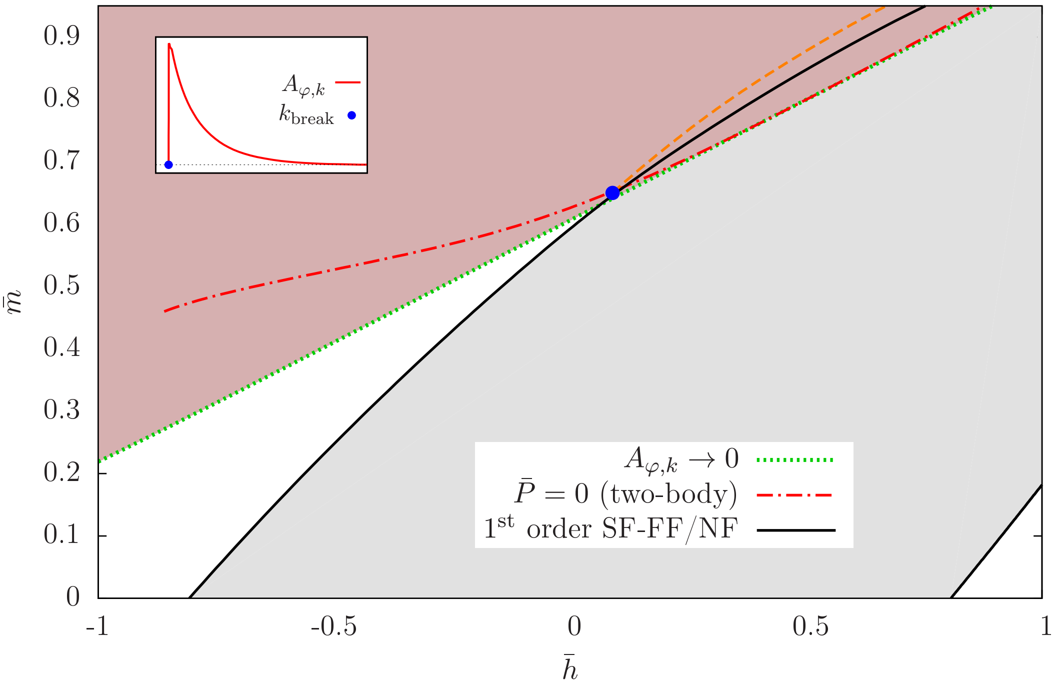

Figure 4.16: Domains of vanishing $A_{\varphi,k_{\text{break}}}$ (red, dark shading) and complete evolution (light gray or no shading) separated by a green (dotted) line at $\bar{T} = 0$. For $\bar{m} \gtrsim 0.6$, the latter agrees very well with the two-body bound for pairing with $\bar{P} > 0$ (red, dot-dashed line). Both cross the mean-field phase boundary in the close vicinity of the endpoint (blue dot) of the Fulde-Ferrell-to normal transition (orange, dashed line).

in fig. 4.16 (red, dark shading), striking coincidences are found: The domain of vanishing $A_{\varphi,k}$ and the mean-field Fulde-Ferrel phase are well compatible in the region where condensation is predicted. There, the agreement between the onset of the $A_{\varphi,k_{\text{break}}} = 0$ criterion and the formation of finite center-of-mass momentum bound states as predicted by the Schrödinger equation is almost perfect. Ultimately, the Fulde-Ferrel-to-normal transition (orange, dashed line), the two-body boundary for $\bar{P} > 0$ pair formation (red dot-dashed line) and the onset of $A_{\varphi,k} = 0$ (green, dotted line) all intersect the mean-field first order transition between homogeneous and normal phases (black, solid line) almost at the same point (blue dot).

It is therefore tempting to associate the $A_{\varphi,k_{\text{break}}} = 0$ criterion with the occurrence of inhomogeneous phases directly. Just as for the two-body argument, however, it should be viewed merely as a strong hint for a number of reasons:

- The most crucial drawback of the $A_{\varphi,k_{\text{break}}} = 0$ criterion is its occurrence at finite k by definition. It thus carries no direct physical meaning within the fRG framework. A priori, it is not clear whether the nontrivial minimum of the inverse boson propagator that is supposed to occur at k_{break} persists down to $k = 0$. This question may only be answered by actually evolving to lower k with a modified ansatz for $\bar{P}_{\varphi}^{-1}$, e.g. along the lines of ref. [256]. In this respect, the meaning of the occurrence of $A_{\varphi,k_{\text{break}}} = 0$ might be rather similar to that of the "pseudocritical" temperature $\bar{T}^*$ for homogeneous condensates discussed in sec. 4.3.2 above. Interestingly, scanning tunneling microscopy measurements on cuprate high temperature superconductors have indeed identified inhomogeneous pseudogap states even in the presence of an actual homogeneous gap [258]. The fRG picture once again appears to be rewarding physical insight beyond its strict bounds of validity. These aspects certainly deserve further investigation. This is, however, beyond the scope of this work.

- The coincidences in fig. 4.16 and similarities to the findings of [256] should not hide the fact that the actual meaning of a nontrivial minimum $Q > 0$ of $\bar{P}_{\varphi}^{-1}$ has not been touched upon yet. In fact, it provides information only on the relative energetic preference of bosonic states with finite momentum Q. Whether these constitute actual bound states of fermions or only virtual particles, i.e. fluctuations, is not clear. Of course, if deeply-bound states are present, they can be expected to exert dominating influence on the functional shape of $\bar{P}_\varphi^{-1}$. This may explain why the $A_{\varphi,k_{\text{break}}} = 0$ and two-body boundaries agree so well in the large-$\bar{m}$ regime, cf. also fig. 4.3 for a map of bound state energies. On the other hand, in domains where even the energetically most favorable pair configurations are bound rather shallowly, fluctuation modes with momenta substantially different from the favored $\bar{P}$ may dominate the propagator structure. Indeed, the green (dotted) line in fig. 4.16 deviates considerably from the red (dot-dashed) in the low-$\bar{m}$ regime where bound states are found to be less deep. It even extends to regimes where $\bar{P} = 0$ states are favored (low mass imbalances) or no bound states at all could be found (large $\bar{m}$, large negative $\bar{h}$).

- Focusing on the large-$\bar{m}$ domain of the phase diagram designated by mean-field calculations to foster condensation, the agreement between the green (dotted) and red (dot-dashed) lines in fig. 4.16 does indeed point to the predominance of finite momentum bound states. This is, however, not necessarily sufficient for the occurrence of an actual inhomogeneous condensate as already discussed previously in secs. 4.1.2 and 3.2.2. Two arguments were given there: although the most deeply-bound state may have nonzero center-of-mass momentum, it may still be the $\bar{P} = 0$ states that eventually condense. On the other hand, the FF ansatz is only expected to work well in the vicinity of the transition to the normal state and a more complicated inhomogeneity structure takes over in the bulk of the condensate where the FF solution is inferior even to the homogeneous ground state. Both arguments in principle remain valid in the present context. However, as the $A_{\varphi,k_{\text{break}}} = 0$ criterion comes from the genuinely many-body fRG setup employed here, it tends to favor the second explanation of an insufficient ansatz for the inhomogeneity.

In summary it can be said, that the occurrence of $A_{\varphi,k_{\text{break}}} = 0$ proves the dominance of finite momentum bosonic fluctuations in the red (dark) shaded region of the phase diagram 4.16 at least for some scales $k < k_{\text{break}}$. It gives strong hints on the existence and location of inhomogeneous phases if it is considered in connection with other approaches such as explicit mean-field or bound state calculations. To enhance its conclusiveness, the flow would have to be continued with an extended ansatz for the inverse boson propagator. Only then it could also be clarified whether an inhomogeneous condensate forms and persists until the scale of physical observability $k = 0$ is at least approximated reasonably well. In fact, it may even be found that $A_{\varphi,k_{\text{break}}} = 0$ is not a necessary condition for inhomogeneous ordering to occur. If the final propagator was shaped like the blue (dotted) line in fig. 4.15b, the occurrence of a nontrivial minimum $Q > 0$ would be possible that is missed completely in the present framework. There is no fully compelling reason why something like this should not happen. Nevertheless, given the good agreement of the three different methods in fig. 4.16, this scenario appears to be rather unlikely in large parts of the phase diagram.

Impact of bosonic fluctations Based on the discussions in the previous paragraph, the finite-temperature phase diagram obtained from the full set of flow equations can now be interpreted. It is given in fig. 4.17.

The sign change of $\eta_{A,k}$ and eventual vanishing of $A_{\varphi,k}$ associated with the possible occurrence of an inhomogeneous phase is found to survive at finite temperature and upon inclusion of bosonic fluctuations. Indeed, contrary to the misgivings expressed when discussing the tenuity of the mean-field FF phase in fig. 4.2, the supposed inhomogeneous phase appears to be stabilized. The red (dark) shaded domain in fig. 4.17 extends to lower mass imbalances $\bar{m} \approx 0.53$ compared to the mean-field case where the limit was at $\bar{m} \approx 0.6$. As discussed above, the $A_{\varphi,k_{\text{break}}} = 0$ criterion does not provide insight into actual condensation physics, wherefore no boundary between the (suspected) inhomogeneous and the normal phase can be drawn. The assumption of the existence of such a boundary is indicated by the fade-out of the red (dark) shading towards smaller $\bar{h}$.

The apparent stabilization of the inhomogeneous phase by bosonic fluctuations has to be taken with some care. Besides the arguments enumerated above, that sketch the limits of interpretability for the $A_{\varphi,k_{\text{break}}} = 0$ criterion, peculiarities introduced by bosonic fluctuations have to be taken into account. Contrary to the dotted (green) line in fig. 4.16, the dotted (pink) line for the critical temperature $\bar{T}_{\text{cp}}^{\text{I}}$ in fig. 4.17 does not signify the onset of $A_{\varphi,k_{\text{break}}} = 0$ directly. In fact, the situation is considerably more involved.

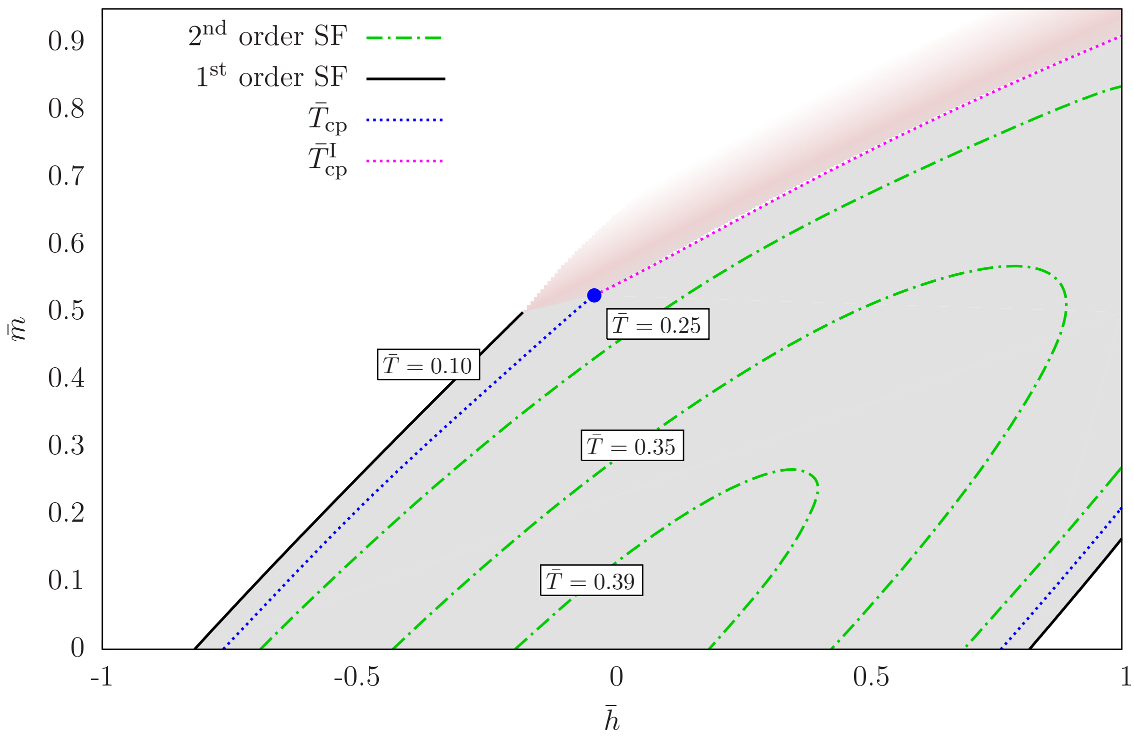

Figure 4.17: Full phase diagram of the unitary spin- and mass-imbalanced Fermi gas. The low-$\bar{m}$ regime corresponds to fig. 4.12. For $\bar{m} \gtrsim 0.53$, the red (dark) shaded region delimited by a pink (dotted) line symbolizes the onset of unphysical behavior and eventually vanishing $A_{\varphi,k}$. Since the magnitude of (inhomogeneous) condensates is not accessible when $A_{\varphi,k_{\rm break}} = 0$ occurs, the supposed transition to the normal phase is indicated by a fade-out of the red (dark) shading.

Recall the prototypic shapes of the $A_{\varphi,k}$ evolution plotted in fig. 4.15a, in particular the yellow (dashed) line. The latter behavior was associated with the occurrence of a finite $|\Delta_{k>k_{\rm break}}|$ inhibiting the vanishing of $A_{\varphi,k}$. This type of evolution plays a much bigger role for the full set of flow equations for two reasons:

- The occurrence of multiple sign changes of $\eta_{A,k}$ is not necessarily connected to infrared condensate formation. Since the advent of $|\Delta_{k>k_{\rm break}}|$ is sufficient, it may also happen in the precondensation regime. The latter becomes in general much larger when bosonic fluctuations are included, cf. fig. 4.11.

- Since the evolution equations are now fully coupled, the flow of $A_{\varphi,k}$ exerts influence on the behavior of $|\Delta_k|$. The dramatic drop of $A_{\varphi,k}$ or, equivalently, the growth of the Yukawa coupling $h_{\varphi,k}$, can be expected to leave its traces in the values of infrared observables as well.

In fig. 4.18a, fRG results for the infrared fermion gap $|\Delta_0|(\bar{h})$ are plotted for two different temperatures and fixed $\bar{m} = 0.74$. This value corresponds to a ^{6}Li-^{40}K mixture. If $\bar{T} = 0.20$, the bosonic wave function renormalization coefficient vanishes for $\bar{h} \leq 0.5$ which is indicated by red (dark) shading. But even before reaching this limit, the reliability of the result becomes questionable as $|\Delta_0|(\bar{h})$ exhibits an up-bending shape. This is in marked contrast to the concave shape observed so far and found for slightly higher temperatures (green, dot-dashed curve in fig. 4.18a) also in this setting.
Similar behavior was found for fixed spin imbalance and varying mass imbalance in one dimension in accordance with predictions from bound state calculations, cf. figs. 3.4a and 3.10a. However, nothing comparable for constant $\bar{m}$ and varying $\bar{h}$ can be discerned in the respective three-dimensional results in fig. 4.3. The up-bending behavior of the $\bar{T} = 0.20$ curve in fig. 4.18a is therefore probably unphysical. Its occurrence is used as a criterion for an estimate of the critical temperature $\bar{T}^{\rm I}_{\rm cp}$ signifying the possible onset of inhomogeneous condensation.
Such behavior may occur due to a number of reasons. The first and most obvious one is an incomplete convergence of the fRG evolution that leaves considerable contributions of bosonic fluctuations from the regime of $k < k_{\rm IR}$ unaccounted for. This is not the case here. In fact, convergence is even better in the regime where up-bending occurs in fig. 4.18a. While the flow is stopped as early as $k_{\rm IR} \approx 4 \cdot 10^{-2}\sqrt{\mu}$ for

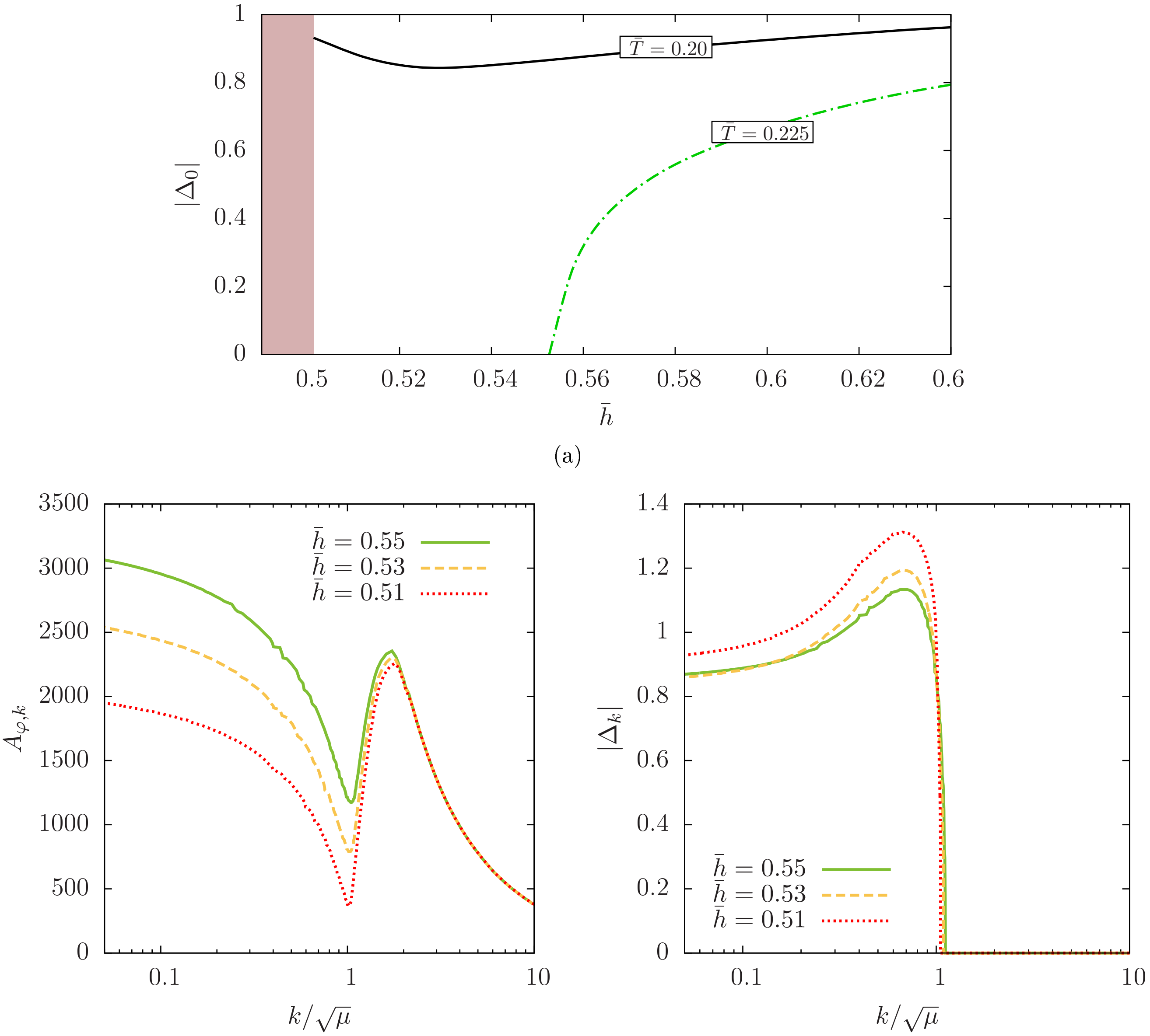

(a)

(b)

(c)

Figure 4.18: Impact of bosonic fluctuations on the condensate in the vicinity of $A_{\varphi,k_{\text{break}}} = 0$ for fixed $\bar{m} = 0.74$. For sufficiently low $\bar{T}$ and $\bar{h}$, an "up-bending" shape of $|\Delta_0|(\bar{h})$ is observed (a). It is caused by the peculiar "dent" in the evolution of $A_{\varphi,k}$ (b) that indirectly leads to an initial increase of $|\Delta_k|$ (c).

$\bar{h} = 0.6$ due to numerical cost, $k_{\text{IR}} \approx 1 \cdot 10^{-2}\sqrt{\mu}$ is reached for $\bar{h} < 0.53$. Varying other parameters of the numerical implementation (cf. sec. 4.3.1), the precise value of $|\Delta_0|$ indeed appears to be more sensitive in the vicinity of the onset of $A_{\varphi,k_{\text{break}}} = 0$. The general up-bending behavior is, however, not affected and must therefore be considered to be due to the flow equations themselves rather than due to numerical artifacts.

Figs. 4.18b and 4.18c show the evolution of $A_{\varphi,k}$ and $|\Delta_k|$ for spin imbalances $\bar{h} = 0.51, 0.53, 0.55$, respectively. For the behavior of $A_{\varphi,k}$, there is an obvious analogy to the situation of the yellow (dashed) curve in fig. 4.15a. The only qualitative difference is the more smooth drop of $A_{\varphi,k}$ due to finite temperature blurring. It is again the occurrence of $|\Delta_{k_{\text{sb}}}| > 0$ that qualitatively changes the flow and inhibits a vanishing of $A_{\varphi,k}$. The crucial difference to the mean-field case is that now $\eta_{A,k}$ is fed back into the flow of the effective potential both by its value directly and by its contribution to the flow of $h_{\varphi,k}$. The "dent" in the evolution of $A_{\varphi,k}$ in fig. 4.18b and the corresponding growth of the Yukawa coupling $h_{\varphi,k}$ thus leads to an initial increase of $|\Delta_k|$ that renders the maximum of the latter higher than even at mean field. This effect is partially compensated by a stronger suppression of fermionic fluctuations due to the larger running fermion gap and an increase of bosonic ones that tend to destroy ordering. The yellow (dashed) line ($\bar{h} = 0.53$) in fig. 4.18c thus crosses the green (solid) one ($\bar{h} = 0.55$) and leads to a smaller $|\Delta_0|$ as it should be. For even lower $\bar{h} = 0.51$ (red, dotted line), however, the initial increase of $|\Delta_k|$ becomes too strong and is not compensated for by bosonic or the absence of fermionic fluctuations anymore. This is essentially the mechanism being responsible for the up-bending shape in fig. 4.18a.

The above described mechanism has a number of consequences for the interpretation of the phase diagram in fig. 4.17. While it is hard to believe that the up-bending shape of $|\Delta_0|(\bar{h})$ should be physical, it cannot be ruled out completely on the basis of the present choice for the ansatz Γ_k. After all, the boson propagator remains positive definite for all k. But the up-bending itself is only "the tip of the iceberg". Obviously, the local drop of $A_{\varphi,k}$ and subsequent interception by and amplification of $|\Delta_k| > 0$ occurs already in the regime where $|\Delta_0|(\bar{h})$ is still concave. In fact, the kink-like feature in the evolution of $A_{\varphi,k}$ can be discerned up to spin imbalances as high as $\bar{h} = 0.70$ for $\bar{T} = 0.20$ and $\bar{m} = 0.74$. On the one hand, this exerts influence on the resulting values of the infrared fermion gap $|\Delta_0|$ deep in the homogeneous superfluid region. On the other hand, it is also present at higher temperatures and consequently impacts the location of transitions to the normal phase, as it may stabilize the condensate.

Clearly, finite momentum bosonic fluctuations have to be dealt with more carefully to unambiguously resolve the question which of these observations are physical or just artifacts of the truncation.

4.4.3 Further developments

The most problematic aspect of the discussions in the previous section above is the inability to continue the flow to $k \to 0$ in the domain of parameter space that is most relevant for the investigation of inhomogeneous phases. While deep insight can already be attained from the indirect arguments presented so far, it would be highly desirable to gain direct access to the suspected inhomogeneous phase to settle the questions that had to be left open. There are at least two different ways to approach this problem. Fully implementing either of them presents a formidable task that is beyond the scope of this work. The present section will therefore be restricted to a description of the basic concepts and prospective advantages and disadvantages of these approaches, respectively. Its goal is to provide a firm basis upon which future functional RG studies of inhomogeneous phases in ultracold gases and related systems may be built.

Explicit inhomogeneity At mean field, the existence of inhomogeneous phases was shown by "simply" admitting a spatially varying order parameter and proving its superiority to the constant one in certain regions of parameter space. While this may become arbitrarily complicated for generic spatial structures, a simple plane-wave or Fulde-Ferrell ansatz is in general sufficient to prove the existence and locate outer boundaries of a crystalline phase, cf. chap. 3. Such an FF ansatz therefore appears to be a good starting point for an fRG analysis that admits explicitly inhomogeneous ground state configurations. It is particularly convenient to be dealt with, as $\rho = \varphi\varphi^*$ is still constant if $\varphi = \varphi_0 e^{i\mathbf{Q}\cdot\mathbf{x}}$.

The formal implementation of this ground state ansatz requires only a subtle change in the projection rule (4.23) yielding the flow equation for the effective potential:

$$k\partial_k U_k = \partial_t \Gamma_k\big|_{\bar{\psi}=\psi=0,\varphi=\varphi_0 e^{i\mathbf{Q}\cdot\mathbf{x}}} - P^{-1}_{\varphi,k=0}(\mathbf{Q})\,. \tag{4.41}$$

Here, $P^{-1}_{\varphi,k=0}(\mathbf{Q})$ is the infrared contribution from the inverse boson propagator evaluated at the inhomogeneity momentum $\mathbf{Q}$. It has to be subtracted by hand due to the projection on a space dependent ground state that retains contributions from terms involving derivatives.

As discussed in secs. 3.1.2 and 3.3.1, the dependence on $\mathbf{Q}$ can be shifted into the fermion kinetic terms completely at mean-field level, rendering the full inverse propagator matrix diagonal in momentum space. The fRG approach works differently in the sense that a *projection* onto some particular ground state configuration does not prohibit fluctuations about this state as the *restriction* coming along with the mean-field approximation does. In other words, the simplifications introduced by the choice of the FF ansatz do not render $\Gamma_k^{(2)}$ diagonal in momentum space anymore as they can only be applied after the derivation of the full inverse propagator. Consequently, $\Gamma_k^{(2)} + R_k$ cannot be inverted exactly anymore as required for the construction of a general evolution equation for U_k, see app. D. A polynomial ansatz for the effective potential like the one in eq. (4.15) therefore appears to be mandatory.

Finite inhomogeneity momenta $\mathbf{Q}$ introduce additional complications, as fermionic regulator functions of the type (4.19) are not particularly well suited for the resulting propagator structure. The inconsistency of regularization schemes for thermal and quantum fluctuations, respectively, becomes manifest, as the fermion averaging procedure implied by the analytic treatment of the Matsubara sums renders the flow equations ill-defined. If a (costly) numerical treatment of Matsubara sums is still to be avoided, a sharp-cutoff-type regulator as, e.g., in ref. [259] is most promising from a technical point of view.

Even neglecting bosonic fluctuations, the evolution equations for the effective potential become very unwieldy. Nevertheless, the mean-field FF-to-normal phase transition could be reproduced by the above described method. An inclusion of order parameter fluctuations and the flow of anomalous dimensions requires massive additional effort. While this is mainly an issue of diligence and computational cost, there is unfortunately also a more severe conceptual drawback.

From the considerations in sec. 4.4.2, it is apparent that the relative importance of bosonic fluctuation modes with different momenta changes during the flow, since $k_{\text{break}} \sim \mathcal{O}(\sqrt{\mu})$ which indicates a change of shape of the boson propagator at low $k \ll \Lambda$. In other words, the location Q of the boson propagator's minimum in momentum space changes during the RG evolution. It is not easy to map this picture directly to the present setup, since the explicit inhomogeneity is computationally connected to a change of the momentum structure primarily of the fermion propagators. However, it is clear that the characteristic momentum $\mathbf{Q}$ is part of the general setup and does not change during the flow. It is not obvious how important a k-dependent momentum $\mathbf{Q}_k$ would be, but the results of sec. 4.4.2 suggest that it has to be accounted for.

Hence, it can be said that the inclusion of explicit inhomogeneous order parameters in an fRG framework is feasible albeit with great computational effort. Mean-field results can be reproduced, but additional complications of computational as well as conceptual nature arise if bosonic fluctuations are to be included. Possible results, especially for fixed k-independent inhomogeneity momentum $\mathbf{Q}$, have to be treated with care and should best be confirmed with complementary methods as the one presented below.

Generalized Boson propagators The request for a continuation of the flow beyond k_{break} can be fulfilled by extending the ansatz (4.16) for the inverse boson propagator to allow for more complicated spatial momentum structures and, in particular, the actual formation of a nontrivial minimum at finite momentum $\mathbf{Q}$. This approach has been employed successfully in [256] and can thus in principle be expected to work also for the unitary Fermi gas.

The dispersion relation in the latter case is, however, not limited to a finite Brillouin zone as for the lattice Hubbard model in [256], inhibiting a reuse of this ansatz here. Even a simple extension of eq. (4.16) by a term $\sim B_{\varphi,k} q^4$ is not straightforward as it would require a smoother fermion regulator due to the occurrence of fourth order momentum derivatives in the corresponding projection rule. The suitable choice of an extended ansatz for the inverse boson propagator and the associated construction of a proper regularization scheme is therefore a complicated technical problem by itself that shall not be addressed in detail here.

Assuming this problem to be solvable, the question is still open in what way a nontrivial minimum of the inverse boson propagator can actually reveal information about inhomogeneous phases. After all, no projection on a space-dependent ground state as in the above paragraph is involved. It is therefore not obvious, how the outcome of a calculation with such an extended ansatz should be interpreted.

Suppose, the true ground state of an imbalanced unitary Fermi gas for some particular set of parameters $(\bar{m}, \bar{h}, \bar{T})$ is characterized by a space-dependent order parameter $\rho(\mathbf{x})$. The Wetterich equation is based on the average effective action $\Gamma_k \sim \int_{\tau,\mathbf{x}} U_k[\rho(\mathbf{x})]$. This implies that a projection on some particular space dependent ρ is feasible but not required to account for the possibility of inhomogeneous order parameters. Indeed, the mean-value theorem for integration guarantees the existence of a constant $\tilde{\rho}$ such that

$$\int_{\mathbf{x}} U_k[\rho(\mathbf{x})] = V U_k[\tilde{\rho}] , \tag{4.42}$$

where V is the spatial volume. This "averaged" order parameter field cannot be interpreted as the magnitude of a fermion gap as for truly homogeneous ground states. When projecting onto constant ρ, it is thus very well possible that an inhomogeneous condensate is realized by the fRG flow without this fact being visible in the structure of the condensate itself.[7] Such behavior is reasonable insofar as the magnitude of the condensate is not the order parameter for spontaneous breaking of translational

---

[7] In fact, this might actually be the case in the up-bending regime in fig. 4.18a.

invariance but rather its spatial structure that has been integrated out. This can be understood in analogy to the mean-field situation, where the respective role was transferred to the characteristic frequency $\omega_{\bar{\Delta}}$ in 1D or momentum $\mathbf{Q}$ in 3D. Here, it is a minimum of the inverse boson propagator at some finite $Q > 0$ in the infrared limit $k \to 0$ that indicates a predominance of bosonic states with finite momentum.
Strictly speaking, this qualitative interpretation alone does not qualify the position of the minimum to be an actual order parameter. In summary it can thus be concluded that a conclusive identification of inhomogeneous phases by means of functional RG may be achieved by a combination of the two methods presented in this section. While the first one is limited by a specifically chosen ansatz and its results are possibly distorted by an improper handling of finite momentum fluctuations at $k > 0$, the second one does not suffer from either of these drawbacks. On the other hand, the first methods grants direct access to inhomogeneous condensates while the second one gives strong indirect hints at best. If, however, for some particular configuration $(\bar{m}, \bar{h}, \bar{T})$, an inhomogeneous condensate is found by the first method while the second one predicts some finite $\tilde{\rho}_{0,k=0}$ along with a nontrivial minimum $Q > 0$ for the boson propagator, this can be considered compelling evidence for the existence of an inhomogeneous condensate beyond mean field. Having thus confirmed the interpretation, further physical information should best be read off the results from the second approach.

Chapter 5

Conclusions

Probably the most central insight transported by this thesis is the nonexistence of *the one* single method that is capable of uncovering all of the many mysteries strongly correlated Fermi gases present to their explorers. It is rather the combination of complementary strengths and the awareness of individual drawbacks of several approaches that facilitates a most deep understanding of these fascinating systems. This is not necessarily intuitive, given the comparably "simple" field theoretical structure of the underlying actions such as eq. (1.6). Although representing idealized effective theories of what actually takes place in experiments with cold atoms, the physical results extracted from these actions prove to be remarkably rich. In order to summarize the host of phenomena identified, but in particular demonstrate the complementarity of the methods developed and applied in a comprehensive way, the main results of this work are recapitulated from this point of view in the following.

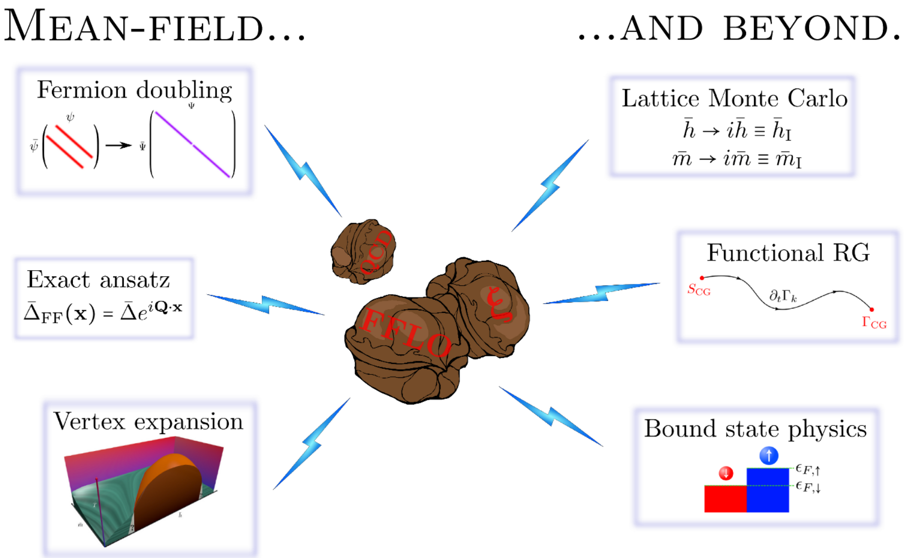

Figure 5.1: Pictorial summary of this thesis.

Strongly correlated quantum systems such as the unitary Fermi gas call for the application of non-perturbative methods due to the lack of a small expansion parameter. A very prominent approach is the numerical treatment by means of Monte Carlo simulations. However, even though the latter are widely considered the "gold standard" in terms of quantitatively precise predictions, it took years until the equation of state for balanced setups, i.e. with equal particle masses and densities, could be computed with satisfactory accuracy. Adding spin or mass imbalance to the system made the whole problem largely intractable to Monte Carlo methods due to a severe sign problem. In chap. 2 of this thesis it was shown that, in analogy to the previously known behavior of finite chemical potential in QCD, complex imbalance parameters do lift this sign problem. However, an analytic continuation of the so-obtained MC data to real (physical) imbalances had to be performed before physical predictions could be extracted. In sec. 2.2, an analysis of the corresponding mean-field model was carried out in order to investigate conditions for and limitations of the continuation procedure. It was found that non-analyticities of the observables such as phase transitions strictly limit the range of applicability of the method. At mean-field level, quantitative estimates for radii of convergence of an analytic continuation by means of polynomial series could be provided.

Guided by these considerations, actual Monte Carlo data obtained with an imaginary-imbalance DHMC algorithm have been evaluated in sec. 2.3. Limited by the amount of data points available for extrapolation, the benchmarking result of the mass-balanced Bertsch parameter $\xi = 0.44 \pm 0.01$ was found to be in good, although not perfect agreement with recent experimental data and other MC simulations. The error of about 20% may be assumed to carry over to the complete equation of state $\xi(\bar{h} = \bar{m})$ that was obtained with the help of a simple Padé fit of the imaginary imbalance data and analytic continuation. This error along with remaining ambiguities in the choice of the fit function may systematically be improved by generating more data points in terms of a longer temporal evolution, larger lattice size and higher sampling density of the imbalance parameter domain. Nevertheless, the result for the equation of state along the $\bar{h} = \bar{m}$ line is the first of its kind with lattice MC and although there is room for improvement, it constitutes already now a far better quantitative prediction than the mean-field values do. As experiments with unequal mass mixtures of fermionic gases are indeed in preparation [86], there is hope that these predictions may soon be benchmarked against actual measurements.

While the mean-field analysis in sec. 2.2 was able to demonstrate the general mechanisms that limit the trustworthiness of analytically continued results, it could not provide reliable quantitative predictions for the range of applicability in terms of imbalance parameters for actual MC data treatment. MC simulations with imaginary imbalances themselves, on the other hand, are most often not capable of detecting all non-analyticities such as transitions between superfluid and normal phases. Up to this point it has therefore been left completely unclear, in which domain $\bar{m} \in [0, r_{\bar{m}}]$ the result (2.50) for $\xi(\bar{h} = \bar{m})$ is in fact trustworthy. This gap may now be closed by considering the fRG results of sec. 4.4. The fRG approach, at least within the truncation employed in this work, is not particularly well suited to quantitatively compute the equation of state. In contrast, the obtained results for the phase boundaries compare very well with Monte Carlo and experimental data where available. This concerns not only the critical temperature $\bar{T}_\mathrm{c}^\mathrm{fRG} = 0.40$ for balanced systems, but in particular also the critical spin imbalance at (approximately) vanishing temperature $\bar{h}_\mathrm{c}^\mathrm{fRG} = 0.83$ which is, counterintuitively, larger than the mean-field value. Notably, the latter feature has been found experimentally as well [243]. It seems thus reasonable to trust the fRG results for the localization of phase transition manifolds also in the mass-imbalanced regime and extract some insight that might be useful for the interpretation of MC data.

Extrapolating the fRG data underlying the phase diagram in fig. 4.17 to vanishing temperature, no transition between the homogeneous superfluid and normal phases can be discerned along the line of equal spin and mass imbalance parameters $\bar{h} = \bar{m}$. There are, however, indications that the employed ansatz for the average effective action Γ_k might be an insufficient truncation and inhomogeneous ordering might play a certain role. Without anticipating the more detailed discussion of these findings below, it should as a precaution be assumed that non-analyticities associated with the transition to an inhomogeneous superfluid phase might be present at very high mass imbalances. Although it seems unlikely for this to occur along the $\bar{h} = \bar{m}$ axis of equal Fermi momenta, it appears be advisable to trust the MC prediction for $\xi(\bar{h} = \bar{m})$ only up to $r_{\bar{m}}^\mathrm{fRG} \approx 0.8$ at this point. Notably, this is already larger than the value $\bar{m} = 0.74$ associated to the prominent example of a ^{6}Li-^{40}K mixture. Future investigations on inhomogeneous phases within the fRG framework should further improve the understanding of the large-$\bar{m}$ regime and it might well be possible that the domain beyond $r_{\bar{m}}^\mathrm{fRG}$ is trustworthy as well.

The occurrence of inhomogeneous phases in imbalanced Fermi gases is an additional complication that must be addressed. Exact results for the one-dimensional Gross-Neveu model as in fig. 1.3 show that large portions of the phase diagram may be dominated by spatially varying condensates, which are missed completely within the usual homogeneous frameworks. If the equation of state for arbitrary imbalance could just be determined by MC simulations without a sign problem, the presence of such an inhomogeneous phase should be revealed by changes in the properties of ξ. Due to the presence of the sign problem, however, and the analyticity requirement of the imaginary imbalance approach, the occurrence of such inhomogeneous phases just adds to the complications at this point. Different methods of localizing and characterizing these exotic states are therefore needed. Major parts of this thesis have been devoted to the development of approaches capable of performing these tasks.

Experimental evidence of inhomogeneous (FFLO) superfluidity is rare. While solid superconductors are anything but an ideal playground to understand this phenomenon due to their intrinsic complexity, low-dimensional Fermi gases are more promising. It has been suggested in the literature and confirmed in chap. 3 of this work that the extent of FFLO phases in the space spanned by the imbalance parameters is much larger in one compared to three spatial dimensions. However, these results have to be taken with care, as the occurrence of actual long range order is strictly forbidden in 1D. Finite-size effects of the experimentally employed traps may still stabilize local ordering, rendering it observable. Nevertheless, the mean-field results of chap. 3 were not geared towards quantitative predictiveness for this kind of phenomenon. Instead, the one-dimensional setting along with the exact solution of the Gross-Neveu model were considered a good testing ground for the development of methods that might later on be applied to more realistic systems as well.

In a first attempt to systematically characterize the (inhomogeneous) phase diagram of strongly coupled one-dimensional spin- and mass-imbalanced Fermi gases, a vertex expansion of the mean-field effective action was employed. This expansion that incorporated and extended the well-established Ginzburg-Landau scheme, proved indeed capable of detecting the presence of inhomogeneous phases. However, once bulk properties of superfluid phases were addressed, the number of terms necessary to maintain satisfactory precision quickly became unmanageably high. It turned out that a simple Fulde-Ferrell plane wave ansatz reproduces the inhomogeneous-to-normal phase boundaries equally well. However, this finding did not render the vertex expansion technique useless. The effort required to address bulk superfluid properties may be high, but is still achievable in a systematic way. Furthermore, the insight that a simple plane wave is capable of reliably detecting the desired phase transition manifolds is not a priori trivial. The true ground state fermion gap is in general a complicated space dependent function. While the reduction of this function to a cosine-like shape for small condensate magnitudes was proven analytically in the case of the Gross-Neveu model [97], no comparable theorem exists in the non-relativistic setting. The disproportionate drop of higher order Fourier coefficients observed by means of the vertex expansion in fig. 3.6b is therefore a useful insight. This finding does in turn not necessarily imply an analogous behavior in three spatial dimensions. However, it constitutes a strong support of the general assumption of the plane-wave ansatz being capable of correctly detecting inhomogeneous phase boundaries.

Besides these methodical considerations, the obtained mean-field phase diagram revealed an intriguing non-intuitive structure. For fixed, negative spin-imbalance, an increase of $\bar{m}$ resulted in a decrease of the critical temperature $\bar{T}_\mathrm{c}$ for (any type of) condensation for low to intermediate mass imbalances. At some $\bar{h}$ dependent value, however, a stabilization and increase of $\bar{T}_\mathrm{c}$ could be observed, resulting in a "hook-like" structure of the inhomogeneous phase at large $\bar{m}$, see fig. 3.4. In order to understand the origin of this peculiar shape, the original Cooper problem was extended to the imbalanced unitary Fermi gas. By solving the resulting Schrödinger equation (3.14) for two distinguishable fermions in the presence of their respective Fermi seas for a range of possible center-of-mass momenta of the pair, interesting links between two- and many-body physics could be revealed. The stability of the condensate at large $\bar{m}$ could thus be traced back to the stability of the Cooper pairs themselves in this regime. Furthermore, the characteristic momentum of the many-body inhomogeneity turned out to be determined largely by the optimal center-of-mass momentum for pair formation at least when the total number of pairs was small. Generally speaking, a complex interplay between two-body properties determining characteristics of the condensate, and genuine many-body effects like phase space depletion was discovered. Further investigations of the interface between few- and many-body physics may for sure be expected to be rewarding. Another step in this direction is the exploration of three-body physics in a similar setup performed in [208].

The initial motivation as well as the insight that plane-wave inhomogeneities may be sufficient to detect boundaries of inhomogeneous phases, originated from the Gross-Neveu model and its exact solution. However, in contrast to the non-relativistic setting, a plane-wave ansatz did not constitute such a major simplification of the mean-field equations such that the effective action could have been determined exactly - at least if only scalar chiral condensates ~ $\langle\bar{\psi}\psi\rangle$ were admitted. The latter constraint was motivated by the existence of finite quark masses in nature, which distinguish the scalar channel. In order to profit from the simplicity of the plane-wave ansatz on the one hand and the well-developed homogeneous mean-field machinery on the other hand, an approached called "fermion doubling trick" was developed in sec. 3.3. Although only approximative in terms of the effective action, it could be proven to reproduce second order phase transitions between chirally broken and symmetric phases exactly regardless of inhomogeneity. Even the characteristic momenta at the inhomogeneous phase boundary known from the analytic solution were reproduced within limits of numerical accuracy. As the doubling trick is not limited to one spatial dimension or the particular interaction of the Gross-Neveu model, it could subsequently be applied to the

Polyakov-loop extended Nambu-Jona-Lasinio model as well. Previous results from the literature for the homogeneous chiral condensate as well as the existence of an inhomogeneous phase could be confirmed. For the first time, the interplay of inhomogeneous condensation and the behavior of the confinement order parameters $\bar{\Phi}$ and Φ with respect to the introduction of a μ-dependent parameter T_0 could be observed. The latter provided a more realistic description of gluon contributions compared to other, μ-independent parametrizations of the Polyakov-loop potential. The low-cost nature of the doubling trick enabled a fairly quick high-resolution mapping of the phase diagram. In the present case, this led, for example, to the discovery that the chiral and deconfinement transitions lie on top of each other also in the inhomogeneous region when employing the $T_0(\mu)$ parametrization. The doubling trick is not suited for a further investigation of findings like the curious behavior of the inhomogeneous phase boundary close to the Lifshitz point, but the results presented in this work may serve as a motivation to take a closer look at the interplay of inhomogeneous chiral symmetry breaking and confinement near P_{L} with methods able to address bulk properties of the condensate phases as well.

Applying the fermion doubling trick to the PNJL model also meant employing a method to a three-dimensional situation that was initially devised for a one-dimensional setting. In the first section of chap. 4, the idea of reusing methods developed for lower-dimensional problems was extended to the imbalanced unitary Fermi gas. Its phase diagram was investigated with standard mean-field techniques and an adapted FF ansatz for the inhomogeneity as well as by a characterization of in-medium bound states. Once again, the qualitative reliability of the mean-field inhomogeneous phase was confirmed by two-body results. This is notable in particular since the latter are neither restricted to some specific inhomogeneity ansatz nor to the contributions admitted by the mean-field approximation due to the absence of long-range fluctuations. On the other hand, these statements are somewhat coarse and delicate. The agreement between two- and many-body results was very good in one dimension as well, but any condensation seen by mean-field was clearly an artifact of this approximation. While it is plausible that bound state properties carry over to the condensate formed by these pairs, the actual condensate formation itself is a genuine many-body effect and cannot be predicted by the in-medium Schrödinger equation (4.4).

In order to close this gap as far as possible, a functional renormalization group scheme, that had previously been set up for the BCS-BEC crossover [55], was extended to accommodate the imbalanced situation. This scheme allowed for the systematic incorporation of order parameter fluctuation effects that were not included in the mean-field approximation. Extensive benchmarking of the employed numerical method of solving the RG flow equations on an order parameter grid provided confidence on the reliability of the approach. The quality of the results obtained by this scheme, in particular for the location of phase transition manifolds, has already been discussed above. Further insight could be gained concerning the stability of a Sarma phase in the large-$\bar{m}$ regime and pseudogap physics.

The accuracy of fRG calculations for interacting systems is usually limited by the choice of some finite ansatz for the effective average action Γ_k. If chosen inappropriately, solving the flow equations cannot be expected to yield reliable results - if the flow can be evolved to the physical infrared limit $k \to 0$ at all. For phase transitions in the spin-imbalanced unitary gas, the presence of such artifacts was found to be unlikely due to the stability of the results with respect to a change of the regularization scheme. Moving to finite mass imbalances $\bar{m} \gtrsim 0.5$, a breakdown of the flow occurred for certain $\bar{h}$, indicating the insufficiency of the employed truncation. Most pleasantly, this breakdown did not just put an end to the fRG investigations in the present scheme. Its peculiarities were considered strong hints on the attempted formation of a nontrivial momentum space minimum for the boson propagator, which was bound to fail in the low order derivative expansion employed. With the help of similar previous findings for the Hubbard model [256], this behavior could be related to the formation of finite momentum fermionic pairs and possibly inhomogeneous condensation. The striking coincidence of the FF-mean-field, in-medium bound state and fRG predictions gave further credibility to the assumption that there is indeed an FFLO-type phase in the high-$\bar{m}$ regime of the unitary Fermi gas, being located as a layer upon the homogeneous superfluid phase.

With the present fRG setup, a more direct characterization of this domain is not possible. No discrimination between an actual infrared crystalline condensate and a mere "inhomogeneous pseudogap" state or just dominating influence of finite momentum bosonic fluctuations for some range of scales k can be achieved. In order to obtain final certainty and also determine the location of phase boundaries as well as, e.g., characteristic inhomogeneity momenta beyond mean field, an extension of the formalism is required. Two generalizing suggestions have been made in the very last section of chap. 4. However, their complete elaboration and application is way beyond the scope of this thesis and therefore left for future work. Boldly extrapolating from the results hitherto obtained, a further investigation of strongly correlated Fermi gases with enhanced versions of the methods presented here should be worth a serious thought. In any case, many of the diverse findings on the properties of strongly correlated imbalanced Fermi gases presented this thesis should become verifiable through the experimental realization of such systems awaited in the near future.

Appendices

Appendix A

Notational and Fourier conventions

The calculations this thesis is based on require frequent switching between position and momentum space. For consistency, it is thus necessary to declare the Fourier or Matsubara conventions that are used throughout this work. In general, fields and their complex conjugates are transformed as

$$\chi_{\tau,\mathbf{x}} = \frac{1}{\sqrt{\beta}} \sum_n \int \frac{\mathrm{d}^d p}{(2\pi)^d}\, \chi_{n,\mathbf{p}} e^{-i(\omega_n \tau + \mathbf{p}\cdot\mathbf{x})}, \quad \chi^*_{\tau,\mathbf{x}} = \frac{1}{\sqrt{\beta}} \sum_n \int \frac{\mathrm{d}^d p}{(2\pi)^d}\, \chi^*_{n,\mathbf{p}} e^{i(\omega_n \tau + \mathbf{p}\cdot\mathbf{x})}, \tag{A.1a}$$

$$\chi_{n,\mathbf{p}} = \frac{1}{\sqrt{\beta}} \int_0^\beta \mathrm{d}\tau \int \mathrm{d}^d x\, \chi_{\tau,\mathbf{x}} e^{i(\omega_n \tau + \mathbf{p}\cdot\mathbf{x})}, \quad \chi^*_{n,\mathbf{p}} = \frac{1}{\sqrt{\beta}} \int_0^\beta \mathrm{d}\tau \int \mathrm{d}^d x\, \chi^*_{\tau,\mathbf{x}} e^{-i(\omega_n \tau + \mathbf{p}\cdot\mathbf{x})}, \tag{A.1b}$$

in d spatial dimensions. Here, χ symbolizes either bosonic or fermionic fields for which the same conventions are used. The only difference comes with the definition of the Matsubara frequencies ω_n (see, e.g., [51]),

$$\omega_n = \begin{cases} \frac{2n\pi}{\beta}, & \text{for boson fields } \varphi, \\ \frac{(2n+1)\pi}{\beta}, & \text{for fermion fields } \psi, \end{cases} \qquad n \in \mathbb{Z}\,, \tag{A.2}$$

reflecting the periodic or antiperiodic temporal boundary conditions required by the respective field types. For conciseness, spatial and momentum integrations are in some instances abbreviated as

$$\int_0^\beta \mathrm{d}\tau \int \mathrm{d}^d x \ldots \equiv \int_{\tau,\mathbf{x}} \ldots, \qquad \sum_n \int \frac{\mathrm{d}^d p}{(2\pi)^d} \ldots \equiv \sum_n \int_{\mathbf{p}} \ldots \equiv \sum\!\!\!\!\!\!\!\int_{n,\mathbf{p}} \ldots\ . \tag{A.3}$$

A normal case italic momentum variable symbolizes the absolute value of the corresponding vector: $q \equiv |\mathbf{q}|$ or $q \equiv |\hat{q}|$ in sec. 4.2.1.

Appendix B

Vertex expansion coefficients

Employing the vertex expansion technique introduced in sec. 3.1.1 requires the computation of the $\Gamma^{(2j)}$ coefficients in the defining equation (3.6) and subsequent minimization of the resulting approximate effective action. While the latter task must be approached with standard numerical techniques, the former may at least partially be solved analytically, saving a great deal of numerical effort. This concerns in particular the Matsubara sums. The goal of this appendix is to illustrate the general approach by way of an explicit calculation of the two-point function. Intricacies coming along with higher oder n-point functions are then discussed along with their resolution by means of computer algebra systems.

The two-point function Plugging explicit expressions into the formal expansion scheme (3.5), the two-point function of the one-dimensional imbalanced Fermi gas for a general momentum dependent order parameter $\bar{\Delta}(q)$ is given by

$$\begin{aligned}\frac{1}{\beta L}\Gamma^{(2)}_{1\mathrm{D,mf}} &= -\frac{1}{g_\delta^{1\mathrm{D}}}\int_{\mathbf{q}}|\bar{\Delta}(q)|^2 - \frac{1}{\beta}\sum_n\int_{\mathbf{q}}\int_{\mathbf{p}}\frac{|\bar{\Delta}(q)|^2}{[-i\omega_n + p^2(1+\bar{m}) - \mu - h]\,[-i\omega_n - (p-q)^2(1-\bar{m}) + \mu - h]} \\ &= -\frac{1}{g_\delta^{1\mathrm{D}}}\int_{\mathbf{q}}|\bar{\Delta}(q)|^2 + \int_{\mathbf{q}}\int_{\mathbf{p}}\oint\frac{\mathrm{d}z}{2\pi i}\frac{1}{e^{\beta z}+1}\frac{|\bar{\Delta}(q)|^2}{[-z + p^2(1+\bar{m}) - \mu - h]\,[-z - (p-q)^2(1-\bar{m}) + \mu - h]}.\end{aligned} \tag{B.1}$$

In the second line of eq. (B.1), the usual reformulation of the Matsubara sum in terms of a circular integral about the complex plane has been employed. The result of the summation is now given by the residues of the integrand's poles or branch cuts [51]. While the computation of the exact homogeneous mean-field effective action e.g. in sec. 2.2.1 involved logarithmic branch cuts only, the vertex expansion requires the treatment of nontrivial pole structures. The order of these poles is of crucial importance for the determination of the associated residues [127]. For the two-point function in eq. (B.1), the integrand exhibits two first order poles almost everywhere in the domain of momentum integration. Evaluating the residues and plugging in the Fourier ansatz (3.7) therefore results in

$$\begin{aligned}\frac{1}{\beta L}\Gamma^{(2)}_{1\mathrm{D,mf}} &= -\frac{1}{g_\delta^{1\mathrm{D}}}\int_{\mathbf{q}}|\Delta(q)|^2 - \int_{\mathbf{q}}\int_{\mathbf{p}}|\Delta(q)|^2\left\{\frac{1}{[p^2(1+\bar{m}) + (p-q)^2(1-\bar{m}) - 2\mu]\left[1+e^{\beta(p^2(1+\bar{m})-\mu-h)}\right]}\right. \\ &\qquad \left. - \frac{1}{[p^2(1+\bar{m}) + (p-q)^2(1-\bar{m}) - 2\mu]\left[1+e^{-\beta[(p-q)^2(1-\bar{m})-\mu+h]}\right]}\right\} \\ &= -\sum_{l_q}\alpha_q^2\left\{\frac{1}{g_\delta^{1\mathrm{D}}} + \int_{\mathbf{p}}\frac{1}{[p^2(1+\bar{m}) + (p-\omega_{\bar{\Delta}}l_q)^2(1-\bar{m}) - 2\mu]}\right. \\ &\qquad \left.\cdot\left[\frac{1}{\left[1+e^{\beta[p^2(1+\bar{m})-\mu-h]}\right]} - \frac{1}{\left[1+e^{-\beta[(p-\omega_{\bar{\Delta}}l_q)^2(1-\bar{m})-\mu+h]}\right]}\right]\right\}.\end{aligned} \tag{B.2}$$

Unfortunately, the pole structures of higher order n-point functions are much more complicated. With the Fourier ansatz (3.7) already plugged in and using the short notation introduced in eq. (3.10), the expressions up to eighth order read as

$$\begin{aligned}
\frac{1}{\bar{\beta}L}\Gamma^{(4)}_{\text{1D,mf}} =& \frac{1}{2}\sum_{l_q,l_r,l_s}\int_{\mathbf{p}}\oint\frac{\mathrm{d}z}{2\pi i}\frac{1}{1+e^{\beta z}}\frac{\alpha_q\alpha_r\alpha_s\alpha_{q+s-r}}{P^o[z;p]P^u\left[z;p+\omega_{\bar{\Delta}}(l_r-l_q-l_s)\right]} \\
&\cdot\frac{1}{P^o\left[z;p+\omega_{\bar{\Delta}}(l_r-l_q)\right]P^u[z;p-\omega_{\bar{\Delta}}l_q]}\,,
\end{aligned} \tag{B.3a}$$

$$\begin{aligned}
\frac{1}{\bar{\beta}L}\Gamma^{(6)}_{\text{1D,mf}} =& \frac{1}{3}\sum_{l_q,l_r,l_s,l_t,l_u}\int_{\mathbf{p}}\oint\frac{\mathrm{d}z}{2\pi i}\frac{1}{1+e^{\beta z}}\frac{\alpha_q\alpha_r\alpha_s\alpha_t\alpha_u\alpha_{q+s+u-r-t}}{P^o[z;p]P^u[z;p-\omega_{\bar{\Delta}}n_q]P^o\left[z;p+\omega_{\bar{\Delta}}(l_r-l_q)\right]} \\
&\cdot\frac{1}{P^u\left[z;p+\omega_{\bar{\Delta}}(l_r-l_q-l_s)\right]P^o\left[z;p+\omega_{\bar{\Delta}}(l_r+l_t-l_q-l_s)\right]} \\
&\cdot\frac{1}{P^u\left[z;p+\omega_{\bar{\Delta}}(l_r+l_t-l_q-l_s-l_u)\right]}\,,
\end{aligned} \tag{B.3b}$$

$$\begin{aligned}
\frac{1}{\bar{\beta}L}\Gamma^{(8)}_{\text{1D,mf}} =& \frac{1}{4}\sum_{\substack{l_q,l_r,l_s,l_t\\ l_u,l_v,l_w}}\int_{\mathbf{p}}\oint\frac{\mathrm{d}z}{2\pi i}\frac{1}{1+e^{\beta z}}\frac{\alpha_q\alpha_r\alpha_s\alpha_t\alpha_u\alpha_v\alpha_w\alpha_{q+s+u+w-r-t-v}}{P^o[z;p]P^u[z;p-\omega_{\bar{\Delta}}l_q]P^o\left[z;p+\omega_{\bar{\Delta}}(l_r-l_q)\right]} \\
&\cdot\frac{1}{P^u\left[z;p+\omega_{\bar{\Delta}}(l_r-l_q-l_s)\right]P^o\left[z;p+\omega_{\bar{\Delta}}(l_r+l_t-l_q-l_s)\right]} \\
&\cdot\frac{1}{P^u\left[z;p+\omega_{\bar{\Delta}}(l_r+l_t-l_q-l_s-l_u)\right]P^o\left[z;p+\omega_{\bar{\Delta}}(l_r+l_t+l_v-l_q-l_s-l_u)\right]} \\
&\cdot\frac{1}{P^u\left[z;p+\omega_{\bar{\Delta}}(l_r+l_t+l_v-l_q-l_s-l_u-l_w)\right]}\,.
\end{aligned} \tag{B.3c}$$

Here, multiple instances of P^o and P^u appear and consequently the order of the occurring poles depends on the distribution of the Fourier indexes l_i. The computation of the residues is thus still straightforward, but increasingly cumbersome for higher order vertex functions and Fourier components.

While the Matsubara summation can at least in principle be performed fully analytically, this is not the case for the momentum integration for any finite temperature due to the Fermi distribution function occurring in the integrands. Therefore and because of the conceptual simplicity of the residue evaluation, it is convenient to leave also the latter to a computer algebra system[1] which may subsequently be used to evaluate the momentum integrals and perform the minimization of $\Gamma_{\text{1D,mf}}$.

For the desired orders $j_{\max}$ of the vertex and $l_{q,\max}$ of the Fourier expansion, all possible combinations of Fourier indexes l_i must be gathered in a first step. In tab. B.1, the number of different summands for the respective vertex functions is listed. Note that for, e.g., a computation of eighth order in the vertex expansion, all terms of the lower order coefficients have to be dealt with as well.

The numbers in tab. B.1 demonstrate why the use of an algebra system for the Matsubara summation is inevitable, but it also shows the practical limitations of the method itself as the integrands for the numerical momentum integrations become correspondingly large and expensive to evaluate.

For each admissible combination of l_i, the occurring poles and their respective order is then identified by a comparison of the associated index structures inside of the $P^{u/o}$ for each vertex function. Having located and characterized all poles, the residues are known and can be used to construct the final version of the integrands which are ready for evaluation.

$l_{q,\max}$	$\Gamma^{(2)}_{\text{1D,mf}}$	$\Gamma^{(4)}_{\text{1D,mf}}$	$\Gamma^{(6)}_{\text{1D,mf}}$	$\Gamma^{(8)}_{\text{1D,mf}}$
0	1	1	1	1
1	3	27	243	2187
2	5	125	3125	78125
3	7	343	16807	823543

Table B.1: Number of different summands contributing to some vertex function $\Gamma^{(2j)}_{\text{1D,mf}}$ at given truncation order $l_{q,\max}$ of the Fourier expansion.

---

[1] *Wolfram Mathematica* was employed for the results presented in this work.

Appendix C

Path integral representation of the fermion doubling trick

The crucial approximation that is involved in the procedure presented as “fermion doubling trick” in sec. 3.3, is the introduction of artificial double spinor fields Ψ_n in eqns. (3.22) and (3.23) and the treatment of their components $\psi_n(p{-}Q)$ and $\psi_n(p{+}Q)$ as independent with respect to path integration. The purpose of this appendix is to provide a more detailed description of what this approximation actually entails and how far it affects results obtained from Γ_D.

Partitioning of the integration domain Consider some function $f \in L^2(\mathbb{R})$ that is integrated over the real axis.[1] Without loss of generality, this integration can be split in parts,

$$\int_\mathbb{R} f(q) = \int_\mathbb{R} \frac{f(q)}{2} + \int_\mathbb{R} \frac{f(q)}{2} = \int_{\mathbb{V}_1} \frac{f(p-Q)+f(p+Q)}{2} + \int_{\mathbb{V}_2} \frac{f(p-Q)+f(p+Q)}{2} \,. \tag{C.1}$$

Here, the following partitioning of the real axis has been introduced:

$$\mathbb{R} = \mathbb{V}_1 \cup \mathbb{V}_2 \text{ with } \mathbb{V}_1 = \bigcup_{k\,\mathrm{even}} [2Qk, 2Q(k+1)) \text{ and } \mathbb{V}_2 = \bigcup_{k\,\mathrm{odd}} [2Qk, 2Q(k+1)) \text{ for } Q > 0\,. \tag{C.2}$$

In the following, Matsubara indexes and sums are omitted for brevity as they do not play a role for the doubling procedure. Consider now the partition functional for a free Fermi gas, where the same partitioning is applied,

$$\begin{aligned} \mathcal{Z}_\mathrm{free} &= \int \mathcal{D}\bar\psi \mathcal{D}\psi e^{\int_\mathbb{R} \bar\psi D_{2\times2} \psi} = \left(\int \mathcal{D}\bar\psi \mathcal{D}\psi e^{\int_\mathbb{R} \bar\psi D_{2\times2} \psi}\right)^{\frac{1}{2}} \cdot \left(\int \mathcal{D}\bar\psi \mathcal{D}\psi e^{\int_\mathbb{R} \bar\psi D_{2\times2} \psi}\right)^{\frac{1}{2}} \\ &= \left(\int \mathcal{D}_1\bar\Psi \mathcal{D}_1\Psi e^{\int_{\mathbb{V}_1} \bar\Psi D_{Q,4\times4} \Psi}\right)^{\frac{1}{2}} \cdot \left(\int \mathcal{D}_2\bar\Psi \mathcal{D}_2\Psi e^{\int_{\mathbb{V}_2} \bar\Psi D_{Q,4\times4} \Psi}\right)^{\frac{1}{2}} . \end{aligned} \tag{C.3}$$

The D matrices here are the usual inverse propagators for the respective fields, given by

$$D_{2\times2} = \begin{pmatrix} G_+^{-1}(p) & 0 \\ 0 & G_-^{-1}(p) \end{pmatrix} \tag{C.4}$$

and

$$D_{Q,4\times4} = \begin{pmatrix} G_+^{-1}(p-Q) & 0 & 0 & 0 \\ 0 & G_-^{-1}(p-Q) & 0 & 0 \\ 0 & 0 & G_+^{-1}(p+Q) & 0 \\ 0 & 0 & 0 & G_-^{-1}(p+Q) \end{pmatrix}, \tag{C.5}$$

with the notation introduced on page 49. As the domains $\mathbb{V}_1$ and $\mathbb{V}_2$ are disjoint, the path integration in the last line of could be changed to the composite fields Ψ which effectively comes up to a reordering

---

[1] The one-dimensional case is considered here for convenience. While a proper partitioning of domains will be more complicated in higher dimensions, it is in principle straightforward and does not obstruct the general argument.

and splitting of fermionic measures,

$$\mathcal{D}\psi = \prod_{p\in\mathbb{R}} \mathrm{d}\psi_p = \prod_{p\in\mathbb{V}_i} \mathrm{d}\psi_{p+Q} \cdot \prod_{p\in\mathbb{V}_i} \mathrm{d}\psi_{p-Q} \rightarrow \begin{pmatrix} \prod_{p\in\mathbb{V}_i} \mathrm{d}\psi_{p+Q} \\ \prod_{p\in\mathbb{V}_i} \mathrm{d}\psi_{p-Q} \end{pmatrix} \equiv \mathcal{D}_i\Psi \,. \tag{C.6}$$

The last step leads to an equivalent integration procedure if and only if the integrand is defined on the domain $\mathbb{V}_i$ alone.

Calculating the effective action from the second line of eq. (C.3) yields

$$\Gamma_{\text{free}} = -\ln \mathcal{Z}_{\text{free}} = -\frac{1}{2}\mathrm{Tr}_{\mathbb{V}_1}\mathrm{D}_{\mathrm{Q},4\times4} - \frac{1}{2}\mathrm{Tr}_{\mathbb{V}_2}\mathrm{D}_{\mathrm{Q},4\times4} = -\frac{1}{2}\mathrm{Tr}_{\mathbb{R}}\mathrm{D}_{\mathrm{Q},4\times4} = -\mathrm{Tr}_{\mathbb{R}}\mathrm{D}_{2\times2} \,, \tag{C.7}$$

which coincides with the well-known result from the first line. Without any interaction, the doubling trick is therefore just an equivalence transformation as it should be.

Interacting theory Consider now the interacting Gross-Neveu model with a cosine ansatz. The action is characterized by the non-diagonal $\Delta S_{\mathrm{B}}^{(2)}$ instead of free propagators alone. In fact, any model that leads to a structurally equivalent $\Delta S_{\mathrm{B}}^{(2)}$ such as NJL type models may be investigated along the same lines. The crucial difference to the free case is, that a clean separation of the exponentials inside the (mean-field) partition functional is not possible anymore:

$$\begin{aligned} \mathcal{Z}_{\text{int}} &\sim \int \mathcal{D}\bar{\psi}\mathcal{D}\psi e^{\int_{\mathbb{R}} \frac{1}{2}\bar{\Psi}\Delta S_{\mathrm{B}}^{(2)}\Psi} \\ &= \left(\int \mathcal{D}\bar{\psi}\mathcal{D}\psi e^{\left[\int_{\mathbb{V}_1} \bar{\Psi}D_{Q,4\times4}\Psi\right] + \left[\frac{1}{2}\int_{\mathbb{V}_1} \bar{\Psi}M_{4\times4}\Psi\right] + \left[\frac{1}{2}\int_{\mathbb{V}_2} \bar{\Psi}M_{4\times4}\Psi\right]}\right)^{\frac{1}{2}} \\ &\quad\cdot \left(\int \mathcal{D}\bar{\psi}\mathcal{D}\psi e^{\left[\int_{\mathbb{V}_2} \bar{\Psi}D_{Q,4\times4}\Psi\right] + \left[\frac{1}{2}\int_{\mathbb{V}_2} \bar{\Psi}M_{4\times4}\Psi\right] + \left[\frac{1}{2}\int_{\mathbb{V}_1} \bar{\Psi}M_{4\times4}\Psi\right]}\right)^{\frac{1}{2}} . \end{aligned} \tag{C.8}$$

$M_{4\times4}$ is the off-diagonal (interacting) part of $\Delta S_{\mathrm{B}}^{(2)}$ which had to be split in order to achieve equivalence to the first line. In contrast to the free case, the reordering (C.6) of fermionic measures does not help, since both exponentials comprise contributions for domains $\mathbb{V}_1$ as well as $\mathbb{V}_2$. A direct gaussian integration with respect to the Ψ fields is a priori not possible anymore.

In the homogeneous limit $Q \to 0$, the domains of integration $\mathbb{V}_i$ are set equal to the real axis. Equation (C.8) may then be integrated, as $\Delta S_{\mathrm{B}}^{(2)}$ can be rewritten in block-diagonal form without changing the integrands. The doubling trick does therefore not affect the interacting case for homogeneous ground states.

The third terms of the respective exponentials in eq. (C.8) are the problematic ones as they inhibit the exploitation of a reordering of measures as in eq. (C.6). The doubling trick basically consists in altogether ignoring their presence and integrating with respect to the Ψ fields regardless. The consequences are twofold. Firstly, the factor of $\frac{1}{2}$ in front of the second terms effectively results in a corresponding overall factor for each n-point function that is extracted from $\mathcal{Z}_{\text{int}}$. This has been observed in sec. 3.3.1 for the two-point function.

Secondly, the missing third terms are responsible for corrections of order $\mathcal{O}(M^3)$, i.e. to higher order n-point functions. The two-point function is not affected. This can be understood by the following argument. A Gaussian integration with measure, say $\mathcal{D}_1\bar{\Psi}\mathcal{D}_1\Psi$, implies a momentum structure which the bilinear $\bar{\Psi}M_{4\times4}\Psi$ defined on $\mathbb{V}_2$itself cannot exhibit by definition. Although fermion fields with the respective momentum indexes are available, their combination does not correspond to the order required by the $\mathcal{D}_1\bar{\Psi}\mathcal{D}_1\Psi$ integration. Only when the exponential of the above bilinear is expanded, higher order terms can be found that exhibit the appropriate structure.

Therefore, to lowest nontrivial order, the only error introduced by the doubling trick consists in the global numerical factor. The momentum structure of the two-point function coincides with the exact one. This insight constitutes the keystone of the method.

Generalized Fourier ansatz As briefly mentioned in the end of sec. 3.3.1, the doubling trick can in principle be generalized to a “multiplication trick” by extending the ansatz for the chiral order parameter to a general Fourier series,

$$\bar{\sigma}(x) = \sum_{n=0}^{n_{\max}} M^{(n)} \cos(2Qnx)\,. \tag{C.9}$$

Now, a doubling of fermion fields has to be performed for each coefficient $M^{(n)}$ in order to achieve straightforward diagonalizability:

$$\bar{\Psi} = \left(\bar{\psi}(p), \bar{\psi}(p-Q), \bar{\psi}(p+Q), \bar{\psi}(p-2Q), \bar{\psi}(p+2Q), \ldots\right). \tag{C.10}$$

The number of domains into which the real axis must be split for integration grows along,

$$\mathbb{R} = \bigcup_i \mathbb{V}_i \text{ with } \mathbb{V}_i = \bigcup_{\{k_i\}} [Qk_i, Q(k_i+1)) \text{ where } \{k_i\} = \{k \in \mathbb{Z} : \mathrm{mod(k, 2n_{max}+1) = i}\} \text{ for } Q > 0\,. \tag{C.11}$$

As before, the approximation to be made would consist in the ignorance of contributions from all domains except the one which is integrated over in the analog of eq. (C.8). The number of terms that are affected by this grows linearly with $n_{\max}$. While the two-point function receives just a modified global numerical factor, higher order n-point functions are represented worse. Given the complicated interplay of truncations in the vertex and Fourier expansions explored in sec. 3.1.2 for the related case of cold atoms, the usefulness of a generalized Fourier ansatz within the fermion multiplication framework is at least questionable.

Appendix D

Flow equations for the imbalanced Fermi gas

In this appendix, some details on the derivation of the explicit flow equations (4.26) and (4.32) are provided. The computational framework employed here is described in detail in [55]. In the present work, it has been extended by the admission of spin and mass imbalance. The peculiarities introduced by these deformations will therefore be the main focus here. Computations that are largely analogous to the ones in [55] are kept brief accordingly.

D.1 Flow of the effective potential

In Matsubara and momentum space, the renormalized ansatz (4.17) for the effective average action reads as

$$\begin{aligned}\Gamma_k = \sum_n \int_{\mathbf{q}} \Big\{ &\psi^\dagger \left(-i\omega_n + \mathbf{q}^2 + \sigma_3 \bar{m}\mathbf{q}^2 - \mu - \sigma_3 h\right)\psi + \varphi^* \left(-i\omega_n + \frac{1-\bar{m}^2}{2}\mathbf{q}^2\right)\varphi \\ &- \frac{h_\varphi}{2\sqrt{\beta}} \sum_m \int_{\mathbf{p}} \left[\varphi^*(\omega_n+\omega_m, \mathbf{p}+\mathbf{q})\psi^T(\omega_m,\mathbf{p})\epsilon\psi(\omega_n,\mathbf{q}) - \varphi(\omega_n+\omega_m,\mathbf{p}+\mathbf{q})\psi^\dagger(\omega_m,\mathbf{p})\epsilon\psi^*(\omega_n,\mathbf{q})\right]\Big\} \\ &+ \int_\tau \int_{\mathbf{x}} U_k \left[\sum_{m,n}\int_{\mathbf{p},\mathbf{q}} e^{i[(\omega_n-\omega_m)\tau + (\mathbf{p}-\mathbf{q})\cdot\mathbf{x}]} \varphi^*(\omega_n,\mathbf{p})\varphi(\omega_m,\mathbf{q})\right], \qquad \epsilon = \begin{pmatrix} 0 & 1 \\ -1 & 0 \end{pmatrix}.\end{aligned} \tag{D.1}$$

Here, the assumption that $S_{\varphi,k} = 1$ during the flow has already been implemented. The full inverse propagator is obtained by a second functional derivative with respect to the fields,

$$\begin{aligned}\Gamma_k^{(2)} &= \begin{pmatrix} \frac{\vec{\delta}}{\delta\varphi_1(-p)} \\ \frac{\vec{\delta}}{\delta\varphi_2(-p)} \\ \frac{\vec{\delta}}{\delta\psi^T(-p)} \\ \frac{\vec{\delta}}{\delta\psi^\dagger(p)} \end{pmatrix} \Gamma_k \left(\frac{\overleftarrow{\delta}}{\delta\varphi_1(q)}, \frac{\overleftarrow{\delta}}{\delta\varphi_2(q)}, \frac{\overleftarrow{\delta}}{\delta\psi(q)}, \frac{\overleftarrow{\delta}}{\delta\psi^*(-q)} \right) \\ &= \left[\begin{pmatrix} \mathcal{P}_\varphi^{-1} & 0 \\ 0 & \mathbb{O}_{2\times2} \end{pmatrix} + \begin{pmatrix} \mathbb{O}_{2\times2} & 0 \\ 0 & \mathcal{P}_\psi^{-1} \end{pmatrix} + \mathcal{F}_k\right]\delta(p-q) = \left[\mathcal{P}_{\boldsymbol{\varphi}}^{-1} + \mathcal{F}_k\right]\delta(p-q)\,,\end{aligned} \tag{D.2}$$

where $\mathbb{O}_{a\times a}$ are square matrices of dimension a filled with zeros. Again, the Cartesian representation of the complex boson field $\varphi = \frac{1}{\sqrt{2}}[\varphi_1 + i\varphi_2]$ has been used. The free bosonic and fermionic propagator matrices are given by

$$\mathcal{P}_{\varphi}^{-1} = \begin{pmatrix} (1-\bar{m}^2)\frac{\mathbf{q}^2}{2} & \omega_n \\ -\omega_n & (1-\bar{m}^2)\frac{\mathbf{q}^2}{2} \end{pmatrix}, \tag{D.3a}$$

$$\mathcal{P}_{\psi}^{-1} = \begin{pmatrix} 0 & -i\omega_n - \mathbf{q}^2(1+\bar{m}\sigma_3) + \mu + h\sigma_3 \\ -i\omega_n + \mathbf{q}^2(1+\bar{m}\sigma_3) - \mu - h\sigma_3 & 0 \end{pmatrix}, \tag{D.3b}$$

whereas the field-dependent fluctuation matrix in its simplified, projected form reads as

$$\mathcal{F}_k\big|_{\psi=\bar{\psi}=\varphi_2=0,\varphi_1=\sqrt{2\rho}} = \begin{pmatrix} U_k' + 2\rho U_k'' & 0 & 0 & 0 \\ 0 & U_k' & 0 & 0 \\ 0 & 0 & -h_{\varphi}\epsilon\sqrt{\rho} & 0 \\ 0 & 0 & 0 & h_{\varphi}\epsilon\sqrt{\rho} \end{pmatrix}. \tag{D.4}$$

As it is the *regulated* full propagator $\mathcal{G}_{\varphi,k}^{-1} = \left(\Gamma_k^{(2)} + R_{\varphi,k}\right)^{-1}$ that appears on the RHS of the Wetterich equation, the free propagator matrices have to be complemented with the respective regulator structures,

$$\mathcal{P}_{\varphi,k}^{-1} = \mathcal{P}_{\varphi}^{-1} + \begin{pmatrix} k^2 r_{\varphi,k} & 0 \\ 0 & k^2 r_{\varphi,k} \end{pmatrix}, \qquad \mathcal{P}_{\psi,k}^{-1} = \mathcal{P}_{\psi}^{-1} + \begin{pmatrix} 0 & -k^2 r_{\psi,k}\cdot \mathbb{1}_{2\times 2} \\ k^2 r_{\psi,k}\cdot \mathbb{1}_{2\times 2} & 0 \end{pmatrix}. \tag{D.5}$$

Due to its momentum-diagonal structure (see eq. (D.2)), obtaining $\mathcal{G}_{k,\varphi}$ is merely an algebraic problem that is straightforwardly solved. The flow equation for the effective potential can then be written down in terms of its components,

$$[\partial_k U_k]^{\varphi+\psi} = \frac{1}{2}\sum_n \int_{\mathbf{q}} \left\{\left[\mathcal{G}_{\varphi,k}^{(11)} + \mathcal{G}_{\varphi,k}^{(22)}\right] A_{\varphi}^{-1}\partial_k\left[A_{\varphi}k^2 r_{\varphi,k}\right] - \left[\mathcal{G}_{\psi,k}^{(13)} + \mathcal{G}_{\psi,k}^{(24)} - \mathcal{G}_{\psi,k}^{(31)} - \mathcal{G}_{\psi,k}^{(42)}\right]\partial_k\left[k^2 r_{\psi,k}\right]\right\}. \tag{D.6}$$

The remaining problem consists in computing and simplifying the components of the full propagator by doing the algebraic inversion and performing Matsubara sums and momentum integrations.
For the bosonic contribution, this leads to

$$\begin{aligned}[k\partial_k U_k]^{\varphi} &= \sum_n \int_{\mathbf{q}} \frac{\left[(1-\bar{m}^2)\frac{\mathbf{q}^2}{2} + k^2 r_{\varphi,k} + U_k' + \rho U_k''\right] A_{\varphi}^{-1} k\partial_k\left[A_{\varphi}k^2 r_{\varphi,k}\right]}{\omega_n^2 + \left[(1-\bar{m}^2)\frac{\mathbf{q}^2}{2} + k^2 r_{\varphi,k} + U_k'\right]\cdot\left[(1-\bar{m}^2)\frac{\mathbf{q}^2}{2} + k^2 r_{\varphi,k} + U_k' + 2\rho U_k''\right]} \\ &= \frac{\sqrt{2}k^5}{3\pi^2}\frac{1}{(1-\bar{m}^2)^{\frac{3}{2}}}\left(1-\frac{\eta_{A,k}}{5}\right)\left[\sqrt{\frac{1+w_1}{1+w_2}} + \sqrt{\frac{1+w_2}{1+w_1}}\right]\left[\frac{1}{2} + N_{\mathrm{B}}\left(\sqrt{1+w_1}\sqrt{1+w_2}\right)\right].\end{aligned} \tag{D.7}$$

The fermionic one is slightly more complicated. Exemplarily, consider the contribution from the (31) component of the full propagator,

$$\begin{aligned}[k\partial_k U_k]^{\psi}_{(31)} &= \frac{1}{2}\sum_n \int_{\mathbf{q}} \frac{\left[-i\omega_n + \mathbf{q}^2(1-\bar{m}) - \mu + h + k^2 r_{\psi,k}\right] k\partial_k\left[k^2 r_{\psi,k}\right]}{\left[-i\omega_n - \mathbf{q}^2(1+\bar{m}) + \mu + h - k^2 r_{\psi,k}\right]\cdot\left[-i\omega_n + \mathbf{q}^2(1-\bar{m}) - \mu + h + k^2 r_{\psi,k}\right] - h_{\varphi}^2\rho} \\ &= \frac{k^5}{8\pi^2}\int_{\max[-\tilde{\mu},-1]}^{1} \mathrm{d}\tilde{z}\frac{\sqrt{\tilde{z}+\tilde{\mu}}\,\mathrm{sign}(\tilde{z})}{\sqrt{1+w_3}}\left\{\frac{\mathrm{sign}(\tilde{z}) + \sqrt{1+w_3}}{e^{\left(\tilde{z}\bar{m}+\tilde{\mu}\bar{m}-\tilde{h}+\sqrt{1+w_3}\right)/\tilde{T}}+1} - \frac{\mathrm{sign}(\tilde{z}) - \sqrt{1+w_3}}{e^{\left(\tilde{z}\bar{m}+\tilde{\mu}\bar{m}-\tilde{h}-\sqrt{1+w_3}\right)/\tilde{T}}+1}\right\}.\end{aligned} \tag{D.8}$$

Making use of symmetries of the free fermion propagator matrix in eq. (D.3), the full fermionic contribution simplifies to

$$\begin{aligned}[k\partial_k U_k]^{\psi} &= [k\partial_k U_k]^{\psi}_{(31)}(\bar{m},h) + [k\partial_k U_k]^{\psi}_{(13)}(\bar{m},h) + [k\partial_k U_k]^{\psi}_{(31)}(-\bar{m},-h) + [k\partial_k U_k]^{\psi}_{(13)}(-\bar{m},-h) \\ &= \frac{k^5}{2\pi^2}\int_{\max[-\tilde{\mu},-1]}^{1} \mathrm{d}\tilde{z}\frac{\sqrt{\tilde{z}+\tilde{\mu}}}{\sqrt{1+w_3}}\sum_{\sigma=\pm 1}\sigma N_{\mathrm{F}}\left(\bar{m}(\tilde{z}+\tilde{\mu}) - \tilde{h} + \sigma\sqrt{1+w_3}\right).\end{aligned} \tag{D.9}$$

The abbreviations used here have been introduced in sec. 4.2.2 and are repeated here for conciseness,

$$N_{\mathrm{F}}(x) = \frac{1}{e^{x/\tilde{T}} + 1}\,, \qquad N_{\mathrm{B}} = \frac{1}{e^{x/\tilde{T}} - 1}\,, \tag{4.27}$$

and

$$w_1 = \frac{U_k'}{k^2}\,, \qquad w_2 = \frac{U_k' + 2\rho U_k''}{k^2}\,, \quad w_3 = \frac{h_{\varphi,k}^2 \rho}{k^4}\,, \tag{4.28}$$

and quantities divided by k^2 are denoted with a tilde sign, e.g. $\tilde{T} \equiv T/k^2$.

D.2 Boson anomalous dimension

The formal projection rule in eq. (4.30), yielding the spatial boson anomalous dimension, is only slightly modified with respect to the one discussed in [55] to allow for finite mass imbalance. However, when determining the explicit expressions, two major differences occur: simplifications made in ref. [55] due to the polynomial expansion cannot be applied here and $\eta_{A,k}^{\psi,2}$ is finite only for $\bar{m} \neq 0$. As the overall $\eta_{A,k}$ is thus not easily comparable to previous results in the literature, some computational details are presented here that are supposed to demonstrate the origin of those modifications.

Fermionic contribution Setting up the explicit expression for the combined fermion contribution $\eta_{A,k}^{\psi}$, the kernel (4.31) of the projection rule (4.30) has to be evaluated first. It is not trivial to apply the projection rule also to the RHS of the Wetterich equation. Since two functional derivatives of the latter are required, the projection onto constant field configurations cannot be applied before computing the full propagator. An exact inversion of $\Gamma_k^{(2)} + R_{k,\varphi}$ with the general field dependence retained is, however, not possible. Fortunately, the full propagator is not needed anyway for the computation of $\eta_{A,k}$, but rather its contributions which are quadratic in the boson field alone. The second term of the expansion

$$\partial_t \Gamma_k = \frac{1}{2}\mathrm{STr}\left[\frac{\partial_t R_{k,\varphi}}{\Gamma_k^{(2)} + R_{k,\varphi}}\right] = \frac{1}{2}\mathrm{STr}\left[\tilde{\partial}_t \ln\left(\mathcal{P}_{k,\varphi}^{-1} + \mathcal{F}_k\right)\right] = \frac{1}{2}\mathrm{STr}\left[\tilde{\partial}_t \ln\left(\mathcal{P}_{k,\varphi}^{-1}\right) - \tilde{\partial}_t \sum_{n=1}^{\infty} \frac{(-1)^n}{n}\left(\mathcal{P}_{k,\varphi}\mathcal{F}_k\right)^n\right], \tag{D.10}$$

thus contains all information that is needed. Here, $\tilde{\partial}_t$ is a symbol that is usually introduced for notational convenience. It represents a t derivative acting exclusively on the k dependence of the regulator functions. The free propagator matrix $\mathcal{P}_{k,\varphi}^{-1}$ may again be inverted straightforwardly, resulting in an explicit expression for

$$\begin{aligned}
\eta_A^{\psi} =& \frac{1}{1-\bar{m}^2}\frac{h_\varphi^2}{4}\frac{\partial^2}{\partial q^2}\left[\tilde{\partial}_t \mathop{\sum\!\!\!\!\!\!\!\int}_{n,\mathbf{p}} \frac{\det_{\mathrm{F}}^{\mathrm{M},+}(\mathbf{p}+\mathbf{q})}{\det_{\mathrm{F}}^{+}(\mathbf{p})\det_{\mathrm{F}}^{+}(\mathbf{p}+\mathbf{q})} + i.c.\right]_{q=0} \\
=& \frac{1}{1-\bar{m}^2}\frac{h_\varphi^2}{4}\frac{\partial^2}{\partial q^2}\left[\mathop{\sum\!\!\!\!\!\!\!\int}_{n,\mathbf{p}} \frac{2f(\mathbf{p}+\mathbf{q})\cdot\det_{\mathrm{F}}^{+}(\mathbf{p}) - 2f(\mathbf{p})\det_{\mathrm{F}}^{\mathrm{M},+}(\mathbf{p}+\mathbf{q})}{\det_{\mathrm{F}}^{+}(\mathbf{p})^2\cdot\det_{\mathrm{F}}^{+}(\mathbf{p}+\mathbf{q})}\cdot\left(\partial_t R_{\psi,k}(\mathbf{p})\right) + i.c.\right]_{q=0} \\
&+ \frac{1}{1-\bar{m}^2}\frac{h_\varphi^2}{4}\frac{\partial^2}{\partial q^2}\left[\mathop{\sum\!\!\!\!\!\!\!\int}_{n,\mathbf{p}} \frac{2f(\mathbf{p}-\mathbf{q})\cdot\det_{\mathrm{F}}^{+}(\mathbf{p}) - 2f(\mathbf{p})\det_{\mathrm{F}}^{\mathrm{M},+}(\mathbf{p}-\mathbf{q})}{\det_{\mathrm{F}}^{+}(\mathbf{p})^2\cdot\det_{\mathrm{F}}^{+}(\mathbf{p}-\mathbf{q})}\cdot\left(\partial_t R_{\psi,k}(\mathbf{p})\right) + i.c.\right]_{q=0}.
\end{aligned} \tag{D.11}$$

The acronym *i.c.* stands for *imbalance conjugate* in analogy to the widely used *h.c.* for hermitean conjugation. It symbolizes additional terms of the same structure as the ones explicitly given, but with $h \to -h$ and $\bar{m} \to -\bar{m}$. Furthermore, the following abbreviations were introduced for clarity:

$$\det_{\mathrm{F}}^{+}(\mathbf{p}) = h_\varphi^2\rho + \omega_n^2 + f^2(\mathbf{p}) - g^2(\mathbf{p}) - 2i\omega_n g(\mathbf{p})\,, \tag{D.12a}$$

$$\det_{\mathrm{F}}^{\mathrm{M},+}(\mathbf{p}+\mathbf{q}) = 2h_\varphi^2\rho + 2\omega_n^2 + 2f(\mathbf{p})f(\mathbf{p}+\mathbf{q}) - 2g(\mathbf{p})g(\mathbf{p}+\mathbf{q}) - 2i\omega_n\left[g(\mathbf{p}) + g(\mathbf{p}+\mathbf{q})\right], \tag{D.12b}$$

$$f(\mathbf{p}) = p^2 - \mu + k^2 r_{\psi,k}(\mathbf{p})\,, \tag{D.12c}$$

$$g(\mathbf{p}) = p^2\bar{m} - h\,. \tag{D.12d}$$

Applying the momentum projection to the integrand of (D.11), it becomes

$$\begin{aligned}&\frac{\partial^2}{\partial q^2}\left[\frac{2f(\mathbf{p}+\mathbf{q})\cdot\det_{\mathrm{F}}^{+}(\mathbf{p})-2f(\mathbf{p})\det_{\mathrm{F}}^{\mathrm{M},+}(\mathbf{p}+\mathbf{q})}{\det_{\mathrm{F}}^{+}(\mathbf{p})^2\cdot\det_{\mathrm{F}}^{+}(\mathbf{p}+\mathbf{q})}\right]_{\mathbf{q}=0}\\&=\frac{2f''(\mathbf{p})}{\det_{\mathrm{F}}^{+}(\mathbf{p})^2}+4\frac{f'(\mathbf{p})g(\mathbf{p})g'(\mathbf{p})-f(\mathbf{p})g'(\mathbf{p})^2+i\omega_n f'(\mathbf{p})g'(\mathbf{p})}{\det_{\mathrm{F}}^{+}(\mathbf{p})^3}\,,\end{aligned}\tag{D.13}$$

where

$$f'(\mathbf{p})=2p\cos\vartheta\left(1+r'_{\psi,k}(\mathbf{p})\right),\tag{D.14a}$$

$$f''(\mathbf{p})=2+2r'_{\psi,k}(\mathbf{p})+4p^2\cos^2\vartheta r''_{\psi,k}(\mathbf{p})\,,\tag{D.14b}$$

$$g'(\mathbf{p})=2\bar{m}p\cos\vartheta\,.\tag{D.14c}$$

Here, ϑ is the angle between the integration momentum $\mathbf{p}$ and the external $\mathbf{q}$. The first term is present also in the mass-balanced setup, whereas the second one is proportional to $g'(\mathbf{p})$ and can thus only be finite for $\bar{m}\neq 0$.

The computation of the momentum integral in eq. (D.11) requires special care due to the occurrence of momentum derivatives of the regulator functions in (D.14). It is

$$\partial_t R_{\psi,k}(\mathbf{p})=2k^2\mathrm{sign}(z)\Theta\left(1-|z|\right),\tag{D.15a}$$

$$f'(\mathbf{p})\cdot\partial_t R_{\psi,k}(\mathbf{p})=2p\cos\vartheta\left[1+\left(\delta(z)-1\right)\Theta\left(1-|z|\right)\right]\cdot 2k^2\mathrm{sign}(z)\Theta\left(1-|z|\right)=0\,,\tag{D.15b}$$

$$f''(\mathbf{p})\cdot\partial_t R_{\psi,k}(\mathbf{p})=4p^2\cos^2\vartheta\left[\delta(1-z)-\delta(1+z)\right]\cdot 2k^2\mathrm{sign}(z)\Theta\left(1-|z|\right)\,,\tag{D.15c}$$

with $z=(\mathbf{p}^2-\mu)/k^2$. While terms $\sim f'(\mathbf{p})$ are thus always canceled, the occurrence of $f''(\mathbf{p})$ requires an evaluation of the step function at its nonanalytic point. As derivatives of Θ or sign functions that have been used here are in any case only defined in a distributional sense, $\Theta(0)=\frac{1}{2}$ here. This has to be kept in mind when evaluating eq. (D.11).

Having deliberated these crucial considerations, the remaining steps are again straightforward. The explicit expressions (D.13), with (D.12) and (D.14) have to be plugged into (D.11). Matsubara sums and momentum integrals may again be performed, which finally leads to the expressions presented in sec. 4.2.2,

$$\begin{aligned}\eta_{A,k}^{\psi,1}=&\frac{1}{1-\bar{m}^2}\frac{h_{\varphi,k}^2}{6\pi^2 k(1+w_3)^{\frac{3}{2}}}\sum_{\sigma,\kappa=\pm1}\left(\tilde{\mu}+\kappa\right)^{\frac{3}{2}}\theta\left(\tilde{\mu}+\kappa\right)\\&\cdot\left[\sigma N_{\mathrm{F}}\left(\bar{m}(\tilde{\mu}+\kappa)-\tilde{h}-\sigma\sqrt{1+w_3}\right)+\sqrt{1+w_3}N'_{\mathrm{F}}\left(\bar{m}(\tilde{\mu}+\kappa)-\tilde{h}-\sigma\sqrt{1+w_3}\right)\right],\end{aligned}\tag{4.32a}$$

$$\begin{aligned}\eta_{A,k}^{\psi,2}=&-\frac{h_{\varphi,k}^2\bar{m}^2}{6\pi^2 k(1-\bar{m}^2)}\int_{\max[-\tilde{\mu},-1]}^{1}\mathrm{d}\tilde{z}\frac{(\tilde{z}+\tilde{\mu})^{\frac{3}{2}}}{(1+w_3)^{\frac{5}{2}}}\sum_{\sigma=\pm1}\left[3\sigma N_{\mathrm{F}}\left(\bar{m}(\tilde{z}+\tilde{\mu})-\tilde{h}+\sigma\sqrt{1+w_3}\right)\right.\\&\left.-3\sqrt{1+w_3}N'_{\mathrm{F}}\left(\bar{m}(\tilde{z}+\tilde{\mu})-\tilde{h}-\sigma\sqrt{1+w_3}\right)-\sigma(1+w_3)N''_{\mathrm{F}}\left(\bar{m}(\tilde{z}+\tilde{\mu})-\tilde{h}-\sigma\sqrt{1+w_3}\right)\right].\end{aligned}\tag{4.32b}$$

Bosonic contribution The computation of $\eta_{A,k}^{\varphi}$ proceeds largely analogous to the fermionic case. The explicit expression of the second term of the expansion (D.10) yields

$$\begin{aligned}\eta_{A,k}^{\varphi}=&\frac{\rho U_k''^2}{1-\bar{m}^2}\frac{\partial^2}{\partial q^2}\left[\tilde{\partial}_t\sum\!\!\!\!\!\!\!\int_{n,\mathbf{p}}\frac{\det_{\mathrm{B}}^{\mathrm{M}}(\mathbf{p}+\mathbf{q})}{\det_{\mathrm{B}}(\mathbf{p})\cdot\det_{\mathrm{B}}(\mathbf{p}+\mathbf{q})}\right]_{q=0}\\=&\frac{\rho U_k''^2}{1-\bar{m}^2}\frac{1}{2}\frac{\partial^2}{\partial q^2}\left[\sum\!\!\!\!\!\!\!\int_{n,\mathbf{p}}\left(\frac{\det_{\mathrm{B}}(\mathbf{p})\cdot[a_1+a_2]\,(\mathbf{p}+\mathbf{q})-\det_{\mathrm{B}}^{\mathrm{M}}(\mathbf{p}+\mathbf{q})\cdot[a_1+a_2](\mathbf{p})}{\det_{\mathrm{B}}(\mathbf{p})^2\cdot\det_{\mathrm{B}}(\mathbf{p}+\mathbf{q})}\right)\partial_t R_{\varphi,k}(\mathbf{p})\right]_{q=0}\\&+\frac{\rho U_k''^2}{1-\bar{m}^2}\frac{1}{2}\frac{\partial^2}{\partial q^2}\left[\sum\!\!\!\!\!\!\!\int_{n,\mathbf{p}}\left(\frac{\det_{\mathrm{B}}(\mathbf{p})\cdot[a_1+a_2]\,(\mathbf{p}-\mathbf{q})-\det_{\mathrm{B}}^{\mathrm{M}}(\mathbf{p}-\mathbf{q})\cdot[a_1+a_2](\mathbf{p})}{\det_{\mathrm{B}}(\mathbf{p})^2\cdot\det_{\mathrm{B}}(\mathbf{p}-\mathbf{q})}\right)\partial_t R_{\varphi,k}(\mathbf{p})\right]_{q=0}.\end{aligned}\tag{D.17}$$

Here, the abbreviations

$$\begin{aligned}\det{}_{\mathrm{B}}(\mathbf{p}) &= \omega_n^2 + \left[\frac{1-\bar{m}^2}{2}p^2 + k^2 r_{\varphi,k}(\mathbf{p}) + w_1\right]\left[\frac{1-\bar{m}^2}{2}p^2 + k^2 r_{\varphi,k}(\mathbf{p}) + w_2\right] \\ &\equiv \omega_n^2 + a_1(\mathbf{p})a_2(\mathbf{p})\,, \qquad \text{(D.18a)} \\ \det{}_{\mathrm{B}}^{\mathrm{M}}(\mathbf{p}+\mathbf{q}) &= 2\omega_n^2 + a_1(\mathbf{p}+\mathbf{q})a_2(\mathbf{p}) + a_1(\mathbf{p})a_2(\mathbf{p}+\mathbf{q})\,, \qquad \text{(D.18b)}\end{aligned}$$

were introduced. Making use of the identities

$$\begin{aligned}\det{}_{\mathrm{B}}^{\mathrm{M}}(\mathbf{p}+\mathbf{q})_{\mathbf{q}=0} &= 2\det{}_{\mathrm{B}}(\mathbf{p})\,, \qquad \text{(D.19a)} \\ \det{}'^{\mathrm{M}}_{\mathrm{B}}(\mathbf{p}+\mathbf{q})_{\mathbf{q}=0} &= \det{}'_{\mathrm{B}}(\mathbf{p})\,, \qquad \text{(D.19b)} \\ \det{}''^{\mathrm{M}}_{\mathrm{B}}(\mathbf{p}+\mathbf{q})_{\mathbf{q}=0} &= \det{}''_{\mathrm{B}}(\mathbf{p}) - 2a'_1(\mathbf{p})a'_2(\mathbf{p})\,, \qquad \text{(D.19c)} \\ a'_i(\mathbf{p}) &= p\cos\vartheta(1-\bar{m}^2)\Theta(y-k^2)\,, \qquad \text{(D.19d)} \\ a''_i(\mathbf{p}) &= 2y\cos^2\vartheta(1-\bar{m}^2)\delta(y-k^2) + (1-\bar{m}^2)\Theta(y-k^2)\,, \qquad \text{(D.19e)}\end{aligned}$$

where $y = \left(1-\bar{m}^2\right)q^2/(2k^2)$ and the fact, that $\partial_t R_{\varphi,k}(\mathbf{p}) \sim \Theta\left(k^2 - y\right)$, the overall bosonic contribution to $\eta_{A,k}$ is reduced to

$$\begin{aligned}\eta^{\varphi}_{A,k} &= 2\frac{\rho U''^2_k}{1-\bar{m}^2}\sum_n \int_{\mathbf{p}} \left(\frac{a''_1(\mathbf{p}) + a''_2(\mathbf{p})}{\det{}^2_B(\mathbf{p})} - 2\frac{a'^2_1(\mathbf{p})a_2(\mathbf{p}) + a_1(\mathbf{p})a'^2_2(\mathbf{p})}{\det{}^3_B(\mathbf{p})}\right)\partial_t R_{\varphi,k}(\mathbf{p}) \\ &= \frac{\rho_{0,k}U''^2_k}{(1-\bar{m}^2)^{\frac{3}{2}}}\frac{\sqrt{2}}{3\pi^2 k}\frac{1}{[(1+w_1)(1+w_2)]^{\frac{3}{2}}}\cdot\left[1 + 2N_{\mathrm{B}}\left(\sqrt{1+w_1}\sqrt{1+w_2}\right) - 2N'_{\mathrm{B}}\left(\sqrt{1+w_1}\sqrt{1+w_2}\right)\right]. \\ & \qquad \text{(4.32c)}\end{aligned}$$

Bibliography

[1] F. Jegerlehner and A. Nyffeler, *The muon g-2*, Phys. Rep. **477**(1–3), 1 (2009).

[2] P. J. Mohr, B. N. Taylor, and D. B. Newell, *CODATA recommended values of the fundamental physical constants: 2010*, Rev. Mod. Phys. **84**, 1527 (2012).

[3] P. W. Higgs, *Broken symmetries, massless particles and gauge fields*, Phys. Lett. **12**(2), 132 (1964).

[4] F. Englert and R. Brout, *Broken Symmetry and the Mass of Gauge Vector Mesons*, Phys. Rev. Lett. **13**, 321 (1964).

[5] P. W. Higgs, *Broken Symmetries and the Masses of Gauge Bosons*, Phys. Rev. Lett. **13**, 508 (1964).

[6] G. S. Guralnik, C. R. Hagen, and T. W. B. Kibble, *Global Conservation Laws and Massless Particles*, Phys. Rev. Lett. **13**, 585 (1964).

[7] G. Aad *et al.*, *Observation of a new particle in the search for the Standard Model Higgs boson with the ATLAS detector at the LHC*, Phys. Lett. B **716**(1), 1 (2012).

[8] S. Chatrchyan *et al.*, *Observation of a new boson at a mass of 125 GeV with the CMS experiment at the LHC*, Phys. Lett. B **716**(1), 30 (2012).

[9] S. Weinberg, *Phenomenological Lagrangians*, Physica A **96**(1–2), 327 (1979).

[10] H. Bohr and H. Nielsen, *Hadron production from a boiling quark soup*, Nucl. Phys. B **128**(2), 275–293 (1977).

[11] J. Bardeen, L. N. Cooper, and J. R. Schrieffer, *Theory of Superconductivity*, Phys. Rev. **108**(5), 1175–1204 (1957).

[12] J. Bednorz and K. Müller, *Possible high T_c superconductivity in the Ba-La-Cu-O system*, Z. Phys. B **64**(2), 189 (1986).

[13] K. Bennemann and J. Ketterson, in K. Bennemann and J. Ketterson, eds., *Superconductivity* (Springer Berlin Heidelberg, 2008), pp. 3–26, ISBN 978-3-540-73252-5, `http://dx.doi.org/10.1007/978-3-540-73253-2_1`.

[14] A. A. Kordyuk, *Pseudogap from ARPES experiment: three gaps in cuprates and topological superconductivity*, Low Temp. Phys. **41**, 319 (2015).

[15] G. Martinez, (2013), arXiv:1304.1452.

[16] K. Bennemann and J. Ketterson, eds., *Superconductivity* (Springer Berlin Heidelberg, 2008), ISBN 978-3-540-73253-2, `http://dx.doi.org/10.1007/978-3-540-73253-2`.

[17] M. H. Anderson, J. R. Ensher, M. R. Matthews, C. E. Wieman, and E. A. Cornell, *Observation of Bose-Einstein condensation in a dilute atomic vapor*, Science **269**(5221), 198 (1995).

[18] C. C. Bradley, C. Sackett, J. Tollett, and R. Hulet, *Evidence of Bose-Einstein condensation in an atomic gas with attractive interactions*, Phys. Rev. Lett. **75**(9), 1687 (1995).

[19] K. B. Davis, M.-O. Mewes, M. R. Andrews, N. Van Druten, D. Durfee, D. Kurn, and W. Ketterle, *Bose-Einstein condensation in a gas of sodium atoms*, Phys. Rev. Lett. **75**(22), 3969 (1995).

[20] S. Jochim, M. Bartenstein, A. Altmeyer, G. Hendl, S. Riedl, C. Chin, J. H. Denschlag, and R. Grimm, *Bose-Einstein condensation of molecules*, Science **302**(5653), 2101 (2003).

[21] C. Regal, M. Greiner, and D. S. Jin, *Observation of resonance condensation of fermionic atom pairs*, Phys. Rev. Lett. **92**(4), 040403 (2004).

[22] M.-O. Mewes, M. R. Andrews, D. M. Kurn, D. S. Durfee, C. G. Townsend, and W. Ketterle, *Output Coupler for Bose-Einstein Condensed Atoms*, Phys. Rev. Lett. **78**(4), 582–585 (1997).

[23] M. W. Zwierlein, J. R. Abo-Shaeer, A. Schirotzek, C. H. Schunck, and W. Ketterle, *Vortices and superfluidity in a strongly interacting Fermi gas*, Nature **435**(7045), 1047–1051 (2005).

[24] L. A. Sidorenkov, M. K. Tey, R. Grimm, Y.-H. Hou, L. Pitaevskii, and S. Stringari, *Second sound and the superfluid fraction in a Fermi gas with resonant interactions*, Nature **498**(7452), 78–81 (2013).

[25] H.-J. Briegel, T. Calarco, D. Jaksch, J. I. Cirac, and P. Zoller, *Quantum computing with neutral atoms*, J. Mod. Opt. **47**(2-3), 415–451 (2000).

[26] U.-J. Wiese, *Towards quantum simulating QCD*, Nucl. Phys. A **931**, 246–256 (2014).

[27] H. Feshbach, *Unified theory of nuclear reactions*, Ann. Phys. **5**(4), 357 (1958).

[28] H. Feshbach, *A unified theory of nuclear reactions. II*, Ann. Phys. **19**(2), 287 (1962).

[29] S. Diehl, *The BCS-BEC Crossover in Ultracold Fermi Gases*, Doktorarbeit, University of Heidelberg (2006), `http://www.ub.uni-heidelberg.de/archiv/6965`.

[30] H. T. Stoof, K. B. Gubbels, and D. B. Dickerscheid, *Ultracold quantum fields*, vol. 1 (Springer, 2009), ISBN 978-1-4020-8763-9.

[31] M. Randeria, W. Zwerger, and M. Zwierlein, in W. Zwerger, ed., *The BCS-BEC Crossover and the Unitary Fermi Gas* (Springer Berlin Heidelberg, 2012), vol. 836 of *Lecture Notes in Physics*, pp. 1–32.

[32] C. Chin, R. Grimm, P. Julienne, and E. Tiesinga, *Feshbach Resonances in Ultracold Gases*, Rev. Mod. Phys. **82**, 1225 (2008).

[33] L. D. Landau and E. M. Lifschitz, *Lehrbuch der Theoretischen Physik III - Quantenmechanik* (Akademie-Verlag Berlin, 1979).

[34] A. L. Fetter and J. D. Walecka, *Quantum Theory of Many-Particle Systems* (Dover Publications, 2003), ISBN 0-486-42827-3.

[35] E. Braaten and H.-W. Hammer, *Universality in few-body systems with large scattering length*, Phys. Rep. **428**(5-6), 259–390 (2006).

[36] D. M. Eagles, *Possible Pairing without Superconductivity at Low Carrier Concentrations in Bulk and Thin-Film Superconducting Semiconductors*, Phys. Rev. **186**(2), 456–463 (1969).

[37] A. J. Leggett, in *Modern trends in the theory of condensed matter* (Springer, 1980), pp. 13–27.

[38] C. Chin, *Observation of the Pairing Gap in a Strongly Interacting Fermi Gas*, Science **305**(5687), 1128–1130 (2004).

[39] M. W. Zwierlein, C. A. Stan, C. H. Schunck, S. M. F. Raupach, A. J. Kerman, and W. Ketterle, *Condensation of Pairs of Fermionic Atoms near a Feshbach Resonance*, Phys. Rev. Lett. **92**(12), 120403 (2004).

[40] T. Bourdel, L. Khaykovich, J. Cubizolles, J. Zhang, F. Chevy, M. Teichmann, L. Tarruell, S. J. J. M. F. Kokkelmans, and C. Salomon, *Experimental Study of the BEC-BCS Crossover Region in Lithium 6*, Phys. Rev. Lett. **93**(5), 050401 (2004).

[41] G. B. Partridge, K. E. Strecker, R. I. Kamar, M. W. Jack, and R. G. Hulet, *Molecular Probe of Pairing in the BEC-BCS Crossover*, Phys. Rev. Lett. **95**(2), 020404 (2005).

[42] I. Bloch, J. Dalibard, and W. Zwerger, *Many-body physics with ultracold gases*, Rev. Mod. Phys. **80**(3), 885 (2008).

[43] S. Giorgini, L. P. Pitaevskii, and S. Stringari, *Theory of ultracold atomic Fermi gases*, Rev. Mod. Phys. **80**(4), 1215–1274 (2008).

[44] W. Zwerger, ed., *The BCS-BEC Crossover and the Unitary Fermi Gas* (Springer, Berlin, 2012), ISBN 978-3-642-21977-1.

[45] M. Randeria and E. Taylor, *Crossover from Bardeen-Cooper-Schrieffer to Bose-Einstein Condensation and the Unitary Fermi Gas*, Ann. Rev. Cond. Matt. Phys. **5**(1), 209–232 (2014).

[46] K. Gubbels and H. Stoof, *Imbalanced Fermi gases at unitarity*, Phys. Rep. **525**(4), 255–313 (2013).

[47] J. Braun, *Fermion interactions and universal behavior in strongly interacting theories*, J. Phys. G **39**(3), 033001 (2012).

[48] S. R. White, *Density matrix formulation for quantum renormalization groups*, Phys. Rev. Lett. **69**(19), 2863–2866 (1992).

[49] P. Hohenberg and W. Kohn, *Inhomogeneous Electron Gas*, Phys. Rev. **136**(3B), B864–B871 (1964).

[50] M. Takahashi, *Thermodynamics of One-Dimensional Solvable Models* (Cambridge University Press, 2005), ISBN 978-0521551434.

[51] A. Altland and B. D. Simons, *Condensed Matter Field Theory* (Cambridge University Press, 2010), ISBN 978-0-521-76975-4.

[52] J. I. Kapusta and C. Gale, *Finite-Temperature Field Theory: Principles and Applications (Cambridge Monographs on Mathematical Physics)* (Cambridge University Press, 2006), ISBN 0-521-82082-0.

[53] R. Stratonovich, in *Sov. Phys. Dokl.* (1957), vol. 2, p. 416.

[54] J. Hubbard, *Calculation of Partition Functions*, Phys. Rev. Lett. **3**(2), 77–78 (1959).

[55] S. Diehl, S. Floerchinger, H. Gies, J. M. Pawlowski, and C. Wetterich, *Functional renormalization group approach to the BCS-BEC crossover*, Ann. Phys. **522**, 615 (2010).

[56] S. Flörchinger, *Functional Renormalization and Ultracold Quantum Gases* (Springer Berlin Heidelberg, 2010), `http://dx.doi.org/10.1007/978-3-642-14113-3`.

[57] T. Kugo, *Eichtheorie* (Springer, 1997), ISBN 3-540-62063-X.

[58] J. Goldstone, *Field theories with Superconductor solutions*, Il Nuovo Cimento **19**(1), 154–164 (1961).

[59] A. Schmitt, in *Introduction to Superfluidity* (Springer International Publishing, 2015), vol. 888 of *Lecture Notes in Physics*, pp. 1–6, ISBN 978-3-319-07946-2, `http://dx.doi.org/10.1007/978-3-319-07947-9_1`.

[60] J.-P. Blaizot, (2008), arXiv:0801.0009.

[61] R. Grimm, M. Weidemüller, and Y. B. Ovchinnikov, *Optical dipole traps for neutral atoms*, Adv. At., Mol., Opt. Phys. **42**, 95 (2000).

[62] R. M. Dreizler and E. K. U. Gross, *Density Functional Theory* (Springer Science + Business Media, 1990), ISBN 978-3-642-86105-5, `http://dx.doi.org/10.1007/978-3-642-86105-5`.

[63] E. Engel and R. M. Dreizler, *Density Functional Theory* (Springer Berlin Heidelberg, 2011), ISBN 978-3-642-14090-7, `http://dx.doi.org/10.1007/978-3-642-14090-7`.

[64] A. Recati, C. Lobo, and S. Stringari, *Role of interactions in spin-polarized atomic Fermi gases at unitarity*, Phys. Rev. A **78**(2), 023633 (2008).

[65] J. Braun, J. E. Drut, T. Jahn, M. Pospiech, and D. Roscher, *Phases of spin- and mass-imbalanced ultracold Fermi gases in harmonic traps*, Phys. Rev. A **A89**(5), 053613 (2014).

[66] P. Dyke, E. D. Kuhnle, S. Whitlock, H. Hu, M. Mark, S. Hoinka, M. Lingham, P. Hannaford, and C. J. Vale, *Crossover from 2D to 3D in a Weakly Interacting Fermi Gas*, Phys. Rev. Lett. **106**(10), 105304 (2011).

[67] V. E. Barlette, M. M. Leite, and S. K. Adhikari, *Quantum scattering in one dimension*, Eur. J. Phys. **21**(5), 435–440 (2000).

[68] M. Olshanii, *Atomic Scattering in the Presence of an External Confinement and a Gas of Impenetrable Bosons*, Phys. Rev. Lett. **81**(5), 938–941 (1998).

[69] D. Gross and A. Neveu, *Dynamical symmetry breaking in asymptotically free field theories*, Phys. Rev. D **10**(10), 3235–3253 (1974).

[70] U. Wolff, *The phase diagram of the infinite-N Gross-Neveu model at finite temperature and chemical potential*, Phys. Lett. B **157**(4), 303–308 (1985).

[71] V. Schön and M. Thies, *Emergence of the Skyrme crystal in Gross-Neveu and 't Hooft models at finite density*, Phys. Rev. D **62**(9), 096002 (2000).

[72] A. Brzoska and M. Thies, *No first-order phase transition in the Gross-Neveu model?*, Phys. Rev. D **65**(12), 125001 (2002).

[73] M. Thies and K. Urlichs, *Revised phase diagram of the Gross-Neveu model*, Phys. Rev. D **67**(12), 125015 (2003).

[74] M. Thies, *Analytical solution of the Gross-Neveu model at finite density*, Phys. Rev. D **69**(6), 067703 (2004).

[75] H. Takayama, Y. R. Lin-Liu, and K. Maki, *Continuum model for solitons in polyacetylene*, Phys. Rev. B **21**(6), 2388–2393 (1980).

[76] D. K. Campbell and A. R. Bishop, *Solitons in polyacetylene and relativistic-field-theory models*, Phys. Rev. B **24**(8), 4859–4862 (1981).

[77] A. F. Andreev, *Thermal conductivity of the intermediate state of superconductors.*, Zh.Eksp.Theor.Fiz. **46**, 1823 (1964), (Sov.Phys.-JETP 1964, 19, 1228).

[78] L. P. Pitaevskii, in K. Bennemann and J. B. Ketterson, eds., *Superconductivity* (Springer Berlin Heidelberg, 2008), pp. 27–71.

[79] P. Fulde and R. A. Ferrell, *Superconductivity in a Strong Spin-Exchange Field*, Phys. Rev. **135**(3A), A550–A563 (1964).

[80] A. Larkin and Y. Ovchinnikov, *Nonuniform state of superconductors*, Zh. Eksp. Teor. Fiz. **47**, 1136 (1964).

[81] M. W. Zwierlein, A. Schirotzek, C. H. Schunck, and W. Ketterle, *Fermionic superfluidity with imbalanced spin populations*, Science **311**(5760), 492 (2006).

[82] M. W. Zwierlein, C. H. Schunck, A. Schirotzek, and W. Ketterle, *Direct observation of the superfluid phase transition in ultracold Fermi gases*, Nature **442**(7098), 54 (2006).

[83] G. B. Partridge, W. Li, R. I. Kamar, Y.-a. Liao, and R. G. Hulet, *Pairing and phase separation in a polarized Fermi gas*, Science **311**(5760), 503 (2006).

[84] G. Partridge, W. Li, Y. Liao, R. G. Hulet, M. Haque, and H. Stoof, *Deformation of a trapped Fermi gas with unequal spin populations*, Phys. Rev. Lett. **97**(19), 190407 (2006).

[85] E. Wille, F. M. Spiegelhalder, G. Kerner, D. Naik, A. Trenkwalder, G. Hendl, F. Schreck, R. Grimm, T. G. Tiecke, J. T. M. Walraven, *et al.*, *Exploring an Ultracold Fermi-Fermi Mixture: Interspecies Feshbach Resonances and Scattering Properties of Li 6 and K 40*, Phys. Rev. Lett. **100**(5), 053201 (2008).

[86] R. Grimm, *private communication.*

[87] M. Lu, N. Q. Burdick, and B. L. Lev, *Quantum degenerate dipolar Fermi gas*, Phys. Rev. Lett **108,**, 215301 (2012).

[88] A. Frisch, K. Aikawa, M. Mark, F. Ferlaino, E. Berseneva, and S. Kotochigova, *Hyperfine structure of laser-cooling transitions in fermionic erbium-167*, Phys. Rev. A **88**(3), 032508 (2013).

[89] W. Meissner and R. Ochsenfeld, *Ein neuer Effekt bei Eintritt der Supraleitfähigkeit*, Naturwissenschaften **21**(44), 787 (1933).

[90] L. Shubnikov, V. Khotkevich, D. Shepelev Yu, and N. Riabinin Yu, *Magnetic properties of superconducting metals and alloys*, Zh. Eksp. Teor. Fiz **7**, 221 (1937).

[91] A. A. Abrikosov, *Opredelenie velichiny dielektricheskoi pronitsaemosti v normal'noi provodimosti sverkhprovodnikov*, Dokl. Akad. Nauk SSSR [Sov. Phys. Dokl.] **86**(43), 489 (1952).

[92] P. S. Riseborough, G. M. Schmiedeshoff, and J. L. Smith, in K. Bennemann and J. B. Ketterson, eds., *Superconductivity* (Springer Berlin Heidelberg, 2008), pp. 1031–1154.

[93] Y. Matsuda and H. Shimahara, *Fulde–Ferrell–Larkin–Ovchinnikov State in Heavy Fermion Superconductors*, J. Phys. Soc. Jpn. **76**(5), 051005 (2007).

[94] R. Kleiner, R. Hott, T. Wolf, G. Zwicknagl, M. Belogolovskii, S. T. Ruggiero, S. C. Wimbush, F. Grilli, and F. Sirois, *Fundamentals* (Wiley-VCH Verlag GmbH & Co. KGaA, 2015), chap. 1, pp. 1–104, ISBN 9783527670635, `http://dx.doi.org/10.1002/9783527670635.ch1`.

[95] H. Heiselberg, in W. Zwerger, ed., *The BCS-BEC Crossover and the Unitary Fermi Gas* (Springer Berlin Heidelberg, 2012), vol. 836 of *Lecture Notes in Physics*, pp. 49–97.

[96] G. Başar and G. V. Dunne, *Twisted kink crystal in the chiral Gross-Neveu model*, Phys. Rev. D **78**(6), 065022 (2008).

[97] M. Thies, *From relativistic quantum fields to condensed matter and back again: updating the Gross–Neveu phase diagram*, J. Phys. A **39**(41), 12707–12734 (2006).

[98] G. Bertsch, in R. Bishop, K. Gernoth, N. Walet, and Y. Xian, eds., *Recent Progress in Many-Body Theories.* (World Scientific, 2000).

[99] M. G. Endres, D. B. Kaplan, J.-W. Lee, and A. N. Nicholson, *Lattice Monte Carlo calculations for unitary fermions in a finite box*, Phys. Rev. A **87**(2), 023615 (2013).

[100] J. Carlson, S.-Y. Chang, V. R. Pandharipande, and K. E. Schmidt, *Superfluid Fermi Gases with Large Scattering Length*, Phys. Rev. Lett. **91**(5), 050401 (2003).

[101] G. E. Astrakharchik, J. Boronat, J. Casulleras, Giorgini, and S., *Equation of State of a Fermi Gas in the BEC-BCS Crossover: A Quantum Monte Carlo Study*, Phys. Rev. Lett. **93**(20), 200404 (2004).

[102] J. Carlson and S. Reddy, *Asymmetric Two-Component Fermion Systems in Strong Coupling*, Phys. Rev. Lett. **95**(6), 060401 (2005).

[103] D. Lee, *Ground-state energy of spin-$\frac{1}{2}$ fermions in the unitary limit*, Phys. Rev. B **73**(11), 115112 (2006).

[104] A. Bulgac, J. E. Drut, and P. Magierski, *Quantum Monte Carlo simulations of the BCS-BEC crossover at finite temperature*, Phys. Rev. A **78**(2), 023625 (2008).

[105] T. Abe and R. Seki, *From low-density neutron matter to the unitary limit*, Phys. Rev. C **79**(5), 054003 (2009).

[106] J. Carlson, S. Gandolfi, K. E. Schmidt, and S. Zhang, *Auxiliary-field quantum Monte Carlo method for strongly paired fermions*, Phys. Rev. A **84**(6), 061602 (2011).

[107] M. Bartenstein, A. Altmeyer, S. Riedl, S. Jochim, C. Chin, J. H. Denschlag, and R. Grimm, *Crossover from a Molecular Bose-Einstein Condensate to a Degenerate Fermi Gas*, Phys. Rev. Lett. **92**(12), 120401 (2004).

[108] L. Luo and J. Thomas, *Thermodynamic Measurements in a Strongly Interacting Fermi Gas*, J. Low Temp. Phys. **154**(1-2), 1 (2009).

[109] N. Navon, S. Nascimbène, F. Chevy, and C. Salomon, *The equation of state of a low-temperature Fermi gas with tunable interactions*, Science **328**(5979), 729 (2010).

[110] M. J. Ku, A. T. Sommer, L. W. Cheuk, and M. W. Zwierlein, *Revealing the superfluid lambda transition in the universal thermodynamics of a unitary Fermi gas*, Science **335**(6068), 563 (2012).

[111] F. Chevy and C. Mora, *Ultra-cold polarized Fermi gases*, Rep. Prog. Phys. **73**(11), 112401 (2010).

[112] R. H. Landau, M. J. Páez, and C. C. Bordeianu, *Computational Physics: Problem Solving with Computers* (Wiley-VCH, 2007), ISBN 978-3-527-40626-5.

[113] A. Wipf, *Statistical Approach to Quantum Field Theory: An Introduction (Lecture Notes in Physics)* (Springer, 2012), ISBN 978-3-642-33104-6.

[114] U.-J. Wiese, *An introduction to lattice field theory.*

[115] D. Lee, *Lattice simulations for few- and many-body systems*, Prog. Part. Nucl. Phys. **63**(1), 117–154 (2009).

[116] J. E. Drut and A. N. Nicholson, *Lattice methods for strongly interacting many-body systems*, J. Phys. G **40**(4), 043101 (2013).

[117] D. Roscher, J. Braun, J.-W. Chen, and J. E. Drut, *Fermi gases with imaginary mass imbalance and the sign problem in Monte Carlo calculations*, J. Phys. G **41**, 055110 (2014).

[118] J. Braun, J. E. Drut, and D. Roscher, *Zero-temperature equation of state of mass-imbalanced resonant Fermi gases*, Phys. Rev. Lett. **114**(5), 050404 (2015).

[119] N. Metropolis, A. W. Rosenbluth, M. N. Rosenbluth, A. H. Teller, and E. Teller, *Equation of State Calculations by Fast Computing Machines*, J. Chem. Phys. **21**(6), 1087 (1953).

[120] W. K. Hastings, W. K.ngs, *Monte Carlo Sampling Methods Using Markov Chains and Their Applications*, Biometrika **57**(1), pp. 97 (1970).

[121] E. Dagotto, A. Moreo, R. L. Sugar, and D. Toussaint, *Binding of holes in the Hubbard model*, Phys. Rev. B **41**(1), 811–814 (1990).

[122] M. Alford, A. Kapustin, and F. Wilczek, *Imaginary chemical potential and finite fermion density on the lattice*, Phys. Rev. D **59**(5), 054502 (1999).

[123] P. de Forcrand and O. Philipsen, *The QCD phase diagram for small densities from imaginary chemical potential*, Nucl. Phys. B **642**(1-2), 290–306 (2002).

[124] M. D'Elia and M.-P. Lombardo, *Finite density QCD via an imaginary chemical potential*, Phys. Rev. D **67**(1), 014505 (2003).

[125] J. Braun, J.-W. Chen, J. Deng, J. E. Drut, B. Friman, C.-T. Ma, and Y.-D. Tsai, *Imaginary polarization as a way to surmount the sign problem in Ab Initio calculations of spin-imbalanced Fermi gases*, Phys. Rev. Lett. **110**, 130404 (2013).

[126] M. Lombardo, **CPOD2006**, 003 (2006).

[127] R. Remmert, *Funktionentheorie* (Springer, Berlin u.a, 1995), ISBN 3-540-59075-7.

[128] F. Karbstein and M. Thies, *How to get from imaginary to real chemical potential*, Phys. Rev. D **75**(2), 025003 (2007).

[129] H. Kleinert, *Path Integrals in Quantum Mechanics, Statistics, Polymer Physics, and Financial Markets* (World Scientific Publishing Company, 2009), ISBN 978-981-4273-55-8.

[130] M. Iskin and C. A. R. Sá de Melo, *Two-Species Fermion Mixtures with Population Imbalance*, Phys. Rev. Lett. **97**(10), 100404 (2006).

[131] M. M. Parish, F. M. Marchetti, A. Lamacraft, and B. D. Simons, *Polarized Fermi Condensates with Unequal Masses: Tuning the Tricritical Point*, Phys. Rev. Lett. **98**(16), 160402 (2007).

[132] N. Bogolyubov, *On the theory of superfluidity*, J. Phys. (USSR) **11**, 23 (1947).

[133] J.-W. Chen, *private communication.*

[134] A. Roberge and N. Weiss, *Gauge theories with imaginary chemical potential and the phases of QCD*, Nucl. Phys. B **275**(4), 734–745 (1986).

[135] D. Lee, *Ground state energy at unitarity*, Phys. Rev. C **78**(2), 024001 (2008).

[136] H. F. Trotter, *On the product of semi-groups of operators*, Proc. Am. Math. Soc. **10**(4), 545–545 (1959).

[137] M. Suzuki, *Generalized Trotter's formula and systematic approximants of exponential operators and inner derivations with applications to many-body problems*, Commun. Math. Phys. **51**(2), 183–190 (1976).

[138] M. Lüscher, *Volume dependence of the energy spectrum in massive quantum field theories*, Commun. Math. Phys. **104**(2), 177–206 (1986).

[139] M. Lüscher, *Volume dependence of the energy spectrum in massive quantum field theories*, Commun. Math. Phys. **105**(2), 153–188 (1986).

[140] J. E. Drut, *Improved lattice operators for nonrelativistic fermions*, Phys. Rev. A **86**(1), 013604 (2012).

[141] D. J. Toms, *Casimir effect and topological mass*, Phys. Rev. D **21**(4), 928–932 (1980).

[142] C. Runge, *Über empirische Funktionen und die Interpolation zwischen äquidistanten Ordinaten*, Z. Math. Phys. **46**, 224–243 (1901).

[143] D. Lee, *The symmetric heavy-light ansatz*, Eur. Phys. J. A **35**(2), 171–187 (2008).

[144] A. Gezerlis, S. Gandolfi, K. E. Schmidt, and J. Carlson, *Heavy-Light Fermion Mixtures at Unitarity*, Phys. Rev. Lett. **103**(6), 060403 (2009).

[145] K. Yang, *Inhomogeneous superconducting state in quasi-one-dimensional systems*, Phys. Rev. B **63**(14), 140511 (2001).

[146] M. M. Parish, S. K. Baur, E. J. Mueller, and D. A. Huse, *Quasi-One-Dimensional Polarized Fermi Superfluids*, Phys. Rev. Lett. **99**(25), 250403 (2007).

[147] G. Orso, *Attractive Fermi Gases with Unequal Spin Populations in Highly Elongated Traps*, Phys. Rev. Lett. **98**(7), 070402 (2007).

[148] H. Hu, X.-J. Liu, and P. D. Drummond, *Phase Diagram of a Strongly Interacting Polarized Fermi Gas in One Dimension*, Phys. Rev. Lett. **98**(7), 070403 (2007).

[149] A. E. Feiguin and F. Heidrich-Meisner, *Pairing states of a polarized Fermi gas trapped in a one-dimensional optical lattice*, Phys. Rev. B **76**(22), 220508 (2007).

[150] M. Tezuka and M. Ueda, *Density-Matrix Renormalization Group Study of Trapped Imbalanced Fermi Condensates*, Phys. Rev. Lett. **100**(11), 110403 (2008).

[151] G. G. Batrouni, M. J. Wolak, F. Hébert, and V. G. Rousseau, *Pair formation and collapse in imbalanced fermion populations with unequal masses*, Europhys. Lett. **86**(4), 47006 (2009).

[152] M. Casula, D. M. Ceperley, and E. J. Mueller, *Quantum Monte Carlo study of one-dimensional trapped fermions with attractive contact interactions*, Phys. Rev. A **78**(3), 033607 (2008).

[153] B. Wang, H.-D. Chen, and S. Das Sarma, *Quantum phase diagram of fermion mixtures with population imbalance in one-dimensional optical lattices*, Phys. Rev. A **79**(5), 051604 (2009).

[154] A. Perali, A. Bianconi, A. Lanzara, and N. Saini, *The gap amplification at a shape resonance in a superlattice of quantum stripes: A mechanism for high Tc*, Solid State Commun. **100**(3), 181–186 (1996).

[155] A. A. Shanenko, M. D. Croitoru, M. Zgirski, F. M. Peeters, and K. Arutyunov, *Size-dependent enhancement of superconductivity in Al and Sn nanowires: Shape-resonance effect*, Phys. Rev. B **74**(5), 052502 (2006).

[156] D. Roscher, J. Braun, and J. E. Drut, *Inhomogeneous phases in one-dimensional mass- and spin-imbalanced Fermi gases*, Phys. Rev. A **89**(6), 063609 (2014).

[157] J. Braun, S. Finkbeiner, F. Karbstein, and D. Roscher, *On the Search for Inhomogeneous Phases in Fermionic Models*, Phys. Rev. D **91**(11), 116006 (2015).

[158] J. Braun, F. Karbstein, S. Rechenberger, and D. Roscher, *in preparation.*

[159] Y.-a. Liao, A. S. C. Rittner, T. Paprotta, W. Li, G. B. Partridge, R. G. Hulet, S. K. Baur, and E. J. Mueller, *Spin-imbalance in a one-dimensional Fermi gas*, Nature **467**(7315), 567–569 (2010).

[160] N. D. Mermin and H. Wagner, *Absence of Ferromagnetism or Antiferromagnetism in One- or Two-Dimensional Isotropic Heisenberg Models*, Phys. Rev. Lett. **17**(22), 1133–1136 (1966).

[161] P. C. Hohenberg, *Existence of Long-Range Order in One and Two Dimensions*, Phys. Rev. **158**(2), 383–386 (1967).

[162] V. L. Berezinskiǐ, *Destruction of Long-range Order in One-dimensional and Two-dimensional Systems having a Continuous Symmetry Group I. Classical Systems*, Sov. Phys. JETP **32**, 493 (1971).

[163] V. L. Berezinskiǐ, *Destruction of Long-range Order in One-dimensional and Two-dimensional Systems Possessing a Continuous Symmetry Group. II. Quantum Systems*, Sov. Phys. JETP **34**, 610 (1972).

[164] J. M. Kosterlitz and D. J. Thouless, *Ordering, metastability and phase transitions in two-dimensional systems*, J. of Phys. C **6**(7), 1181–1203 (1973).

[165] K. Arutyunov, D. Golubev, and A. Zaikin, *Superconductivity in one dimension*, Phys. Rep. **464**(1-2), 1–70 (2008).

[166] M. Buballa and S. Carignano, *Inhomogeneous chiral condensates*, Prog. Part. Nucl. Phys. **81**, 39–96 (2015).

[167] R. Casalbuoni and G. Nardulli, *Inhomogeneous superconductivity in condensed matter and QCD*, Rev. Mod. Phys. **76**(1), 263–320 (2004).

[168] L. D. Landau and V. Ginzburg, *On the theory of superconductivity*, Zh. Eksp. Teor. Fiz. **20**, 1064 (1950).

[169] L. D. Landau, E. M. Lifschitz, and L. P. Pitaevskii, *Lehrbuch der Theoretischen Physik V - Statistische Physik, Teil I* (Akademie-Verlag Berlin, 1979), ISBN 3-05-500069-2.

[170] P. G. L. Dirichlet, *Sur la convergence des séries trigonométriques qui servent à représenter une fonction arbitraire entre des limites données*, Journal für reine und angewandte Mathematik **4**, 157 (1829).

[171] L. Carleson, *On convergence and growth of partial sums of Fourier series*, Acta Math. **116**(1), 135–157 (1966).

[172] L. N. Cooper, *Bound Electron Pairs in a Degenerate Fermi Gas*, Phys. Rev. **104**(4), 1189–1190 (1956).

[173] A. M. Clogston, *Upper Limit for the Critical Field in Hard Superconductors*, Phys. Rev. Lett. **9**(6), 266–267 (1962).

[174] B. S. Chandrasekhar, *A NOTE ON THE MAXIMUM CRITICAL FIELD OF HIGH-FIELD SUPERCONDUCTORS*, Appl. Phys. Lett. **1**(1), 7 (1962).

[175] F. Marsiglio and J. P. Carbotte, *Electron-Phonon Superconductivity*, Superconductivity p. 73–162 (2008).

[176] P. Niemann and H.-W. Hammer, *Pauli-blocking effects and Cooper triples in three-component Fermi gases*, Phys. Rev. A **86**(1), 013628 (2012).

[177] L. D. Landau, *Über die Bewegung der Elektronen im Kristallgitter*, Phys. Z. Sowjetunion **3**, 644 (1933).

[178] F. Chevy, *Universal phase diagram of a strongly interacting Fermi gas with unbalanced spin populations*, Phys. Rev. A **74**(6), 063628 (2006).

[179] A. J. Leggett, *Quantum Liquids* (Oxford University Press (OUP), 2006), ISBN 9780198526438, `http://dx.doi.org/10.1093/acprof:oso/9780198526438.001.0001`.

[180] Y. Nambu and G. Jona-Lasinio, *Dynamical Model of Elementary Particles Based on an Analogy with Superconductivity. I*, Phys. Rev. **122**(1), 345–358 (1961).

[181] Y. Nambu and G. Jona-Lasinio, *Dynamical Model of Elementary Particles Based on an Analogy with Superconductivity. II*, Phys. Rev. **124**(1), 246–254 (1961).

[182] C. Ratti, M. A. Thaler, and W. Weise, *Phases of QCD: Lattice thermodynamics and a field theoretical model*, Phys. Rev. D **73**(1), 014019 (2006).

[183] F. Dautry and E. M. Nyman, *Pion condensation and the σ-model in liquid neutron matter*, Nucl. Phys. A **319**(3), 323–348 (1979).

[184] J. O. Andersen and L. T. Kyllingstad, *Pion condensation in a two-flavour NJL model: the role of charge neutrality*, J. Phys. G **37**(1), 015003 (2009).

[185] G. 't Hooft, *A two-dimensional model for mesons*, Nucl. Phys. B **75**(3), 461–470 (1974).

[186] G. Başar, G. V. Dunne, and M. Thies, *Inhomogeneous condensates in the thermodynamics of the chiral NJL 2 model*, Phys. Rev. D **79**(10), 105012 (2009).

[187] S. Weinberg, *The Quantum Theory of Fields, Volume 2: Modern Applications* (Cambridge University Press, 2005), ISBN 978-0-521-67054-8.

[188] R. Alkofer and J. Greensite, *Quark confinement: the hard problem of hadron physics*, J. Phys. G **34**(7), S3–S21 (2007).

[189] K. Fukushima, *Chiral effective model with the Polyakov loop*, Phys. Lett. B **591**(3-4), 277–284 (2004).

[190] L. D. McLerran and B. Svetitsky, *Quark liberation at high temperature: A Monte Carlo study of SU(2) gauge theory*, Phys. Rev. D **24**(2), 450–460 (1981).

[191] F. Karsch and H. W. Wyld, *Complex Langevin Simulation of the SU(3) Spin Model with Nonzero Chemical Potential*, Phys. Rev. Lett. **55**(21), 2242–2245 (1985).

[192] F. Karsch and E. Laermann, in R. C. Hwa and X.-N. Wang, eds., *Quark-Gluon Plasma* (2004), pp. 1–59.

[193] G. Boyd, J. Engels, F. Karsch, E. Laermann, C. Legeland, M. Lütgemeier, and B. Petersson, *Thermodynamics of SU(3) lattice gauge theory*, Nucl. Phys. B **469**(3), 419–444 (1996).

[194] B.-J. Schaefer, J. M. Pawlowski, and J. Wambach, *Phase structure of the Polyakov-quark-meson model*, Phys. Rev. D **76**(7), 074023 (2007).

[195] S. Carignano, D. Nickel, and M. Buballa, *Influence of vector interaction and Polyakov loop dynamics on inhomogeneous chiral symmetry breaking phases*, Phys. Rev. D **82**(5), 054009 (2010).

[196] J. Carlomagno, D. Gómez Dumm, and N. Scoccola, *Generalized Ginzburg–Landau approach to inhomogeneous phases in nonlocal chiral quark models*, Phys. Lett. B **745**, 1–4 (2015).

[197] J. Braun and A. Janot, *Dynamical locking of the chiral and the deconfinement phase transition in QCD*, Phys. Rev. D **84**(11), 114022 (2011).

[198] L. McLerran and R. D. Pisarski, *Phases of dense quarks at large*, Nucl. Phys. A **796**(1-4), 83–100 (2007).

[199] S. Weinberg, *The Quantum Theory of Fields, Volume 1: Foundations* (Cambridge University Press, 2005), ISBN 978-0-521-67053-1.

[200] I. Boettcher, J. Braun, T. K. Herbst, J. M. Pawlowski, D. Roscher, and C. Wetterich, *Phase structure of spin-imbalanced unitary Fermi gases*, Phys. Rev. A **91**(1), 013610 (2015).

[201] D. Roscher, J. Braun, and J. E. Drut, *Phase structure of mass- and spin-imbalanced unitary Fermi gases*, Phys. Rev. A **91**(5), 053611 (2015).

[202] J. E. Baarsma and H. T. C. Stoof, *Inhomogeneous superfluid phases in 6 Li- 40 K mixtures at unitarity*, Phys. Rev. A **87**(6), 063612 (2013).

[203] I. Boettcher, J. M. Pawlowski, and C. Wetterich, *Critical temperature and superfluid gap of the unitary Fermi gas from functional renormalization*, Phys. Rev. A **89**(5), 053630 (2014).

[204] J. Wang, Y. Che, L. Zhang, and Q. Chen, (2014), arXiv:1404.5696.

[205] D. E. Sheehy and L. Radzihovsky, *BEC-BCS Crossover in "Magnetized" Feshbach-Resonantly Paired Superfluids*, Phys. Rev. Lett. **96**(6), 060401 (2006).

[206] H. Hu and X.-J. Liu, *Mean-field phase diagrams of imbalanced Fermi gases near a Feshbach resonance*, Phys. Rev. A **73**(5), 051603 (2006).

[207] W. H. Dickhoff and D. Van Neck, *Many-body theory exposed!* (World Scientific, 2008), ISBN 978-981-281-379-4.

[208] J. Braun, H.-W. Hammer, P. Niemann, and D. Roscher, *in preparation.*

[209] Z. Nussinov and S. Nussinov, *Triviality of the BCS-BEC crossover in extended dimensions: Implications for the ground state energy*, Phys. Rev. A **74**(5), 053622 (2006).

[210] Y. Nishida and D. T. Son, ϵ *Expansion for a Fermi Gas at Infinite Scattering Length*, Phys. Rev. Lett. **97**(5), 050403 (2006).

[211] M. Y. Veillette, D. E. Sheehy, and L. Radzihovsky, *Large- N expansion for unitary superfluid Fermi gases*, Phys. Rev. A **75**(4), 043614 (2007).

[212] S. Diehl and C. Wetterich, *Universality in phase transitions for ultracold fermionic atoms*, Phys. Rev. A **73**(3), 033615 (2006).

[213] R. Haussmann, W. Rantner, S. Cerrito, and W. Zwerger, *Thermodynamics of the BCS-BEC crossover*, Phys. Rev. A **75**(2), 023610 (2007).

[214] N. Kaiser, *Resummation of fermionic in-medium ladder diagrams to all orders*, Nucl. Phys. A **860**(1), 41–55 (2011).

[215] T.-L. Ho, *Universal Thermodynamics of Degenerate Quantum Gases in the Unitarity Limit*, Phys. Rev. Lett. **92**(9), 090402 (2004).

[216] S. Tan, *Energetics of a strongly correlated Fermi gas*, Ann. Phys. **323**(12), 2952–2970 (2008).

[217] S. Tan, *Large momentum part of a strongly correlated Fermi gas*, Ann. Phys. **323**(12), 2971–2986 (2008).

[218] S. Tan, *Generalized virial theorem and pressure relation for a strongly correlated Fermi gas*, Ann. Phys. **323**(12), 2987–2990 (2008).

[219] C. Wetterich, *Exact evolution equation for the effective potential*, Phys. Lett. B **301**(1), 90–94 (1993).

[220] K. Wilson, *The renormalization group and the ϵ expansion*, Phys. Rep. **12**(2), 75–199 (1974).

[221] J. Berges, N. Tetradis, and C. Wetterich, *Non-perturbative renormalization flow in quantum field theory and statistical physics*, Phys. Rep. **363**(4-6), 223–386 (2002).

[222] H. Gies, *Introduction to the Functional RG and Applications to Gauge Theories*, Renormalization Group and Effective Field Theory Approaches to Many-Body Systems p. 287–348 (2012).

[223] D. F. Litim and J. M. Pawlowski, *Completeness and consistency of renormalization group flows*, Phys. Rev. D **66**(2), 025030 (2002).

[224] Y. Tanizaki, G. Fejös, and T. Hatsuda, *Fermionic functional renormalization group approach to superfluid phase transition*, Prog. Theor. Exp. Phys. **2014**(4), 43I01–0 (2014).

[225] J. Braun, H. Gies, L. Janssen, and D. Roscher, *Phase structure of many-flavor QED*$_3$, Phys. Rev. D **90**(3), 036002 (2014).

[226] S. Diehl, H. Gies, J. M. Pawlowski, and C. Wetterich, *Renormalization flow and universality for ultracold fermionic atoms*, Phys. Rev. A **76**(5), 053627 (2007).

[227] S. Diehl, H. Gies, J. M. Pawlowski, and C. Wetterich, *Flow equations for the BCS-BEC crossover*, Phys. Rev. A **76**(2), 021602 (2007).

[228] I. Boettcher, J. M. Pawlowski, and S. Diehl, *Ultracold atoms and the Functional Renormalization Group*, Nucl. Phys. B - Proc. Suppl. **228**, 63–135 (2012).

[229] H. Gies and C. Wetterich, *Renormalization flow of bound states*, Phys. Rev. D **65**(6), 065001 (2002).

[230] S. Floerchinger, M. Scherer, S. Diehl, and C. Wetterich, *Particle-hole fluctuations in BCS-BEC crossover*, Phys. Rev. B **78**(17), 174528 (2008).

[231] D. F. Litim, *Optimisation of the exact renormalisation group*, Phys. Lett. B **486**(1-2), 92–99 (2000).

[232] D. F. Litim, *Optimized renormalization group flows*, Phys. Rev. D **64**(10), 105007 (2001).

[233] N. Dupuis and K. Sengupta, *Non-perturbative renormalization group approach to zero-temperature Bose systems*, Europhys. Lett. **80**(5), 50007 (2007).

[234] C. Wetterich, *Functional renormalization for quantum phase transitions with nonrelativistic bosons*, Phys. Rev. B **77**(6), 064504 (2008).

[235] P. Jakubczyk, W. Metzner, and H. Yamase, *Turning a First Order Quantum Phase Transition Continuous by Fluctuations: General Flow Equations and Application to d -Wave Pomeranchuk Instability*, Phys. Rev. Lett. **103**(22), 220602 (2009).

[236] P. Strack and P. Jakubczyk, *Fluctuations of Imbalanced Fermionic Superfluids in Two Dimensions Induce Continuous Quantum Phase Transitions and Non-Fermi-Liquid Behavior*, Phys. Rev. X **4**(2), 021012 (2014).

[237] A. Savitzky and M. J. E. Golay, *Smoothing and Differentiation of Data by Simplified Least Squares Procedures.*, Anal. Chem. **36**(8), 1627–1639 (1964).

[238] G. Engeln-Mullges, *Formelsammlung zur numerischen Mathematik mit Turbo-Pascal-Programmen (German Edition)* (B.I. Wissenschaftsverlag, 1991), ISBN 3-411-15003-3.

[239] T. K. Herbst, *private communication.*

[240] D. F. Litim, J. M. Pawlowski, and L. Vergara, (2006), arXiv:hep-th/0602140.

[241] B. Krippa, *Pairing in asymmetric many-fermion systems: Functional renormalisation group approach*, Phys. Lett. B **744**, 288–292 (2015).

[242] O. Goulko and M. Wingate, *Thermodynamics of balanced and slightly spin-imbalanced Fermi gases at unitarity*, Phys. Rev. A **82**(5), 053621 (2010).

[243] N. Navon, S. Nascimbène, X. Leyronas, F. Chevy, and C. Salomon, *Condensation energy of a spin-1/2 strongly interacting Fermi gas*, Phys. Rev. A **88**(6), 063614 (2013).

[244] J. Braun, *Thermodynamics of QCD low-energy models and the derivative expansion of the effective action*, Phys. Rev. D **81**(1), 016008 (2010).

[245] C. A. R. Sá de Melo, M. Randeria, and J. R. Engelbrecht, *Crossover from BCS to Bose superconductivity: Transition temperature and time-dependent Ginzburg-Landau theory*, Phys. Rev. Lett. **71**(19), 3202–3205 (1993).

[246] M. Randeria and N. Trivedi, *PAIRING CORRELATIONS ABOVE Tc AND PSEUDOGAPS IN UNDERDOPED CUPRATES*, J. Phys. Chem. Solids **59**(10-12), 1754–1758 (1998).

[247] M. Randeria, *Precursor Pairing Correlations and Pseudogaps*, arXiv:cond-mat/9710223.

[248] J. P. Gaebler, J. T. Stewart, T. E. Drake, D. S. Jin, A. Perali, P. Pieri, and G. C. Strinati, *Observation of pseudogap behaviour in a strongly interacting Fermi gas*, Nat. Phys. **6**(8), 569–573 (2010).

[249] A. Perali, F. Palestini, P. Pieri, G. C. Strinati, J. T. Stewart, J. P. Gaebler, T. E. Drake, and D. S. Jin, *Evolution of the Normal State of a Strongly Interacting Fermi Gas from a Pseudogap Phase to a Molecular Bose Gas*, Phys. Rev. Lett. **106**(6), 060402 (2011).

[250] Y. Sagi, T. E. Drake, R. Paudel, R. Chapurin, and D. S. Jin, *Breakdown of the Fermi Liquid Description for Strongly Interacting Fermions*, Phys. Rev. Lett. **114**(7), 075301 (2015).

[251] S. Tsuchiya, R. Watanabe, and Y. Ohashi, *Single-particle properties and pseudogap effects in the BCS-BEC crossover regime of an ultracold Fermi gas above T c*, Phys. Rev. A **80**(3), 033613 (2009).

[252] R. Watanabe, S. Tsuchiya, and Y. Ohashi, *Superfluid density of states and pseudogap phenomenon in the BCS-BEC crossover regime of a superfluid Fermi gas*, Phys. Rev. A **82**(4), 043630 (2010).

[253] G. Sarma, *On the influence of a uniform exchange field acting on the spins of the conduction electrons in a superconductor*, J. Phys. Chem. Solids **24**(8), 1029–1032 (1963).

[254] W. V. Liu and F. Wilczek, *Interior Gap Superfluidity*, Phys. Rev. Lett. **90**(4), 047002 (2003).

[255] I. Boettcher, T. Herbst, J. Pawlowski, N. Strodthoff, L. von Smekal, and C. Wetterich, *Sarma phase in relativistic and non-relativistic systems*, Phys. Lett. B **742**, 86–93 (2015).

[256] H. C. Krahl, S. Friederich, and C. Wetterich, *Incommensurate antiferromagnetic fluctuations in the two-dimensional Hubbard model*, Phys. Rev. B **80**(1), 014436 (2009).

[257] J. Hubbard, *Electron Correlations in Narrow Energy Bands*, Proc. R. Soc. A **276**(1365), 238–257 (1963).

[258] M. C. Boyer, W. D. Wise, K. Chatterjee, M. Yi, T. Kondo, T. Takeuchi, H. Ikuta, and E. W. Hudson, *Imaging the two gaps of the high-temperature superconductor Bi2Sr2CuO6+x*, Nat. Phys. **3**(11), 802–806 (2007).

[259] R. Schmidt and T. Enss, *Excitation spectra and rf response near the polaron-to-molecule transition from the functional renormalization group*, Phys. Rev. A **83**(6), 063620 (2011).

Danke!

While writing this thesis, I often faced the problem of putting complicated issues into understandable, yet fully representative words. Indeed, it appears to me that it is even harder to express in an adequate and comprehensive way my gratitude towards my advisor Jens Braun for his tremendous support during the whole time of my PhD studies.

From the choice of the primary goals, over the uncountably many fruitful discussions about physics and much more, his sharing of experience, and up to joint publications, the research this thesis is based on bears his mark. I'm also grateful for his confidence regarding teaching and the external representation of the group, supporting me in these and many other fields - not least also in the fabrication of this thesis. While, on the one hand, his guidance and overview opened up fertile areas of research to me, there was always room to pursue my own ideas. It is this well-balanced mixture of guidance and freedom that made possible many of the results at hand in the first place.

Thank you for everything!!!

Large portions of my research owe its success to collaborations with other physicists. In particular, I would like to thank Joaquín E. Drut. His practical implementation of our basic ideas in Monte Carlo simulations of imbalanced systems were a great success. His inventiveness and his always friendly and optimistic mindset, but also his concrete and helpful comments have contributed a lot also to the other projects and their presentation.

For many enlightening discussions and subsequent publications, I would like to thank Igor Boettcher, Jiunn-Wei Chen, Stefan Finkbeiner, Hans-Werner Hammer, Tina Herbst, Thomas Jahn, Felix Karbstein, Patrick Niemann, Martin Pospiech and Stefan Rechenberger.

I would like to thank all members of our group for a continuously superb working atmosphere. The premium-quality discussions about physics and... other subjects with Stefan Rechenberger and Sandra Kemler deserve a special mention. In the end, it is not only knowledge about physics that facilitates the achievement of a PhD. I would like to thank Stefan Rechenberger for proofreading and Patrick Niemann and Sandra Kemler for helping me to comply with the diverse administrative requirements. Sandra, you are truly a source of administrative wisdom and in-depth understanding of the dark mysteries of the university!

It is not only professional collaborations that foster the flourishing of PhD studies. Besides the persons mentioned so far, there are many others who have their share in the success of my endeavor.

Therefore, I would like to thank my growth group for the great time here in Darmstadt - and for friendship in the best sense of the word!

Rike, you gave me an enormous boost in the decisive final stage of this work, when I was really in need of it. Thank you for this, but above all for who and what and how you are!

Almut and Basti, you are the best siblings I could think of. I am not going to go into any details here, but your fundamental and practical support was and is invaluably precious.

Mom and Dad, it is outright impossible to choose something representative of the unmeasurable amount of good I owe to you. Let me put it this way: without your support, I would never have been able to produce this thesis.

Therefore, I am dedicating it to you.

It is good to give thanks to the LORD, to sing praises to your name, O Most High;
to declare your steadfast love in the morning, and your faithfulness by night.
How great are your works, O LORD! Your thoughts are very deep!
Psalm 92,1-2+6

Das Verfassen dieser Arbeit stellte mich des Öfteren vor das Problem, recht komplexe Sachverhalte in verständliche und doch korrekt repräsentierende Worte zu fassen. Tatsächlich erscheint es mir jetzt sogar noch weitaus schwieriger, meinen Dank für die enorme Unterstützung, die ich während meiner gesamten Promotionszeit von meinem Doktorvater Jens Braun erfahren habe, umfassend und angemessen auszudrücken.
Angefangen bei der grundlegenden Auswahl der Zielrichtung über die unzähligen fruchtbaren Diskussionen fachlicher und darüberhinausweisender Natur, das Teilhabenlassen an seinem Erfahrungsschatz bis hin zu gemeinsamen Publikationen trägt die dieser Arbeit zugrundeliegende Forschung seinen Stempel. Nicht unerwähnt lassen möchte ich auch sein in mich gesetztes Vertrauen hinsichtlich der Lehre und der Außendarstellung der Arbeitsgruppe bei gleichzeitiger praktischer Unterstützung in diesen und vielen weiteren Fragen, nicht zuletzt auch bei der Anfertigung der vorliegenden Arbeit.
Während mich seine Anleitung und sein Überblick einerseits auf mehrere ertragreiche Forschungsfelder führten, hatte ich andererseits immer genügend Spielraum, auch eigene Ideen zu verfolgen. Es war diese gelungene Mischung aus Führung und Freiheit, die viele der vorliegenden Ergebnisse erst ermöglicht hat.
Danke für alles!!!
Große Teile meiner Forschung verdankt ihre Ergebnisse der Zusammenarbeit mit weiteren Physikern. Insbesondere möchte ich hier Joaquín E. Drut nennen. Seine praktische Umsetzung der grundlegenden Ideen führten die Monte-Carlo-Simulationen für polarisierte Systeme zu sichtbarem Erfolg. Sein Ideenreichtum und seine immer freundliche und optimistische Haltung, sowie nicht zuletzt auch konkrete, hilfreiche Kommentare haben viel zu den anderen Projekten und ihrer Präsentation beigetragen.
Für viele erhellende Diskussionen, die schließlich in Publikationen mündeten, möchte ich auch Igor Boettcher, Jiunn-Wei Chen, Stefan Finkbeiner, Hans-Werner Hammer, Tina Herbst, Thomas Jahn, Felix Karbstein, Patrick Niemann, Martin Pospiech und Stefan Rechenberger danken.
Für eine stets hervorragende Arbeitsatmosphäre gilt allen Mitgliedern der Arbeitsgruppe mein Dank. Besonders hervorheben möchte ich dabei die hochwertigen Diskussionen über Physik und... Anderes mit Stefan Rechenberger und Sandra Kemler, welche zudem eine unerschöpfliche Quelle der Verwaltungsweisheit und des Universitätenverständnisses für mich war. Letztendlich reicht Physikwissen allein zum Erlangen eines Doktorgrades nicht aus, weshalb ich Stefan Rechenberger auch für sein Korrekturlesen sowie Sandra Kemler und Patrick Niemann für ihre Hilfe bei der Einhaltung diverser Verwaltungsvorschriften danken möchte.
Es ist nicht nur fachliche Zusammenarbeit, die eine solche Arbeit gedeihen lässt. Neben den bisher genannten Personen haben auch eine Reihe weiterer recht direkten Anteil am Gelingen des Unternehmens Promotion.
Meinem Hauskreis möchte ich fuer die geniale gemeinsame Zeit hier in Darmstadt danken - und für echte Freundschaft im besten Sinne!
Rike, du hast mir in der entscheidenden Endphase einen enormen Boost verschafft, als ich ihn sehr gut brauchen konnte. Danke dir dafür, aber vor allem für wer und was und wie du bist!
Almut und Basti, ihr seid die besten Geschwister die ich mir vorstellen kann. Die Details gehören hier nicht her, aber euer grundlegender und ganz praktischer Beistand war und ist unschätzbar wertvoll!
Mama und Papa, es ist unmöglich aus der unzählbaren Menge guter Dinge, die ich euch zu verdanken habe, etwas hinreichend repräsentatives zur direkten Erwähnung auszuwählen. Es ist einfach so: ohne eure Unterstützung gäbe es diese Arbeit und was dahintersteht nicht.
Und deshalb möchte ich sie euch widmen.

Es ist gut, den HERRN zu preisen und deinen Namen, du Höchster, zu besingen;
am Morgen zu verkünden deine Gnade, und deine Treue in den Nächten.
Wie groß sind deine Werke, HERR. Sehr tief sind deine Gedanken!
Psalm 92,1-2+6

Lebenslauf

Name	Dietrich Roscher
Geburtsdatum	24.08.1987
Geburtsort	Schlema
Staatsangehörigkeit	deutsch

10. 2012 -	Wissenschaftlicher Mitarbeiter Doktorand	Technische Universität Darmstadt Intitut für Kernphysik
08. 2010 - 07. 2011	Auslandsstudium	Michigan State University East Lansing, USA Abschluss: Master of Science
04. 2007 - 09. 2012	Physikstudium	Friedrich-Schiller-Universität Jena Abschluss: Diplom
07. 2006 - 03. 2007	Wehrdienst	17./LwAusbRgt 1 Strausberg AbgTZg 132 Schwarzenbach/Wald
07. 2006	Abitur	Clemens-Winkler-Gymnasium Aue

Erklärung

Ich erkläre hiermit, dass ich die vorliegende Dissertation selbstständig verfasst, keine anderen als die angegebenen Hilfsmittel verwendet und zuvor noch keinen Promotionsversuch unternommen habe.

——————————————— ———————————————

Ort, Datum Unterschrift